TESIS DE LA UNIVERSIDAD
DE ZARAGOZA

2024

259

Asier Urriolabeitia Rodrigo

Computational Study of Homogeneous Rh and Ir Catalysts for the Activation of Small Molecules

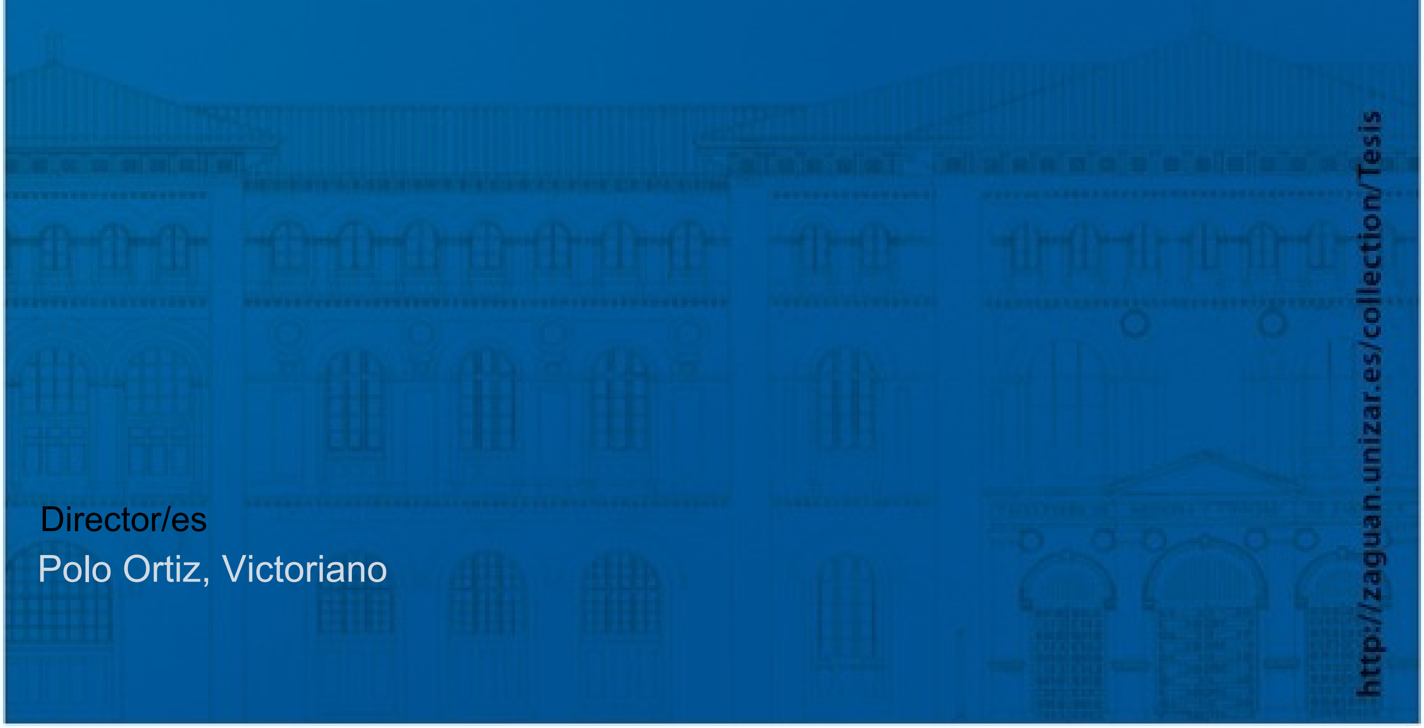

Director/es
Polo Ortiz, Victoriano

ISSN 2254-7606

Prensas de la Universidad
Universidad Zaragoza

Universidad de Zaragoza
Servicio de Publicaciones

ISSN 2254-7606

Tesis Doctoral

COMPUTATIONAL STUDY OF HOMOGENEOUS RH AND IR CATALYSTS FOR THE ACTIVATION OF SMALL MOLECULES

Autor

Asier Urriolabeitia Rodrigo

Director/es

Polo Ortiz, Victoriano

UNIVERSIDAD DE ZARAGOZA
Escuela de Doctorado

Programa de Doctorado en Química Física

2024

Doctoral Thesis

Computational Study of Homogeneous Rh and Ir Catalysts for the Activation of Small Molecules

Asier Urriolabeitia Rodrigo

Supervised by Dr. Víctor Polo Ortiz

Departamento de Química Física

Facultad de Ciencias

Universidad de Zaragoza

2023

Victoriano Polo Ortiz, Catedrático de Universidad de la Facultad de Ciencias en el Departamento de Química Física de la Universidad de Zaragoza,

CERTIFICA:

Que la presente Memoria titulada "Computational Study of Homogeneous Rh and Ir Catalysts for the Activation of Small Molecules" ha sido realizada en el Departamento de Química Física de la Universidad de Zaragoza bajo mi dirección y autoriza su presentación para que sea calificada como Tesis Doctoral. Asimismo, hace constar la realización una estancia de tres meses en el "Hylleraas Centre, Department of Chemistry" (Universidad de Oslo, Noruega), autorizando la solicitud a la mención internacional en el título de Doctor.

Zaragoza, a 12 de diciembre de 2023

Fdo: Dr Victoriano Polo Ortiz.

Agradecimientos

En primer lugar, me gustaría agradecer al director de esta Tesis, el Dr. Victor Polo por tener paciencia conmigo y darme espacio para trabajar y aprender por mi cuenta, pero estar ahí cuando necesitaba una mano. Durante estos años me ha enseñado mucho entre cafés, sobre Química, este mundillo tan particular que es la Universidad y muchas más cosas que seguro me ayudaran en el futuro.

También quiero dar gracias a los dos veteranos del despacho, Julen y Rubén, quienes, aunque no me han acompañado durante todo este viaje los he tenido siempre muy presentes. Desde el día en que estaba debatiendo si sumergirme en este rinconcito de la Química, que aunque me llamaba mucho, no tenía ni idea de lo grande y bonito que podía ser, me recibieron con los brazos abiertos y me han ayudado y dado consejo siempre que han podido. Solo con el tiempo me di cuenta de los dos fenómenos con los que tuve la suerte de compartir despacho: investigadores brillantes, motivados, con un gran amor por la Ciencia y una carrera impresionante; espero poder seguir su ejemplo. Asimismo, a Sergio, otro pedazo de investigador y compañero con el que he tenido la suerte de compartir despacho; gracias por todas las charlas y risas que hemos compartido entre rato y rato metidos en nuestros ordenadores. Y a las nuevas incorporaciones, Noushin y Lucia, que tanta vida han dado al despacho.

Igualmente, quiero expresar mi agradecimiento y reconocer la labor de los compañeros experimentales con los que he compartidos estos trabajos, María, Jefferson, Pablo y Marina, cuyo conocimiento, buena mano y arduo trabajo han hecho esta Tesis posible. Un especial agradecimiento al Dr. Ricardo Castarlenas, mi supervisor de TFG y con quien desde entonces he tenido el privilegio de seguir colaborando desde el lado computacional. Siempre he apreciado su humor y honestidad. Aprendí mucho sobre la catálisis en su laboratorio y tengo la certeza de que el tiempo que pasé ahí me ha hecho un mejor químico computacional.

Asimismo, me gustaría agradecer al difunto Dr. José Ignacio García Laureiro, quien me introdujo al mundo de los cálculos computacionales. Fue un mentor dedicado y jovial; su entusiasmo y amor por la ciencia eran contagiosos.

A su vez, agradecer a todos mis compañeros del TCCM (Raúl, Miguel, Iker, Miriam, María…) que han hecho de este máster una experiencia inolvidable. Del mismo modo, a todos mis compañeros de carrera aquí en Zaragoza con los que tantas horas entre apuntes he pasado y que han quedado como grandes amistades (Nicol, Pola, Jaime, David, Manolo…). A ver si después de esto podemos hacer el viaje de fin de curso que aún tenemos pendiente.

También agradecer la financiación proporcionada por el Ministerio de Ciencia, Innovación y Universidades.

No puedo dejar de mencionar a todos los profesores del departamento (Carlos, Héctor, Asún…) que tanto me han ayudado durante mis primeros pasos como profesor. He tenido la enorme suerte que en mi último año de tesis se me dio la oportunidad de cubrir una plaza de profesor en el Departamento. Esta experiencia me ha dado una nueva apreciación del trabajo de muchos profesores. Aunque el trabajo se me hizo más cuesta arriba de lo que esperaba, disfrute mucho de ver el entusiasmo de jóvenes químicos y químicas y me convenció totalmente de que esto es lo que quiero hacer.

Finalmente, quiero agradecer a mi familia porque han creído en mí y me han apoyado en cada paso del camino. A mi hermano porque siempre hemos sido libros abiertos el uno con el otro. A mi padre, porque siempre ha estado encantado de escucharme desahogarme sobre los distintos problemas que me iban surgiendo y darme consejo experto. A mi madre, por buscar siempre una excusa para juntar a la familia mientras el resto nos encerramos en nuestro trabajo. Así como el de mi amigo Diego, siempre se ha preocupado por mí y ha sacado tiempo para escucharme y hacerme reír. Pero a quien más tengo que agradecer es a mi novia Sara, que ha estado a mi lado desde el principio y a cada año más unidos. Faltan las palabras para decir todo lo que has traído a mi vida. Es que ya no me la imagino sin ti, porque compartimos mucho más que la Química, cosas como la música, la cocina y los viajes con los que hemos hecho tantos bonitos recuerdos. Gracias, porque nunca has dudado en dedicarme tanta ayuda como te ha sido posible durante todo este tiempo. Y por saber apoyarme y darme confianza durante los momentos de dudas y frustraciones. Te quiero Sara.

Abreviations

Abbreviations used along the dissertation are collected below:

Coe	Cyclooctene
CMD	Concerted metalation-deprotonation
CNC	Pincer ligand coordinating to the metal through two C atoms and a central N atom
DFT	Density Functional Theory
HF	Hartree-Fock method
FA	Formic acid
FADH	Formic acid dehydrogenation
FLP	Frustrated Lewis pair
GGA	Generalised Gradient Approximation
KIE	Kinetic isotopic effect
KS	Kohn-Sham method
IPr	1,3-bis-(2,6-diisopropylphenyl)imidazol-2-ylidene
LAPS	Ligand Assisted Proton Shuttle
LDA	Local Density Approximation
LOHC	Liquid Organic Hydrogen Carrier
m-GGA	meta-Generalised Gradient Approximation
Mes	Mesitylene or 1,3,5-trimethylbenzene
NBO	Natural Bond Orbital
NHC	N-Heterocyclic Carbene
NMR	Nuclear Magnetic Resonance
NSi	4-methyl-pyridin-2-yloxy-dimethylsilane
TCC	Theoretical and Computational Chemistry
TOF	Turnover Frequency

Abstract

This Ph.D. Thesis is devoted to the computational study of a series of homogeneous Rh- or Ir-based organometallic catalysts using DFT methodologies. These studies take an emphasis on the interplay between computational and experimental methodologies, incorporating various experimentally-derived insights to aid the proposal of potential reaction pathways to explore as well as validating the computationally-obtained results. The studied systems are divided into two categories, the first one consisting of reactions involving CO_2 and derivatives of it and the second one centered on functionalization reactions of terminal alkynes. A summary of the studied reactions is presented below:

The first category includes the analysis of three catalytic systems related to CO_2 utilization. The activation and selective transformation of these typically inert molecules constitutes a relevant target in the development of environmentally friendly processes.

1. The selective reduction of CO_2 to acetals using hydrosilanes enabled by an Ir-NSi catalyst and a $B(C_6F_5)_3$ cocatalysts. These products can be utilized as an eco-friendly substitute to the formaldehyde for many synthetic applications.
2. The dehydrogenation of HCOOH catalyzed by an Ir-NSi complex in neat HCOOH with NEt_3 as additive. The detailed understanding of this reaction constitutes an essential step to the potential use of CO_2 as H_2 carrier, a promising energy vector.
3. The dehydrogenation of HCOOH catalyzed by a Rh-CNC catalyst in neat HCOOH with HCOONa as additive. This catalyst with a pincer ligand achieved the highest TOF for this reaction with a Rh catalyst in neat HCOOH to date.

The second category addresses the study of two reactions related to the selective functionalization of terminal alkynes, which are highly-sought after reactions due to their diverse applications in synthetic routes. These reactions improve upon the poor selectivity of traditional approaches through a reactivity based on metal-ligand cooperativity.

4. The *gem*-selective dimerization of terminal alkynes enabled by Rh-IPr complex, in which the 2-pyridonate ligand serves as proton shuttle.
5. The *gem*-specific *O*-selective hydropyridonation of terminal alkynes catalyzed by a similar Rh-IPr catalyst, where the 2-pyridone displays a comparable behavior but ultimately acts as substrate.

The determination of the operating mechanisms for these catalyzed reactions, allows to unveil the factors governing the activity and selectivity for these processes. These insights pave the way for the rational design of novel more efficient and environmentally respectful systems.

Resumen

Esta Tesis Doctoral está dedicada al estudio computacional de unos catalizadores organometálicos homogéneos de Rh o Ir empleando metodologías de DFT. Estos estudios ponen énfasis en la interacción entre metodologías computacionales y experimentales, incorporando diversas evidencias experimentalmente para ayudar en la propuesta de rutas de reacción, así como en la validación de los resultados computacionales. Los sistemas estudiados se dividen en dos categorías: reacciones que involucran CO_2 y derivados de este, y reacciones de funcionalización de alquinos terminales. A continuación, se presenta un resumen de las reacciones estudiadas:

La primera categoría incluye el análisis de tres sistemas catalíticos relacionados con la utilización de CO_2. La activación y transformación selectiva de estas moléculas típicamente inertes constituyen un objetivo relevante en el desarrollo de procesos respetuosos con el medio ambiente.

1. La reducción selectiva de CO_2 a acetales con hidrosilanos posibilitada por un catalizador Ir-NSi y un cocatalizador $B(C_6F_5)_3$. Estos productos pueden utilizarse como sustitutos sostenibles del formaldehído en aplicaciones sintéticas.
2. La deshidrogenación de HCOOH catalizada por un complejo Ir-NSi en HCOOH puro con NEt_3 como aditivo. Una comprensión detallada de la reacción es clave para el uso de CO_2 como portador de H_2, un prometedor vector energético.
3. La deshidrogenación de HCOOH catalizada por un complejo Rh-CNC en HCOOH puro con HCOONa como aditivo. Este catalizador con un ligando tipo pinza logró la mayor TOF para esta reacción con un catalizador de Rh hasta la fecha.

La segunda categoría aborda el estudio de dos reacciones relacionadas con la funcionalización selectiva de alquinos terminales, las cuales son de gran interés debido a sus diversas aplicaciones en rutas sintéticas. Estas reacciones mejoran la selectividad de los enfoques tradicionales mediante reactividad basada en cooperatividad metal-ligando.

4. La dimerización selectiva de alquinos terminales habilitada por el complejo Rh-IPr, en el que el ligando 2-piridonato sirve como lanzadera de protones.
5. La hidropiridinación *O*-selectiva *gem*-específica de alquinos terminales catalizada por un catalizador Rh-IPr similar, donde la 2-piridona muestra un comportamiento comparable, pero en ultima estancia actúa como sustrato.

Determinar los mecanismos operativos para estas reacciones catalizadas permite revelar los factores rigiendo la actividad y selectividad de estos procesos. Estos resultados allanan el camino para el diseño racional de sistemas novedosos, más eficientes y ecológicos.

Table of Contents

Chapter 1:
General Introduction

It was during one of the walks to the NMR machine, that my then End of Degree Thesis supervisor, Ricardo, told me something that would be leave a lasting impression in me: “The problem with good catalysis, is that it cannot be seen. Things happen too fast and only a small fraction of everything going on can be captured”. The following year I enrolled into the master’s degree in Theoretical Chemistry and Computational Modelling. While good catalysis may remain invisible, it can be modelled.

1.1 Catalysis in Modern Chemistry: shaping a sustainable chemical future

Modern chemical processes constitute a critical pilar to our standard of living. There is a constant demand of countless chemical products for a wide spectrum of essential applications, to name a few: fuels, fertilizers, cleaning agents, pharmaceutical compounds, and a variety of materials, such as plastics, epoxy resins and synthetic fibers. Nevertheless, the production of many of these commodities can have a significant environmental impact, because of their requirement for hard-to-come-by reactants, high energy consumption or hazardous reaction conditions as well as the emission of contaminant by-products. Therefore, while vital to our well-being, the activity of the chemical industry contributes to many problems threatening our future quality of life, including global warming, the contamination of rivers and seas and the depletion of natural resources.

Thus, there is an ever-growing interest in a more environmentally conscious Chemistry, which is capable to satisfy the consistent demand for these products in a more responsible way. This effort started mid-20th century, as the long-term repercussions of pollution and chemical wastes on the population and environment had become both evident and a pressing matter. In this context, a new goal for chemists and engineers became imperative, a reform of the chemical sector that led to a sustainable future. This undertaking is epitomized by the 12 principles of Green Chemistry, proposed by Paul Anastas and John Warner as the century came to a close.[1,2] In 2015 these principles, shown in Figure 1.1, were included by the United Nations in the Sustainable Development Goals, a framework designed with the goal of setting guidelines for a fair and responsible development of all nations, ensuring respect for both humans and ecosystems.[3]

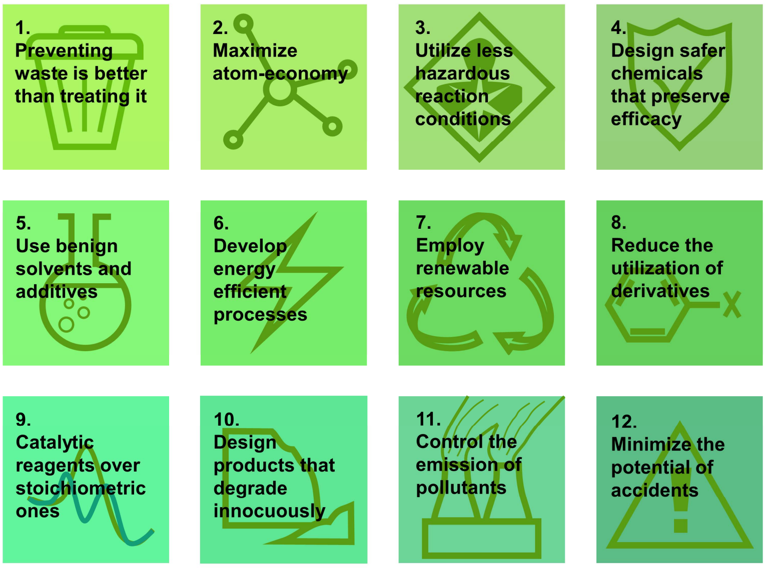

Figure 1.1. The 12 Green Chemistry principles.

Green Chemistry, at its heart, focuses on reimagining chemical processes to minimize energy and raw material consumption, while reducing usage and release of contaminating and hazardous substances. In this context, the design of effective and selective catalysts stands out as one of the most versatile and powerful strategies to tailor reaction pathways with these beneficial traits.[4] The addition of a catalyst to a reaction enables an alternative, lower energy barrier mechanism, in which the catalyst is directly involved. Unlike other additives, catalysts are regenerated post-reaction, allowing a small catalyst loading to yield the same effect as the stoichiometric addition of other reactants, aligning with the sustainable approach advocated by the 9th Green Chemistry principle.

Moreover, the addition of an effective catalyst can offer a wide spectrum of advantages to a reaction that correspond to other Green Chemistry principles. This work focuses on the utilization of organometallic catalysts, a subset of homogeneous catalysts distinguished by the remarkably high activities and selectivities they can achieve along with the great degree of modification that they allow. This versatility stems from their structure, featuring a metallic center that interacts with substrates in various ways, facilitating both the breakage and formation of bonds. Moreover, the ligands coordinated to the metal center indirectly regulate the activity of the complex through factors such as their electron density donation to the metal and steric interactions with the substrates.

The addition of a catalyst to a chemical process enhances its reaction rate under and enables it under milder. Hence, the same reaction can be carried out with a considerably lower energy consumption (as instructed by the 6th principle) and without the necessity for extreme reaction conditions (correlating with the 12th principle).[5] Moreover, effective catalysts can activate conventionally inert substances under reasonable conditions. This is an alternative to the inclusion of functional groups to facilitates subsequent chemical reactions on the afforded derivative. Catalysis enables a more straightforward reaction, thereby maximizing atom-economy, as the otherwise introduced functional group would be excluded from the final product structure (hence, it plays into both the 2nd and 8th principles).[6] Intentionally designed catalysts can prioritize specific processes within reactions where multiple products are possible.[7] This selectivity not only promotes the desired product but also minimizes the generation of by-products, (as advocated by the 1st principle). Additionally, this serves as a viable alternative to employing protecting groups.[8]

In summary, the incorporation of an appropriate catalyst can yield numerous benefits within a chemical process, from both an economical and an environmental standpoint. Consequently, the study and development of catalysts continue to captivate the interest of many researchers, driving the continual evolution in response to the demand for more efficient and eco-friendly catalysts essential for a sustainable future.[9]

1.2 Synergies between Computational Chemistry and organometallic catalysis

One of the most impactful advancements in chemical research in recent history is the establishment of the Theoretical and Computational Chemistry (TCC). This novel branch of Chemistry is based on the utilization of methodologies capable of deriving insights from chemical systems by working with models which draw from empirical data or/and fundamental principles rooted in Quantum Mechanics. These models are based on diverse approaches which are matched to the studied system and their properties of interest, leading to varying levels of detail and complexity.[10] This is supported by the capability of modern computers to perform lengthy and intricate calculations allowing for the utilization of elaborate models that lead to high quality results.

These calculations are capable of accurately reproducing the behavior of the studied systems at a microscopic level and elucidate from it the macroscopic properties of the system. These methodologies can be utilized for the examination and comparison of diverse systems leading to an understanding beyond the observation of trends and the inter- or extrapolation of data. The obtained results can be used to rationalize the activity and properties of the studied systems as well as the determination of the diverse factors governing their behavior.

Numerous TCC methodologies have been developed and adapted for the study of a wide spectrum of chemical systems. These systems can vary in size, ranging from water-solvated enzymes containing tens of thousands of atoms to systems with only a few atoms, where the behavior of individual electrons is examined. Moreover, a great diversity of systems has been investigated, encompassing from strictly organic systems to those containing heavy metals, where relativistic effects must be accounted for. Additionally, these computational studies have been applied for the study of a diverse array of properties of interest, such as molecular structure, intermolecular interactions, spectroscopic properties, thermodynamics, and reaction mechanisms among others. Consequently, TCC methodologies have become invaluable tools in many fields of research, including Chemistry, Physics, Materials Science, and Biochemistry.[11]

One of the fields where TCC methodologies have become a fundamental approach to the study of a system is organometallic catalysis.[12] This is because organometallic catalytic cycles consist of a series of consecutive elementary reactions, which generally cannot be separately studied, as the species yielded by one reaction immediately serve as substrate for the next one. Elementary reactions are the simplest transformations a chemical process can be broken into, meaning that there are no intermediates between the reagents and products of this process.[13] Every modification of the chemical species they entail, including the formation or breakage of bonds as well as the coordination or dissociation of molecular fragments, occurs simultaneously. Consequently, the determination of these reactions, on their own, is straightforward and unambiguous, with their elucidation being attainable by simply comparing the structures of reactants and products. Scheme 1.1 presents some of the most relevant elementary reactions that organometallic complexes commonly undergo.

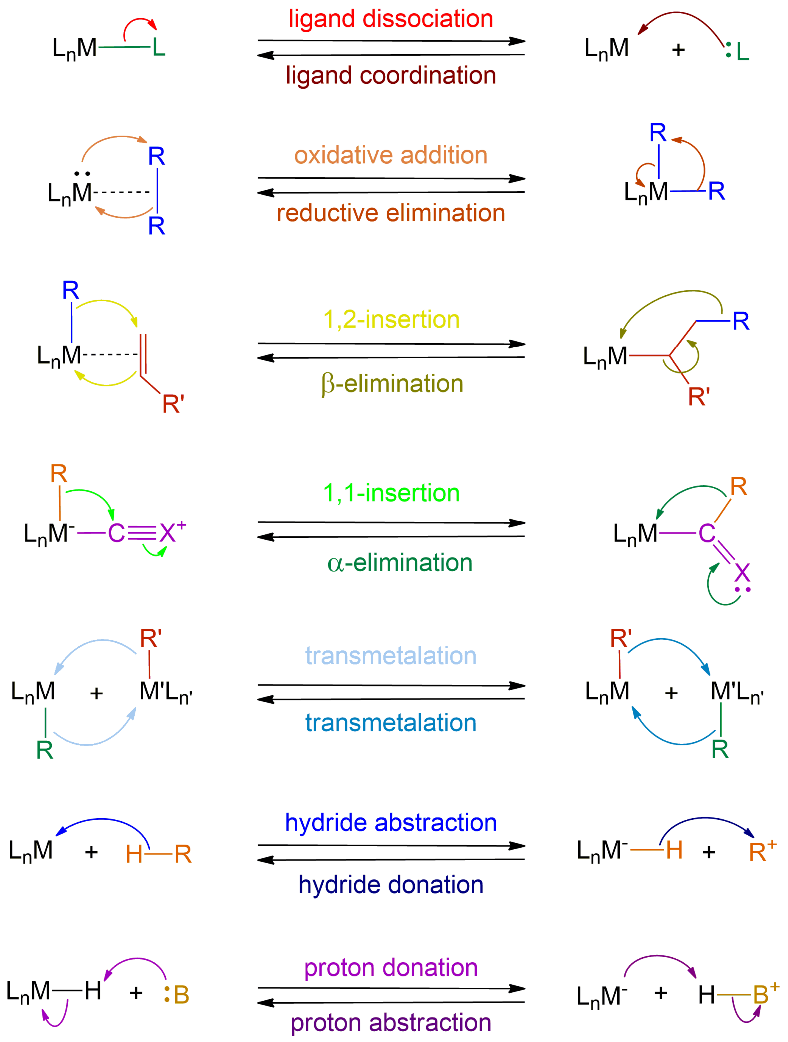

Scheme 1.1. Select examples of elementary reactions of organometallic complexes.

While these processes are simple, in combination they can lead to a broad spectrum of intricate transformations. Hence, unraveling a catalytic cycle consists of determining the sequence of elementary reactions that lead from the substrates to the product. Due to the remarkable versatility of organometallic complexes, many reactions are feasible for most reagents and intermediates involved in a mechanism, leading to branching competing pathways that can yield the same or different products. In many cases, several possible reaction pathways can explain the activity of an organometallic complex, making the proposal of the operating mechanism challenging. Consequently, a detailed analysis of each species involved in the mechanism is necessary for a thorough understanding of the reactivity of the system.[14]

However, the experimental determination of every intermediate involved in a catalytic reaction and the transformations that they undergo can be challenging and, in many cases, impossible. This is because detectable amounts of most of these species are not accumulated at any point in the catalytic process, instead, they are consumed at great speed immediately after their generation. The exception to this occurs with intermediates preceding a reaction step with a sufficiently high effective energy barrier. In these cases, their transformation to progress the reaction is comparatively slower than their formation, leading to the accumulation of sufficiently high concentration of one or more species for detection. At the same time, many other transformations with a lower energy barrier than that of the bottleneck reaction may be possible for this intermediate, including the regression of the reaction or other transformations which are not conducive to the formation of any product (otherwise that product would be observed). The species connected through these faster reactions are on a quasi-equilibrium, with the most stable among them constituting the great majority of the free catalyst. These are referred to as resting states and can be experimentally detected. Hence, while resting states offer an insight on the reactivity of the system, they cannot be directly utilized to elucidate the rate-determining process, as there can be multiple faster reactions separating the observed species and the catalytic cycle bottleneck.[15]

Moreover, other reactions that do not necessarily determine the catalytic rate can play an essential role to the activity of the catalyst, namely those defining its selectivity. Within the intricate roadmap of interconnected plausible reactions, divergent pathways emerge at crucial points, each leading to different products. The stereoelectronic properties of the species at these crossroads determine the favored reaction, with a significant kinetic difference between them translating into a tangible selectivity. Nevertheless, it is possible for these pivotal species to not be experimentally observable, as the selectivity hinges on the relative energetics of one pathway relative to the other, whereas the possibility of experimentally detecting them depends on their stability in relation to the overall mechanism and their position relative to the bottleneck of the cycle.[16] Figure 1.2 displays an example of the reactivity-defining species in a mechanism.

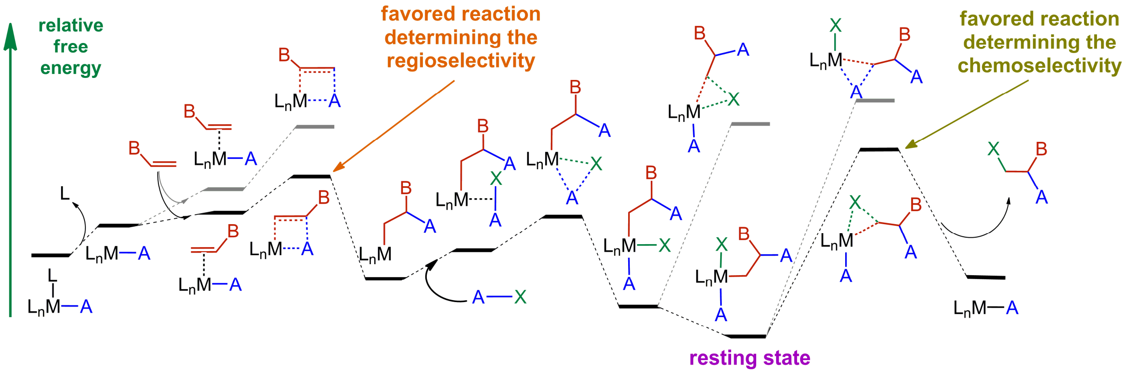

Figure 1.2. Energy difference between reaction pathways determining the selectivity of an example reaction.

Experimental researchers studying catalytic cycles often conduct supplementary experiments beyond the reaction itself with the aim of shedding light on the operating mechanism. A commonly used strategy involves the sequential, stoichiometric addition of the separate substrates to the catalyst and determination of the afforded intermediate, with the goal of discerning the mode of coordination or activation of these molecules. [17] While kinetic studies only allow for the observation of the resting states and the formation of the products, they provide indications of the involvement of different substrates in the rate-limiting elementary reaction.

Alternatively, the utilization of different substrates can offer insights beyond the scope of a reaction. Employing a diverse array of substrates displaying distinct traits, such as their bulkiness, nucleophilicity, or the presence of certain functional groups, can help gauge the impact of these properties on the catalytic rate and selectivity.[18] Conversely, the utilization of isotopically-labeled substrates possibilitate the measurement of the kinetic isotopic effect (KIE) to shed some light on the nature of the transformations occurring on the rate-limiting reaction of the catalytic cycle.[19] Another often utilized diagnostic tool for catalytic mechanisms is the exploration of the reactivity of complexes mimicking proposed intermediates to rationalize and validate their potential role in the operating mechanism.[20]

In essence, experimental researchers have a variety of means at their disposal to derive valuable information about the intermediates involved in a catalytic reaction and the potential transformations they may undergo. However, this information is often incomplete and cannot lead to the determination of every intermediate involved in the operating mechanism and their respective roles. Additionally, the detailed quantification of molecular properties and reaction energetics is inherently challenging for experimental methodologies. Hence, these studies typically provide fragmented reaction pathways and mostly qualitative indications and trends regarding the impact of diverse factors on the catalytic activity and selectivity. This can make it challenging to arrive to fully-supported conclusions in complex systems where several relevant, yet challenging-to-quantify factors are at play. An in-depth understanding of catalytic reactivity is crucial for identifying the factors influencing the selectivity and reaction rate of different reactions.

In this context, numerous TCC methodologies allow for the exhaustive analysis of the reactivity of an organometallic catalyst from a purely theoretical perspective. These methodologies are capable of determining the geometries, relative energies, and other properties of interest for every species potentially involved in the catalytic reactivity. This approach leads to the elucidation of the operating mechanism as the most energetically favored pathway. Moreover, they also enable the exploration of alternative reaction pathways, regardless of whether the involved species are formed or not and their relative energies, offering a more complete understanding of the reactivity.

TCC methodologies explore reaction pathways by inspecting both the intermediates and transition states constituting them. Intermediates are the stable chemical species formed and consumed during a reaction, while transition states can be defined as unstable species corresponding to the higher energy molecular configurations during the transformation of a reactant into a product. Consequently, the experimental determination of transition states is practically impossible. However, computationally, they serve as invaluable tools for assessing reaction kinetics and identifying the most energetically favored pathways. The analysis of these species and their relative energies provides a quantitative understanding of the most favored reactions for a catalyst, as well as the reasons for this preference based on indicators such as the configuration adopted by molecular fragments along this process and bond lengths, especially those of the bonds being broken or formed.

The computational determination of every chemical species corresponding to feasible reactions for a catalyst not only allows for the elucidation of the operating mechanism, but also enables the identification of the most energetically favorable pathways leading to the formation of reaction products other than that of the operating mechanism. This facilitates a quantitative comparison of these pathways based on their effective energy barriers, providing insights into the various types of selectivity that the studied catalytic system may exhibit, as shown in Figure 1.3.

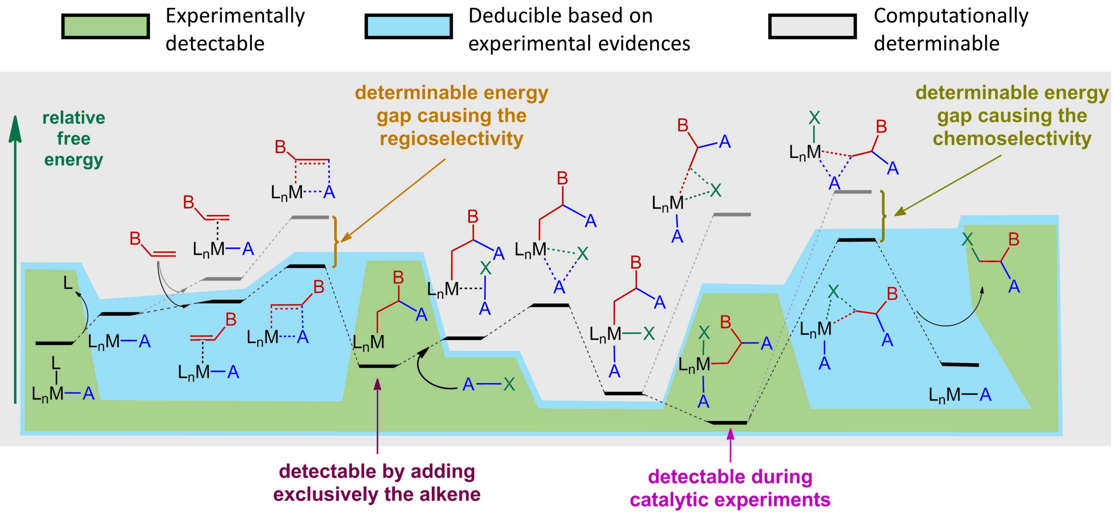

Figure 1.3. Comparison of the capability of different methodologies to determine the different species defining the reactivity of an example catalyst.

Thus, computational methodologies can achieve an all-encompassing analysis of the catalytic reactivity, surpassing the limitations of experimental approaches. This exhaustive study enables the determination of the chemical species defining the reaction rate and those defining the selectivity, as well as the energy differences among them, leading to more in-depth understanding of the catalytic activity.

Furthermore, this study can be replicated utilizing diverse substrates to evaluate and contrast the catalytic activity for them. The quantifiable nature of these results, coupled with the analysis of relevant characteristics of the activity-determining species, contributes to a more informed interpretation of the factors influencing the catalytic activity. Moreover, specific computational methodologies, such as NBO[21] and QTAIM,[22] allow for the detailed deconstruction of the structure and interactions characterizing these species. This facilitates pinpointing the relevant aspects that differentiate them and define catalytic activity.[23]

Consequently, TCC methodologies have become an essential tool for the determination of catalytic mechanisms. Their application facilitates the elucidation of the characteristics of both the catalyst and the substrates defining the catalytic activity, facilitating the rationalization of the experimental results.[24] The detailed understanding of these aspects can be leveraged by researchers in the rational design of novel catalysts to favor the reaction of interest or impede competing reactions.[25]

Arguably, the most challenging obstacle researchers face when working on computational calculations for mechanistic determination is the imperative to consider every reaction pathway to ensure the reliability of their analysis. While, experimentally, the generated species is always the most favored, with the only room for error arising from a wrongful structural determination, computational studies carry the risk of overlooking the existence of one or more species that may be more energetically favored than the determined ones. This introduces the potential for inaccurate conclusions, as the properties of a non-representative species could be used to interpret the behavior of the system. This leads to the necessity for exhaustive consideration of reactions and configurations for the afforded chemical species, which due to the versatile reactivity of organometallic complexes. The multiple molecular fragments composing these species, can make the proper study of many systems remarkably labor intensive.[26]

Consequently, it can be notably advantageous for researchers to support computational analysis with experimental observations to guide the direction of the study and validate their results. These evidences not only suggest reactions to be studied, but a correctly determined operating mechanism must match the experimentally-registered outcomes for a reaction. This alignment encompasses the selectivity of the process, the measured activation energy, and the changes in these observations for different substrates. Furthermore, the observed intermediates must correspond to resting states in the mechanism.[27] Similarly, this mechanism should be able to rationalize the detected species through exploratory tests such as the stoichiometric addition of different substrates. Hence, while these computational methodologies inevitably entail a small margin of error due to intrinsic limitations, experimental techniques can offer a variety of insights into catalyst behavior, which depend on distinct and independent factors. These insights serve as a meeting point between experimental and computational findings, allowing for the validation of the results and conclusions derived from each approach.

While, in theory, both purely experimental and computational approaches can lead to a comprehensive and accurate description of the activity of an organometallic complex, each has its own set of limitations that can impede the study of some systems. Fortunately, findings from one approach can assist the other in navigating these challenges, establishing a cooperative framework. These two entirely independent approaches, rooted in separate fields, can complement, and strengthen each other. This creates a mutually beneficial feedback loop in which results from one approach can guide the selection of experiments or studies that may offer more valuable insights with the alternative approach. Additionally, comparing the results from these contrasting approaches allows for the validation and more informed interpretation of the findings. This offers researchers more powerful tools to determine the activity of a catalyst, understand the causes for this behavior, and how it changes in different situations, as well as valuable insights into how different modifications could enhance the outcomes. In this cooperative framework, the results of one approach validate those of the other and through their cooperation, more insightful and better rationalized results can be drawn from a study (see Figure 1.4).[28]

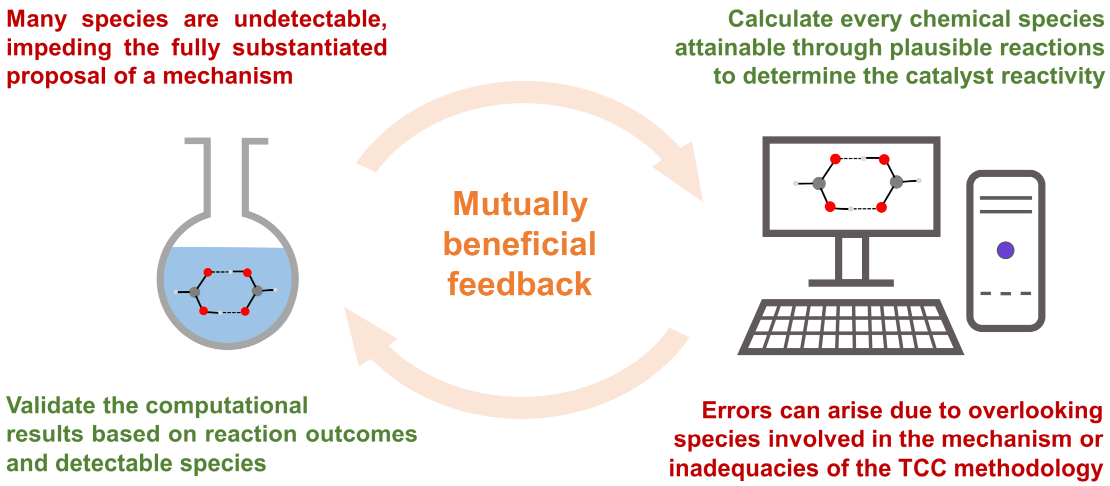

Figure 1.4. Mutually beneficial feedback between experimental and computational approaches in the study of catalytic cycles.

This framework has propelled the field of organometallic catalysis into a newer stage allowing for the attainment of higher quality results and a deeper understanding of the studied systems. It has enabled researchers to propose more ambitious studies delving into more intricate and sophisticated catalysts to design more efficient and environmentally friendly catalysts leading to a more sustainable future.

Chapter 2:
Research Objectives

“Cruel or comforting, this machine unerringly arrives at the truth. That’s what it does.”

Benoit Blanc

This Doctoral Thesis is centered on the computational study of a series of diverse homogeneous catalytic systems. The determination of the operating mechanism for each of these systems is instrumental to their study, constituting a goal in itself for the understanding of their reactivity, as well as an essential step in the derivation of other valuable information that leads to deeper insights into said reactivity. For this reason, the determination of the operating mechanism, along with other reaction pathways necessary to describe the reactivity of the catalyst (e.g., the most energetically favored pathway to generate a product that the catalysis is not selective towards) is considered a primary objective for each of these systems. Additionally, as part of the analysis of the operating mechanisms, it is utilized to rationalize the different experimental observations for each system, validating it.

As previously introduced in the abstract, the studied systems in this dissertation can be divided into two distinct categories. For this reason, the presentation and discussion of results are split into two separate chapters. The first of these chapters, Chapter 4, is centered on the study of reactions involved in the utilization of CO_2, containing three different reactions. The second of them, Chapter 5, includes the study of two reactions involving the hydrofunctionalization of terminal alkynes. Each reaction is thoroughly examined in its dedicated section. Given that each section addresses significantly different catalytic systems with considerably varied points of interest, distinct objectives apart from the determination of the operating mechanism and origin of the selectivity are set for each of them. These objectives are displayed below:

4.1 The determination of the distinct roles played by the Ir-NSi catalyst and the $B(C_6F_5)_3$ cocatalyst in the reduction of CO_2 to acetal using hydrosilanes.

4.2 The elucidation of the involvement of the formic acid and formate molecules in the dehydrogenation of formic acid catalyzed by a Ir-NSi complex.

4.3 The comparison of the catalytic activity of the two possible forms of the Rh-CNC catalyst facilitating the dehydrogenation of formic acid, one presenting a Rh^{I} and the other presenting a Rh^{III} after going through oxidative addition.

5.1 The determination of the role played by a 2-pyridone ligand in the enhancement of the catalytic activity of a Rh-IPr catalyst for terminal alkyne dimerization.

5.2 The comparison of the different factors defining the chemo- and regioselectivity of the *O*-selective *gem*-specific hydropyridonation of terminal alkynes catalyzed by a Rh-IPr complex.

Chapter 3:
Methodology

> “Every time anyone accomplishes anything, they achieve it with the help of a thousand silent heroes.”
>
> Alex Dunphy

All of the work in this Thesis was developed using diverse computational chemistry methodologies, being the most distinguishing of them the use of DFT functionals for the study of the electronic structure. These methodologies have long been validated as some of the most effective approaches to study systems containing transition metals and bulky ligands.[29–31] The great compromise between accuracy and computational cost these methodologies achieve modelling organometallic systems, such as the ones studied in this Thesis, enables researchers to perform exhaustive studies while maintaining a low margin of error.[32] These methodologies make it possible to thoroughly explore the potential energy surface of catalytic systems to determine their reactivity, as well as figuring out the interactions and chemical properties responsible for said reactivity.[33,34] This chapter covers everything needed to model the studied systems and carry out calculations on them as well as the analytical tools used to draw useful information and relevant conclusions out of the resulting data.

3.1. Wave function and electronic structure

The wavefunction of a chemical system contains all of its accessible information, including separate contributions from each particle comprising the system. The time-dependent Schrödinger equation studies the evolution in time of a system. This equation introduces the Hamiltonian, $\hat{\mathrm{H}}$, an operator with two components the kinetic and the potential operators, which together total energy of the system (eq.1).

$$i\hbar \frac{\partial \Psi(q,t)}{\partial t} = \hat{\mathrm{H}}\,\Psi(q,t) = \left(-\frac{\hbar^2}{2m}\,\nabla^2 + \hat{\mathrm{V}}(q,t)\right)\Psi(q,t) \qquad (1)$$

The wave function, $\Psi(q,t)$, presents a dependence on q, the spin-space coordinates of each particle of the system, and t, a parameter accounting for time. For stationary states, meaning those whose energy is constant in time, the temporal wavefunction components can be strip from the equation, leading to the time-dependent Schrödinger equation shown in eq. 2.

$$\hat{\mathrm{H}}\,\Psi(q) = \left(-\frac{\hbar^2}{2m}\,\nabla^2 + \hat{\mathrm{V}}(q)\right)\Psi(q) = \mathrm{E}\,\Psi(q) \qquad (2)$$

The chemical species involved in the vast majority of reactions correspond to stationary states, making the resolution of this equation highly sought-after. This resolution allows for the elucidation of the system’s state, and therefore its properties, under a certain set of conditions. However, the great complexity arising from the numerous contributions to the wavefunction and their correlations, renders the direct resolution of this equation impossible.

For this reason, many strategies such as the Born-Oppenheimer approximation are employed. This approximation assumes that the significant mass difference between nuclei and electrons allows for the separate treatment of nuclear and electron movements. As a consequence, when considering the electron movements, the nuclei are treated as fixed on space. Conversely, when treating the movement of nuclei, the electronic configuration is considered to immediately adapt to that of the nuclei. This allows to separate the nuclei kinetic energy calculation from the rest of the contributions. Following this methodology, the resolution of Schrödinger equation for each fixed nuclear disposition leads to a complete understanding of the system's reactivity. These calculations yield the system's Potential Energy Surface (PES), which describes the most stable atomic configurations of a chemical system, as well as the reaction pathways connecting them. While this approximation simplifies the calculation of nucleus-nucleus and nucleus-electron interactions, electron-electron interactions still pose a significant challenge. Considering that the movement of one electron induces a reorganization on the rest of electrons in the system, the calculation of the interactions between two electrons consists of an integral with two correlated variables, making its resolution an excessive computational burden.

An extensive variety of approximations has been developed in other to facilitate the calculation of the electronic structure. These methodologies can be classified as *ab initio* methods or Density Functional Theory (DFT) methods based on the employed approach.

Ab initio methods aim to solve the Schrödinger equation using an approximated wavefunction. The first methodology to successfully implement this approach was the Hartree-Fock (HF) method, where each electron interacts with an averaged electron density representing all other electrons, resulting in the creation of the Fock operator.[35] Many commonly used methodologies have been developed as improvements to HF. A notable example of this is the Møller–Plesset methods[36] (e.g., MP2[37] and MP4[38]), which introduce electron correlation through the addition of a perturbator to the Fock operator. This function achieves an improved system description through a series of iterative corrections to the HF reference function and energy through the addition of small contributions from higher-level solutions of the Fock operator. Another example of *ab initio* methodologies which sees ample use is the coupled cluster family[39] (e.g., CCSD[40] and CCSD(T)[41]). These methodologies introduce electron correlation via a more sophisticated operator in the form of a Taylor series. This operator applies the Fock operator on the ground state as well as every possible electronic configuration resulting from a series of electronic excitations.

While the more sophisticated *ab initio* methodologies can produce exceptionally precise results they come at a remarkably high computational cost, making them unviable for medium to large systems, such as the organometallic complexes studied in this Thesis.

Density Functional Theory (DFT) methodologies propose a drastically different approach, utilizing the electron density instead of the wavefunction to derive relevant system properties.[42,43] The electron probability density (more commonly referred to as simply electron density) at a point, $\rho(\boldsymbol{r})$, is calculated as the combined probability density of every electron described by the wavefunction to be located at said point, as shown in eq. 3.

$$\rho(\boldsymbol{r}) = |\Psi(\boldsymbol{r})|^2 \qquad (3)$$

This approach was validated by the Hohenberg-Kohn theorems.[44] The first states that for any system of N interacting particles under an external potential, V_{ext} (namely, the one imposed by the fixed nuclei), there is a univocal relationship between it and the ground state particle density (meaning the electron density). The second states that for any valid external potential, an energy functional in terms of electron density, $E[\rho]$, can be defined (eq. 4), with the global minimum of this functional corresponding to the exact ground state energy of the system.

$$E[\rho] = F[\rho] + \int \rho(\boldsymbol{r})\, V_{ext}(\boldsymbol{r})\, d\boldsymbol{r} \qquad (4)$$

Hence geometry and energy of a system can be explored utilizing exclusively its electron density instead of its wavefunction. While these theorems prove the existence of $F[\rho]$ the formulation of this functional is unknown. Since the description of electron-electron interactions exclusively using electron density was extremely challenging, Kohn and Sham proposed a formulation which utilizes the electron density of a fictitious system with non-interacting electrons.[45] This strategy substitutes the external potential by an effective potential whose effect on the non-interacting electrons leads to their density to be identical to that of the interacting electrons when they are exposed to the external potential, and its formulation is shown in eq. 5.

$$V_{eff}(\boldsymbol{r}) = V_{ext}(\boldsymbol{r}) + e^2 \int \frac{\rho(\mathbf{r}')}{|\boldsymbol{r} - \boldsymbol{r}'|}\, d\mathbf{r}' + \frac{E_{XC}[\rho(\mathbf{r})]}{d\rho(\boldsymbol{r})} \qquad (5)$$

Hence. this effective potential includes: the nuclei-electron interactions, the coulombic interactions between electrons and the exchange-correlation interactions between electrons. In this context, exchange refers to the electron interactions caused by the Pauli exclusion principal, not allowing two electrons to occupy the same spin and spatial state. Moreover, the correlation is introduced to correct the errors caused by the mean-field approach. As electron-electron interactions are integrated over each point in space, the electron density should adapt to represent the most stable configuration of the rest of electrons if that point was occupied by an electron. Instead, the same density is considered for every point in space. The correlation term arises as a correction to account for this limitation.

Therefore, the system’s energy can be calculated as the electronic kinetic energy and effective potential contributions, all derived from the electron density.

$$E[\rho] = T_s[\rho] + \int \rho(\boldsymbol{r})\, V_{ext}(\boldsymbol{r})\, d\boldsymbol{r} + e^2 \int \frac{\rho(\mathbf{r})\rho(\mathbf{r}')}{|\boldsymbol{r} - \boldsymbol{r}'|}\, d\mathbf{r}\, d\mathbf{r}' + E_{XC}[\rho] \qquad (6)$$

Within this framework defined by Kohn and Sham, referred to as KS-DFT, the energy of a system can be univocally determined based purely on its electron density. Consequently, every nuclear configuration (V_{ext}) leads to a unique electron density and energy, allowing for the study of the reactivity and derivation of other system’s properties. However, the exact exchange-correlation term is unknown to this day.

Nonetheless an extensive variety of approximations to the E_{XC} term have been utilized and validated for the study of a wide range of systems. These density functional approximations (DFA) or more commonly referred to as, DFT functionals, have been developed using a variety of approaches leading to a diverse array of methodologies for the study of the electronic structure of a chemical system.

3.2. DFT functionals

DFT functionals allow for the computational study of a chemical system employing its electron density rather than its wavefunction. This substitution significantly reduces the dimensionality of the function describing the system, greatly reducing the computational cost of the calculations required for its study. While this alternative approach to describing the electronic structure makes calculations for larger systems, such as organometallic complexes, manageable, an adequate methodology to study the system’s properties has to be selected. A plethora of DFT functionals that use very different approaches, levels of detail or parametrization procedures have been developed.[46,47] One of the most popular methods of classification for DFT functionals is Jacob's ladder, which places functionals in different rungs based on the level of complexity on their formulation.[48] Consequently, simpler functionals occupy lower rungs, while more complex, and presumably more accurate methods, occupy higher rungs, closer to heaven. However, the performances of these functionals can significantly vary depending on other factors, namely the studied systems and properties of interest.[49] Meaning that it is necessary for researchers to understand the functionals better suited for their study, their limitations and if necessary, any corrections they might require to accurately represent the system.

In the field that this dissertation is inscribed on, computational determination of homogeneous organometallic catalytic cycles, a great number of diverse functionals has seen ample use and their accuracy has been validated employing many different strategies. The local-density approximation (LDA)[50] is the simplest approach and its use to study organometallic complexes is generally discouraged.[32] LDA exclusively takes into account the local electron density to calculate the exchange-correlation term (eq. 7) and assumes that said density changes slowly and homogeneously. This fails to represent the steep fluctuations that can be observed in the electronic densities of most molecules, especially those bearing metals.[51–53]

$$E_{xc}^{LDA} = \int \rho(\boldsymbol{r})\, \epsilon_{xc}^{LDA}(\{\rho_\sigma(\boldsymbol{r})\})\, d\boldsymbol{r} \tag{7}$$

Nonetheless, we can find examples of every other rung of Jacob's ladder among the most popular methodologies in this field. PBE[54,55] and B97-D3[56] are examples of generalized gradient approximation (GGA) functionals used to great success. These functionals describe the exchange-correlation term not only using the local electron density but also its gradient (eq. 8). This formulation makes them the least computationally expensive of the bunch yet still great options for our studies.

$$E_{xc}^{GGA} = \int \rho(\boldsymbol{r})\, \epsilon_{xc}^{GGA}(\{\rho_\sigma(\boldsymbol{r})\}, \{\nabla\rho_\sigma(\boldsymbol{r})\})\, d\boldsymbol{r} \tag{8}$$

The next step in the ladder is the meta-GGA functionals (mGGA), exemplified by TPSS[57] and M06L[58] which are some of the better suited functionals for the study of organometallic complexes. This family of functionals considerably raises the computational cost of calculation due to its inclusion of the electron density Laplacian and/or the kinetic energy density in the calculation of the exchange-correlation term (eq. 9), but generally improves with respect to GGAs.

$$E_{xc}^{mGGA} = \int \rho(\boldsymbol{r})\, \epsilon_{xc}^{mGGA}(\{\rho_\sigma(\boldsymbol{r})\}, \{\nabla\rho_\sigma(\boldsymbol{r})\}, \{\nabla^2\rho_\sigma(\boldsymbol{r})\}, \{\tau_\sigma(\boldsymbol{r})\})\, d\boldsymbol{r} \tag{9}$$

Continuing our ascension of Jacob's ladder, we find the hybrid functionals, which take a different approach to improving GGA functionals by a partial or full inclusion of HF exchange. B3LYP[59] and PBE0[60] are examples of hybrid functionals which are widely used, not only in the study of organometallic catalysts, but in computational chemistry as a whole. Among the literature very diverse formulations of these functionals can be found, eq. 10 shows a simplistic example of this approach, but in many cases more terms are included.

$$E_{xc}^{HGGA} = E_{xc}^{GGA} + \alpha\left(E_x^{HF}\left(\left\{\rho_\sigma(\boldsymbol{r})\right\}\right) - E_x^{GGA}\right) \tag{10}$$

The HF term must be simultaneously but separately calculated using independent wavefunctions for each electron rather than the electron density as a whole, which significantly raises the complexity of the calculation, scaling with N^4 rather than N^3, as the calculation for the GGA portion. However, the higher computational cost this entails is generally worth it, since the inclusion of the HF exchange helps mitigate the self-interaction error that can be a great source of inaccuracies in many systems.[61] At a higher computational cost, we find methods which combine both corrections, labeled hybrid meta-GGA. Some examples of these methods used to great success in the study of organometallic complexes are M06[62] and TPSSh.[63–65]

Progressing further up the ladder we find range separated hybrids, which try to improve the poor performance of DFT at larger distances by calculating two instances of electron-electron interactions, one designed to represent short range interactions and the other for longer ranges. This is shown in eq. 11, where μ stands for the range-separation parameter, which is either empirically fit using a training set[66] or by minimizing the deviation from a series of constrains the exact KS functional must obey[67].

$$E_{xc}^{RSH} = E_{xc}^{SR}(\mu) + E_{xc}^{LR}(\mu) \tag{11}$$

Some popular examples of this approach are CAM-B3LYP[66] and LRC-ωPBEh[68]. Despite their seemingly more complex formulation, these methods consist of two calculations, each of them being at the same level than the previously seen hybrid functionals. As such, their computational cost is not significantly higher than that of a regular hybrid while improving the results. Regardless, these functionals are almost exclusively used in heavily delocalized systems, such as systems that present charge transfer excitations.[69] Instead, most researchers use dispersion corrections, such as DFT-D3, an even simpler and less expensive approach to improving long range interactions. These corrections are discussed in depth further on this text, on Section 3.3.

Lastly, double hybrid methods occupy the higher rung of the ladder. In addition to HF exchange, these functional include a MP2 term to further improve electron correlation (eq. 12). Some examples of this group of functionals are PBE0-DH[70] and B2PLYP[71]. However, calculating the MP2 term drastically increases the computational cost, scaling with N^5. While these methods can afford a great degree of accuracy even for challenging systems, it is generally excessive for most studies in this field, making their high computational cost rarely justifiable.

$$E_{xc}^{DHGGA} = E_{xc}^{GGA} + \alpha(E_x^{HF} - E_x^{GGA}) + \beta(E_c^{MP2} - E_c^{GGA}) \tag{12}$$

Thus, we have delimited Jacob's ladder based on dismissing those rungs where functionals systematically fall short in their description of our systems and those which are unnecessarily computationally expensive for the accuracy required for our study.

As we have just observed going up Jacob's ladder translates to the inclusion of increasingly computationally demanding terms which help us better deal with complicated issues in the representation of our system. Having said that, the DFT functional landscape is far from such a rigid structure. There is great diversity in how these functionals are designed and developed, even within the same rung, which greatly affects how suitable for a certain system a functional is. Among the top performers in our field, we can find functionals whose formulation employed no empirical data, like PBE, and others that are heavily parametrized like M06-L. The components and fitting of a functional determines their validity for whatever application we intend to use them. The previously mentioned M06-L functional was parametrized to be used in the study of systems containing both transition metals and main group elements. As such, M06-L performs the best when studying the thermochemistry, thermochemical kinetics, and non-covalent interactions of these systems, outperforming a great deal of the most popular methods, many of them being more computationally expensive than M06-L.[58] However, when studying purely main group systems M06-L generally presents worse results than most of those same functionals. This is especially relevant when talking about hybrids, since developers have to empirically fit the amount of HF exchange the functional uses. However, the ideal amount varies not based only on the system but also the studied properties.[72,73] Another issue heavily parametrized methods can suffer from is "giving the right answer for the wrong reason", meaning they can very accurately give the energy value they were fitted to obtain, but in the process, yield a flawed electron density, which would worsen the description of other properties.[74] A newcomer to computational chemistry may look at Jacob's ladder and assume that all that is needed to improve the accuracy of a study is to climb to "better" methods, however this is a terribly naïve approach to DFT studies and selecting a functional is a far more complex issue.

A great hurdle researchers have to face in this field is that the only way to reliably determine the accuracy of a functional for a study is to compare their results to experimental ones or those obtained with a higher accuracy method like CCSD(T)[41]. Unfortunately, the later can easily become unmanageably computationally expensive for many systems. Additionally, given the black box nature of DFT functionals it is impossible to determine the sources of error which muddles the search for a more accurate method. This fact combined with the constantly growing overabundance of methods[75] may tip some researchers in a never-ending search for the perfect functional. Instead, we can make a much better use of our time by testing a set as small as possible of functionals in search of sufficiently accurate methodology for our study. Further testing would exhaust computational resources and most commonly increase the accuracy in a meaningless way.

A great starting point to finding the appropriate methodology for a study is looking into validated studies of similar systems. Similarly, benchmarking studies can clue us in into the most accurate methodologies for the application that we are looking for. Yet again, the complex formulation of DFT functionals can make it so a small change in the system may unknowingly throw off the functional's accuracy. For this reason, the recommended approach is "trust, but verify"[76] and whenever possible consult as much experimental, or in its absence higher level calculation, data as possible relative to the studied system to validate the results obtained.

3.3. Dispersion interactions

As mentioned before, with the exception of some of the most sophisticated functionals the accuracy of most DFT methods declines significantly when dealing with long distance interactions. At longer ranges molecular fragments interact through dispersion forces, caused by a transient fluctuation in the electron distribution of one fragment which then brings about a similar fluctuation in the second fragment by electronic correlation.[77] These stabilizing interactions are crucial to a correct system representation, especially when dealing with large systems such as organometallic complexes.[78,79]

Therefore, dispersion interactions are attractive interactions arising from long range electron correlation effects without the need of polarity nor wavefunction or electron density overlap of the involved fragments. This effect is poorly represented by mean field methods such as HF and KS-DFT functionals, because of them exclusively using occupied orbitals to describe the state of the system and its properties.[80] More sophisticated methods such as coupled cluster or double hybrids use virtual orbitals to improve the description of the system. These orbitals represent how the system would respond to an external perturbation. While their contribution is generally minor, it considerably improves the description of these charge fluctuations. However, for large systems, as the ones studied in this work these methods are exceedingly computationally costly. Instead, dispersion interactions can accurately be represented with simpler functionals at a trivial computational cost by using dispersion corrections.

Three different approaches are utilized to include dispersion interactions in DFT and other mean-field methods. The most commonly used one is the semiclassical C_6-based schemes, in which dispersion is calculated as a separate energy contribution including the dispersion interactions between every atom pair, and in seldom cases also interactions between larger atom groups.[81] The energy for each of these dispersion interactions depends on parameters specific to the interacting elements and the distance between these atoms. Another common approach is the inclusion of these interactions as an empirically parametrized one-electron potential.[46,82] As the name suggests, these potentials exclusively depend on properties that can be calculated using only information of one point of the wave function or electron density at a time such as the local dynamic polarizability. Lastly, nonlocal density-based dispersion corrections include these interactions as an exchange-correlation functional for medium to long ranges. These functionals are differentiated from the formerly mentioned ones because of their use of a two-electron integral.[83,84] Thus, they are able to consider interactions between distant parts of the system without the need for parametrizations although at a higher computational cost.

Despite its simplicity and insignificant computational cost, the semiclassical approach can considerably improve the accuracy of mean field methods.[85] This approach pioneered by Grimme et al. has spawned many different correction schemes following a similar formula. The defining parameters of this approach can be observed in the D2 correction scheme (eq. 13).[86]

$$E_{disp}^{D2} = -\sum_{AB} s_6 \frac{C_6^{AB}}{R^6} f_{damp}^{(6)}(R) \tag{13}$$

This scheme exclusively takes into account the two-atom dipole-dipole interaction, with C_6^{AB} being a parameter specific to the atom pair AB and R being the distance between them. The C_6^{AB} dispersion parameter can be easily obtained using the dispersion parameter corresponding to the homoatomic pair of each involved atom, C_6^{AA} and C_6^{BB} (eq. 14). The homoatomic parameters are specific to each element and depend on a scaling factor corresponding to their row in the periodic table, N, their static dipole polarizability, α_A^0, and their ionization potential, I_A. These two last quantities are obtained using the PBE0 functional (eq. 15).

$$C_6^{AB} = \sqrt{C_6^{AA}\,C_6^{BB}} \tag{14}$$

$$C_6^{AA} = 0.05\,N\,I_A\,\alpha_A^0 \tag{15}$$

The $f_{damp}^{(6)}(R)$ is a Fermi-type damping function that either reduces or stabilizes the dispersion interactions as R diminishes so that they are only relevant at the longer ranges, while at shorter ranges the behavior is defined by the original mean field method.[87] Lastly, the s_6 is a functional-specific scaling parameter set to avoid possible artifacts in the transition between short and long range.

Many different schemes have been developed as improvements to the D2 correction scheme by including additional terms to improve the description of the dispersion interactions. These may include terms higher in the multipole expansion or/and terms considering a higher number of bodies. While more sophisticated and complex methods are available, currently the D3 correction scheme is generally considered among the best options to include dispersion interactions. This approach stands out because of its accuracy, efficiency for geometry optimization and availability for a wide range of DFT functionals. The D3 generation of schemes improves upon the previous by including an additional term to include dipole-quadrupole interactions, $E_{disp}^{(8)}$. Additionally, the D3 scheme, shown in eq. 16, considers the bonding and hybridization of each atom when assigning the dispersion parameter.[88]

$$E_{disp}^{D3} = -\sum_{AB}\sum_{n=6,8} s_n\,\frac{C_n^{AB}}{R^n}\,f_{damp}^{(n)}(R) \tag{16}$$

The D3(0) scheme refers to the one originally developed by Grimme et al. which uses a so-called zero-damping function.[89] This function makes it so that dispersion energy tends to zero at shorter ranges. The D3(BJ) scheme is a variant developed by Becke and Johnson which uses a different damping function that instead converges to a finite negative value at lower distances, while behaving indistinctly at longer ranges.[90] This approach is generally preferred, becoming the option by default. This preference is due to the fact that in some relevant cases methodologies employing the D3(0) scheme would stabilize longer ranges over medium ranges when considering the sum of the decaying functional stabilization and the damped dispersion interaction correction. This would result in larger bond distances than those obtained using only the functional which clashes with the idea of dispersion interactions being exclusively attractive.

As mentioned before, one-electron potentials are empirically parametrized to replicate the two-electron dependent dispersion interactions based exclusively on local or semilocal properties. While these methods cannot accurately represent the R^{-6} electron density decay, a certain wavefunction or density overlap can be found between two molecular fragments bound through non-covalent interactions. These methods obtain information relating to the dispersion interactions based on the accumulated density and its distortion in this region.[80] This approach has become increasingly popular, mainly due to the great success of the Minnesota functionals suite. These functionals utilize an extensive set of parameters fitted to represent a series of properties for an ample array of reference systems. Starting at the 2006 generation of these functionals,[62] the exchange-correlation term included parameters hailing from the Van Voorhis and Scuceria functional, characterized for their improvement in the description of the exchange-correlation energy by including terms dependent on the kinetic energy density.[91] Among the properties studied to fit these parameters are the non-covalent interaction energies and distances, which are then reproduced with a great degree of accuracy.

For the calculations carried out in this Thesis whenever the B3LYP functional, known to be over-repulsive to the point of yielding unbonded Van der Waals complexes, was utilized it was supplemented with the D3(BJ) dispersion correction. The B97-D3 functional was also used which not only includes the D3(BJ) scheme as part of its construction, it is a version of the B97 functional reparametrized to describe electron correlation at medium to long ranges exclusively through the dispersion correction term. Lastly the M06-L functional was also employed in this work. Since this functional already contains an accurate description of attractive non-covalent interactions at medium range distances no dispersion corrections were added to it. While some authors recommend adding a semiclassical dispersion correction scheme to improve their description of the long-range interactions,[72] other studies suggest that this may cause double counting effects in the medium range region.[92]

3.4. Basis sets

Basis set are a series of functions with adjustable parameters used by *ab initio* and semi-empirical methods to describe the wavefunction or electron density of a chemical system. These functions are centered on the atoms that comprise the system and during calculations are combined in a way that minimizes its energy, yielding the electronic structure of the molecule as a whole. While in theory a basis set composed of an infinite number of functions could perfectly describe the electron density of any system, a compromise between the accuracy of the basis set and the computational cost it brings about must be found.[93]

A minimal basis set is the simplest possible set of functions to describe a system's electronic structure. It contains the atomic orbitals of each atom making up the molecule. These orbitals arise from the resolution of Schrödinger equation for the H atom in gas phase. Consequently, this approach suffers errors when describing more complex systems. Effects like bonding or polarization are specially challenging to model since these phenomena cannot be observed for atomic orbitals.

For this reason, basis sets are upgraded by including additional functions which gives greater flexibility to the fitting process. Since bonding processes exclusively involve the valence orbitals, the description of the molecular electronic structure can be significantly improved by adding complementary sets of valence orbitals for every atom. These complementing orbitals correspond to different effective nuclear charges so that they help describe situations that might be poorly covered by the unenhanced basis set. A basis set that includes two sets of valence orbitals is denominated as doble-zeta. Following this notation, a triple-zeta basis set presents three sets of valence orbitals and so on.

Additionally, basis sets can be further improved by including polarized basis sets, which include the orbitals with the consecutive angular momentum quantum number to those of the valence orbitals of every atom.[94] The contribution from these orbitals pushes electron density away from the nuclei and induces asymmetry on the valence orbitals. As an example, a *p* orbital can be included to H atoms leading to a higher population in the direction of the lobe presenting a constructive interaction with the s orbital. This creates a *sp* orbital of sorts to help describe situations like hydrogen bonding or covalent bonds with H atoms more accurately. Polarized basis sets are commonplace in the study of organometallic complexes and their reactivity since they are key for the accurate representation of polarization or breakage of bonds as well as metal-ligand interactions.

Another possible addition to basis sets are diffuse functions which are a set of valence orbitals with considerably lower effective nuclear charge, meaning that they are more extended away from the nucleus. These functions are generally reserved for anionic or weakly bonded systems or cases where the dipole moment is of great relevance.

It should be mentioned that rather than using the exact orbitals, computational chemistry software employs functions that replicate their behavior closely but are considerably less computationally expensive to integrate. Nevertheless, the additional sets more than make up for the lesser accuracy of using these functions while staying at a lower computational cost. Many different basis sets have been designed with different degrees of complexity, and therefore compromises between accuracy and computational cost.

A commonly utilized strategy to reduce the computational cost of calculations is to use effective core potentials (ECPs) to describe the core electrons of every atom.[95] This means that all core electrons are substituted by a simple potential that surrounds the nucleus and interacts with the valence electrons through electrostatic repulsions. This approximation is valid for most studies since only the valence electrons define the reactivity and properties of molecules while core electrons only affect it indirectly. ECPs can significantly reduce the computational cost of calculations since only the valence electrons are treated explicitly. Furthermore, in some cases these potentials are used to include relativistic effects.

In every study presented in this Thesis the same basis sets, coming from the Karlsruhe def2 family, were employed. These basis sets were chosen since they cover most metals and include effective core potentials.[96] def2-SVP, a double-zeta basis set with polarization in all atoms, was employed for geometry optimization and frequency calculations and def2-TZVP, a triple-zeta basis set with polarization, was used for energy refinement. Therefore, an affordable basis set was employed for the optimization and frequency calculation, as these operations are the bottleneck of the calculation, specially the former one, and experience very marginal improvements from using a more elaborate basis set. Following that, a more expensive basis set was used to recalculate the electronic structure for a set optimized geometry. Compared to the previous operations this calculation is not computationally demanding, but significantly improves the quality of the results. This way, a low computational cost is maintained while reducing errors due to an insufficient basis set such as basis set incompleteness error (BSIE)[97,98] and basis set superposition error (BSSE)[99,100]. An ultrafine integration grid was used in every studied case, as the utilization of a thorough integration scheme has been shown to be pivotal to a correct convergence of the calculation and accurate results.[101]

3.5. Thermodynamic properties

To determine the thermodynamic properties of a certain chemical system a representative statistical ensemble of said system has to be studied. Yet, DFT calculations model a discrete isolated system. Thus, a partition function is used to describe the ensemble of interest based on thermodynamic state variables, such as temperature and electronic energy of the system. Internal thermal energy (from now on only referred as energy) and entropy are derived from the partition function. In most cases this function is constructed using a very simple statistical thermodynamic model, in which the system is treated as an ideal gas under a 1 atm pressure. As it can be observed in eq. 17 the partition function is expressed as the product of its four independent components.[102]

$$q(V,T) = q_{elec}\, q_{vib}\, q_{rot}\, q_{trans} \tag{17}$$

The first term refers to the electronic partition function. This function is expressed as the summation of each energy level contribution which depends on the degeneracy of said level, ω_n, and its energy, E_n. However, for the great majority of cases the difference between the energy of the lowest excited state and that of the fundamental electronic state is significantly higher than $k_B T$. Meaning it can be assumed that only the ground state is populated regardless of temperature, considerably simplifying the partition function as depicted eq. 18.

$$q_{elec} = \sum_n \omega_n\, e^{E_n/k_B T} \approx \omega_0\, e^{E_0/k_B T} \tag{18}$$

Thus, the electronic contribution to the system energy in most cases is the so-called electronic energy of the ground state. On account of DFT functionals being based on the Born-Oppenheimer approximation, the energy contribution corresponding to nuclei kinetic energy has been stripped from the functional formulation to be added posteriorly. Hence, DFT functionals yield the electronic energy, while the contribution from nuclei movement is calculated using the remaining partition function components. While errors caused by calculations converging exclusively based on the electronic energy rather than the complete system energy are negligible in most cases, these additional energy contributions are key to a correct understanding of the thermodynamic properties of a chemical system.

Vibrational energy is calculated as the summation of each normal mode contribution, meaning that imaginary frequencies are ignored. Considering the K normal modes of a system, each having a vibrational frequency of υ_K, vibrational energy can be expressed as shown in eq. 19.

$$E_{vib} = R \sum_K e^{h\upsilon_K/k_B} \left(\frac{1}{2} + \frac{1}{e^{h\upsilon_K/k_B T} - 1} \right) \tag{19}$$

The calculation of vibrational energy contains two terms, one independent of temperature which corresponds to the zero-point energy, and the second one corresponding to the population of higher vibrational states due to temperature. In most cases each vibration is treated as a harmonic oscillator. This translates to the frequency easily being calculated using the second derivative of the electronic energy based on the mass weighted cartesian coordinates. This approximation can lead to errors when calculating the energy contributions of low frequencies. In cases where this error becomes noticeable a few corrections can be applied. The most commonly used ones are the quasi-harmonic corrections that target the frequencies lower than a certain threshold, generally around 50cm^{-1} or 100cm^{-1}. The correction developed by Grimme et al. uses the free rotor harmonic oscillator for those frequencies rather than the rigid rotor harmonic oscillator to improve the energy contribution accuracy.[103] Alternatively, the correction developed by Truhlar et al. treats each frequency below the threshold as if its value was that of the threshold.[104] Lastly another possibility is using a more complex approximation to the calculation of the frequencies, such as an anharmonic oscillator. However, given its elevated computational cost the latter approach is rarely used.

For any non-linear molecule rotational and translational energy contributions are obtained as shown in eq. 20.

$$E_{rot} = E_{trans} = \frac{3}{2}RT \tag{20}$$

Furthermore, as demonstrated by the following equations, the partition function can be used to obtain any thermodynamic property of the system of interest (eq. 21-23).

$$H = E + k_B T \tag{21}$$

$$S = R\left(\ln q + T\left(\frac{\partial \ln q}{\partial T}\right)_V\right) \tag{22}$$

$$G = H + TS \tag{23}$$

Examining the free energies, also referred to as Gibbs energies, *G*, of chemical species plausibly involved in the system's reactivity allows determining the spontaneity and feasibility of different chemical processes under certain reaction conditions.

Although this approach performs satisfactorily calculating the thermodynamical properties of most solvated systems, it should be noted that the gas phase model is unable to properly account for the solvent suppressing effects. Solutes are expected to experience hindrance to their rotational and translational movements in the presence of solvent when compared to a gas. Hence, their respective contributions should be quenched. While this movement reduction is expected to be accounted for in the solvation free energy[105] (discussed at length further in the text, on Section 3.6), the translational entropy is known to be a significant source of error in some studies (eq. 24).

$$S_{trans} = R\left(\ln\left(\left(\frac{2\pi m k_B T}{h^2}\right)^{3/2} + \frac{k_B T}{P}\right) + \frac{5}{2}\right) \tag{24}$$

This can be related to the used models overestimating the loss of translational entropy caused by the binding between two molecules.[106,107] Meaning that associative reaction steps are somewhat energetically penalized. Although many different schemes have been proposed to improve entropy calculations, the discussion on which correction, if any, leads to better results is still wide open.[108] It has been reported that in some cases these corrections can increase the error, causing significant differences depending on the studied system.[76,109] Thus, the effects of these corrections must be carefully and thoroughly evaluated when used. Nevertheless, for catalytic cycles in which the molecularity considerably changes this correction can become necessary, especially when comparing reaction paths whose change in molecularity is different.[110]

The approach to this correction preferred by our group and applied when deemed necessary in this Thesis is that proposed by Morokuma et al.[111] This election is based on the idea that a better approximation to the movement of solvated molecules is to treat them as if they were frozen rather than as a gas or with an arbitrary fraction of the movement of the gas, e.g., half of it as proposed by Plata and Singleton.[112]

An often-used strategy to minimize errors arising from translational entropies is to incorporate reagent molecules before they undergo any reaction or product molecules after they have been released as part of the modeled system. These molecules are included in segments of the reaction pathway where they are not directly involved in the reactivity to maintain consistent molecularity throughout. This approach, which was also included in the study of some systems in this Thesis, aids in the comparison of steps in a catalytic cycle or competing reaction pathways that otherwise would present different changes in molecularity.

3.6. Solvation models

Solvation effects can play a key role in determining the behavior of chemical systems. Solute interactions with the solvent molecules surrounding it affect its electron density distribution and, in many cases, defines the relative stability of different conformations. Meaning that for many systems, especially those in very polar solvents, a correct representation of its properties requires properly addressing solvation.[113,114]

While the most rigorous way to represent solvent effects would be to include enough solvent molecules to perfectly solvate the studied system, this approach, denominated as explicit solvent model, is seldom used for a series of reasons. Firstly, given how the cost of DFT calculation scales, even the inclusion of a few solvent molecules will significantly increase the computational cost. Furthermore, the many possible configurations the solvent molecules can be arranged in have to be considered, drastically increasing the number of calculations required to properly study a system. Lastly, the added solvent molecules should also be stabilized by other solvating molecules.[115] In the rare cases where this approach is employed, many layers of these molecules are included to accurately represent their behavior. Thus, this approach makes calculations considerably more complex and unreasonably expensive. For this reason, the only cases where it is employed it is paired with hybrid methodologies, such as QM/MM, that enable the use of a less expensive methods for the bulk of the system while using more precise methods for zones of interest. [116]

The vast majority of DFT studies use implicit models to incorporate solvent effects. Without the explicit inclusion of solvent molecules in the employed model, the chemical system is isolated in a vacuum exhibiting the behavior of a gas rather than that of a solute. Implicit solvent models calculate the solvation free energy which is then added as another free energy contribution of the system. This calculation is based on the use of a continuum dielectric medium to emulate the solvent effects on the chemical system without the need to include any solvent molecule.[117] Most implicit solvent methods consider four possible contributions to the solvation free energy, as shown in eq. 25.

$$\Delta G_{solv} = \Delta G_{elec} + \Delta G_{disp} + \Delta G_{rep} + \Delta G_{cav} \tag{25}$$

The first contribution, ΔG_{elec}, arises from the electrostatic interactions between the solute and the dielectric medium. The second and third represent the non-electrostatic interactions between the solvent and the solute, corresponding to the dispersion, ΔG_{disp}, and the repulsion energies, ΔG_{rep}, respectively. Lastly, the energy of cavitation, ΔG_{cav}, corresponds to the energy that would be required to open a cavity in the solvent to accommodate the solute. How these terms are defined radically change based on the employed method. In this Thesis, both the IEFPCM[118] and SMD[119] methods were employed. Both these methods are polarizable continuum models (PCMs), which constitute one of the most utilized approaches to including solvent effects because of their low computational cost and high accuracy.

PCMs methods calculate the electrostatic interactions applying the Poisson-Boltzmann equation[120] which uses the solute charge density and the solvent dielectric constant[121,122]. The other three terms comprising the solvation energy depend on the solvent-accessible surface. This surface is defined by a series of spheres centered on every solute atom with a parametrized radius. For IEFPCM these radii are obtained as 1.2 times the corresponding van der Waals radii, while the SMD model utilizes Bondi's values,[123] which are based on X-ray diffraction data. Effectively the calculation of the three non-electrostatic terms can be bundled into one for most methods, including the ones used in this work. This calculation considers the solvent-accessible surface area for each solute atom[124] and a coefficient specific to that atom and solvent pair, the surface tension.[125] Different methods propose different surface tension formulations, but in all cases, they are fitted with experimentally determined solvation free energies. Conveniently, the experimental fitting of implicit solvents leads to the solvation energies they afford already including the effect of the ensemble average of solvent structures that is burdensome to include using explicit solvent models. Additionally, they also account for other effects that are challenging to study computationally, namely the reduction in translational and rotational entropies when going from gas to solvated. Therefore, not only are implicit methods cheaper and easier to use, but they also include relevant effects that otherwise would be challenging to calculate.

Interactions between solute and implicit solvent cause a mutual polarization that is adjusted through an iterative process called Self-Consistent Reaction Field (SCRF).[126] It should be remarked that solvent with reduced polarity have a considerably limited effect on the solute properties. Consequently, as an approximation for these systems, implicit solvents are solely utilized on the energy refinement calculations. Hence, solvation energies are calculated for already optimized geometries, adjusting exclusively the solute electronic structure and the implicit solvent electrostatic term in the SCRF process. While this approach considerably reduces the computational cost, it is exclusively applicable for low polarity solvents such as benzene (ε_r=2.27) and chloroform (ε_r=4.71). Conversely, for high polarity solvents, such as formic acid (ε_r=51.1) and water (ε_r=78.4), a considerable change in the optimized geometry can be observed for calculations with or without implicit solvent. In such cases the use of the solvent model is necessary at every calculation stage to an accurate study of the system's properties.[127] Thus, the iterative optimization process includes the implicit solvent polarization and cavity reconfiguration.

The solvents models used in this Thesis, as for most implicit models, present lower accuracies when working on charged systems and in a lesser manner can also struggle with high polarity solvents. In specific cases reaction mechanisms are impossible to model using exclusively an implicit model. This includes cases in which solvent molecules act as ligands or mediate in the mechanism in some form, but also include cases in which a heavily polarized group has to be stabilized and the implicit solvent falls short. In these instances, the inclusion of select solvent molecules in addition to the implicit solvent can be the best suited approach.[128] Nevertheless, it is easy to introduce errors with this approach and only solvent molecules expected to be strongly bonded to a position, so that they accurately represent the statistical average structure, should be included.

Therefore, the addition of each solvent molecule must be justified and the afforded results carefully evaluated.

In this Thesis, solvent effects were included exclusively in the energy refinement step for the systems solvated in benzene or chloroform, while for the ones solvated in formic acid the implicit solvent was included throughout the whole calculation. The IEFPCM was applied in the calculations performed using the B3LYP-D3(BJ) functionals while the SMD, which was designed by the group responsible for the Minnesota functionals, was used with the M06-L functional.

3.7. Analysis of reactivity

Computational analysis of catalytic cycles is based on the capacity of these techniques to accurately determine the energies of every species involved in a reaction. Utilizing these energies, the reaction barrier for any chemical process can be calculated which can then be related to its reaction rate constant using Eyring equation (eq. 26).

$$k = \frac{k_B T}{h} e^{-\Delta G^{\ddagger}/_{RT}} \tag{26}$$

Nevertheless, this rather simplistic approach to determining reaction rate constants is susceptible to large errors, mainly due to the exponential dependence in the free energy barrier. Thus, a conservative margin of error should be considered when deriving conclusions directly from an energy barrier. Such as the rule of thumb used by many researchers stating that a barrier lower than 20 kcal/mol corresponds to a process that occurs at great speed at room temperature, a barrier between 20 and 25 kcal/mol corresponds to a process that can be observed at room temperature, a process between 25 and 30 kcal should require heating in order to be observable and anything above that may require extreme conditions in order to progress. However, it's essential to note that the expected cancellation of errors when modelling similar processes allows for the comparison of mechanisms with significant accuracy. These results can then be contrasted with experimental ones such as stereoselectivity, chemoselectivity or the different activities reported for different substrates.

Catalytic cycles can be complex processes consisting of many consecutive reactions with many species in equilibrium, which can considerably complicate determining the factors defining the rate or turnover frequency (TOF) of the complete cycle. In this work the framework proposed by Kozuch and Shaik was employed. This framework is based on transition state theory (TST)[129] and proposes that in every cycle a TOF-determining intermediate (TDI) and a TOF-determining transition state (TDTS) can be found. The TDI and TDTS correspond to whichever intermediate and subsequent transition state in the operating mechanism show the largest energy difference, as exemplified in Figure 3.1. This energy difference is referred to as energetic span (δE) and is equivalent to an energy barrier for the whole cycle, therefore defining the turnover frequency.

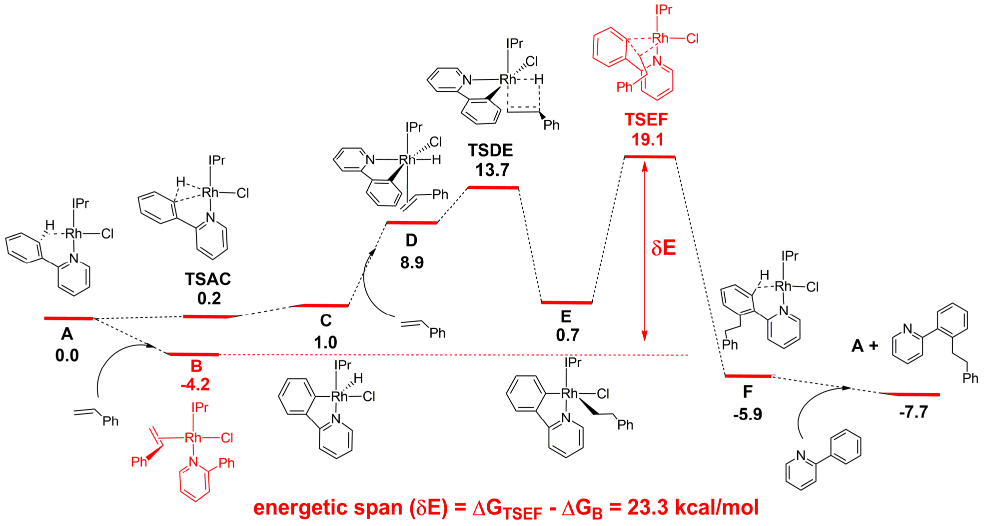

Figure 3.1. Determination the catalytic cycle energetic span of using the DFT calculated relative free energies in kcal/mol. Data taken from Castarlenas et al. ACS Catalysis **2019**, 9, 9372-9386.

The TDI is the most stable accessible intermediate preceding the TDTS, as such it acts as "resting state". Therefore, the TDI is the most populated intermediate during the catalysis, hence it should match experimental observations, such as NMR spectra used to monitor the reaction. The TDTS acts as the bottleneck in the cycle, with the rate of every other process being inconsequential to the turnover rate. The TDI and TDTS do not have to be consecutive in the cycle as every species connected by lower barriers than the energetic span is assumed to be in quasi-equilibrium. However, if many processes show a similar energetic span, especially in competing pathways this framework may become insufficient. In such cases other more complex approaches, such as microkinetic studies may become necessary to properly study the system.[130]

A factor to consider when comparing reaction rates of different processes is the concentration of every involved species. The concentration of DFT calculated system is that of an ideal gas under the conditions set for the thermodynamics calculations (typically standard conditions, 1 atm and 298.15K, are utilized). Generally, this concentration is considerably lower than that of the experiment causing the overestimation of the relative free energy of higher molecularity species. In every system studied in this Thesis the correction proposed by Goddard et al. was employed to treat every species as if they were in a 1M concentration.[131] To this end, eq. 27 was employed to calculate the free energy exchanged to reduce the volume occupied by 1 mol of the gas species to 1 L under the set conditions.

$$\Delta G_{gas}^{1atm\rightarrow 1M} = -T\Delta S_{gas}^{1atm\rightarrow 1M} = -TR\ \ln\left(\frac{V^{1atm}}{V^{1M}}\right) \tag{27}$$

3.8. Study of KIEs

The kinetic isotopic effect (KIE) is one of the most useful and easy to implement tools in the determination of reaction mechanisms. This technique consists of the measurement of reaction rates for a certain substrate and that same substrate with one or more of its atoms substituted by their respective isotopes. The difference or lack thereof can serve as an indicator of the process bottlenecking a mechanism.[132] Similarly, calculations can be performed to determine the energetic span of a process with and without isotopically marking the substrate. Eq. 28 shows how these results can easily be used to calculate the reaction KIE. It should be noted that even though in this case it is exemplified with hydrogen (H) and deuterium (D), the most commonly used nuclei, many other pairs can be used for these experiments.

$$KIE = \frac{k_H}{k_D} = \frac{\frac{k_B T}{h} e^{-\Delta G_H^{\ddagger}/RT}}{\frac{k_B T}{h} e^{-\Delta G_D^{\ddagger}/RT}} = \frac{k_B T}{h} e^{-\Delta\Delta G_{H/D}^{\ddagger}/RT} \tag{28}$$

As mentioned previously, DFT results are considerably more reliable when comparing the results of two or more similar modelled systems due to the beneficial effects of the cancellation of errors. For this reason, despite the considerable margins of error in the calculation of reaction constants, KIE calculations generally match experimental results with remarkable precision. Accurately matching the experimental KIE result is an indicator of the correct identification of the TDI and TDTS (see Figure 3.2)

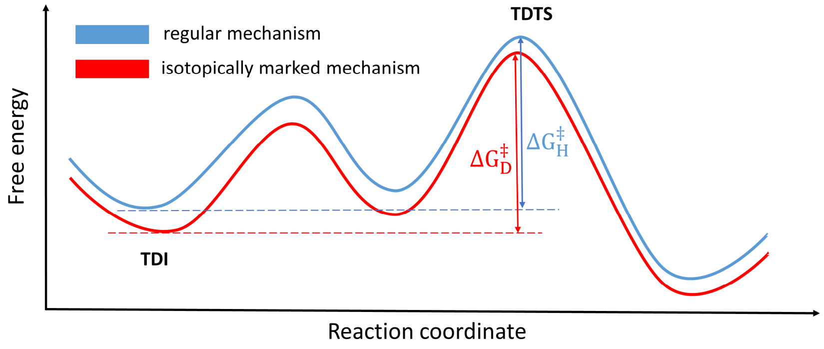

Figure 3.2. Energy span difference between the regular and isotopically marked reaction.

Thus, eq. 29 yields the KIE for a proposed reaction pathway, making it a valuable resource not only for mechanistic determination but also for theoretical result validation.

$$KIE = \frac{k_B T}{h} e^{(\Delta \mathrm{G}_{TDTS,D} - \Delta \mathrm{G}_{TDI,D}) - (\Delta \mathrm{G}_{TDTS,H} - \Delta \mathrm{G}_{TDI,H}) \big/ \mathrm{RT}} \qquad (29)$$

This equation was employed for every KIE calculated in this Thesis. This formulation is based on TST theory, meaning that effects such as tunneling effect or barrier recrossing are not considered. In such cases, more complex formulations can be employed to include said factors. Conveniently, in cases where the discrepancy is caused by an erroneous determination of the rate determining species, the KIE numerical value offers information of the role played by the marked nuclei in the rate determining process. It reveals if the marked atom is part of a bond being broken or formed, or if the atom is bonded to an atom whose hybridization changes during said process. Hence, this easy-to use technique serves not only as a great meeting point between experimental and computational findings, but also as indicator of the operating mechanism which can guide computational researchers to consider reaction pathways that may have been initially overlooked.

3.9. NBO orbitals

Natural Bond Orbitals (NBOs) are a form of localized orbitals used in computational chemistry to unravel electron density contributions and render a simpler description of orbitals. These straightforward orbital descriptions more closely correlate to various intuitive chemical concepts broadly used in Chemistry to describe molecular structures such as Lewis structures.[21]

Orbitals can be defined as one-electron wave functions, which are determined by a potential field depending on the nuclei and other electrons within the systems. In the context of KS-DFT, KS orbitals are derived from the fictitious system of non-interacting electrons that replicates the electron density of the actual system. Consequently, KS orbitals lack actual physical meaning. However, similar to wave function orbitals, KS orbitals have been proven to give insight into the electronic structure and bonding of a molecule, aiding in the rationalization of molecular properties, for instance reactivity.

As previously mentioned, complex electronic distributions can be described using a wide array of simple orbitals meant to be complemented through linear combination among them. In the optimization of the system energy and its canonical molecular orbitals the superposition of every orbital, even those at great distances is considered. Consequently, canonical orbitals typically display many minor contributions which may arise from orbitals at significant distances from the main orbital components. These contributions offer negligible improvements to the system energy and lack any significance towards its properties.[133] Other effects such as hyperconjugation or resonance effects, can further contribute to the orbital delocalization. This delocalization obscures the interpretation and comparison of molecular orbitals, obfuscating the relationships between electronic distribution and other characteristics of the molecule.

Like other forms of localized orbitals, natural orbitals limit the interactions among orbitals to regions of chemical significance, such as atoms or bonds, restricting the optimization process to the orbitals centered within these regions. As a result, natural orbitals exclude minor contributions leading to more interpretable orbitals, that allow for a better understanding of the system's electronic structure and elucidation of its properties.

The simplest natural orbitals are the Natural Atomic Orbitals (NAOs), which do not combine the original atomic orbitals in any form. However, NAOs are affected by neighboring orbitals in the form of electrostatic and steric interactions with the environment. This results in NAOs being more diffuse or compacted and, in some cases, the apparition of new nodes. Considering exclusively the orbitals with an appreciable occupancy, a minimal basis set containing the core and valence orbitals of the molecule is obtained.

The next step in complexity is the Natural Hybrid Orbitals (NHOs), which are obtained through the combination of NAOs corresponding to each atom to optimize their energy. The linear combination of valence atomic orbitals results in the formation of hybrid orbitals, such as the sp^2 and sp^3 orbitals. These hybrids orbitals provide a more accurate description of the electronic distribution which accounts for the chemical environment of each atom. Both NHOs and NAOs are a series of orbitals centered on individual atoms, which also are orthonormal among themselves.

The NBOs are obtained by optimizing NHOs while allowing for the linear combination of orbitals corresponding to one, two and occasionally three atoms, also referred to as centers, since in this case the orbitals can be centered in different atoms. One-center NBOs refer to core orbitals or lone pairs if they are occupied or Rydberg orbitals or lone vacancies if they are unoccupied. Two-center NBOs combine a pair of overlapping orbitals of different atoms. Depending on whether the interaction is constructive or destructive the resulting orbital is bonding or antibonding, respectively.

The calculation of the NBOs leads to the exploration of the optimal bonding pattern that maximizes the occupancy of "Lewis-type" NBOs, meaning those corresponding to bonds and lone pairs. This results in the determination of the Lewis structure that better represents the wavefunction or electron density. These orbitals provide insights into the nature and strength of chemical bonds. A thorough analysis of the composition and occupancy of a system NBOs yields a detailed and easy-to-interpret description of its electronic distribution which helps rationalize many of its properties such as dipole moment or ionization potential. Furthermore, a comparative analysis of the electronic distribution of key species involved in a reaction can provide comprehensive understanding of their chemical behavior and reactivity (see Figure 3.3).

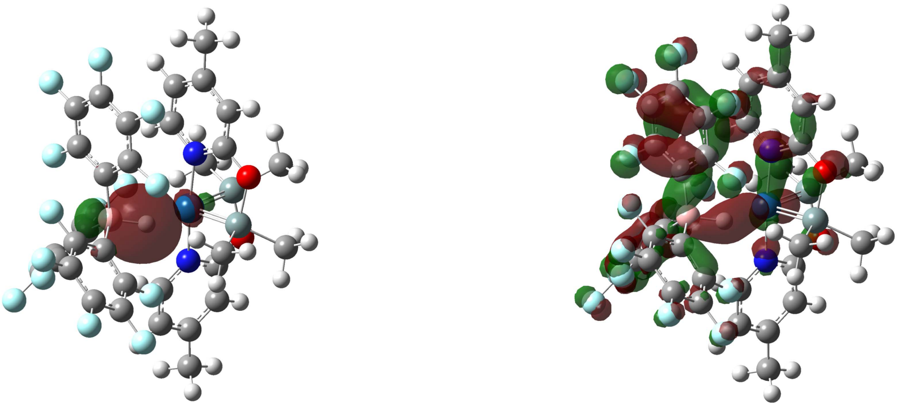

Canonical Molecular Orbital

Natural Bonding Orbital

Figure 3.3. Comparison of a canonical molecular orbital and the same orbital as a natural bonding orbital using eigenvalue 0.03 in both cases.

The occupancy of the obtained NBOs is a key factor in the validation of the Lewis structure defined by these orbitals as a representation of the electron density. For a closed shell system, the occupancy of an orbital can oscillate between 0 and 2. Natural orbitals whose occupancy is close to the latter, accurately fit the distribution of the electron density, rendering a faithful Lewis structure. Effects such as resonance that NBOs struggle to describe result in lower occupancies in some Lewis-type orbitals, populating antibonding and Rydberg orbitals instead. Thus, researchers that use NBOs to describe a specific interaction of a system such as the bond strength of a bond refer to the occupancy of said bond.

Another relevant application of natural orbitals is the natural population analysis (NPA) which calculates the system's atomic charges using the sum of electronic population from the NAOs corresponding to each atom.[134] This approach is considered to be a more accurate descriptor of the system charge distribution than the generally used Mulliken Population Analysis which derives the atomic charges directly from the wavefunction.[135] In this work, as in many others the NPA-obtained charges will be referred to as NBO charges, since the calculation of the NBO orbitals requires the calculation of the NAOs which are then used to determine the atomic charges.

3.10. Computational details

This section outlines the computational details employed for the theoretical calculations of each system discussed along this Thesis.

All DFT calculations were carried out using the Gaussian09 program package,[136] while specific aspects of the utilized methodology varied on a system-by-system basis.

Geometry optimizations and frequency calculations for the studied systems related to CO_2 utilization (Chapter 4) were performed using the B3LYP-D3(BJ) method and def2-SVP basis set. Whereas for the systems involved in terminal alkyne hydrofunctionalization reactions (Chapter 5) these calculations were performed at a B97D3/def2-SVP level of theory. Additionally, for the study of reactions in neat formic acid (Sections 4.2 and 4.3) these calculations included the IEFPCM solvation model to account for the effects of the strongly polarizing solvent. Analytical frequency analysis was employed to confirm the nature of stationary points.

Electronic energies were refined using single point calculations at the M06-L/def-TZVP level of theory, with the exception of those of Section 4.2 in which B3LYP-D3(BJ)/def-TZVP was utilized instead. The SMD solvation model (IEFPCM for Section 4.2) corresponding to the reaction solvent was included to these energy refinement calculations (benzene for Sections 4.1 and 5.1, formic acid for Sections 4.2 and 4.3 and dichloromethane for Section 5.2).

Thermochemical corrections were computed for the respective reaction temperature of each catalytic system (323 K for Section 4.1, 353 K for Sections 4.2 and 4.3 and 298 K for Sections 5.1 and 5.2). All corrections were referenced to a 1M standard state at 1 atm and the reaction temperature using the approximation method proposed by Goddard et al.

For the study of CO_2 hydrosilylation reactions (Section 4.1) translational entropies were removed to avoid errors arising from these contributions in the comparison of reaction pathways with different molecularities. For the studied reactions taking place in neat formic acid (Sections 4.2 and 4.3) translational entropy contributions of formic acid molecules were removed to negate the free energy penalty caused by the coordination of a solvent molecule to the complex which is, in principle, already solvated. Additionally, in systems for which many significantly low vibration modes were observed for catalytic activity determining species (Sections 4.1, 5.1 and 5.2) Grimme's quasi-harmonic correction was applied setting a 100 cm^{-1} threshold.

Chapter 4:
CO_2 utilization

> "Science is not about big words. It's not about lab coats and safety goggles, and it's definitely not about trying to make yourself sound fancy. Science is not an end in itself, but a path. It's a method to help you discover the underlying order of the world around you and to use those discoveries to help you predict how things will behave in the future."
>
> J. Kenji López-Alt

The accumulation of carbon dioxide in the atmosphere is considered a leading cause of climate change because of its greenhouse effect. The emission of this gas has experienced rampant growth for more than a century, because of the world's reliance on fossil fuels. Natural processes are incapable of curbing the CO_2 build-up caused by these emissions, necessitating proactive measures to mitigate its damaging impact on the environment. Consequently, the pursuit of strategies aimed at reducing the atmospheric CO_2 levels has become a goal of critical importance for a sustainable future.[137]

While reducing CO_2 emission is imperative to decrease its concentration in the atmosphere, additional measures are necessary for an effective approach to this objective. The capture of CO_2, whether as it is being produced in a large-scale process or from the atmosphere, offers a way to reduce the accumulation of this gas and has seen significant progress during the last years.[138] However, the capture and storage of ever-increasing quantities of CO_2 for an indefinite amount of time is not only costly, it can only be considered a temporary solution rather than a sustainable one. Though some industrial processes make use of CO_2, their consumption does not add up to 1% of the emissions of this gas.[139] Hence, there is a necessity for the development and/or optimization of pathways that provide an outlet for this product.[140,141] As shown in Figure 4.1, these may take many forms, such as using it as a substitute of other commonly used chemicals (e.g., using supercritical CO_2 instead of hexane for caffeine extraction), or as a substrate for synthesis (e.g., the formation of carbamates using amines).[142,143] Despite the environmental benefits of these applications making them highly desirable, it can be challenging to refine them to the point of becoming economically viable so they can make a genuine impact. Thus, many research projects are focused on the utilization of CO_2 and this topic has become of great relevance across many fields of research.

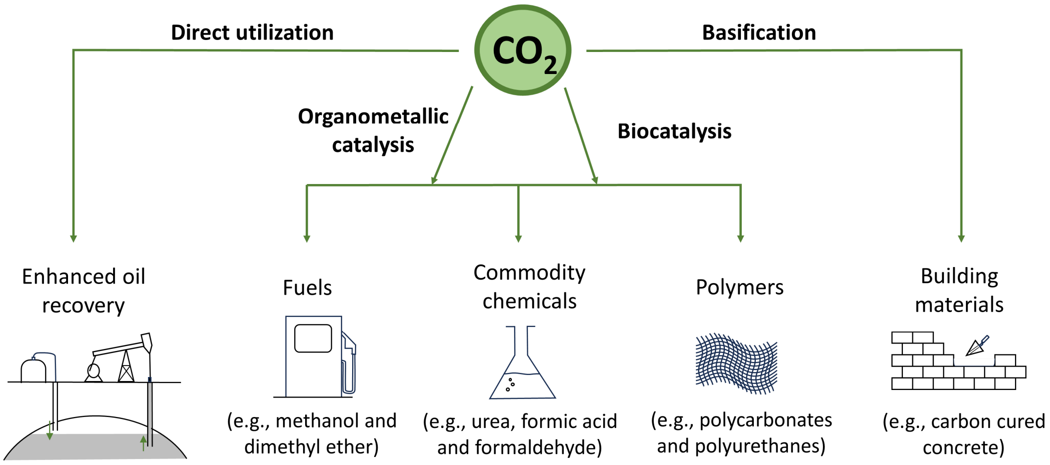

Figure 4.1. Examples of strategies and possible types of products of CO_2 utilization.

From a chemical standpoint, the main challenge in CO_2 utilization is the inertness of this molecule and some of its derivatives, such as the formic acid. Catalysis offers a way to activate these molecules under milder conditions, providing an ideal approach for the development of sustainable processes for CO_2 utilization.[144,145] The photosynthesis is a paradigmatic example of CO_2 utilization, combining it with water to form sugars, a higher value chemical that can be used as a fuel. This process is catalyzed by a series of organometallic complexes present in chloroplasts which are able to dehydrogenate the water and activate the inert CO_2 to reduce it. Similarly, other organometallic catalysts are used to transform CO_2 into higher value products such as urea, utilized on fertilizers, and methanol, which can be used as both a commodity chemical and a fuel.

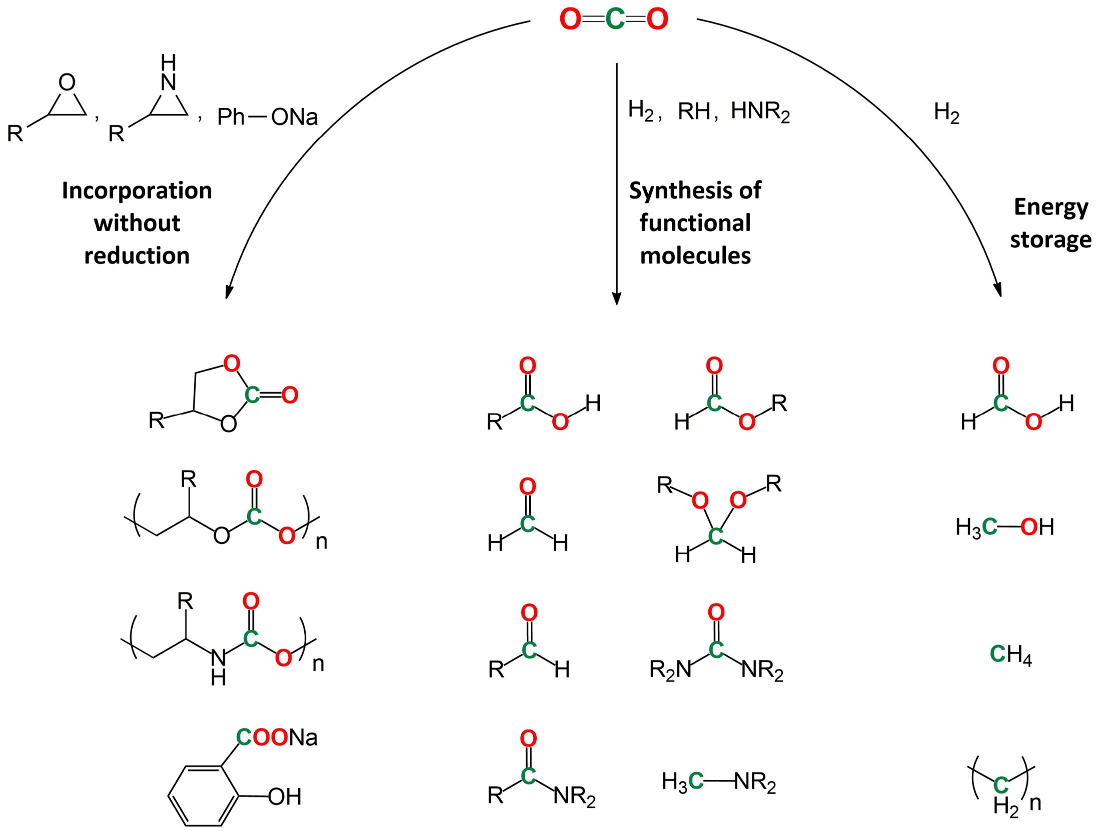

Figure 4.2. Examples of products that can be obtained through catalized reactions with CO_2

The design of efficient catalysts for transformations of interest can elevate by-products into high value reactants. In such a way, CO_2 could serve as an abundant, inexpensive, and renewable substrate, perfectly exemplifying the concept of Circular Chemistry.[146] Organometallic catalysts, characterized by their ability to polarize otherwise notably strong bonds and facilitate their attack, stand out as an ideal candidate for this objective.

4.1 Selective reduction of CO_2 with tertiary silanes using an Ir-NSi catalyst and a $B(C_6F_5)_3$ cocatalyst

Introduction and objectives

In recent years, the exploration of strategies to harness CO_2 as a C1 carbon source in synthesis has captured significant attention.[147,148] This promising prospect holds the key to unlocking the potential of CO_2 in an array of diverse synthetic pathways, offering exciting opportunities for sustainable chemical production.[149,150] Despite using a catalyst, the remarkable kinetic and thermodynamical stability of CO_2 imposes significant limitations on its reactivity, restricting its applicability to a select few processes. These reported processes require extreme reaction conditions or the utilization of extremely reactive reagents that compensate for the inertness of the CO_2.[151] Consequently, very few of them are used in larger scale to obtain these products. Scheme 4.1 shows some examples of reported synthetic routes that employ CO_2.

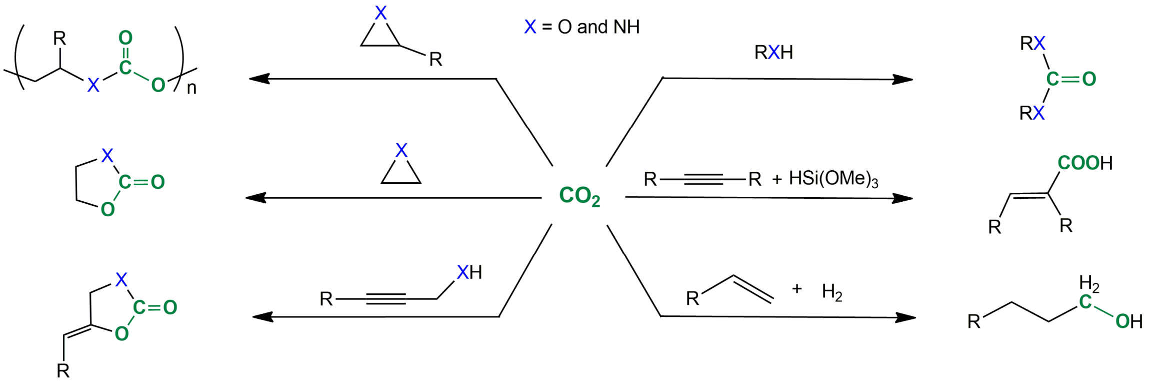

Scheme 4.1. Representative examples of catalyzed synthetic routes using CO_2 as C1 carbon source.

Alternatively, CO_2 can be functionalized to improve its reactivity, opening pathways to its utilization. One effective approach to the functionalization of CO_2 is the utilization of silanes. This reduction can be achieved under mild conditions, being thermodynamically favored over other commonly used reductants such as H_2. This can be attributed to the polarized H—Si bond being easy to break and the strength of the afforded Si—O bond. A CO_2 molecule can go through multiple consecutive hydrosilylation processes to yield a series of products with different levels of reduction, namely silylformates, bis(silyl)acetals, methoxysilanes, and methane, as shown in Scheme 4.2. It has been demonstrated that through deliberate selection of the catalyst and conditions utilized for this reduction its selectivity can be controlled. Lastly, it should be noted that some silanes stand out for their stability to air and moisture and being obtained through inexpensive and environmentally benign processes, making them ideal reagents for circular chemistry.[152]

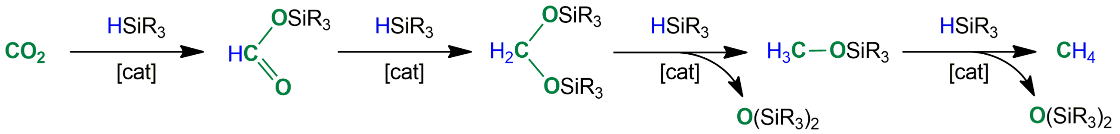

Scheme 4.2. Stepwise reduction of CO_2 to methane with hydrosilanes.

This work is focused on the selective CO_2 reduction to bis(silyl)acetals. These reactions are referred to as reduction to formaldehyde level because acetals exhibit a comparable reactivity to formaldehyde. Formaldehyde is a high-value chemical used in over 50 industrial processes for diverse products such as pharmaceuticals, paints, polymers, and adhesives, amounting to an annual demand of 30 million tons.[153] It presents great potential as C1 carbon source, since it can be used to include CH or CH_2 moieties in simple and straightforward reactions.[154] Currently, formaldehyde is solely produced by partial oxidation of methanol at extremely high temperatures.[155] Finding CO_2-based alternatives to this process has proven to be challenging and very few reports on this topic can be found.[156] Nonetheless, many examples of catalysts capable of reducing CO_2 to bis(silyl)acetals have been reported. Not only can these products be easily converted to formaldehyde, but more importantly, they present the same capability to be used to introduce CH and CH_2 moieties, as illustrated by Scheme 4.3, making them potential synthetical substituent for the formaldehyde.

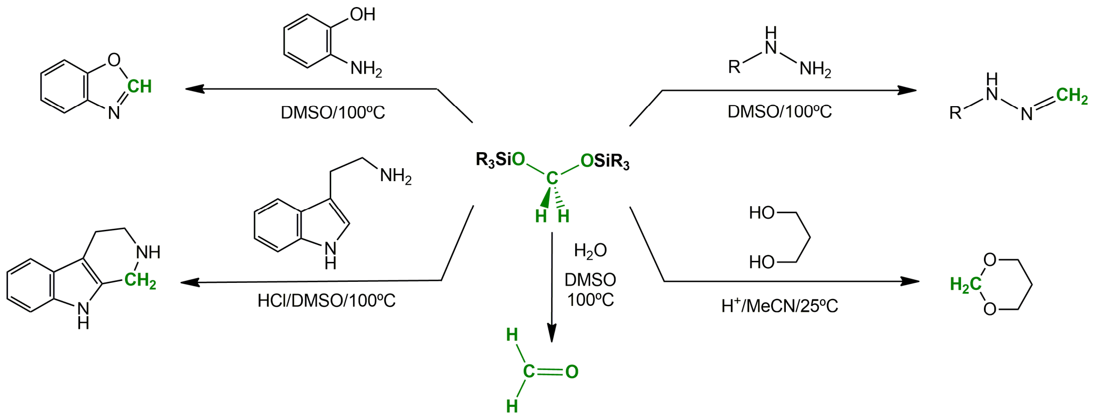

Scheme 4.3. Representative examples of bis(silyl)acetal reactivity and its use as C1 carbon source.

Among the organometallic catalysts for the selectively CO_2 reduction to bis(silyl)acetals, a remarkable diversity of metals and ligands is available. Yet, interestingly all these catalytic systems have one common aspect, they all include a Lewis acid, in most cases $B(C_6F_5)_3$.[157–160] While $B(C_6F_5)_3$ and other Lewis acids are effective catalyst for the reduction with silanes of many substrates, CO_2 is not reduced by them alone.[161] Likewise, without the presence of the Lewis acid the organometallic complexes cannot catalyze the

CO_2 hydrosilylation or their selectivity is radically changed. Figure 4.3 shows how the Lewis acid may take many forms as part of the catalytic systems.

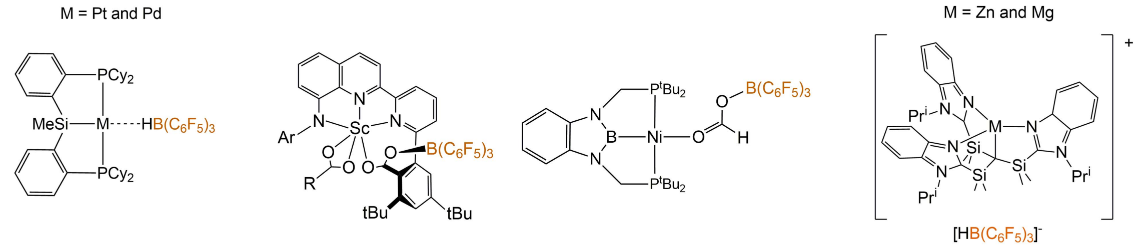

Turculet et al. *Chem. Eur. J.* **2012**, *18*, 15258–15262

Parvez al. *Angew. Chem. Int. Ed.* **2014**, *53*, 789–792

Parvez al. *Angew. Chem. Int. Ed.* **2014**, *53*, 789–792

Parkin et al. *J. Am. Chem. Soc.* **2017**, *139*, 18162–18165

Figure 4.3. Selected examples of catalysts used for selective CO_2 hydrosilylation to bis(silyl)acetals.

Exploring these reactions presents particular challenges as they involve competing pathways leading to diverse products corresponding to distinct levels of reduction. While many catalysts have been reported to reduce CO_2 to formate level, the number of catalysts able to perform the subsequent reductions is considerably lower.[162] Moreover, in instances where the acetal is formed, controlling the following reductions leading to methanol derivatives has proven to be difficult.[163] Thus, there is significant interest in catalytic systems able to selectively reduce to formaldehyde level and how the reactivity of this process is determined. Yet, to date, research into the mechanism of these select catalytic systems has been scarce. The discussion on the operating mechanism and the role of the metal and that of the Lewis acid in these processes remains open.

Henceforth, this section focuses on the results obtained for the CO_2 reduction with tertiary silanes to formaldehyde level catalyzed by $[Ir(CF_3CO_2)(\kappa^2\text{-NSi}^{Me})_2]$ (which will be referred as **A**) and $B(C_6F_5)_3$ in equivalent loads (see Scheme 4.4). A computational study was carried out with the following goals:

1. Elucidating the operating mechanism for the reduction.
2. Determining the rate- and selectivity-determining steps.
3. Unraveling the effect of the Lewis acid in the catalytic activity.

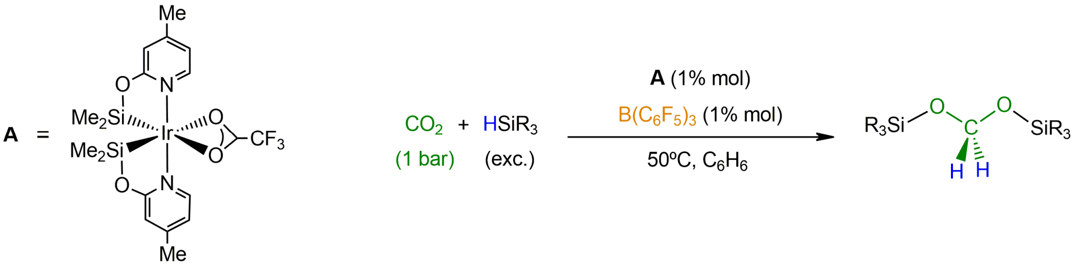

Scheme 4.4. Catalyzed reaction of CO_2 with tertiary silanes in the presence of $B(C_6F_5)_3$.

Results and Discussion

Experimental results show that the selectivity of the $[Ir(CF_3CO_2)(\kappa^2\text{-}NSi^{Me})_2]$ complex is dependent on a series of factors. These observations, presented in Table 4.1, were taken into account to determine the model used and goals for this computational study.

Table 4.1. Experimental results obtained for the catalyzed reduction of CO_2 in C_6D_6 at 323 K.

Silane	CO_2 (bar)	Catalytic system	Time (h)	Conversion (%)	Ratio of reaction products (%)			
					$HCOOSiR_3$	$H_2C(OSiR_3)_2$	H_3COSiR_3	CH_4
$HSiEt_3$	1	**A**+$B(C_6F_5)_3$	16	12		>99	<1	
$HSiMePh_2$	1	**A**+$B(C_6F_5)_3$	16	78		>99	<1	
$HSiMe_2Ph$	1	**A**+$B(C_6F_5)_3$	16	93		>99	<1	
$HSiMe_2Ph$	1	**A**	24	50	90	2	8	
$HSiMe_2Ph$	1	**A**+BPh_3	8	>99	81	12	7	
$HSiMe_2Ph$	1	**A**+0.5$B(C_6F_5)_3$	24	93	82	18		
$HSiMe_2Ph$	1	**A**+2$B(C_6F_5)_3$	24	48				>99
$HSiMe_2Ph$	3	**A**+$B(C_6F_5)_3$	8	>99	83	13	4	

This array of results provides many valuable insights into the catalytic activity. The first three entries of the table show that while different silanes may present varying reaction rates, all of them exhibit the same selectivity. In order to reduce computational costs, $HSiMe_3$ was chosen as model reductant for the study. While it was not experimentally tested, due to its gaseous nature complicating experimental operations, it is still expected to show the same selectively towards bis(silyl)acetal formation.

The fourth to seventh entries highlight the importance of the Lewis acid towards defining the reaction selectivity. The fourth entry demonstrates that in absence of $B(C_6F_5)_3$ the process is selective towards silylformate formation. The bis(silyl)acetal is only formed as a by-product and the presence of relatively higher amounts of methoxysilanes indicates that the acetal reduction is not controlled. The fifth entry emphasizes the importance of using $B(C_6F_5)_3$ for the model, as the reaction with simpler Lewis acids, namely BPh_3, lead to the preferential formation of silylformate. Hence, simpler Lewis acids could not be used to explore the selectivity of interest.

Even though the sixth to eighth entries are not directly relevant to the modeling of the catalytic system, they provide valuable information to determine its activity. The sixth one emphasizes the necessity of an equivalent loading of $B(C_6F_5)_3$ to that of **A** for achieving the desired selectivity. This indicates that the Lewis acid and **A** act as a unit in the catalytic cycle, rather than having independent roles which they would be able to perform separately, even at different concentrations. The seventh entry shows that adding a second $B(C_6F_5)_3$ equivalent results in the CO_2 reduction to CH_4 rather than to formaldehyde level. This can be surmised as the first equivalent of the borane and **A** reducing the CO_2 to acetal as expected, while the second $B(C_6F_5)_3$ equivalent further reduces the acetal to CH_4 in a separate catalytic cycle. The reduction to CH_4 of diverse CO_2 derivatives with silanes has been reported for similar systems. [164,165]

Lastly, the eighth entry reveals that while using higher CO_2 pressures increases the reaction rate, the selectivity is compromised. This is indicative of the modest difference between the energy span of the catalytic cycle producing the formate and that of the cycle yielding the acetal. Hence, a moderate change in the relative concentration of the two substrates can significantly alter the selectivity. Consequently, it is critical to the selectivity to meticulously control the reaction conditions. Likewise, taking into account these conditions will be key to an accurate understanding of the catalytic activity and origin of the selectivity.

As stated earlier, in absence of a Lewis acid **A** selectively catalyzes CO_2 reduction with tertiary silanes to formate level. This reaction was previously studied by our group. In said study the active species was confirmed to be the metallic hydride, which will be referred to as **A'**. Figure 4.4 presents the mechanism determined for this reaction.

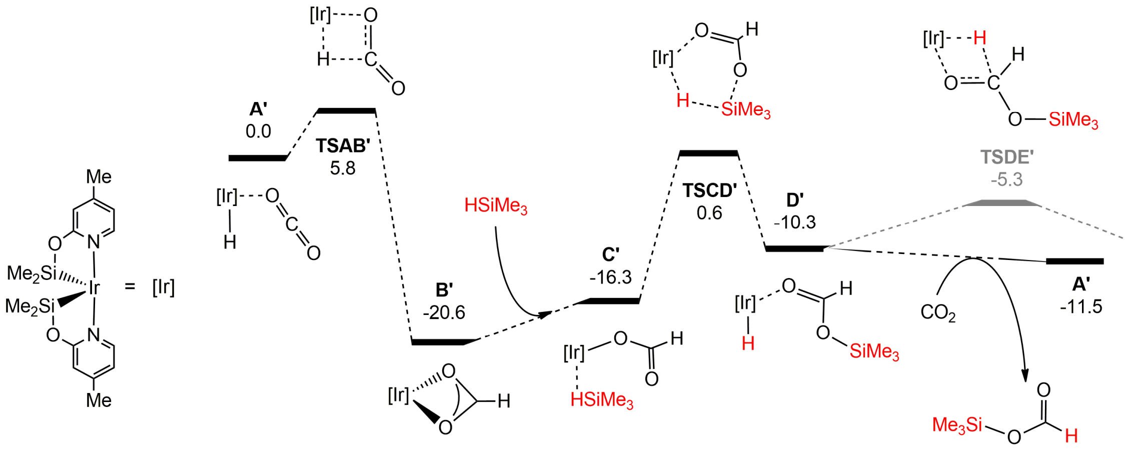

Figure 4.4. DFT calculated free energy profile (in kcal mol^{-1} relative to **A'** and isolated molecules) for silylformate formation. Compound names from the original work have been changed for clarity and energies recalculated using the methodology used for other calculations in this section.

The catalytic cycle starts from intermediate **A’**, presenting a hydride and a CO_2 molecule in its catalytic sites. The reaction begins with the migratory insertion of the metallic hydride into the CO_2, characterized by transition state **TSAB’**, to produce the formate intermediate, **B’**. The formate can be unbonded from one of the active sites to enable the coordination of a $HSiMe_3$ molecule yielding intermediate **C’**. The reaction continues with the cleavage of the silane H—Si bond via transition state **TSCD’**, regenerating the metallic hydride and bonding the $SiMe_3$ group to the formate, affording a the silylformate intermedite, **D’**. At this point, two reaction pathways arise. The first one involves the release of the silylformate molecule and coordination of a new CO_2 molecule. The second, less energetially favored, pathway entails a further CO_2 reduction. It starts with the migratory insertion of the second hydride through transition state **TSDE’** and ultimately leads to either the formation of bis(silyl)acetal or methoxysilane.

Therefore, the reactivity of the Ir complex is based on the presence of a metallic hydride which can be inserted on CO_2 or CO_2 derivatives. This reaction is followed by the silane activation, breaking the H—Si bond to form the stronger Si—O bond with the CO_2 or CO_2 derivative, and regenerating the hydride.

In the presence of a $B(C_6F_5)_3$ equivalent susbtancial differences in the active species arise, leading to the observed selectivity changes. Figure 4.5 presents the generation of the active species for the selective reduction to formaldehyde level.

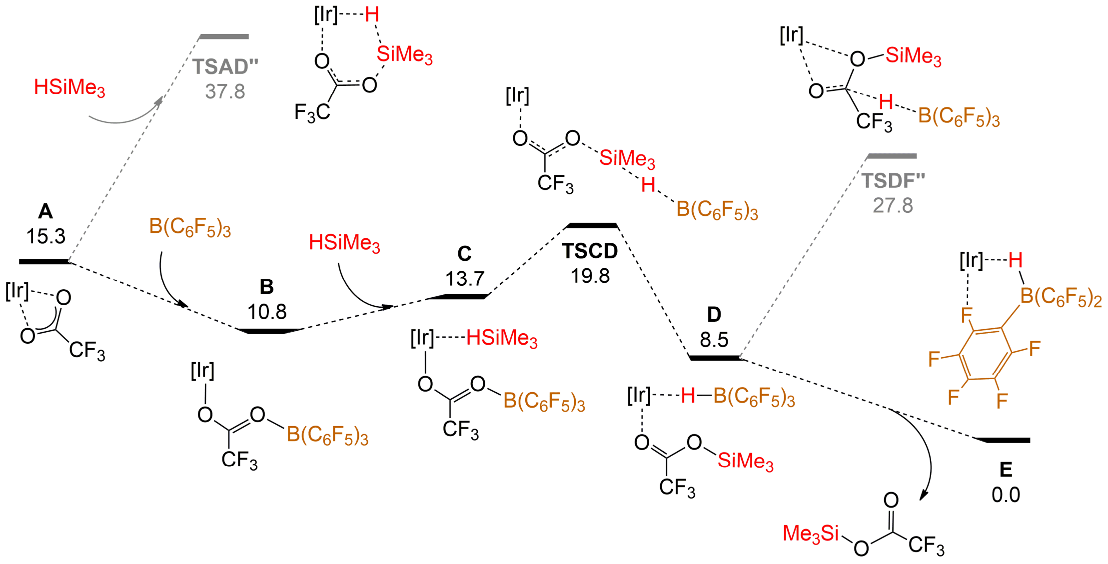

Figure 4.5. DFT calculated free energy profile (in kcal mol^{-1} relative to **E** and isolated molecules) for the activation of the catalyst.

$B(C_6F_5)_3$ acts as a Lewis acid forming strong adducts with atoms able to donate an electron pair. The formation of **B** consists of the borane bonded to a triflouroacetate O atom. This process is thermodynamically favored, being 4.5 kcal mol^{-1} more stable than **A**, despite the fact that the acetate is detached from one catalytic site due to the notable steric hindrance of $B(C_6F_5)_3$. This coordination mode was experimentally observed through X-ray cristalography (Figure 4.6).

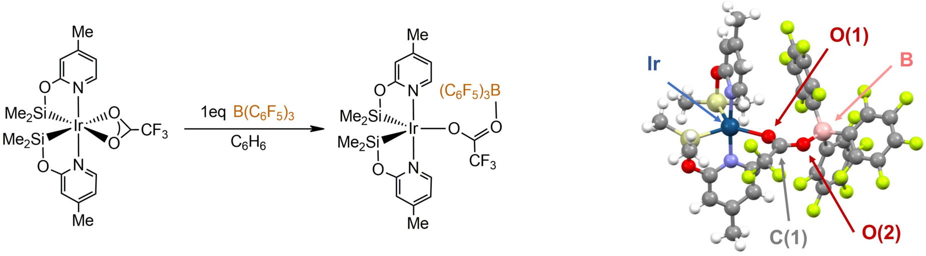

Distances (Å)	Ir — O(1)	O(1) — C(1)	C(1) — O(2)	O(2) — B
X-ray structure	2.285(3)	1.220(5)	1.271(4)	1.550(5)
DFT structure	2.346	1.236	1.264	1.549

Figure 4.6. X-ray structure of the product of the addition of 1 equivalent of $B(C_6F_5)_3$ to **A** and a comparison of some key distances in this structure to those of the DFT-determined **B**.

The activation process continues with the coordination of the partially negatively charged H atom of a silane molecule in the vacant site, forming intermediate **C**. Subsequently, the Si—H bond is broken through **TSCD**, a linear S_N2 nucleophilic attack of the acetate terminal oxygen to the silicon atom while the leaving hydride is captured by the $B(C_6F_5)_3$, effectively making it a remarkably better leaving group. This process is significantly favored over the silane activation without $B(C_6F_5)_3$ collaboration (**TSAD'**). Thus, in the presence of a $B(C_6F_5)_3$ equivalent the reaction exclusively takes place through the cocatalyzed pathway. Lastly, the silylacetate is released yielding the active species, **E**, an intermediate presenting a hydride bonded to the borane. The hydride formation was experimentally validated by a NMR experiment (Figure 4.7).

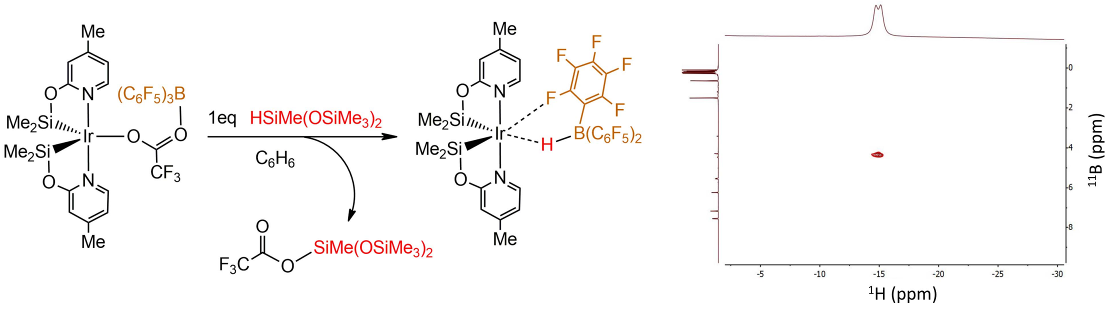

Figure 4.7. ^{11}B-^{1}H HSQC NMR spectrum of the product of the addition of 1 equivalent of $B(C_6F_5)_3$ and 1 equivalent of $HSiMe(OSiMe_3)_2$ to **A**.

Typically, strong Lewis acids, such as $B(C_6F_5)_3$, form strong bonds with ligands able to donate electron pairs (e.g. trifluroacetate or formate). However, the steric hindrance arising from the bulkiness of both $B(C_6F_5)_3$ and the Ir complex makes this pair of molecules act as frustrated Lewis pairs (FLP).[166] Their respective capabilities to accept and donate electron density allow them to polarize substrate bonds, assisting its breakage. Hence, $B(C_6F_5)_3$ acts as cocatalyst with the Ir-catalyst, facilitating the heterolitic cleaveage of Si—H bonds through a S_N2 nucleophilic attack. Within this reaction the partially positively charged SiR_3 fragment is attacked by a ligand O atom, in this case of the trifluoroacetate, while the partially negatively charged hydride acts as leaving group and is captured by the borane. This process, defined as $B(C_6F_5)_3$ promoted, is significantly more favored than the Ir promoted one, in which the metallic hydride is formed, as shown in Figure 4.8.

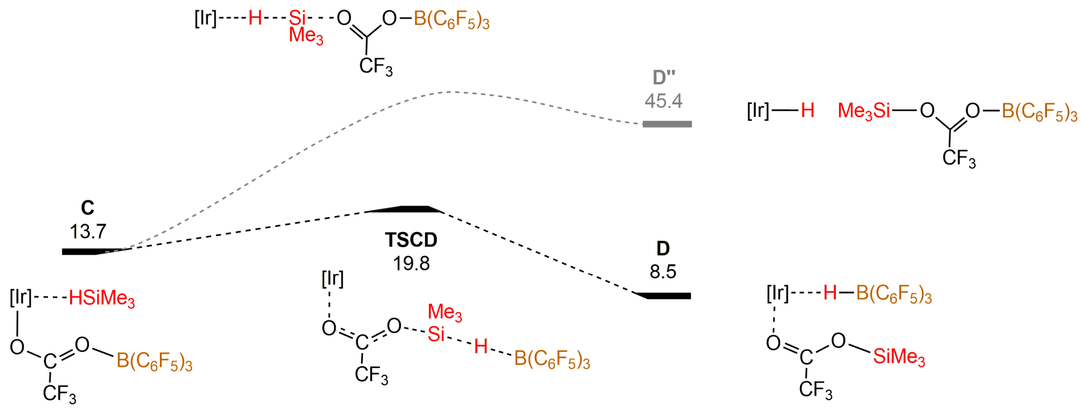

Figure 4.8. DFT calculated free energy profile (in kcal mol^{-1} relative to **E** and isolated molecules) for a compassion between borane promoted Si—H cleavage and Ir promoted Si—H cleavage.

$B(C_6F_5)_3$ acts as the acidic component of the FLP, forming a strong adduct with the hydride as it is generated. The hydride donates its electron pair to the vacant $B(C_6F_5)_3$ *p*-orbital, forming a σ-bond which significantly stabilizes the hydride. This bond is a relevant feature of the active species, **E**, presenting a B—H distance of 1.28 Å, while the interaction between the Ir and the hydride is noticeably weaker exhibiting a Ir—H distance of 1.95 Å. This is the key difference between the active species of the catalytic cycles with and without the presence $B(C_6F_5)_3$. The active species in absence of Lewis acid, **A'**, presents a 1.71 Å Ir—H bond, which is considerably weakened by the strong *trans* effect of a silyl group. The disparity in hydride stabilization between these two catalytic systems is reflected in their energy differences, as the reduction processes can be described as cycles involving the insertion of the hydride and its regeneration through the cleavage of a silane. Figure 4.9 illustrates the significant differences in stability of between **E** and **A'** and the NBO orbitals corresponding to the bond formed by the electron pair of the hydride.

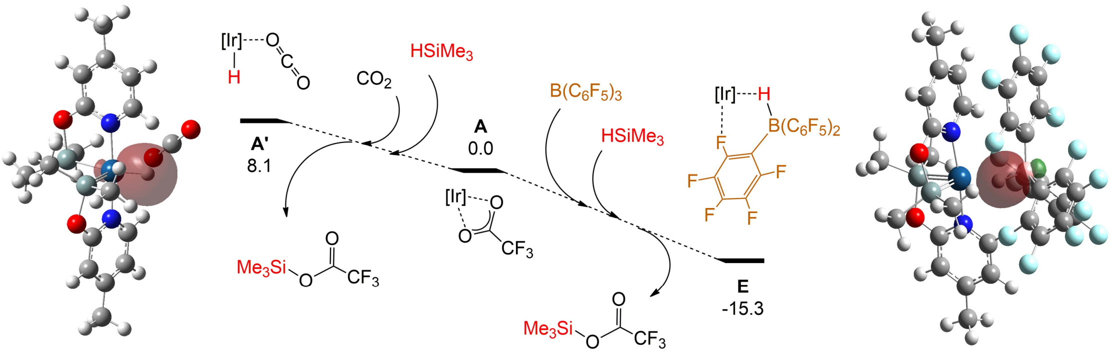

Figure 4.9. Relative free energies (in kcal mol^{-1}) of the hydrides compared to **A** and the NBO orbitals of the bond formed by the hydrides.

Lastly, it is worth noting that the migratory insertion of the hydride in the trifluoroacetate, characterized by **TSDF''** at a relative free energy of 27.8 kcal mol^{-1}, is heavily energetically unfavored compared to the insertion in the CO_2 occurring in the catalytic cycle (22.2 kcal mol^{-1}). NMR studies conducted under catalytic conditions validate this result, as silyltrifluoroacetate is observed and no product of its reduction is detected, while CO_2 is reduced to formaldehyde level. Moreover, experiments with **B** with an excess of silane and no CO_2 resulted in the reduction of the trifluoroacetate to formaldehyde level but not to methanol level, therefore showing the same selectivity than the CO_2.

Therefore, the catalytic cycle begins with the formation of **E**, in which the two catalytic sites of the Ir are occupied through weak interactions with the hydride and a $B(C_6F_5)_3$ fluoride. This species facilitates the CO_2 hydrosilylation, as shown by Figure 4.10.

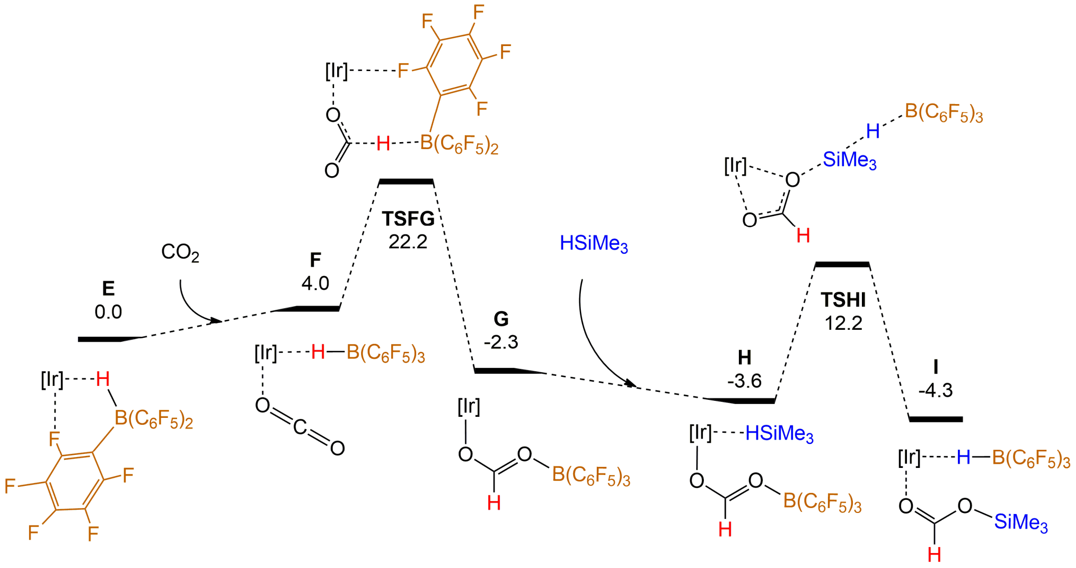

Figure 4.10. DFT calculated free energy profile (in kcal mol^{-1} relative to **E** and isolated molecules) for the catalytic hydrosilylation of a CO_2 molecule from **E**.

This reaction starts with the coordination of a CO_2 molecule to the Ir, yielding intermediate **F**, which is an endergonic process by 4.0 kcal mol^{-1} due to the poor electron-donating ability of CO_2. Following this coordination, the hydride is transferred from the $B(C_6F_5)_3$ to the CO_2 through transition state **TSFG**, presenting an effective energy barrier of 22.2 kcal mol^{-1} and yielding the formate intermediate, **G**, at -2.3 kcal mol^{-1}. Similarly to what could be observed for intermediate **B**, the steric hindrances of $B(C_6F_5)_3$ and the catalyst impede the simultaneous coordination of the formate O atom to the borane and the Ir. This oxygen atom stays at a 2.76 Å distance from the Ir, while the coordinated one is 2.36 Å from the metal. The coordination of a $HSiMe_3$ molecule in the metal vacancy yields intermediate **H**, at a relative energy of -3.6 kcal mol^{-1}. Subsequently, the $B(C_6F_5)_3$ promoted cleavage of the silane via **TSHI** (12.2 kcal mol^{-1}) takes place affording a silylformate molecule and a hydride which is captured by the $B(C_6F_5)_3$. Thus, the resulting **I** intermediate, at -4.3 kcal mol^{-1}, contains the product of the CO_2 hydrosilylation and the regenerated hydride forming an adduct with the borane.

At this point in the reaction, two different pathways arise. The first one involves the release of silylformate as the reaction product, regenerating **E** and therefore closing the catalytic cycle. This cycle is exergonic by 7.7 kcal mol^{-1} and presents an energy span of 22.2 kcal mol^{-1} defined by intermediate **E** and transition state **TSFG**. Alternatively, a second hydrosilylation can take place, leading to bis(silyl)acetal formation. The mechanistic pathway for the formation of this product is illustrated by Figure 4.11.

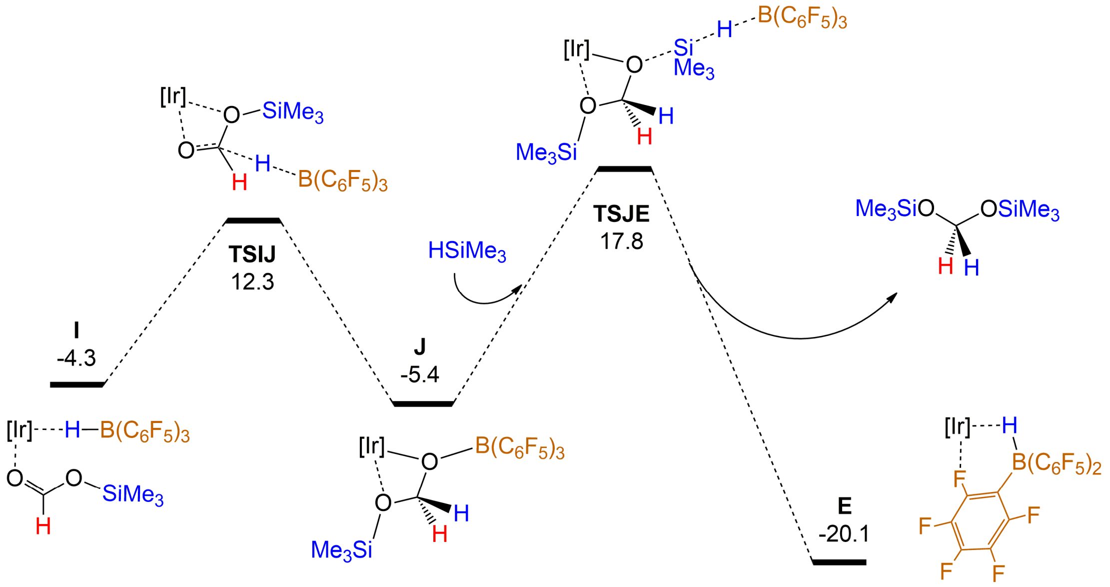

Figure 4.11. DFT calculated free energy profile (in kcal mol^{-1} relative to **E** and isolated molecules) for the catalytic hydrosilylation of a silylformate molecule from **I**.

The second CO_2 hydrosilylation follows a very similar process to the previous one. It starts with the hydride transfer to the carbon atom of the silylformate through transition state **TSIJ** (12.3 kcal mol^{-1}), resulting in the formation of intermediate **J** (-5.4 kcal mol^{-1}). This intermediate contains a (silyloxy)methanolate ligand, which presents longer C—O bonds than other less reduced CO_2 derivative (1.41 and 1.39 Å compared to the 1.23 and 1.29 Å of the formate). This allows both (silyloxy)methanolate oxygens to coordinate to the Ir, while the alkoxylic oxygen is also bonded to the $B(C_6F_5)_3$. This more stabilizing coordination scheme in which the ligand occupies both catalytic sites, along with the larger size of the ligand-borane adduct, impede the coordination of another silane molecule to the Ir. Consequently, the formation of **J** is followed by the S_N2 nucleophilic alkoxide attack to a silane molecule and capture of the leaving hydride by the $B(C_6F_5)_3$ via transition state **TSJE** (17.8 kcal mol^{-1}). This results in the formation of the bis(silyl)acetal product and regeneration of the hydride-$B(C_6F_5)_3$ adduct. After the product release this adduct occupies both the vacant sites of the Ir, restoring **E** and thereby completing the catalytic cycle. This catalytic cycle is exergonic by 20.1 kcal mol^{-1} and presents an energy span of 23.2 kcal mol^{-1} defined by intermediate **J** and transition state **TSJE**.

Despite sharing many commonalities, the two competing catalytic cycles exhibit significant differences that shape the selectivity of this process. For the catalytic silylformate formation, the reaction rate is determined by the energy difference between the intermediate **E**, characterized by the strong hydride-$B(C_6F_5)_3$ adduct, and the transition state **TSFG** in which this adduct is split to transfer the hydride to the inert CO_2 molecule (see Figure 4.12). This energy span stands in stark contrast to the 5.8 kcal mol^{-1} barrier observed for hydride insertion into CO_2 in absence of $B(C_6F_5)_3$, owing to the significantly higher stability of the hydride when captured by the borane rather than bonded to the Ir.

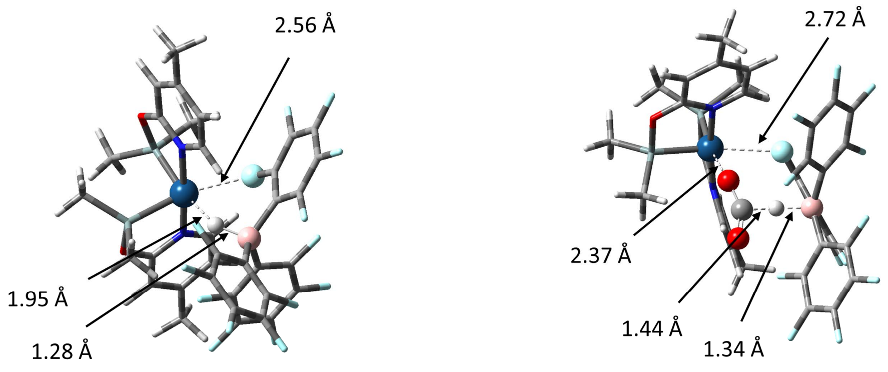

E (0.0 kcal mol^{-1})

TSFG (22.2 kcal mol^{-1})

Figure 4.12. Representations of **E** and **TSFG** with key distances and relative energies.

While reduction to bis(silyl)acetal begins via the same hydride transfer, the energy span for this catalytic cycle is instead defined by the slightly higher energy difference between intermediate **J** and transition state **TSJE**, 23.2 kcal mol^{-1}. Figure 4.13 presents the geometries for these two species and their relative free energies.

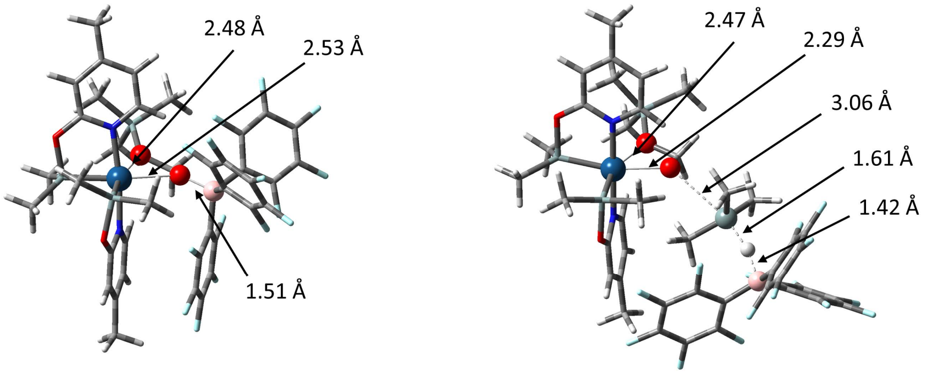

J (-5.4 kcal mol^{-1})

TSJE (17.8 kcal mol^{-1})

Figure 4.13. Representations of **J** and **TSJE** with key distances and relative energies.

Interestingly, the effective energy barrier obtained for the S_N2 nucleophilic attack of (silyloxy)methanolate to $HSiMe_3$ is considerably higher than those obtained for the attack of trifluoroacetate and formate, **B** to **TSCD** and **H** to **TSHI**, presenting barriers of 9.0 and 15.8 kcal mol^{-1} respectively. Despite alkoxide groups being stronger nucleophiles than carboxylates, this attack is relatively disfavored. This result can be related to the methanolate alkoxylic oxygen being the only attacking oxygen among the studied nucleophiles which is coordinated to the Ir at the transition state. As previously mentioned, the longer (silyloxy)methanolate C—O bonds allow for the coordination of both its O atoms to the Ir at the same time it forms an adduct with $B(C_6F_5)_3$. The alkoxylic oxygen retains its Ir coordination during the nucleophilic attack, presenting a 2.29 Å distance to the metal, while in the transition states **TSCD** and **TSHI** these distances are 2.92 and 2.56 Å, respectively. This can be tied with a comparatively greater electron density donation to the Ir in **TSJE**, effectively making the attacking (silyloxy)methanolate a weaker nucleophile. Furthermore, the larger size of this ligand also makes it a weaker nucleophile.

It should be remarked that despite the DFT calculated energy span for the reduction to acetal being slightly higher energy than that of the reduction to silylformate, the catalysis is selective towards the former. This fact can be correlated to the significant concentration differences of CO_2 and silane in the reaction medium. While in catalytic conditions the silane used as reductant was in excess, the low CO_2 pressure coupled with its low solubility in benzene leads to a considerably lower CO_2 concentration in the reaction media. Interestingly, reactions under higher CO_2 pressures exhibited a selectivity loss (Table 4.1, entry 8) with the silylformate becoming the primary product. This can be correlated to the greater CO_2 concentration in solution favoring the exchange of the just-formed silylformate with a CO_2 molecule before a second hydrosilylation occurs.

The Gibbs energies have been calculated for a 1M concentration of each species. The reaction rate for CO_2 reduction to formate level is determined by the energy barrier defined by **E** and **TSFG** (22.2 kcal mol^{-1}), with the coordination of a CO_2 molecule taking place between these two species. Conversely, the reaction rate for CO_2 reduction to formaldehyde level is determined by **J** and **TSJE** (22.3 kcal mol^{-1}), with the coordination of a $HSiMe_3$ molecule occurring between these two species. While equivalent concentrations of all species have been considered to calculate these energy spans, under catalytic conditions silane concentration is significantly greater than that of CO_2. The comparatively low CO_2 concentrations, disfavors the hydride insertion into this molecule, while the higher silane concentration favors the nucleophilic attacks onto this reductant. Thus, under catalytic conditions the effective energy barrier defined by **E** and **TSFG** is expected to increase relative to that defined by **J** and **TSJE**. While specific substrate concentrations are not considered, their effects are known and experimentally validated. The experimentally observed selectivity indicates that under catalytic conditions these barriers change to the point where the second hydrosilylation is more energetically favored than the silylformate-CO_2 exchange and subsequent hydride insertion (see Figure 4.14).

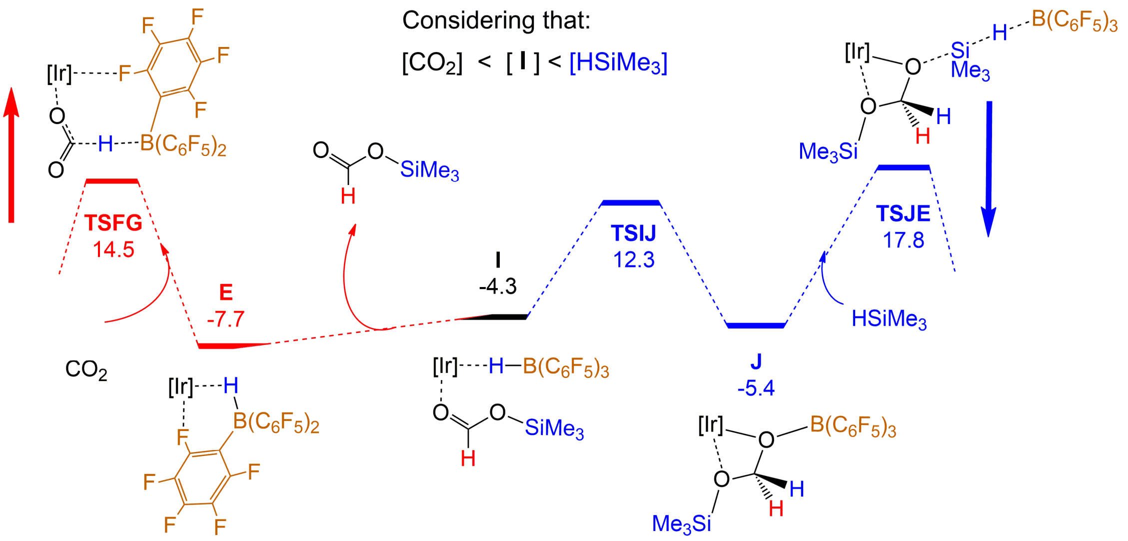

Figure 4.14. DFT calculated free energy profile (in kcal mol^{-1} relative to **E** and isolated molecules) comparing the 2nd hydrosilylation to the release of the silylformate and restart of the cycle. The vertical arrows represent the effects of the considering the catalytic substrate concentrations.

4.2 Dehydrogenation of formic acid using a Ir-NSi catalyst

Introduction and objectives

The current reliance of humanity on fossil fuels raises multiple sustainability challenges that demand immediate attention. Among these, one of the most pressing is the detrimental impact of fossil fuels emissions on the environment. Additionally, the finite nature of these resources imposes constraints on their utilization. Experts estimate that at the current consumption rate, gas and petroleum reserves will last approximately 50 years, while coal reserves are expected to persist a few more decades.[167] Despite these limitations and the projected rise in their price as reserves diminish, roughly 80% of the world's energy production relies on these sources, with many major global economies depending on them.[168] Consequently, developing renewable and clean alternatives to fossil fuels is a global imperative.

As the world shifts towards alternative means of power generation,[169] especially renewable ones such as wind, hydropower, solar and biomass, new challenges emerge. Storage and transfer of energy produced using these power sources are considerably more complex than those of fuels like petrol or gas. These technologies are key to a robust and efficient power grid. They enable power plants to harness the full potential of peak production conditions, even if consumer needs are lower at the time, and ensure sufficient and stable power during periods of intermittent or insufficient production. Barring hydroelectrical plants, which pump water to store excess power, most plants use batteries for this purpose.[170] Other industries seeking alternatives to fossil fuels, such as automotive and transportation, also favor batteries as the most popular option. However, despite a long and ongoing history of research and innovation of this technology, it still presents many deterrents and limitations.[171,172] Batteries have a significantly limited lifespan, as their chemical components degrade over charge and discharge cycles, resulting in declining capacity during their usage. Batteries have to be routinely replaced, raising concerns about the limited availability of certain components, namely cobalt and lithium, and the environmental impact of their disposal. Additionally, batteries present significantly lower energy densities than most fuels. Hence, scaling up operations that use batteries incurs considerably higher costs and challenges compared to most fuels. For these reasons, there is great interest in the development of alternative energy vectors that may better suit these applications. One of the most promising candidates is molecular hydrogen, whose potential application has been studied for over two centuries since it was proposed by Sir William Grove.[173] Interest in hydrogen was revived during the global energy crisis of the 1970s and in recent years has seen significant advances.

H_2 displays a calorific value of 141.8 MJ/kg, surpassing methane, diesel, and anthracite with values of 55.5, 44.8, and 32.5 MJ/kg, respectively. Moreover, its combustion yields only water, emitting no hazardous by-products. Additionally, H_2 stands out as a renewable fuel, regenerable through processes like electrolysis or water splitting.[174] While these processes are considerably more energy demanding than commonly used methods to generate hydrogen, namely methane steam reforming,[175] they solve sourcing issues. Furthermore, ongoing research is projected to enhance their efficiency. In this context, the idea of hydrogen economy emerges, a conceptual framework in which chemical processes and infrastructure are advanced to the point where hydrogen can be used as energy vector and replace fossil fuels. However, several challenges including the efficiency of hydrogen generation, as well as, the difficulties and risks associated with its storage and delivery, hinder this concept from becoming a reality.

H_2 gas storage has proven to be a roadblock in its use as fuel. Due to its uniquely low molecular weight, H_2 has a significantly lower density than that of any typically used fuel. In its liquid state, H_2 presents a density of 70.8 g/L (at its boiling point at 1.013 bar of 20.3 K), implying that even using extremely high pressure and/or low temperature conditions, H_2 still requires significantly higher storage volumes than most fuels. Moreover, due to its extreme lightness there exists a non-negligible risk of leakage from high-pressure containers. Leaks are a particularly concerning hazard given the gas's high flammability and explosiveness.[176] Consequently, due to the substantial costs, risks and cumbersome volumes associated to H_2 storage, many researchers have proposed an alternative solution: using liquid organic hydrogen carriers (LOHCs). LOHCs encompass a series of liquids thar exhibit ideal properties to be stored and transported and are formed through the reversible incorporation of H_2 into organic molecules.[177] A prime example of this concept is formic acid (FA), obtained via CO_2 hydrogenation, a kinetically stable liquid under atmospheric condition with low toxicity or flammability. Figure 4.15 illustrates the reversible cycle that enables the FA to be a H_2 carrier.

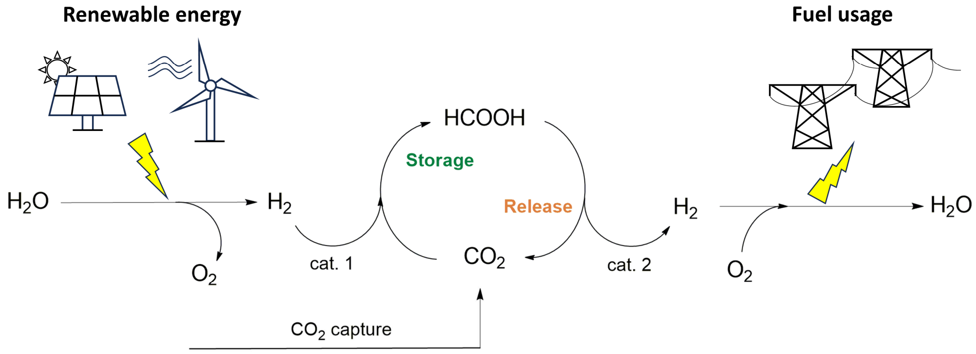

Figure 4.15. Usage of formic acid for the storage of hydrogen as an energy vector.

FA stands out over other LOHCs because 4.4 % of its molecular weight corresponds to the hydrogen it liberates, which is a considerably higher ratio than most other LOHCs. FA boasts lower toxicity and flammability when compared to many unsaturated hydrocarbons proposed as carriers, such as toluene and azobenzene. Moreover, the H_2 release and incorporation processes, integral to its function as carrier, occur under mild conditions through catalytic processes. Lastly, the environmental benefits of this process are further enhanced by the potential usage of captured CO_2 for FA generation, presenting an additional avenue for the important goal of CO_2 utilization. Another environmentally benign option is starting this cycle at FA, since it can also be obtained via sustainable processes such as biomass fermentation.

The development of efficient catalytic systems for CO_2 hydrogenation and formic acid dehydrogenation (FADH) are determinant to the performance of FA as a hydrogen carrier. On a larger scale, it determines the viability of H_2 as an energy vector. This study is centered on the homogeneous catalytic FADH, which despite being first reported in 1967 by Coffey,[178] received little attention during the subsequent decades. During this period most references to this reaction allude to it as the unwanted back-reaction of CO_2 hydrogenation, which at the time was extensively studied alongside various strategies for CO_2 utilization as a C1 building block. Although seldom studies of that time recognized the applicability of FADH in H_2 generation, they purposed it as a reductant rather than a fuel. For instance, in 2003 Himeda et al. reported a Rh complex which used FA as a H_2 donor for the reduction of ketones.[179] The publications by Beller et al.[179] and Laurenczy et al. [180,181] in 2008, remarked the importance of the FADH as the FA was identified as a potential H_2 carrier, causing a surge of interest in this reaction.

Many catalytic systems reported for this reaction include high loadings of a base to improve the reaction rate, generally around 40 mol% of the FA. The base, in most cases an amine, deprotonates the FA, shifting the equilibrium between the FADH and the CO_2 hydrogenation. While the base thermodynamically favors FA generation, it kinetically favors its dehydrogenation. The afforded formate leads to a higher reaction rate since its decomposition is less kinetically impeded than that of FA.[182] Additionally, the base may dissociate FA dimers facilitating their reaction. This approach has been successfully applied for a great variety of catalysts, including complexes of Ir,[183] Rh,[184] Ru,[185] Fe[186] among other metals. Figure 4.16 presents a diverse set of catalysts which have been reported to catalyze the dehydrogenation of formic acid. With the exception of the one reported Coffey, in all these cases the authors noted the importance of including a base to the catalytic mixture.

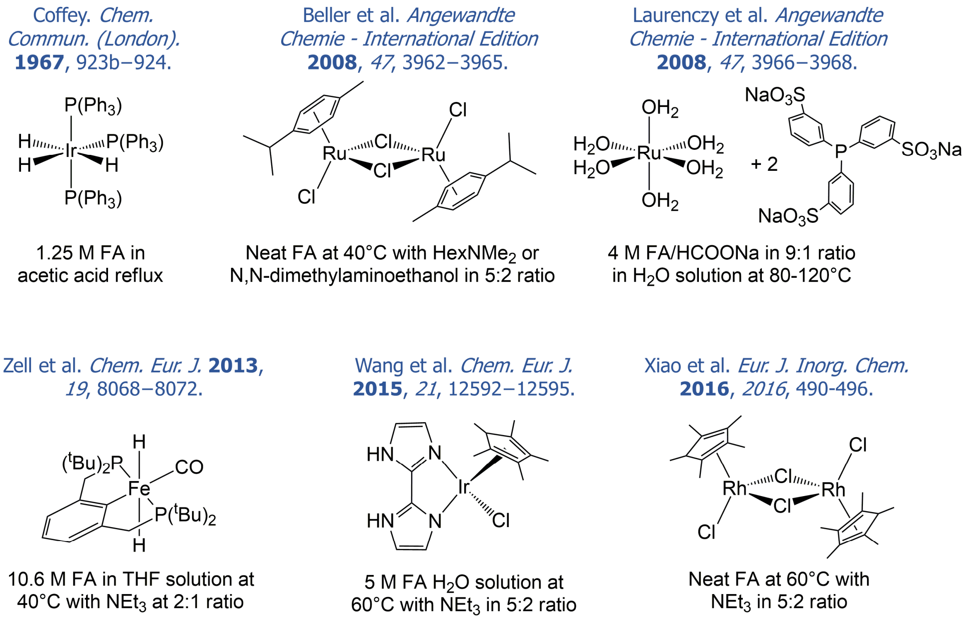

Figure 4.16. Relevant examples of catalysts employed in FADH.

On recent years there has been an extensive study on the catalyzed FADH leading to the development of numerous highly active catalysts for the FADH in various solvents, namely water[187] and DMSO[188]. Nonetheless, reports for catalytic systems in neat FA are still scarce. The development of catalysts for solventless FADH is highly sought after since it bypasses diluting the FA for the reaction, considerably reducing the H_2 volumetric density.

It is significant to note that the FA decomposition can occur through two distinct pathways: dehydrogenation and dehydration. The former results in the production of one molecule each of hydrogen and carbon dioxide, while the latter yields a water molecule and carbon monoxide. The formation of carbon monoxide not only represents an undesirable by-product but poses a potential risk of catalyst poisoning. Therefore, achieving high selectivity towards the FADH is critical to ensure the optimal activity of the catalyst.

The subsequent part of this section presents the mechanistic study of the selective dehydrogenation of formic acid catalyzed by $[Ir(CF_3SO_3)(\kappa^2\text{-NSi}^{Me})_2]$ under solventless conditions with a 5:2 FA/NEt_3 mixture. The goals for this computational study are:

1. Determining the operating mechanism for the dehydrogenation.
2. Validating through this mechanism the effect of the base in the reaction rate.
3. Studying the unfavorable formation of the CO.

Results and Discussion

Experimental results show the transformation of the starting $[\{Ir(\kappa^2\text{-NSiMe})_2\}_2(\mu\text{-}CF_3SO_3)_2]$ complex into the active species, which served as the starting point for the computational calculations. NMR spectra demonstrate that while this complex is stable at room temperature, after 30 min of heating at 323 K it evolves into $[Ir(HCO_2)(\kappa^2\text{-NSi}^{Me})_2]$, as shown in Scheme 4.5. Simultaneously the formation of H_2 is observed indicating the start of the catalysis. Therefore, the $[Ir(HCO_2)(\kappa^2\text{-NSi}^{Me})_2]$ complex is determined to be the active species and will be referred to as **A** from now on.

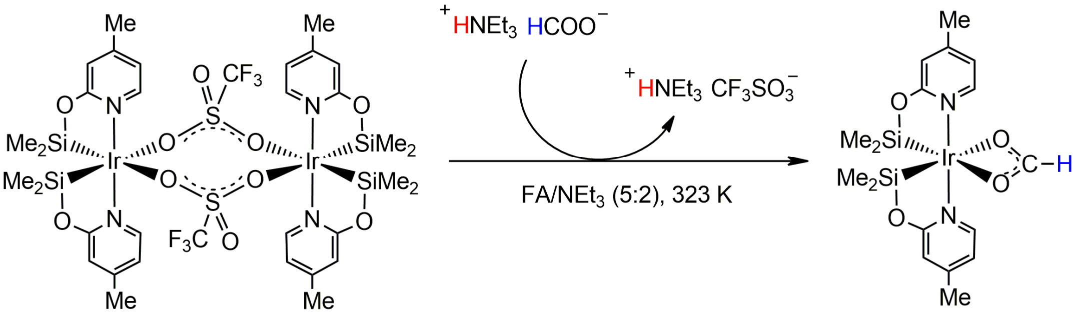

Scheme 4.5. Formation of the active species, **A**, under catalytic conditions.

Considering **A** as the starting point, the FADH catalytic cycle was studied using DFT calculations. The proposed energetic profile is shown in Figure 4.17.

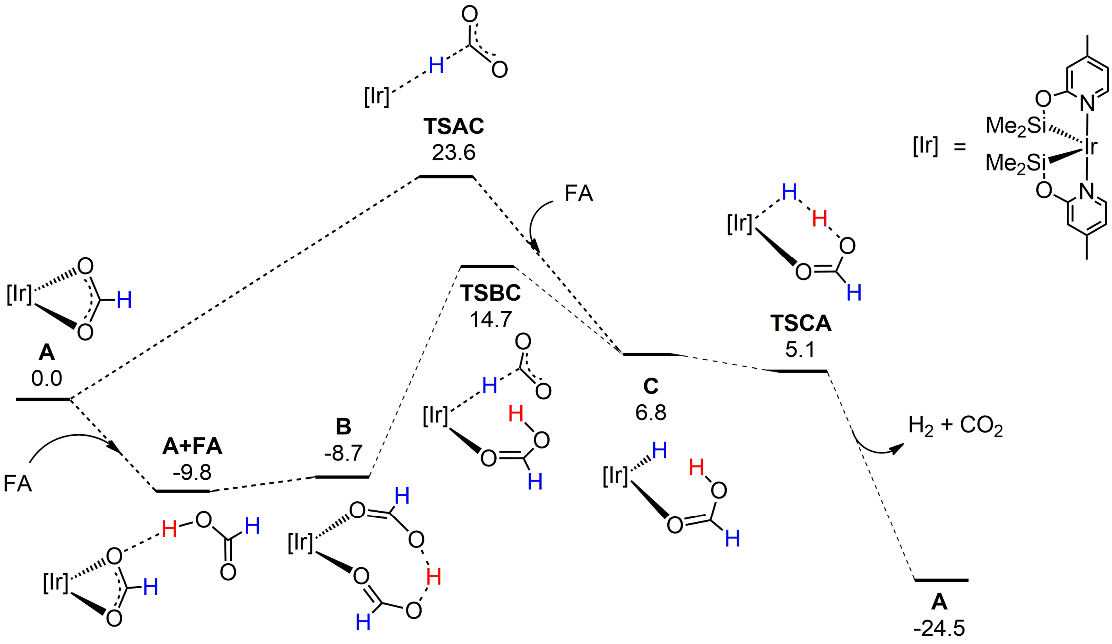

Figure 4.17. DFT calculated free energy profile (in kcal mol^{-1}, relative to **A** and isolated molecules) for the catalyzed formic acid dehydrogenation.

Previous works on similar systems propose the β-hydride elimination as the pathway towards the formation of a hydride which then leads to the formation of H_2.[189,190] However, the transition state corresponding to this reaction could not be found for this system due to the strong polarizing effect of the solvent model. Instead, hydride abstraction occurs through transition state **TSAC**, in which the positively charged Ir complex and the partially negatively charged formate oxygens are separated to match the solvent model dipole moment. Figure 4.18 demonstrates the differences between these two reactions.

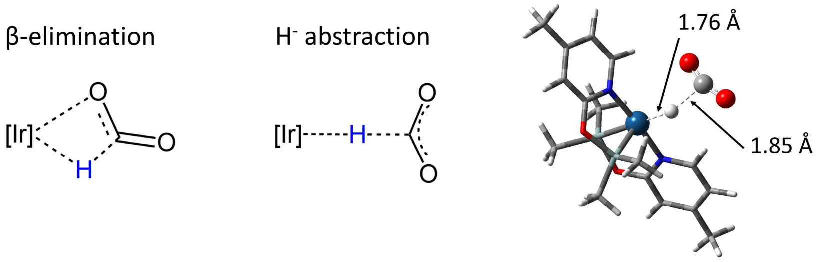

Figure 4.18. β-hydride elimination and hydride abstraction compared to **TSAC**.

However, transition state **TSAC**, at a relative energy of 23.6 kcal mol^{-1}, is significantly more energy demanding than the FA assisted **TSBC**. This transition state effectively achieves the same result but includes a FA molecule facilitating the process in the vacant site left by the separation of the formate. Thus, the operating mechanism starts with the coordination of a FA molecule through its acidic proton to one of the formate oxygens of **A**. This coordination yields intermediate **A + FA**, at a relative energy of -9.8 kcal mol^{-1}. Subsequently, the formate oxygen bonded to the FA acidic proton can be dissociated from the Ir, leaving that vacant site for the FA carbonyl group to occupy. This leads to the formation of intermediate **B**, at the slightly higher relative energy of -8.7 kcal mol^{-1}. Following that the other formate oxygen can be unbound so that its hydrogen atom can be transferred to the Ir via the transition state **TSBC**. The coordinated FA facilitates this process through the stabilizing electrostatic interaction between its acidic proton and the newly formed hydride (see Figure 4.19).

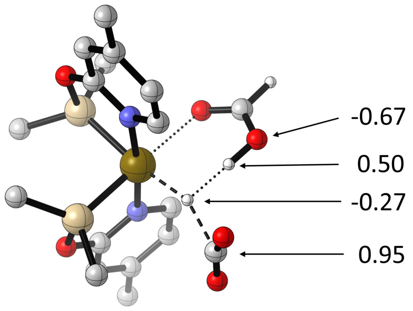

Figure 4.19. Representations of **TSBC** with relevant NBO atomic charges (in a.u.) indicated.

This leads to the formation of intermediate **C**, exhibiting a metallic hydride that still interact with the acidic proton of the coordinated FA. This hydride is relatively destabilized, at a relative free energy of 6.8 kcal mol^{-1}, due to the *trans* effect of the silyl group, as previously mentioned for the complex studied in Section 4.1. Subsequently, the heterolytic formation of the H—H bond occurs as characterized by transition state **TSCA**, depicted in Figure 4.20.

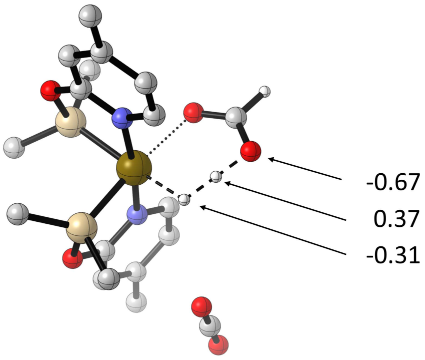

Figure 4.20. Representations of **TSCA** with relevant NBO atomic charges (in a.u.) indicated.

The H_2 formation is facilitated by the instability of the metallic hydride and the hydrogen bond between the FA and the hydride aiding the proton transfer. This results in the reaction presenting no effective energy barrier. While it might seem counterintuitive that this transition state presents a lower relative free energy (5.1 kcal mol^{-1}) than the preceding intermediate, it can be attributed to the calculation of the free energy contributions, since in terms of electronic energy, used to optimize these species, **TSCA** is less stabilized than **C**. Lastly, the afforded H_2 and CO_2 molecules are released, regenerating **A** and closing the catalytic cycle. The determined catalytic cycle is exergonic by 24.5 kcal mol^{-1} and presents an energy span of 24.5 kcal mol^{-1} defined by the resting state **A + FA** and the rate determining transition state **TSBC**.

Therefore, this process's catalytic rate is determined by the hydride abstraction from a formate, which is immediately followed by the deprotonation of a FA molecule to regenerate the formate. This can be correlated with the relevance of the presence of a base in the solution, as it raises the formate concentration, consequently raising the reaction rate. Experimental kinetic studies demonstrated an increase in reaction rate at higher NEt_3/FA ratios. Moreover, a series of catalytic experiments were performed at temperatures in the range between 313 and 373 K using NEt_3 10 mol% to FA. The Arrhenius analysis resulted in a barrier of 27.5 ± 0.9 kcal mol^{-1} and the Eyring analysis yielded a barrier of 22.8 ± 0.8 kcal mol^{-1} at 353 K. Therefore, the computationally obtained barrier of 24.5 kcal mol^{-1} falls between these two values and is considered accurate.

Additionally, a KIE study was performed to validate the determined operating mechanism. The experimentally obtained KIEs were 1.33 and 2.86 for the HCOOD and DCOOH respectively. The computational KIEs were calculated using the rate-determining minimum (**A + FA**) and transition state (**TSBC**), resulting in 1.18 and 3.08 for HCOOD and DCOOH respectively, accurately matching the experimental values. The high KIE obtained for DCOOH corresponds to a primary KIE caused by the breaking of the C—H/D bond during the hydride abstraction. While the slightly higher than 1 KIE for the HCOOD corresponds to the modest weakening of the O—H/D bond of the FA molecule caused by the strong hydrogen bond to the hydride during its abstraction. Figure 4.21 displays the differences between the structures of **A + FA** and **TSBC** that cause these KIEs.

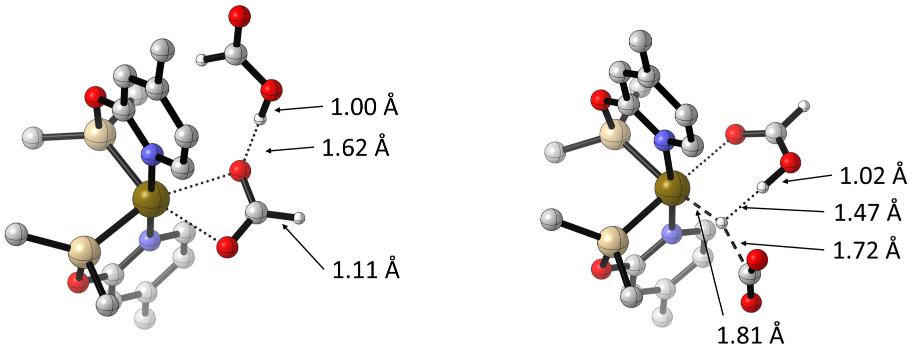

Figure 4.21. Representations of **A + FA** and **TSBC** with relevant distances indicated.

Lastly, the formation of CO was studied to justify the selectivity FA dehydrogenation over its dehydration. The most energetically favored transition state found for this process consists of the transfer of the hydrogen of a formate from its carbon to one of its oxygens, effectively splitting the formate into a CO molecule and a hydroxide anion. While the resulting hydroxide is stabilized by its interactions with the Ir and the FA, this transition state presents a relative free energy of 67.4 kcal mol^{-1}, making the process unviable.

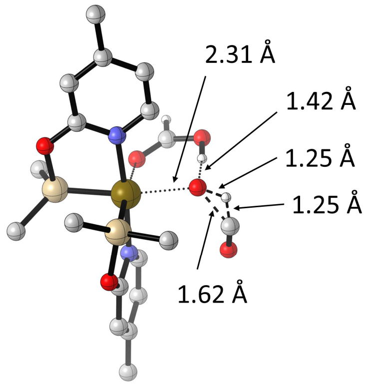

Figure 4.22. Representation of the transition state for CO formation with relevant distances.

4.3 Dehydrogenation of formic acid using a Rh-CNC catalyst

Introduction and objectives

Up to date, a wide spectrum of heterogeneous and homogeneous catalysts for FA dehydrogenation have been documented. While heterogeneous catalysts present great reusability, they display low activities, limiting their applicability.[191] In recent years many organometallic complexes have been reported to reach high efficiencies for the catalyzed FADH, with most of them being based on Ir or Ru. Figure 4.23 presents a few examples of catalysts that have been cited as highly active for the FADH.

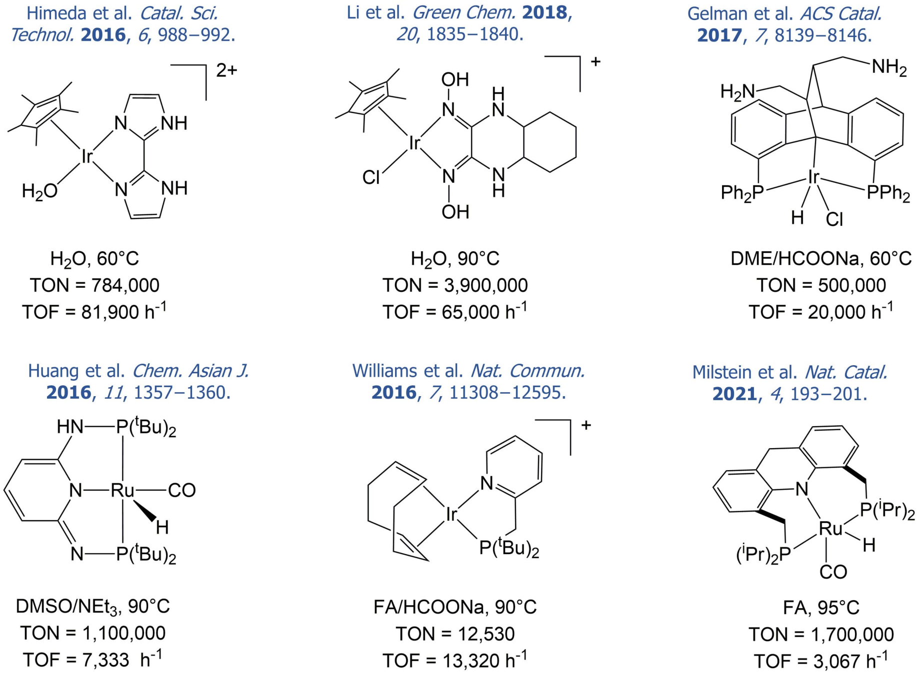

Figure 4.23. Selected examples of catalysts for FA dehydrogenation.

The design of catalysts leverages an extensive and diverse library of ligands to fine-tune the catalytic selectivity and efficiency. Among the most successful catalysts reported for FADH a preponderance of strong electron-donating ligands can be observed. These can take the form of π-donor or σ-donor ligands. The former are unsaturated molecules able to coordinate to a metal through their π-systems, such as arenes or alkynes. The latter are characterized by the presence of moieties able to donate electron pairs to a metal such as phosphine, amine, or alkyl groups. The contributions of these ligands lead to electron-rich metallic centers, promoting a type of reactivity that may be conducive to FADH. This includes reactions increasing the metal oxidation state, namely oxidative additions. Furthermore, hydrides of more electron-rich metals are more nucleophilic, facilitating the formation of H_2 through their protonation as part of FADH.

Another common feature among all these catalysts is the presence of a pincer or chelate ligand. These ligands not only include multiple electron-donating groups, but their chelating effect improves complex stability.

As mentioned previously in Section 4.2, the study of FADH catalysts under solventless conditions has been limited so far. This is reflected not only in the scarce collection of reported catalysts for this reaction, but in their comparably low TOFs and TONs. To date, homogeneous catalysts reported for the solventless FADH exclusively include complexes based on Ir or Ru.[192] Additionally, the application of carbenes as strong electron donating groups for FADH has been sparse.[193]

In this context, a Rh catalyst with a pincer ligand bearing two NHCs (N-heterocyclic carbenes) was proposed for solventless FADH. Additionally, the reaction conditions for this process include HCOONa as an additive. This base plays the same role as NEt_3 did in the system studied in the previous section, increasing the concentration of formate ions in solution and dissociating FA dimers. While this salt presents a somewhat limited solubility in formic acid, it considerably improves the reaction rate, raising it more the higher the HCOONa/FA ratio is. Replacing NEt_3 by a non-volatile salt presents an additional advantage, as volatile components, such as many organic solvents or amines. may mix into the generated gas damaging the fuel cell.[194]

In the ensuing part of this section the mechanism for the selective dehydrogenation of formic acid catalyzed by $[(CNC)^{Mes}Rh(PMe_2Ph)]PF_6$ under solventless conditions with a 5:2 FA/HCOONa mixture is studied in detail (see Scheme 4.6). The objectives for this computational study are:

1. Determining the active species and operating mechanism for the reaction.
2. Defining the rate-determining minimum and transition state and validating this result based on experimental measurements.

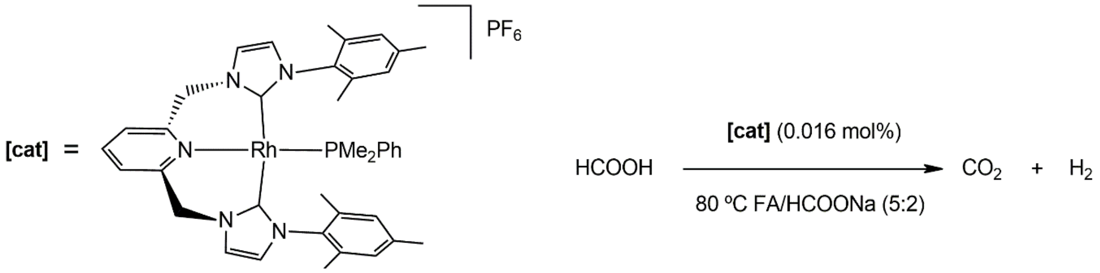

Scheme 4.6. Catalyzed reaction of FADH under solventless conditions.

Results and Discussion

A series of preliminary experimental observations were used to shed light into the nature of the active species for this reaction and its operating mechanism. A solution of $[(CNC)^{Mes}Rh(PMe_2Ph)]PF_6$ (from now on referred to as **[cat]**), in CD_3CN was monitored through NMR experiments. The addition of FA 3 equivalents at temperatures between 262 and 282 K results in the partial transformation of **[cat]** to a species containing a hydride and a formate. The *cis* position of these two ligands indicate that they are the product of the oxidative addition of a FA molecule. After 30 min of monitoring this mixture at 282 K the signals corresponding to a dihydrido complex appear, with these signals becoming more intense the longer the reaction goes. Furthermore, carrying out this experiment at room temperature results in the direct formation of the dihydrido species along with the starting complex. These results indicate that there is a dynamic equilibrium between these three species (see Scheme 4.7).

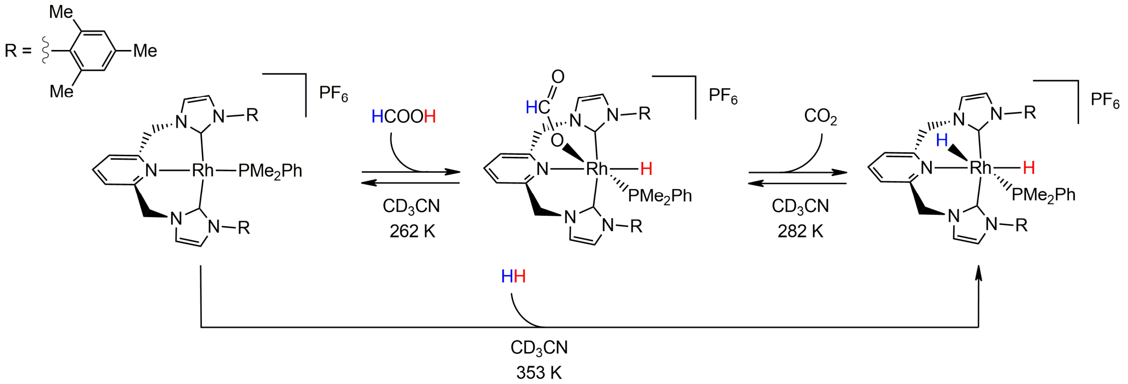

Scheme 4.7. Equilibrium between **[cat]** and hydrido-formate complex and dihydrido species.

Interestingly, as shown in Scheme 4.7, the dihydrido complex can also be generated by addition of H_2 (8 bar) to **[cat]**. However, this process required significantly higher temperatures, only observing results after overnight heating at 353 K. This implies that the oxidative addition of H_2 is notably less favorable than that of FA.

Moreover, the study of a 0.5M FA solution in CD_3CN at 353 K with a 1 mol% loading of **[cat]** but no HCOONa showed no catalytic activity. However, after the addition of 10 mol% of HCOONa to the FA, the formation of H_2 was observed within a minute. Higher activities were observed for higher HCOONa loadings, with the best catalytic results being obtained for a 40 mol% loading. This results demonstrates the importance of a base for the catalytic activity.

It is worth mentioning that analogue complexes obtained by substituting the PMe_2Ph by other ligands, namely CO and $NCCH_3$, show no catalytic activity under these conditions. This may be related with the lesser electron donating capabilities of these ligands and states the passive yet critical role of ligands towards catalytic activity. While the ligands were wholly represented in the computational model for this reason, the counterion PF_6^- was excluded from it, as it was considered to be dissociated from the complex and not involved in the mechanism.

In the computational study of this catalytic system, two alternative reaction pathways were considered: one starting by the coordination of a FA molecule, and the other one beginning with the coordination of a formate molecule. In order to elucidate the operating mechanism, these two pathways were compared to determine which one presents a lower activation energy and whether it aligns with experimental observations. As these processes take place in neat FA, for every species included in these mechanisms, the microsolvation of its strong electron donors or acceptors with a FA molecule has been considered.

The coordination of a FA molecule to the starting complex, from now on referred to as **A**, can lead to its cleavage affording what was found to be an active catalyst for the FADH. The mechanism for this catalyst preactivation is presented in Figure 4.24.

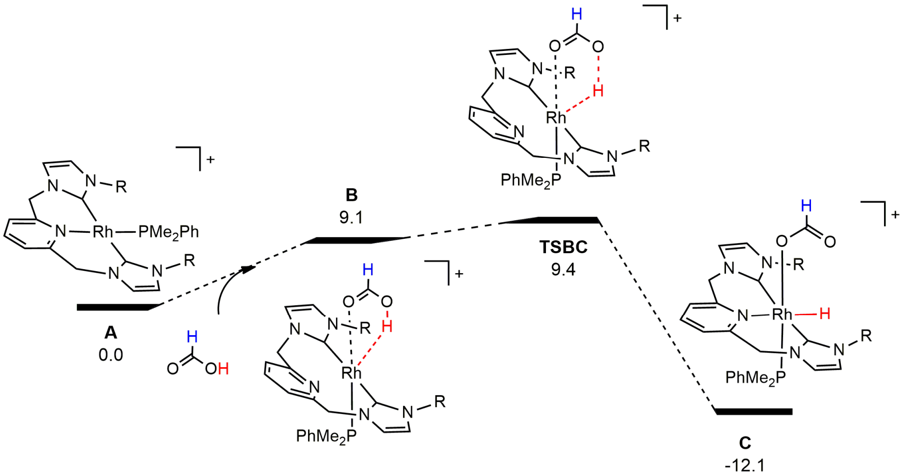

Figure 4.24. DFT calculated profile (kcal mol^{-1}) of the oxidative addition of a FA molecule to **A**.

The coordination of a FA molecule to **A** by its carbonyl oxygen, affords intermediate **B**, at a relative free energy of 9.1 kcal mol^{-1}. Since the Rh maintains its oxidation state of I, it favors a square planar configuration, as the FA binds to the metallic center, the lutidine N is released and the phosphine goes from the *trans* position to this N atom to that of the FA. Moreover, the acidic FA proton exhibits a weak interaction with the Rh at a 2.05 Å distance. Subsequently, oxidative addition of the FA molecule can occur as depicted by transition state **TSBC**, with a relative energy of 9.4 kcal mol^{-1}. The heterolytic O—H bond cleavage leads to the acidic proton transference to the Rh, becoming a hydride due to the oxidation of the metal, presenting an O—H distance of 1.22 Å and a Rh—H distance of 1.76 Å. The resulting intermediate, **C**, at a relative energy of -12.1 kcal mol^{-1}, presents a Rh^{III} and therefore favors an octahedral configuration. As previously mentioned, the newly formed hydride and formate ligands remain coordinated to the Rh in relative *cis* positions. The pyridinic N is again coordinated to the metal with the hydride being on its *trans* position. This configuration is more stabilized than the alternative in which the hydride is in *trans* position to the phosphine, due to the remarkably high *trans* effect of the hydride favoring ligands with a lesser *trans* effect in this position. This result matches the NMR signals observed after the addition of FA at low temperatures.

Following the formation of intermediate **C**, the catalytic FADH is possible following the mechanism depicted in Figure 4.25.

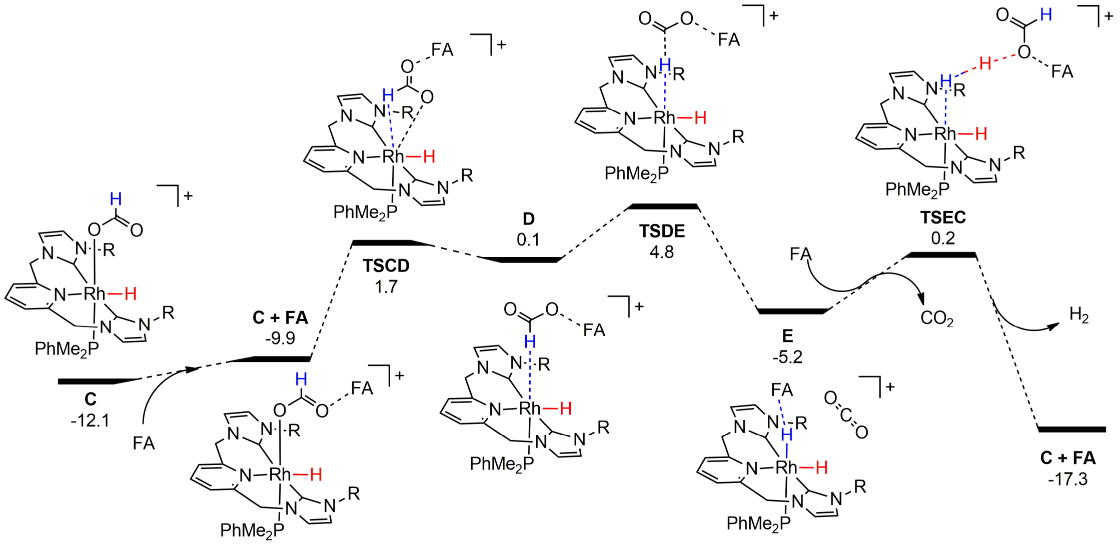

Figure 4.25. DFT calculated free energy profile (in kcal mol^{-1}, relative to **A** and isolated molecules) for the formic acid dehydrogenation catalyzed by **C + FA**.

This mechanism starts with the coordination of a FA molecule to the formate carbonylic oxygen of **C**, yielding intermediate **C + FA**, at a relative energy of -9.9 kcal mol^{-1}. While this process is slightly endergonic, 2.2 kcal mol^{-1} over **C**, the hydrogen bond between the FA and the formate stabilizes the following processes. Subsequently, the formate can change its coordination to the Rh from its oxygen to its hydrogen via transition state **TSCD**. This switch in coordination mode results in the formation of **D**, a comparatively less stabilized intermediate at a relative energy of 0.1 kcal mol^{-1}, with a Rh-formate H distance of 1.85 Å. The reaction continues with the abstraction of this hydrogen atom through transition state **TSDE**, at a relative energy of 4.8 kcal mol^{-1}, leading to the formation of the dihydro intermediate, **E** (-5.2 kcal mol^{-1}), and a CO_2 molecule. **E** presents a hydrogen bond between the FA molecule and the latter-formed hydride, while the interaction with the former-formed hydride is impeded due to the steric hindrance of the Mes groups of the NHCs and the Ph group of the phosphine (see Figure 4.26).

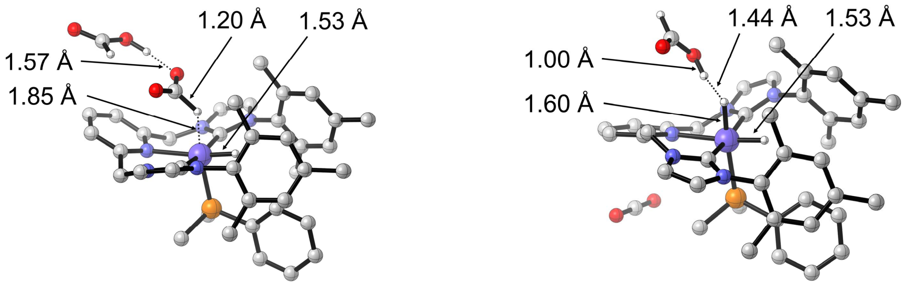

Figure 4.26. Representations of **D** and **E** with relevant distances indicated.

While for intermediate **D**, its formate is microsolvated by a FA molecule, for **E** this FA molecule microsolvates a hydride, as the produced CO_2 does not form strong interactions with FA. Instead, molecularity is maintained by having the CO_2 molecule attached to the complex through dispersion interactions. Lastly, a H_2 molecule is formed through the heterolytic bond formation between the metallic hydride and the acidic FA proton microsolvating it, as characterized by transition state **TSEC** (0.2 kcal mol^{-1}). For this transition state, the CO_2 molecule is exchanged by a FA one, maintaining molecularity and microsolvating the FA being deprotonated. The CO_2 release and formation of the microsolvated formate results in the regeneration of intermediate **C + FA**, at a relative energy of -17.3 kcal mol^{-1}. Therefore, the FADH catalytic cycle is closed, being exergonic by 7.4 kcal mol^{-1}, with its rate-determining intermediate and transition state being **C** and **TSDE** respectively. Thus, the energy span for this catalytic cycle is 16.9 kcal mol^{-1}.

The reductive elimination is an alternative route to produce H_2 from the dihydrido complex, **E**, and close the catalytic cycle. In this reaction the two adjacent hydrides are combined affording a H_2 molecule and the metallic center is reduced to Rh^I regenerating **A**, as depicted by transition state **TSEA** (see Figure 4.27). However, this transition state exhibits a relative energy of 6.3 kcal mol^{-1} making it energetically unviable.

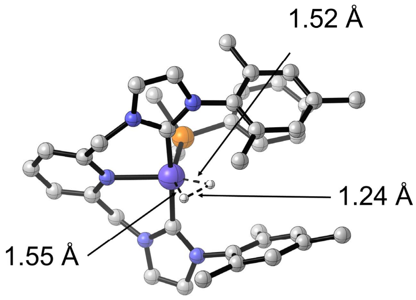

Figure 4.27. Representation of **TSEA** with relevant distances indicated.

The catalyzed FADH starting by the coordination of a formate molecule was also studied. This pathway starts with the formate coordination to **A**, yielding intermediate **B’** at a relative energy of 9.8 kcal mol^{-1}. The coordination of a microsolvating FA molecule to the formate yields **B’ + FA** (8.9 kcal mol^{-1}). Thereafter, the hydride abstraction is possible through transition state **TSBC’** at a relative energy of 23.8 kcal mol^{-1}. This reaction affords intermediate **C’** (13.4 kcal mol^{-1}), presenting a microsolvated metallic hydride. Figure 4.28 displays the free energy profile for this process.

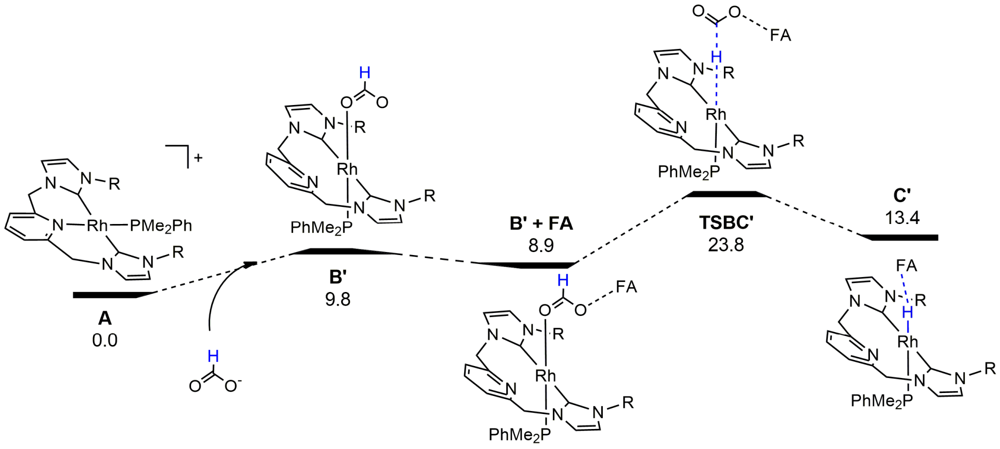

Figure 4.28. DFT calculated free energy profile (in kcal mol^{-1} relative to **A** and isolated molecules) for the coordination of a formate to **A** and its subsequent hydride abstraction.

The FADH catalyzed by this species presents the same overall steps as the previous mechanism, hydride abstraction of a formate and protonation of that hydride by a second FA molecule. Contrarily to the previous pathway, in which the catalytic cycle was preceded by the catalyst activation, in this case the formate is cleaved directly. The oxidative addition of the FA leads to the formation of a Rh^{III} cationic active species, **C**. While in this alternative pathway the Rh maintains its oxidation state of I and the complex presents a neutral charge. This can be correlated with the significantly less favored hydride abstraction for this pathway when compared to the former one, presenting an energy span of 23.8 kcal mol^{-1}, making this mechanism energetically unaffordable.

Moreover, in this mechanism at no point the Rh reaches an oxidation state of III, making it impossible to form the experimentally observed complexes presenting a hydride and a formate or two hydrides. Conversely, in the former pathway after the catalyst activation the Rh presents an oxidation state of III throughout the entire catalytic cycle. The hydride *trans* to the pyridine plays a passive role during the reaction while the site *trans* to the phosphine is iteratively occupied by either a formate or a hydride, matching the experimentally characterized species. Thus, the former pathway is proposed as the operating mechanism.

The experimentally obtained Eyring plot using data from FADH catalyzed by **[cat]** in a range of temperatures between 333 and 353 K determined the activation energy of this process to be 18.12 ± 1.17 kcal mol^{-1}. The computationally obtained 16.9 kcal mol^{-1} barrier is in good agreement with this result. Moreover, KIE experiments were carried out both experimentally and computationally to further validate the proposed mechanism. The substitution of the FA by DCOOH results in a KIE of 2.44, a primary KIE indicating the cleavage of the bond formed by this hydrogen/deuterium in the rate-limiting transition state of the cycle. Experiments with HCOOD revealed a KIE of 1.17 for this acidic hydrogen, a secondary KIE. While some secondary KIEs are the result of a change of hybridization of an adjacent, a considerably more likely cause is the slight elongation of the O—H/D caused by a hydrogen bond in the rate limiting transition state.

The computationally obtained KIEs considering **C** and **TSDE** as rate-determining intermediate and transition state, respectively, are in good agreement with the experimental ones. The KIE for DCOOH is 2.63 while the KIE for HCOOD is 1. Defining **TSEC** as the rate-determining transition state instead, results in a 2.07 for DCOOH and 6.06 for HCOOD, presenting primary KIEs for both hydrogens, as they both are part of forming and breaking bonds in the formation of the H_2. Lastly, the KIE for the alternative pathway was also calculated, taking **A** and **TSBC'** as rate-determining species results in a KIE of 3.98 for DCOOH and 1 for HCOOD. This can be related with the longer C—H/D bond exhibited by **TSBC'** while the microsolvating FA molecule plays a similar role. Figure 4.29 presents the geometrical representation of these species and the bond lengths related to these results.

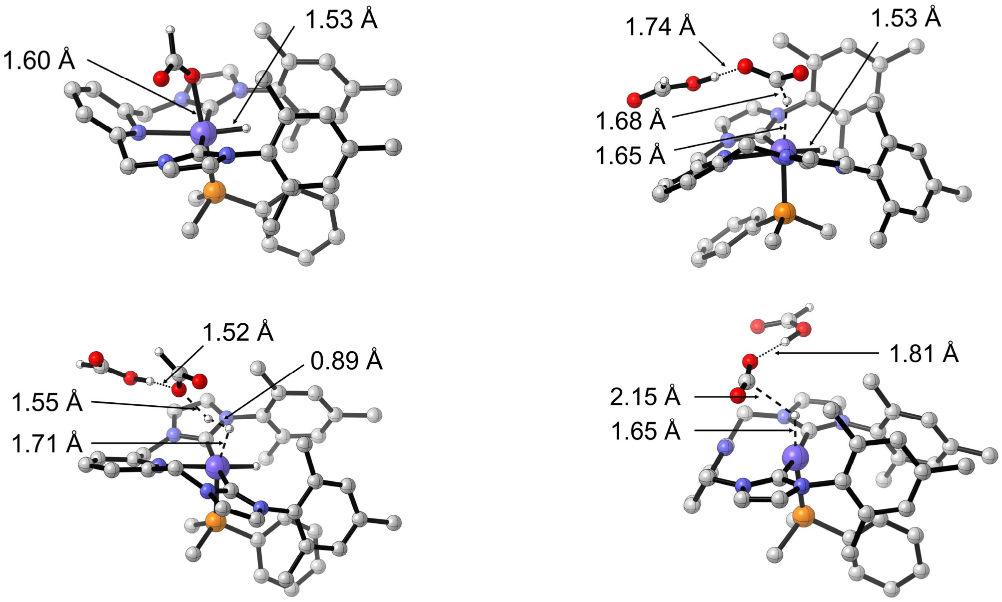

Figure 4.29. Representations of **A**, **TSCD**, **TSEC** and **TSBC'** with relevant distances indicated.

Chapter 5:

Hydrofunctionalization of Terminal Alkynes

“If you challenge conventional wisdom, you will find ways to do things much better than they are currently done.

Bill James

Hydrofunctionalization reactions consist of the addition of a hydrogen atom and a functional group to opposite ends of a carbon-carbon or carbon-heteroatom multiple bond. These reactions are an exceptionally versatile and powerful tool in the design of synthetic routes. Their application allows for the efficient and straightforward insertion of diverse moieties at the cost of breaking down π-bonds in an unsaturated substrate. Copious examples of these reactions have been reported for the incorporation of a variety of groups to a structure, such as hydroalkynylation, hydroarylation, hydrosilylation, hydroamination, and hydroboration This methodology not only possibilitates the direct functionalization of positions of interest, it can also be utilized to introduce groups used for subsequent reactions. Consequently, the hydrofunctionalization is widely used to synthesize all kinds of products and greatly contributes to the widespread utilization of alkenes and alkynes for synthesis.

The functionalization of alkynes yields stereochemically defined olefins, a characteristic structural motif present in many products via a direct and atom-economic route. Hence, these reactions see application in various fields including the formation of bioactive compounds or synthesis of advanced materials. Controlling the selectivity for the obtention of these products can be quite challenging, and hinges on the reaction mechanism for their formation and their distinguishing features. In absence of a catalyst this reaction can take place through two pathways: a nucleophilic addition (e.g. a Michael addition) or an electrophilic addition, as shown by Scheme 5.1.

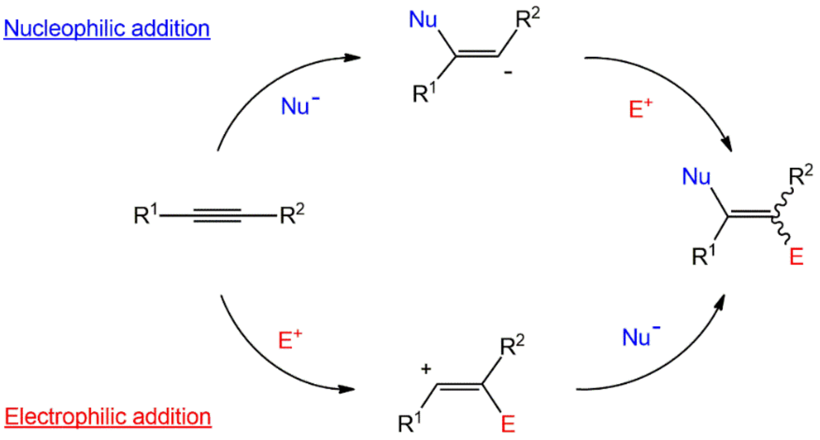

Scheme 5.1. Non-catalyzed addition reactions to alkynes.

However, in most cases for these reactions to occur under mild conditions, or even take place at all, a catalyst is required. Furthermore, the addition of a catalyst can dictate the process selectivity and reduce by-product formation. Organometallic catalysts open a diverse range of possibilities for the activation of alkynes. Catalyzed hydrofunctionalization reactions can be classified into five main reaction pathways:

1) π-coordination to the metallic center followed by a nucleo/electrophilic attack.

The coordination of the alkyne bond to an organometallic complex results in the σ-donation from an alkyne bonding orbital to the metal and the π-backdonation from the metal to an alkyne antibonding orbital. This results in a significant weakening of the triple bond facilitating both nucleophilic and electrophilic attacks to it. Hence, the presence of a catalyst enables considerably weaker reactants to carry out this reaction under mild conditions. A nucleophile can occupy one of the vacant sites of the metal leading to an internal attack, resulting in the *syn*-addition. Conversely, external attacks, which may be both electrophilic or nucleophilic, result in *anti*-additions, as shown by Scheme 5.2.

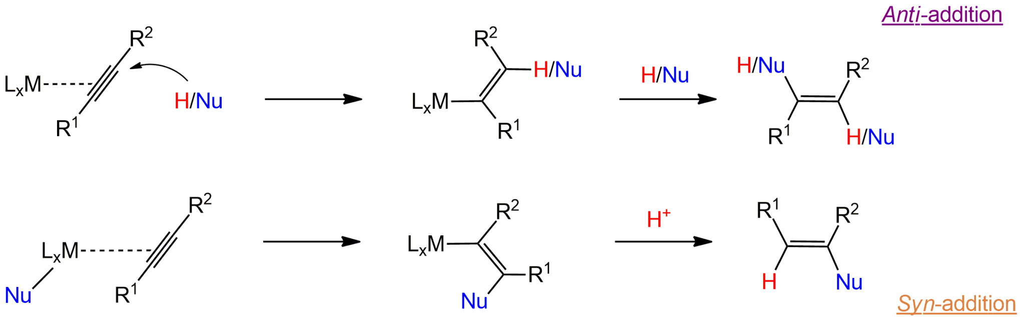

Scheme 5.2. Anti- and syn-additions to metal-coordinated alkynes.

Stereoselectivity in these reactions is defined by the more favorable addition, which depends on many factors, such as catalytic activity, substrate nature and reaction conditions. For non-symmetrical alkynes, these attacks can target two distinct carbons, ultimately leading to two different regioisomers. In the case of terminal alkynes (as the ones treated in this Thesis), external attacks can afford the *gem*- and *cis*-products, while internal attacks can yield the *gem*- and *trans*-products, as exemplified by Scheme 5.3.

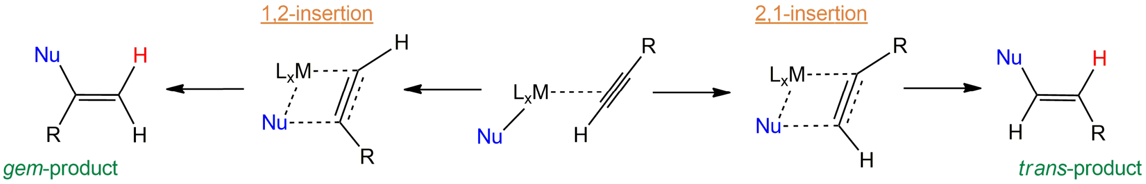

Scheme 5.3. Products resulting of the 1,2 and 2,1-insertion.

The 1,2-insertion refers to the insertion of the metal to the position 1 of the alkyne, meaning the terminal carbon, while the ligand, in this case the Nu, is bonded to the position 2 of the alkyne. This reaction yields an alkenyl bonded to the metal through its terminal carbon, which ultimately results in the formation of the *gem*-product. Conversely the 2,1-insertion yields the alkenyl bonded to the metal by its internal carbon and leads to the formation of the *trans*-product.

2) Oxidative addition of the substrate and alkyne insertion on M—H or M—Nu bond.

This mechanism starts with the cleavage of the substrate H—Nu bond, oxidizing the metallic center and yielding a metallic hydride and a Nu ligand. Following that, the alkyne undergo insertion, as shown for the internal nucleophilic attack (Scheme 5.3). However, in this case, insertion can be into both the M—H or the M—Nu bond, leading to four possible alkenyl ligands. After reductive elimination with the remaining substrate fragment either the *trans* or the *gem*-product is formed. Scheme 5.4 depicts the outcomes of these four possible alkyne insertions following the HNu substrate activation.

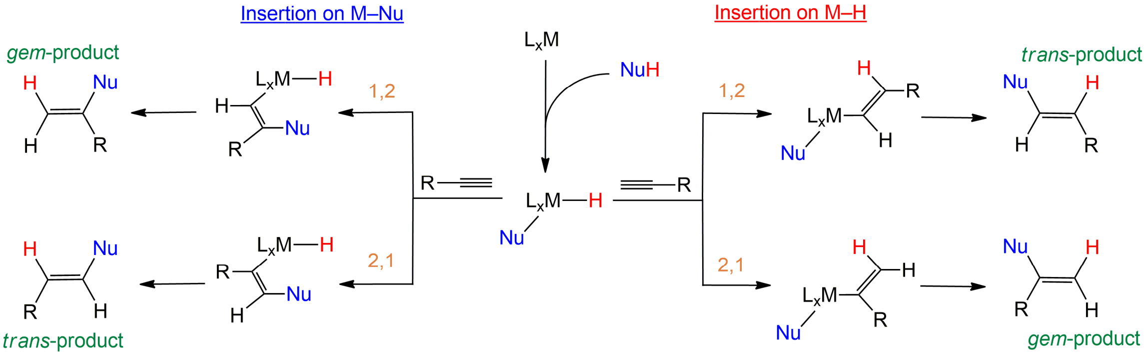

Scheme 5.4. Hydrofunctionalization of alkynes beginning with the oxidative addition of HNu.

3) Non-oxidative process enabled by an internal base.

An alternative pathway for this reaction involves a ligand which can act as a base to activate the HNu substrate without oxidizing the metal center. The base captures the H atom from the substrate subsequently releasing it and leaving its coordination site vacant for Nu. Following Nu coordination, alkyne insertion into the M—Nu bond can occur as described for the previous mechanisms. Lastly, the base donates its proton to form the product and regenerate the initial catalyst (Scheme 5.5).

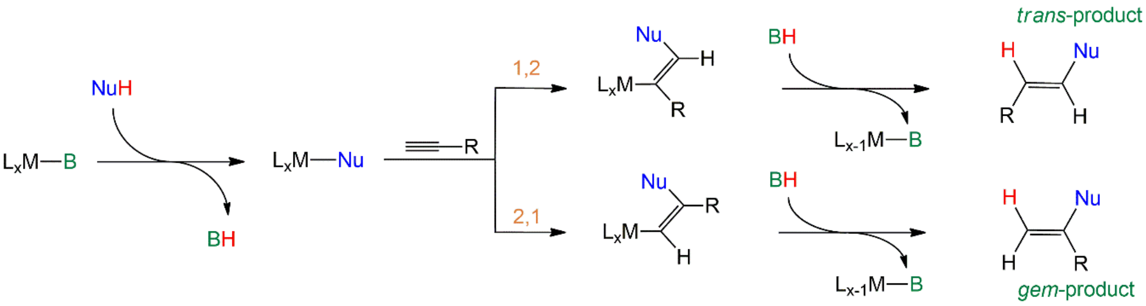

Scheme 5.5. Hydrofunctionalization of alkynes enabled by an internal base.

Compared to the previous one, this methodology presents the advantage of reducing the number of possible reaction pathways, for better selectivity control.

4) Reaction through a vinylidene intermediate.

Vinylidenes are alkyne tautomers that can be formed via the migration of the terminal hydrogen to the internal carbon, rendering the terminal carbon an unsaturated carbene. As such, vinylidenes can act as stronger ligands than a π-coordinated alkyne, presenting great capacity to both σ-donate and π-accept. For this reason, while tautomerization to vinylidene is highly endothermic for most alkynes, coordination to a metal of these species can favor the reaction to the point of the vinylidene being a viable intermediate in mechanisms. Nucleophilic attacks favor their terminal carbon while electrophilic attacks target the internal one. Consequently, the HNu substrate can be activated via the insertion of the Nu group into the terminal carbon and of the H into the internal carbon. Following this, the *cis*- and *trans*-products can be obtained via the β-elimination of a H and subsequent reductive elimination (Scheme 5.6).

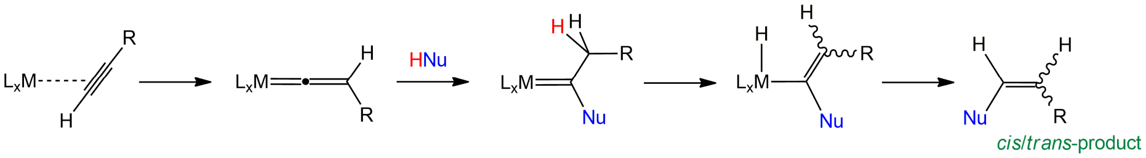

Scheme 5.6. Alkyne hydrofunctionalization through a vinylidene intermediate.

While this reaction is far less common than the previous three, it bears mentioning the interest of this mechanism because of its capability to yield the cis-products (while also possible via external attack, the gem is generally more favored).

5) Reaction through a metallacyclopropene intermediate.

Similar to vinylidenes, metallacycles are intermediates whose formation is enabled by the organometallic catalyst and possibilitate a different type of alkyne reactivity. These species can be formed through isomerization of a metallic alkenyl or the orthogonal proton donation from an acidic ligand to a π-coordinated alkyne (perpendicular to the plane defined by the metal center and the alkyne), as shown by Scheme 5.7.

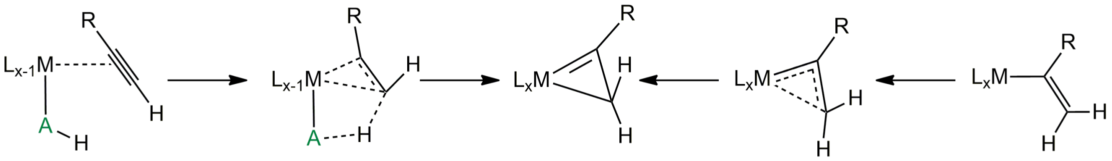

Scheme 5.7. Two possible pathways to the formation of a metallacycle intermediate.

The metallacycle sp^2 carbon is susceptible to nucleophilic attacks. This attack is perpendicular to the cycle and can occur from both sides, leading to the *syn*- or *anti*-addition, however for terminal alkynes both lead to the *gem*-product. (Scheme 5.8).

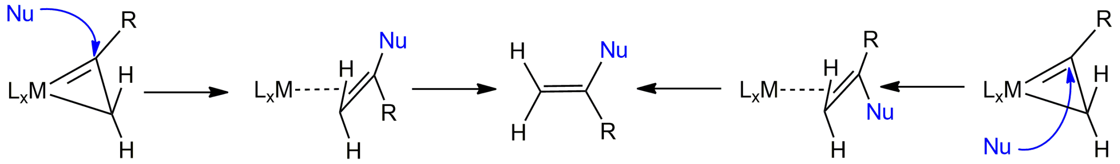

Scheme 5. 8. Metallacyclopropene aperture to yield the gem-product.

In opposition to the reaction through the vinylidene intermediate, the formation of *cis*- or *trans*-products is rare to non-existent in this process. Proton donation to the alkyne terminal carbon is favored due to its more negative partial atomic charge and lesser steric hindrance, resulting in the preferential formation of the *gem*-product. The selectivity achieved through this reaction pathway should be emphasized, as the most commonly used hydrofunctionalization methodologies can lead to a mixture of products due to their challenging-to-control selectivity.

The regioselectivity of the prevailingly utilized methodologies (i.e., the first four mentioned) is defined by a diverse series of stereoelectronic interactions between the alkyne, the electro/nucleophile and the catalyst. For instance, in the study of nucleophile insertion into a π-bonded alkyne, electrostatic interactions favor the insertion in the most positively charged carbon, typically the one not bonded to hydrogen due to its slightly acidic behavior. Conversely, steric hindrance favors the attack to the less substituted carbon, meaning the one bonded to the terminal hydrogen. Assessing the individual impact of these factors on reaction selectivity is challenging and can vary significantly for different substrates. Additionally, the metallic center and ligands can also play a relevant role in the definition of the selectivity. In particular, electron density rich metals favor oxidative addition processes and electrophilic attacks on π-coordinated alkynes, due to their substantial backdonation capacity. This electron density richness of the metal center depends on both, the metallic species, with metals such as Rh^I and Pd^0 being considerably richer than others such as Au^I and Fe^0, and the ligands electronic contribution. The interplay among these and other factors complicates both the prediction and rationalization of the selectivity for these reactions, which can be highly dependent on the substrates and reaction conditions, as a result, making it a less robust synthetic route.

In this context, computational calculations are a valuable tool in the study of these reactions. They offer an objective means to compare diverse possible mechanisms and find the operating one, allowing for the determination of the rate-limiting species. The mechanistic determination not only leads to a better understanding of the reaction, but can also guide catalyst optimization through rational design, refining the pathway to the desired product. Hence, computational calculation can aid in the search for a catalyst to introduce selectivity in reactions that otherwise afford unwanted products.

5.1. *Gem*-specific alkyne dimerization catalyzed via metal-ligand cooperation by a Rh-NHC-pyridonato complex

Introduction and objectives

Alkyne hydroalkynylation is a straightforward and completely atom-economical methodology for generating functionalized conjugated structures. These reactions can yield a range of products, from conjugated enynes to considerably more complex conjugated chemical frameworks via successive additions. Additionally, these conjugated systems contain the functional groups of the inserted alkynyls, which through a selective process can be strategically positioned. In this manner, alkyne oligomerization has the capability to generate a wide array of stereochemically distinct conjugated products. Scheme 5.9 exemplifies the diversity of possible products resulting from the dimerization, trimerization, and polymerization of terminal alkynes.

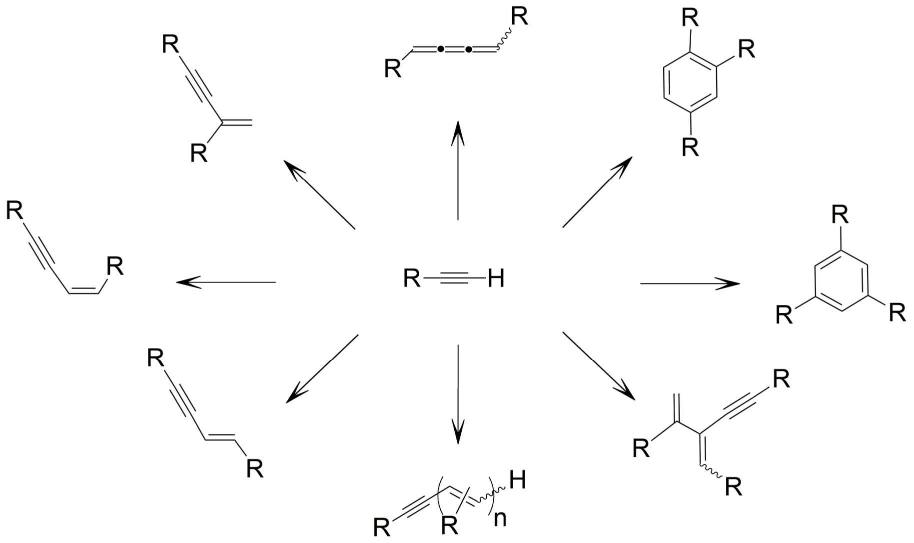

Scheme 5.9. Possible products of the oligomerization of terminal alkynes.

Therefore, these reactions can yield an extensive variety of stereochemically defined products using a unique substrate. These reactions hold significant potential in the construction of chemical scaffolds. The rich chemistry of alkynes, coupled with the ability to incorporate reactive R groups for transformation through subsequent processes, allows for the use of these reactions as foundational elements in the production of considerably more complex structures. Hence, these methodologies demonstrate remarkable versatility and efficiency for a broad spectrum of synthetic applications.

The major obstacle chemists face in the implementation of these methodologies lies in controlling their selectivity. The notable abundance of plausible products with similar structures of these reactions often leads to poor regio- and chemoselectivity.

In this context, the inclusion of specifically designed catalysts not only can reduce the energetic barriers for these reactions but also significantly improves their selectivity. Numerous reports on a wide variety of catalysts for the selective oligomerization of alkynes demonstrate the notable interest of the scientific community on these methodologies. Among these reports, examples of catalysts inducing the preferential formation of various potential products of oligomerization can be found, including dimers,[195] functionalized benzenes,[196,197] dienynes,[197] butatrienes[198], azulenes[199] and polymers.[200] Thus, the application of these catalysts can considerably enhance the effectiveness of these reactions as a strategy for the formation of conjugated products.

This section focuses on the catalyzed dimerization of terminal alkynes to generate conjugated enynes. The efficient synthesis of these products is highly sought-after due to the presence of these substructures (meaning an alkene conjugated to an alkyne) in a diverse variety of biologically active compounds and functional materials. This relevance is reflected in the abundance of studies on these processes. A broad range of catalysts for these reactions have been reported, containing catalysts based on both earth-abundant metals, such as Fe[201] and Ti,[202] and noble metals, Au,[203] Pd,[204] Rh,[205,206] Ir[206] and Pt[207] to name a few. While these systems preferentially form the desired product, they can be far from completely selective, due to the daunting challenge of discriminating between products with considerably similar structures and properties.

Some examples of highly selective catalysts for the formation of *trans*-,[207,208] *cis*-,[209,210] and *gem*-enynes[211,212] have been reported. Figure 5.1 presents some instances of catalysts capable of the selective dimerization of alkynes (using phenylacetylene as an example).

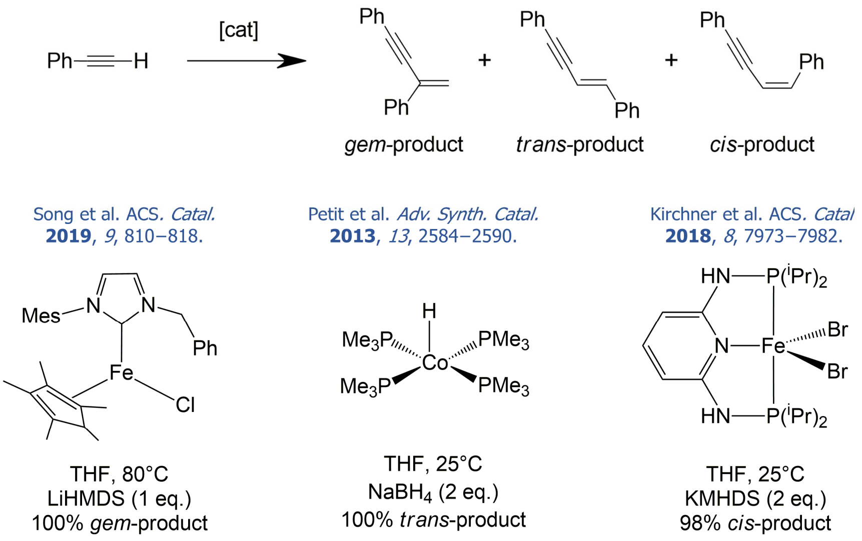

Song et al. ACS. *Catal.* **2019**, *9*, 810–818.

Petit et al. *Adv. Synth. Catal.* **2013**, *13*, 2584–2590.

Kirchner et al. ACS. *Catal* **2018**, *8*, 7973–7982.

THF, 80°C
LiHMDS (1 eq.)
100% *gem*-product

THF, 25°C
NaBH$_4$ (2 eq.)
100% *trans*-product

THF, 25°C
KMHDS (2 eq.)
98% *cis*-product

Figure 5.1. Examples of catalysts for the selective dimerization of phenylacetylene.

Even though high selectivities have been reported for a variety of systems, the determination of the factors responsible for their activity is a complex problem that is many times ignored. Understanding the contributions of the metallic center, the ligands, and the additives (if used) towards the reaction rate and selectivity, can be a complex task. As shown before, various differentiated reaction pathways can afford the same selectivity, at points containing common species, which can considerably obfuscate the elucidation of the operating mechanism. Moreover, the generally small energy differences between the rate determining species of these competing mechanisms for many systems means that seemingly small changes in the ligands or substrates may tip the scales in favor of another reaction pathway. For this reason, the detailed mechanistic study of a system is key to gaining insight into its activity. Studies like these can unravel the influence of auxiliary ligands on the catalytic reactivity, which can be used for the comprehensible tuning of the complex to enhance its catalytic activity. [213,214]

A novel strategy in catalytic design is the metal-ligand cooperation (MLC), which actively involves a ligand and the metallic center of a complex in the bond breaking and forming processes.[215–217] This alternative reaction pathway can lead to increased catalytic rates and selectivities. An example of this cooperation is the ligand-assisted proton shuttle (LAPS) in which a ligand extracts a proton from a substrate, activating it, and donates it to another molecule in a subsequent stage of the reaction, as illustrated by Scheme 5.10. [218]

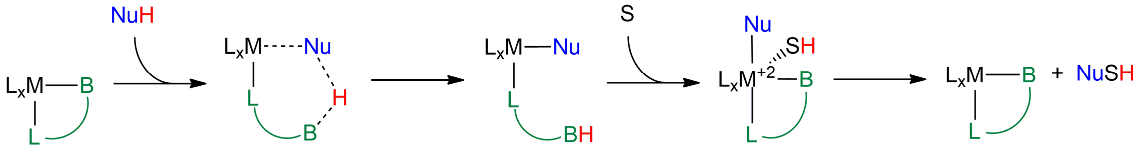

Scheme 5.10. Representation of a LAPS system for the activation of the Nu—H bond.

Next, this section focuses on the study of the selective *gem*-specific dimerization of terminal alkynes catalyzed by [Rh{κ^2-O,N-(Opy)}(η^2-coe)(IPr)] (which will be referred as **preA**). The results obtained for this reaction are significant due to the remarkably higher catalytic rate and selectivity than similar systems that do not include the pyridonate. Even more relevant is the fact that the low activation energy and high selectivity is observed for a wide diversity of terminal alkynes, while for similar catalysts these results can significantly change depending on the substrate. Hence, the objectives for this computational study are:

1. Determining the operating mechanism.
2. Unraveling the role of the pyridonate in this reaction.
3. Identifying the factors influencing the reaction rate and selectivity.

Results and Discussion

This work comes as a follow-up of another work published by our group, in which a [RhCl(py)(η^2-coe)(IPr)] complex was employed for the *gem*-selective dimerization of terminal alkynes. The results obtained with this catalyst compared with those obtained with the novel pyridonate-containing catalyst are presented in Figure 5.2.

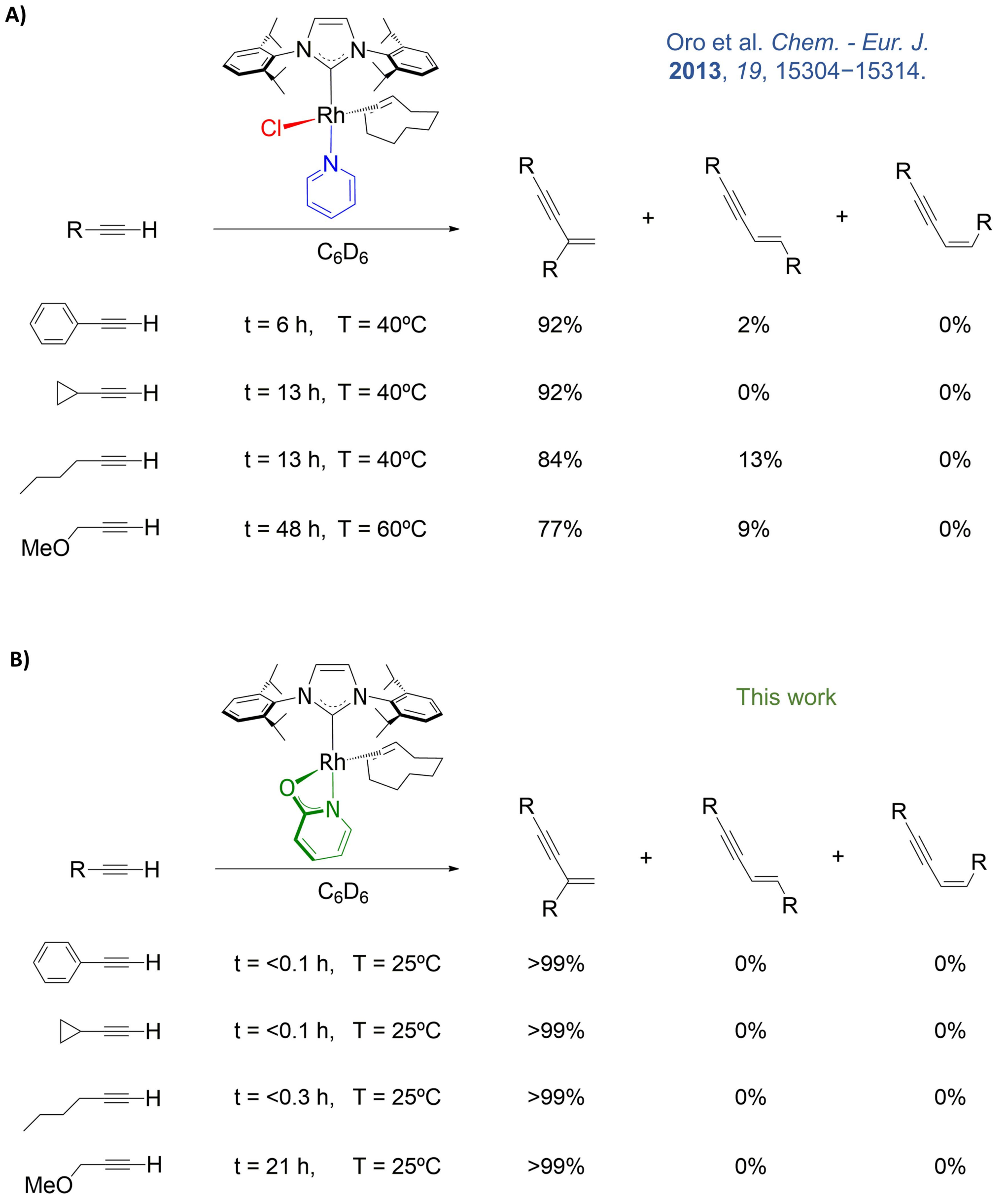

Figure 5.2. Selection of catalytic results obtained for a 1M alkyne solution for **A)** and a 0.4M for **B)** and a 2 mol% catalyst loading for both cases.

While both catalysts promote preferential *gem*-enyne formation for a wide range of terminal alkynes, the pyridine-bearing catalyst also yields minor secondary products, namely the *trans*-enyne and some trimers. In contrast, the pyridonate-containing catalyst exclusively produces the desired product. Moreover, all the reactions with the former catalyst require a certain degree of heating and take hours for complete substrate conversion, whereas with the latter catalyst most reactions conclude in outstandingly lower time frames at room temperature. These results indicate that the pyridonate in the catalyst brings about a substantial modification on the operating mechanism, resulting in a significantly lower energy span for *gem*-product formation and a larger difference between said energy span and those for the formation of alternative products.

Therefore, the mechanistic study for *gem*-dimer formation enabled by the pyridonate-bearing catalyst was carried out. In this study the phenylacetylene was used as model substrate, and all plausible reaction pathways were examined, excluding the external attack on π-coordinated phenylacetylene and vinylidene mediated processes, as they cannot lead to *gem*-product formation. The determined mechanism starts with the activation of the catalyst, which takes place as illustrated in Figure 5.3.

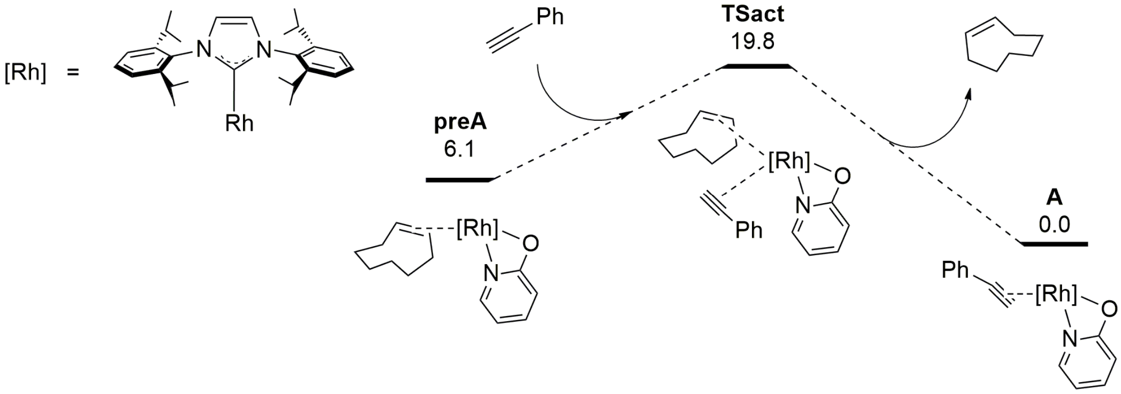

Figure 5.3. Activation free energy profile (kcal mol^{-1}) for the activation of the catalyst.

The active species, **A**, is formed via the exchange of the coe by a phenylacetylene molecule. The starting species, **preA**, at a relative energy of 6.1 kcal mol^{-1}, exhibits a square planar configuration characteristic of Rh^{I} with the pyridonate coordinated as a chelate. From that point, the concerted coe release and phenylacetylene π-coordination occurs as characterized by transition state **TSact** with a relative energy of 19.8 kcal mol^{-1}. Hence, catalyst activation presents an energy barrier of 13.7 kcal mol^{-1}, indicating it can occur at low temperatures. However, the resulting intermediate, **A** (0 kcal mol^{-1}), could not be experimentally determined using NMR, due to the exceedingly rapid catalytic dimerization. Even at 213 K, the reaction leads to the identification of a complex presenting a coordinated *gem*-enyne rather than the alkyne. Nonetheless, an analogous catalyst bearing a pyridine-2-thiolate, which exhibited similar selectivity but a considerably slower catalytic rate, allowed for the observation of the π-coordinated phenylacetylene at 223 K. Following that, if the temperature of the experiment was raised it led to the formation of the *gem*-enyne. These results hint at **A** being a local energy minimum preceding the dimerization reaction, as such is considered the active species.

The first proposed catalytic cycle followed a similar reaction pathway to that determined for the pyridine-bearing catalyst. This mechanism is presented in Figure 5.4.

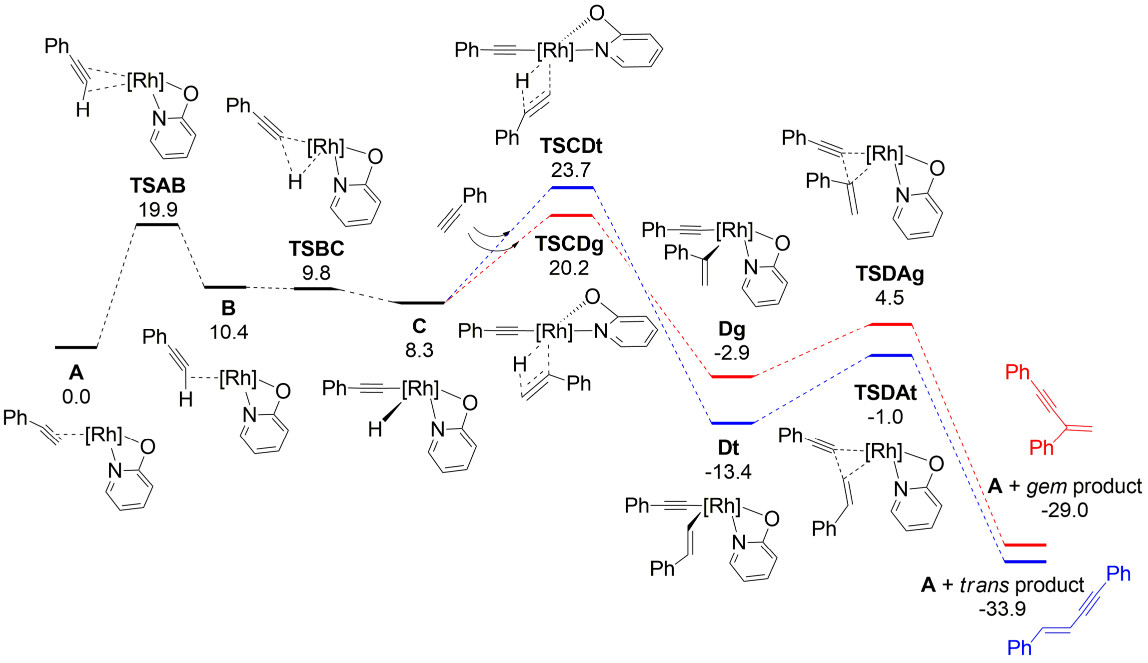

Figure 5.4. DFT calculated free energy profile (in kcal mol^{-1} relative to **A** and isolated molecules) for phenylacetylene dimerization starting with the oxidative addition of phenylacetylene.

This catalytic cycle starts with the slippage of the bond between the Rh and the phenylacetylene, going from η^2-(C≡C)- to η^2-(C—H). This reaction step is characterized by transition state **TSAB**, with a relative energy of 19.9 kcal mol^{-1} and yields intermediate **B** at a relative energy of 10.4 kcal mol^{-1}. This process is remarkably endergonic due to the poorer stabilization of the agostic interaction compared to that of the triple bond π-coordination. Nonetheless, the agostic interaction, enables the C—H bond cleavage through oxidative addition, as depicted by transition state **TSBC** (9.8 kcal mol^{-1}) presenting a negligible energy barrier. This results in the formation of intermediate **C** (8.3 kcal mol^{-1}), which due to the oxidation to Rh^{III} exhibits an octahedral configuration, incorporating the afforded alkynyl and hydride and leaving a vacant site *trans* to the latter.

The vacant site of **C** possibilitates the coordination of a second phenylacetylene molecule, enabling its insertion into the Rh—H bond to progress the reaction. At this point two reaction pathways arise, as the hydrometallation can occur with two possible phenylacetylene orientations, leading to the 2,1-insertion (**TSCDg**, 20.2 kcal mol^{-1}) and the 1,2-insertion (**TSCDt**, 23.7 kcal mol^{-1}), affording the *gem*- and *trans*-alkenyl respectively. It should be noted that for both attacks the most energetically favored configuration has the reacting alkyne in *trans* position to the carbene, with the pyridonate being displaced to the plane defined by the hydride and alkynyl. These insertions yield the intermediates, **Dg** (-2.9 kcal mol^{-1}) and **Dt** (-13.4 kcal mol^{-1}) each of them presenting an alkenyl (*gem* and *trans* respectively), an alkynyl and the pyridonate in its original position. Finally, the enynes are formed via reductive elimination as depicted by transition states **TSDAg** (4.5 kcal mol^{-1}) and **TSDAt** (-1.0 kcal mol^{-1}). The release of the product results in the regeneration of **A**, with the *gem*-enyne formation being exothermic by 29.0 kcal mol^{-1} and that of the *trans*-enyne being exothermic by 33.9 kcal mol^{-1}.

It should be noted that the carbometallation reaction was not considered for this system. This is because, in the case of the pyridine-bearing catalyst, as well as for other similar catalysts,[214] the alkyne insertion into the Rh—C bond presented significantly higher effective energy barriers than into the Rh—H bond.

Based on the obtained results, the energy span for the formation of the *gem*-enyne is defined by the species **A** and **TSCDg**, therefore, it presents an energy span of 20.2 kcal mol^{-1}. Whereas, for *trans*-enyne it is defined by **A** and **TSCDt** resulting in an energy span of 23.7 kcal mol^{-1}. An effective energy barrier difference of 3.5 kcal mol^{-1} in favor of the formation of the *gem*-product adequately aligns with the experimentally observed selectivity. However, a barrier of 20.2 kcal mol^{-1} is somewhat higher than what would generally be expected for a reaction that occurs rapidly at room temperature.

For this reason, further studies to validate this mechanism were conducted. The experimental KIE obtained for the isotopically marked phenylacetylene-d_1 is 1.67 ± 0.12. Whereas the KIE calculated considering **A** and **TSCDg** as the rate-limiting species is 2.61. Although both KIEs are primary, their significant difference in value leads to the conclusion that this mechanism is not the operating one. On a secondary note, the KIE of the phenylacetylene terminal hydrogen being primary indicates that this atom is directly involved in a bond that is either being broken or formed in the rate-limiting transition state. This evidence narrows down which processes could be the rate-limiting transition states, as reactions like carbometallations or reductive eliminations cannot yield this KIE (validating the previous assumption that the carbometallation is not part of the operating mechanism).

Further study of the system leads to the proposal of the mechanism depicted in Figure 5.5, based on the participation of the pyridonate as a proton shuttle.

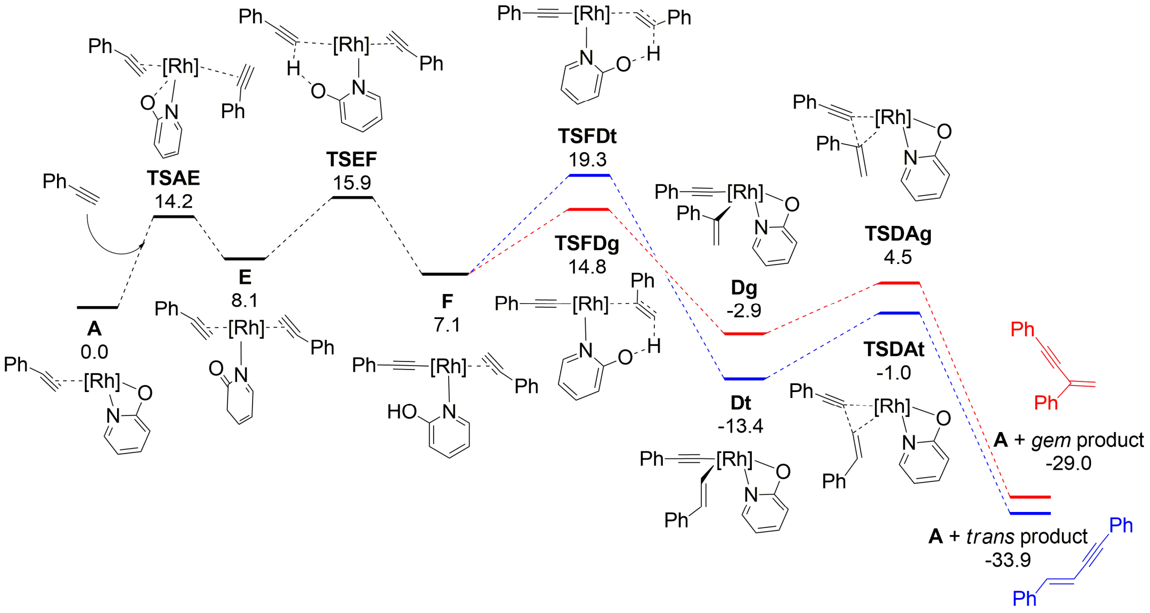

Figure 5.5. DFT calculated free energy profile (in kcal mol^{-1} relative to **A** and isolated molecules) for phenylacetylene dimerization through a pyridonate assisted proton shuttle.

This mechanism starts with the simultaneous decoordination of the pyridonate O and coordination of a second phenylacetylene molecule to **A**, as characterized by transition state **TSAE** (14.2 kcal mol^{-1}). This behavior can be attributed to the Rh oxidation state (I) which favors the square planar configuration of the complex. The resulting intermediate, **E** (8.1 kcal mol^{-1}), contains two π-coordinated alkynes in *trans* position. Even though oxidative addition from this intermediate is less favored than from **A**, due to the larger steric hindrance arising from the second alkyne, the decoordinated pyridonate carbonyl group can act as an internal base. Subsequently, the concerted metalation-deprotonation (CMD) of one of the π-coordinated alkynes can occur, as depicted by **TSEF** (15.9 kcal mol^{-1}). In this transition state the pyridonate captures the terminal hydrogen from one of the alkynes and the remaining alkynyl fragment is coordinated to the Rh. The afforded intermediate, **F** (7.1 kcal mol^{-1}), features a pyridone coordinated to the Rh exclusively through its N atom, allowing it to rotate and position its hydroxy group in proximity of the remaining π-coordinated alkyne. Following that, the pyridone can donate the previously captured proton to either the terminal or internal carbon of the alkyne, resulting in two differentiated reaction pathways.

The donation of the hydroxyl proton to the terminal carbon leads to the formation of the *gem*-alkenyl, as depicted by **TSFDg** (14.8 kcal mol^{-1}). Conversely, the donation to the internal carbon affords the *trans*-alkenyl via the transition state **TSFDt** (19.3 kcal mol^{-1}). These reactions yield the previously mentioned **Dg** and **Dt** intermediates, respectively. Consequently, the catalytic cycle is completed through the same process as that discussed for the previous cycle, namely, reductive elimination.

Therefore, the energy span for *gem*-enyne generation is defined by **A** and **TSEF**, resulting in an effective energy barrier of 15.9 kcal mol^{-1}. This result aligns better with the experimentally observed high reaction rates at low temperatures. In contrast, the energy span for *trans*-enyne formation is defined by **A** and **TSFDt**, yielding an effective energy barrier of 19.3 kcal mol^{-1}. Moreover, the regioselectivity of the catalysis is defined by the selectivity of the proton donation. Meaning that, the regioselectivity is defined by the energy gap between **TSFDg** and **TSFDt**, 4.5 kcal mol^{-1}, leading to the exclusive formation of the *gem*-alkenyl and ultimately the *gem*-product. Lastly, the theoretical KIE considering **A** and **TSEF** as reaction rate-defining species is 1.57, which adequately fits the 1.67 ± 0.12 experimental value. Figure 5.6 presents the geometry of the rate-defining transition states for the two proposed mechanisms, and hints at the origin of the significant different between their KIE values.

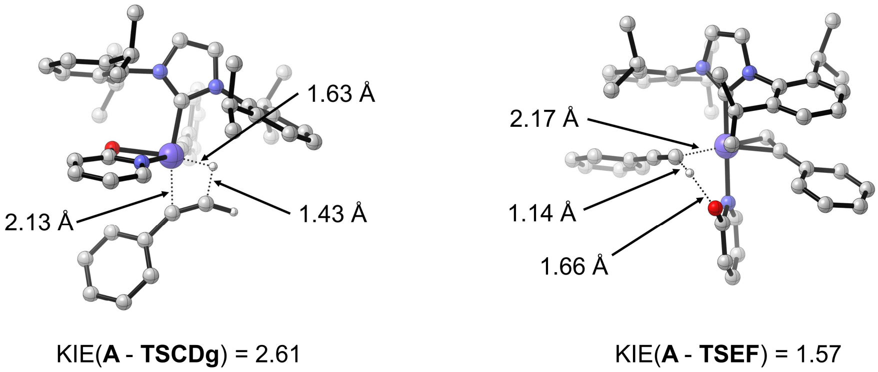

Figure 5.6. Representations of **TSCDg** and **TSEF** with relevant distances and corresponding KIEs.

The unusually low primary KIE obtained for the terminal hydrogen capture can be attributed to the considerable early character of **TSEF**. This is reflected in the minor stretching of the C—H/D bond, going from 1.09 Å for **A** to 1.14 Å for **TSEF**. This less than anticipated elongation can be related to the stabilizing agostic interaction between the Rh and the C—H/D bond. As a result, the point of higher energy in the proton transference is primarily defined by the loss of the agostic interaction, more so than by the cleavage of the C—H/D bond and formation of the O—H/D bond. As **TSCDg** does not present such interactions, the transition state clearly corresponds to the breaking of the Rh—H bond and the formation of the C—H bond, yielding a more conventional primary KIE of 2.61.

On account of the characteristics determined for this mechanism, namely an effective energy barrier that aligns with the experimental observations, a computational KIE that perfectly matches the experimental one and its justification for the process selectivity, this mechanism was considered to be the operating one. Consequently, the role of the pyridone as an internal proton shuttle was confirmed. This conclusion explains the significantly difference activity exhibited by the pyridone-bearing catalyst.

As previously commented, the selectivity for this mechanism is defined by the preference in protonation of the π-coordinated phenylacetylene carbons in **F**. The electrophilic attack of the proton is more favored when the acceptor atom is more negatively charged. This difference in charges is shown in Figure 5.7.

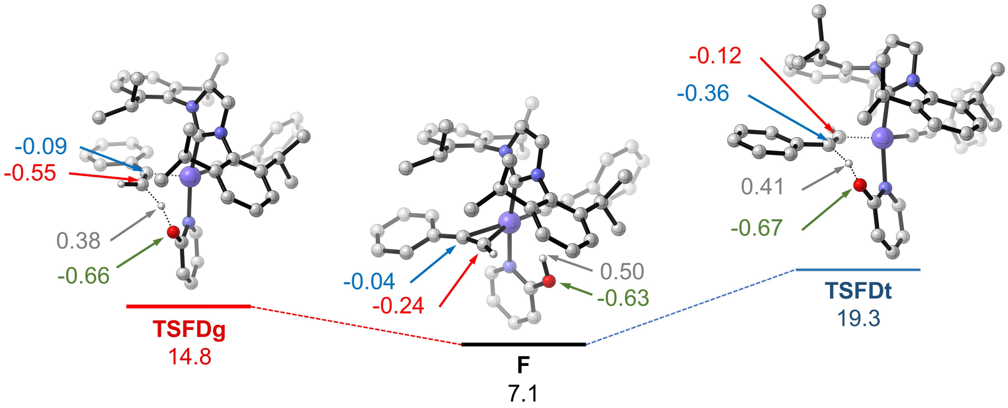

Figure 5.7. Representations of **F**, **TSFDg**, and **TSFDt** with the NBO atomic charges (in a.u.) of the atoms involved in the proton transfer and their relative free energies.

The NBO analysis of **F** derives an atomic charge of -0.24e for the terminal carbon and of -0.04e for the internal carbon. Consequently, the transfer of the partially positively charged proton (0.5e) to the former is more energetically favored. Interestingly, for most alkynes, the terminal carbon is more negatively charged due to the moderately acidic behavior of the terminal hydrogen. Therefore, this strategy for the selective hydrofunctionalization of alkynes is valid for an extensive diversity of alkynes.

The selectivity for most conventional alkyne dimerization pathways is defined by either hydrometallation or carbometallation processes. Nevertheless, controlling the favored alkyne orientation for its insertion in a metallic bond can be extremely challenging. As mentioned in this section's introduction, steric and electronic factors can favor opposite configurations for these processes, leading to significant changes in the selectivity depending on the substrate and leading to product mixtures for many of them.

On the contrary, the LAPS mechanism is versatile and robust, as the great majority of terminal alkynes display a similar difference in polarization between their terminal and external carbons. This is illustrated by the disparate array of alkynes tested experimentally, obtaining exclusively the *gem*-dimer for all of them. Whereas, the pyridine-bearing catalyst, whose selectivity is defined by the hydrometallation of the alkyne, displayed lesser selectivity for many of these alkynes. Figure 5.8 depicts the origin of the selectivity for these mechanisms and their substrate dependence.

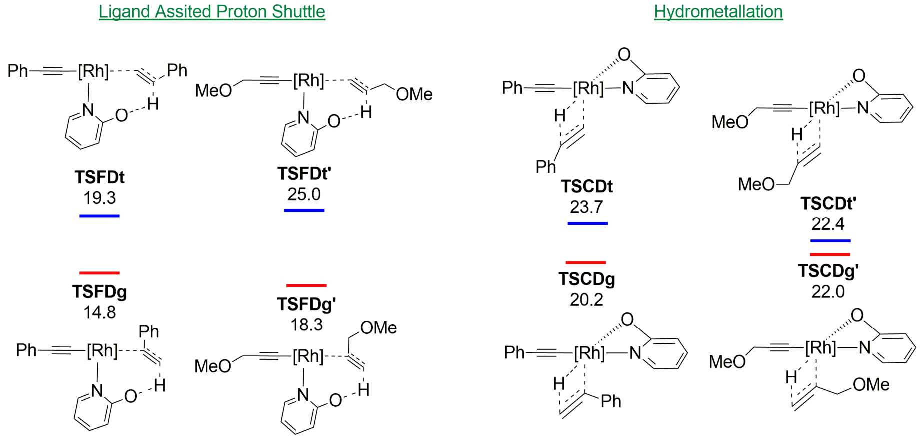

Figure 5.8. Relative free energies (kcal mol^{-1}, relative to **A** and isolated molecules) of the rate determining transition states for phenylacetylene and 3-methoxyprop-1-yne dimerization.

These results align well with those presented in Figure 5.2. The selectivity for the operating mechanism of the pyridine-containing catalyst is defined by the hydrometallation, which leads to the poor selectivity obtained for 3-methoxyprop-1-yne. In contrast, the pyridonate-bearing catalysts operating through LAPS, exclusively yields the *gem*-product for both these alkynes, as expected based on the significant energy difference between the *gem*- and *trans*-alkenyl yielding transition states.

It should be noted that terminal alkynes which present electron-donating groups, such as -SiR_3, can exhibit a similarly or even more negatively charged internal carbon than the terminal one. In these rare cases, the reaction selectivity may be lost or even reversed. Catalytic experiments carried out with ethynyltrimethylsilane resulted in a 48/52 split between *gem*- and *trans*-products.

In summary, the pyridonate enables an alternative reaction pathway based on its hemilability. It allows for the decoordination of its oxygen atom to act as an internal base, capturing a proton from an alkyne. Subsequently, it can rotate towards a second alkyne, and donate to it this proton, all the while remaining bonded to the metal. This mechanism falls under the category of ligand-assisted proton shuttle and offers an alternative route that can yield significant improvements over conventional pathways. For the studied system, this pathway presents a lower effective energy barrier, a greater selectivity, and can be effectively applied to a wider range of alkynes with the same level of selectivity.

5.2 Rh-NHC catalyzed *gem*-specific *O*-selective hydropyridonation of terminal alkynes

Introduction and objectives

2-pyridone exhibits great potential as chemical scaffold for the synthesis of a diverse array of heterocyclic compounds. This fragment is present in a wide range of products of interest, including many biologically active compounds,[219,220] such as antibacterial agents,[221] anti-inflammatory drugs,[222] antioxidants drugs,[223] or the drugs used in the treatment of other medical conditions.[224,225] Some examples of these compounds are shown in Figure 5.9.

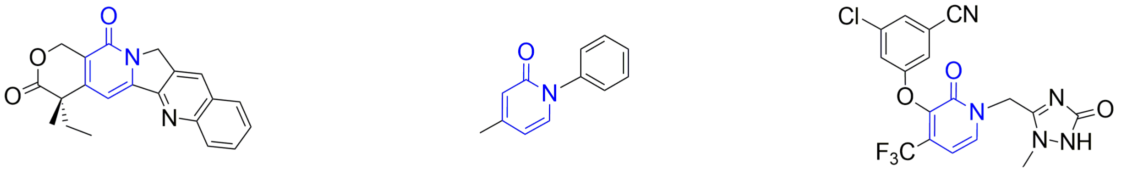

camptothecin
used in cancer treatment

pirfenidone
used in pulmonary fibrosis treatment

doravirine
used in HIV treatment

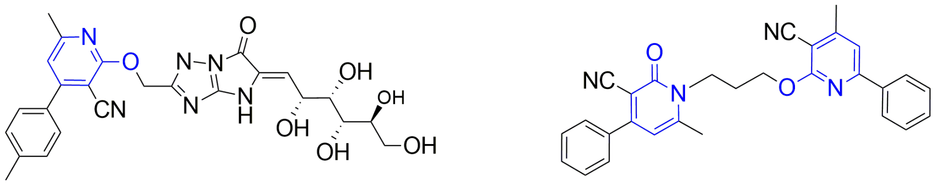

O-substituted 2-pyridone derivative
used as antioxidant agent

O- and *N*-substituted 2-pyridone derivative
used as anti-inflammatory agent

Figure 5.9. Examples of biologically active 2-pyridone based compounds.

Conventionally, the introduction of 2-pyridone fragments was achieved through multiple step processes.[226] However, in recent years many of these strategies are being replaced by more efficient methodologies based on organometallic catalysts.[226,227] The functionalization of carbon atoms in heterocycles is generally based on C—H bond activation.[228] Whereas the functionalization of heteroatoms can be achieved through multiple approaches.

The introduction of unsaturated fragments into the heteroatomic positions of pyridones is considered a relevant objective, due to the ubiquity of this moiety in compounds of interest, as well as its synthetic versatility. A wide range of methodologies for the introduction of these fragments have been reported, such as the use of organohalides,[229] allenes[230] or allylic compounds with a leaving group[231] (see Scheme 5.11).

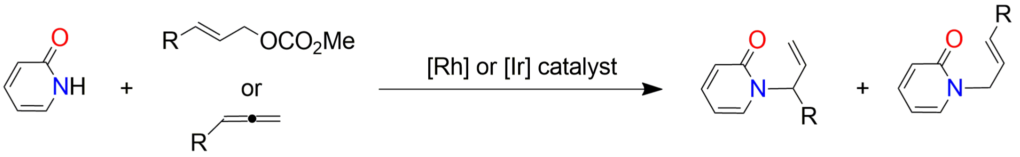

Scheme 5.11. Examples of reaction for the *N*-substitution of 2-pyridone.

Controlling the selectivity of reactions involving 2-pyridones is often challenging due to their keto-enol tautomery, simultaneously enabling the reactivity of the pyridone O and N atoms (see Scheme 5.12), with the latter being preferential for most reaction pathways.[232] Additionally, the *N*-substituted products are generally more thermodynamically favored.

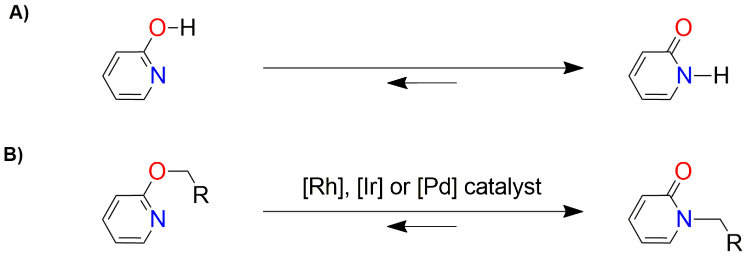

Scheme 5.12. A) Tautomeric equilibrium between 2-pyridone and 2-hydroxipiridine, **B)** reorganization of a substituent from *O* to *N*.

The generation of *N*- or *O*-alkenylated pyridones can be considerably more challenging than the simple substitution of the heteroatomic positions. Only a small subset of the methodologies used for the functionalization of these positions is valid for their alkenylation, while the same selectivity challenges are present for them. Conversely, some synthetic methodologies utilize this behavior to generate *N*-alkenylated pyridones via the isomerization of *O*-alkynylated pyridones, as illustrated by Scheme 5.13.[233]

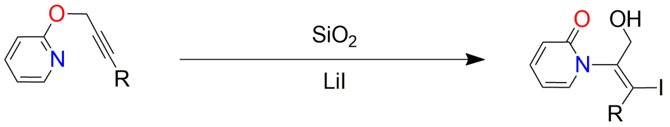

Scheme 5.13. isomerization of *O*-alkynylated pyridones to yield a *N*-alkenylated pyridone.

Even though *O*-alkynylated pyridones can be generated via an alkoxide attack to a 2-halo-pyridine, the application of these methodologies is limited by the presence of residual groups in the resulting alkyne which may be undesired. In contrast, the use of activated reactants, such as vinyl halides[234] or vinyl boronic acids,[235] allows for the formation of a significantly wider range of products via cross-coupling reactions (see Scheme 5.14).[236]

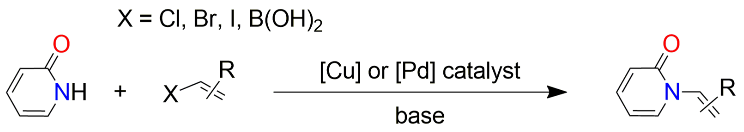

Scheme 5. 14. Pyridone alkenylation through cross-coupling reactions.

While these methodologies present a remarkable versatility, the reactants required for their application are rarely commercially available, and typically have to be synthesized through multiple step processes. A similar approach that utilizes more commonly available reactants, involves the introduction of a methylene moiety containing an electron-withdrawing group (EWG) followed by a subsequent aldol condensation, as illustrated in Scheme 5.15.[237]

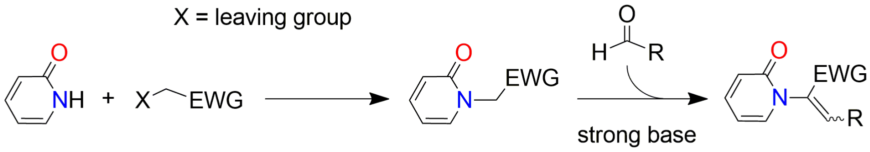

Scheme 5.15. Pyridone alkenylation of a through aldolic condensation.

Alternatively, a more efficient pathway to the formation of *N*- or *O*-alkenylated pyridones is the direct addition of an alkyne to a 2-pyridone. However, this reaction is only feasible when the alkyne contains an electron-withdrawing group (EWG) and/or an electron-donating group (EDG) that enables the reaction. The regioselectivity of this reaction is defined by these groups' resonance effects.[238]

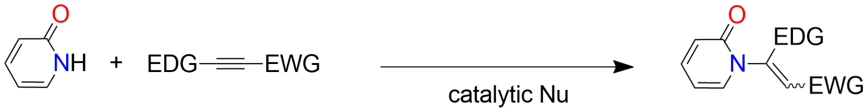

Scheme 5.16. Hydropyridonation of alkynes containing electron-donating or withdrawing groups.

Both these preparative strategies exhibit significant limitations in their scope due to their reliance on directing groups, which ultimately become components of the products. This scope is also limited in the sense that they typically lead to the preferential formation of the *N*-alkenylated products, due to the pyridinic N being a better nucleophile than the alkoxy O for most pyridones.

Hence, while there are diverse pathways for the generation of the *N*- or *O*-alkenylated pyridones, the majority of these pathways present significant limitations on their scope. Conversely, the more widely applicable methodologies require activated reactants which are hard to come by and typically have to be synthesized in situ through laborious synthetic pathways.

Additionally, controlling the selectivity can be challenging for many of these approaches. For most reactions, the formation of the *N*-substituted product is favored. This is either due to the higher nucleophilicity of the N atom or because metal coordination with the pyridinic N is generally more favorable than with the alkoxy O. Due to the preferential coordination of the pyridinic N, reactions in which an organometallic catalyst is involved tend to yield preferentially the *N*-substituted product after reductive elimination. While the regioisomery of the afforded alkenyl is determined by the reaction pathway as well as the reactants properties, in many of the mentioned reactions it can lead to mixtures of *cis*- and *trans*-products. Nonetheless, the methodologies leading to *gem*-alkenyl formation are scarce and either involve multistep procedures[239] or require rare reactants such as tosylhydrazones[240] or benzynes[241].

In this work an alternative synthetic methodology was developed utilizing a Rh-NHC catalyst, exploiting the preferential bonding of the pyridinic N to the metal to promote the *O*-insertion of pyridones on terminal alkynes. This results in a straightforward, atom-economical, and selective methodology for the formation of *gem*-specific and *O*-selective alkenylated pyridones. Further experiments showed that heating the *O*-alkenylated products in the presence of the catalyst for prolonged periods lead to their transformation into the *N*-alkenylated products.

The following part of this section focuses on the results obtained for the *O*-selective *gem*-specific hydropyridonation of terminal alkynes catalyzed by $[Rh(\mu\text{-}Cl)(\eta^2\text{-}coe)(IPr)]_2$ (which will be referred as **preA**). Remarkably, the use of a catalyst and utilization of terminal alkynes circumvents the need for activated reagents. The results obtained for these reactions show the existence of a differentiated kinetic and a thermodynamic product, which interestingly, deviate from those obtained for most synthetic methodologies. Hence, the objectives for this computational study are:

1. Determining the operating mechanism for each of the possible products.
2. Elucidating the origin of the chemo- and regioselectivity for these processes.

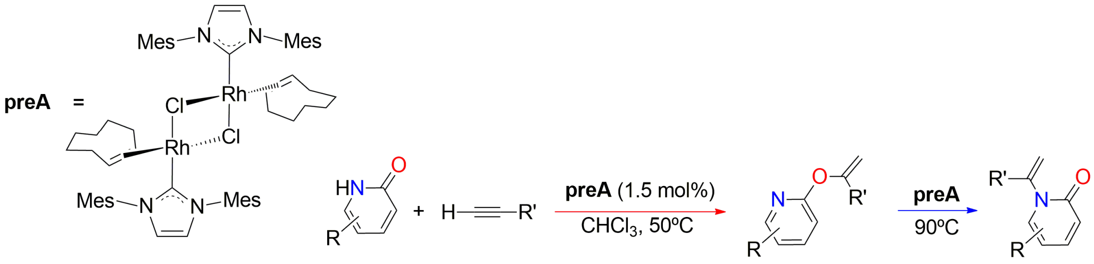

Figure 5.10. Catalyzed *O*- and *N*-selective *gem*-specific terminal alkyne hydropyridonation.

Results and Discussion

The catalyst utilized for terminal alkyne dimerization in the previous Section 5.1, [RhCl(py)(η^2-coe)(IPr)], is synthesized via a reaction involving stoichiometric amounts of 2-pyridone, a base, namely, ^{t}BuOK, and half the amount of **preA**. In some of the catalytic experiments carried out using this catalyst residual amounts of RhCl(IPr)-[κN,η^2-{py-O—C(Ph)=CH_2}], which will be referred to as **E**, were detected. Further experimentation revealed that this complex can be formed through the stoichiometric reaction of half an equivalent of **preA** with 2-pyridone and a terminal alkyne, as shown in Figure 5.11.

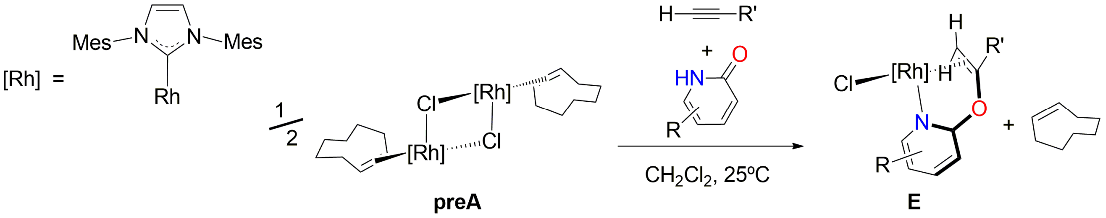

Figure 5.11. Stoichiometric formation of RhCl(IPr)-[κN,η^2-{py-O—C(Ph)=CH_2}].

The ability of this complex to enable the stoichiometric alkyne-pyridone C—O coupling hinted at the possibility of its utilization for the catalytic hydropyridonation of terminal alkynes This reaction would constitute a straightforward and efficient method, for the generation of *N*- or *O*-alkenylated pyridones.

The catalytic activity was tested for a wide range of terminal alkynes and functionalized 2-pyridones, using a stoichiometric mixture of the two reactants. This methodology led to the selective *gem*-*O*-alkenylated pyridone formation for the great majority of tested substrates. The highest catalytic rates were observed at 50°C, with the decline at higher temperatures likely caused by the decomposition of the catalyst. In general terms, aromatic alkynes showed higher reaction rates than aliphatic ones, whereas no defined trend was observed for the pyridones. Many catalytic reactions utilizing terminal alkynes are hampered by the pronounced self-reaction of these substrates, leading to the formation of dimers and more complex oligomers. Nonetheless, the yield for alkyne dimers is limited to 1-12% for most studied cases. The exception are the cases in which the hydropyridonation is considerably slower, such as 6-methyl-2-pyridones, where the 1,3-enynes are the prevalent product.

Considering that their reactivity is representative of most cases while constituting the simplest possible system, the 2-pyridone and phenylacetylene were selected as model substrates for the DFT analysis of these reactions. These calculations were utilized to determine the operating mechanism for the hydropyridonation of terminal alkynes and the selectivity origin for this process.

A series of experimental tests were carried out to gain insight into this mechanism. The stoichiometric reaction with 2-pyridone and phenylacetylene was monitored under low temperatures with the aim of determining intermediates involved in the operating mechanism. However, in experiments conducted between room temperature and -60°C, no species other than **E** were detected. Hence, it can be inferred that **E** is the rate-determining intermediate and that there are no significant energy barriers preceding it. Conversely, the catalytic product formation requires slight heating, indicating that there is a step following the formation of **E** that presents a significant energy barrier. Although KIE studies were attempted using either phenylacetylene-d_1 or 2-pyridone-d_1 in order to shed light on the rate-determining transition state, the proton exchange between the acidic terminal alkyne and the basic pyridone obstructed the determination of this effect.

Since the formation of **E** involves the Rh dimer dissociation, it is assumed that the active species is a Rh monomer. Furthermore, given the ligands exhibited by **E**, it can be inferred that coe is decoordinated to form the active species, as it is unlikely for this ligand to be decoordinated and coordinated during the catalytic cycle, while the chlorine and IPr remain coordinated throughout. An exhaustive study using DFT calculations was carried out to determine the most stable active species that can be formed via the coe exchange by reaction substrates, which present higher concentrations under catalytic conditions. This study concluded that **A**, containing a $\kappa^1 N$-hydroxypyridine and a π-coordinated-alkyne, is the active species. Figure 5.12 displays the mechanism for the formation of **E** from **A**, and the calculated energy profile for it.

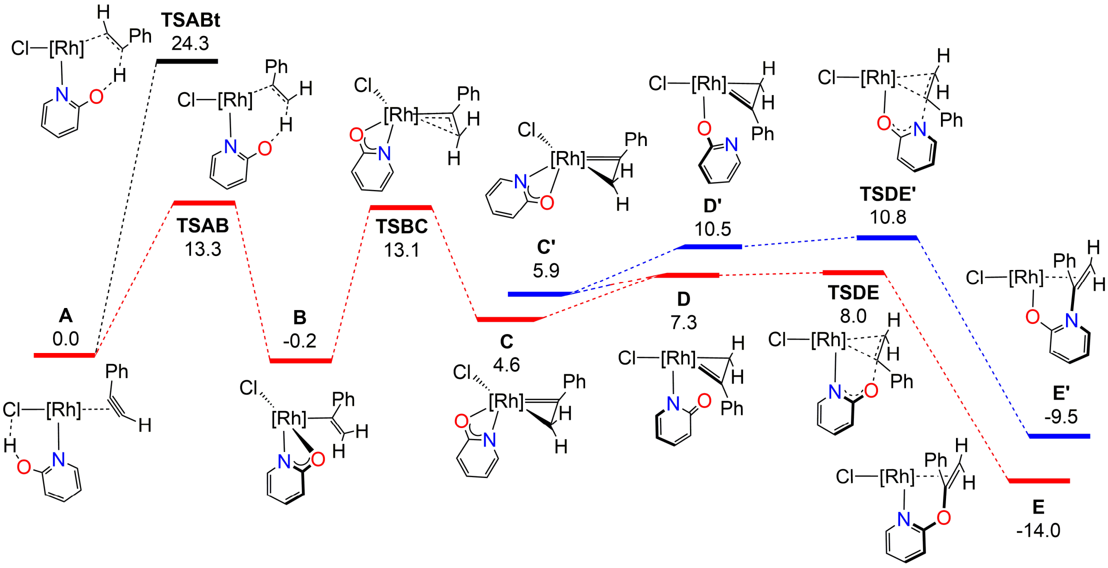

Figure 5.12. DFT calculated free energy profile (in kcal mol^{-1}, relative to **A** and isolated molecules) for alkyne-pyridone C—O coupling (red pathway) and C—N coupling (blue pathway).

The determined mechanism starts from **A** which presents a hydroxypyridine ligand with its hydroxy group forming a hydrogen bond with the chlorine ligand. The rotation of the hydroxypyridine can align this hydroxy group with either of the π-coordinated-alkyne carbons, enabling it to act as a proton donor. The proton transfer to the terminal carbon is depicted by transition state **TSAB** (13.3 kcal mol^{-1}), while donation to the internal carbon is characterized by **TSABt** (24.3 kcal mol^{-1}). The energetically favored proton donation to the terminal carbon leads to the formation of intermediate **B** (-0.2 kcal mol^{-1}), containing the afforded *gem*-alkenyl and pyridone, which is chelated to the metallic center. The reaction continues with the isomerization of the alkenyl to a metallacyclopropene, as illustrated by **TSBC** (13.1 kcal mol^{-1}), yielding intermediate **C** (4.6 kcal mol^{-1}). While the metallacycle formation is thermodynamically unfavored, it entails the transformation of the internal carbon into a carbenic carbon. It makes this carbon atom electron deficient and therefore prone to a nucleophilic attack. This is followed by the decoordination of the pyridone oxygen (**D**, 7.3 kcal mol^{-1}), which possibilitates its attack on the carbenic carbon, as characterized by transition state **TSDE** (8.0 kcal mol^{-1}). This C—O coupling affords the experimentally observed intermediate **E**, which is significantly more stabilized than other intermediates in this catalytic cycle at a relative energy of -14.0 kcal mol^{-1}.

The C—N coupling was also studied, with the most energetically favored pathway for this reaction deviating from that of the C—O coupling at intermediate **D**. From this point the pyridone can have its N atom, by which it is solely coordinated to the Rh, move from the position *trans* to the IPr to the position *trans* to the carbenic carbon so that the carbonylic oxygen can occupy the vacated site. This change in coordination mode yields intermediate **C’** (5.9 kcal mol^{-1}), from which the pyridinic N can be decoordinated to afford intermediate **D’** (10.5 kcal mol^{-1}). This leaves the pyridone coordinated solely by its O atom to the Rh while the pyridinic N is free to attack the metallacyclepropene carbenic carbon, as characterized by **TSDE’** (10.8 kcal mol^{-1}). This attack yields **E’** (-9.5 kcal mol^{-1}), presenting the *gem*-*N*-alkenylated pyridone coordinated to the metallic center by both its O atom and its alkene bond.

Similar to what was previously observed for the catalyzed alkyne dimerization in Section 5.1, the oxidative addition of substrate molecules to form a metallic hydride is a significantly less energetically favored reaction pathway than the proton transfer enabled by hydroxypyridine. The most energetically favored oxidative addition process that could explain the observed reactivity involved the alkyne decoordination and the cleavage of the hydroxypyridine O—H bond (**TSAK**, 31.2 kcal mol^{-1}). Figure 5.13 compares this reaction to the proton transfer to the alkyne from both the 2-hydroxypyridine (**TSAB**) and the 2-pyridone (**TSAB’**, 19.2 kcal mol^{-1}).

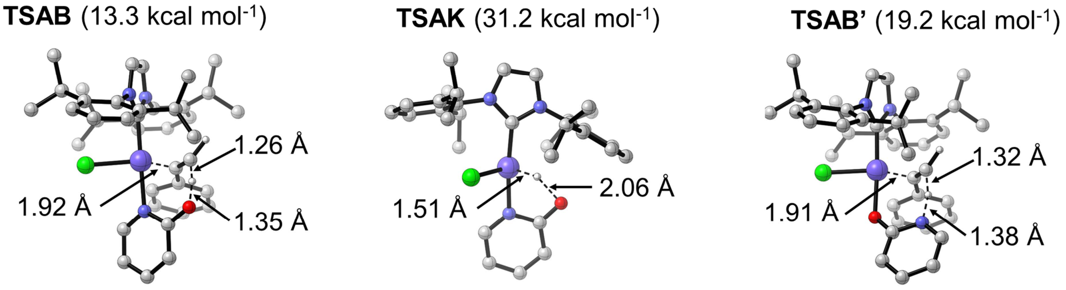

Figure 5.13. Representations of **TSAB**, **TSAK** and **TSAB'** with relevant distances.

Drawing further similarities between these two mechanisms, the *gem*-selectivity of the studied process is also defined by the preferential proton transfer towards the terminal carbon over the internal one, leading to a 11.0 kcal mol^{-1} energy difference between **TSAB** and **TSABt**. Nevertheless, alkyne dimerization continues with the reductive elimination involving the ligand that has donated the proton and the one receiving it (alkynyl and alkenyl respectively). In opposition to this, the direct alkenyl-pyridone C—O coupling for this system, as characterized by **TSRE** is significantly energetically disfavored at a relatively energy of 38.7 kcal mol^{-1}. Figure 5.14 displays the differences between **TSRE** and the C—O coupling process taking place in the operating mechanism (**TSDE**).

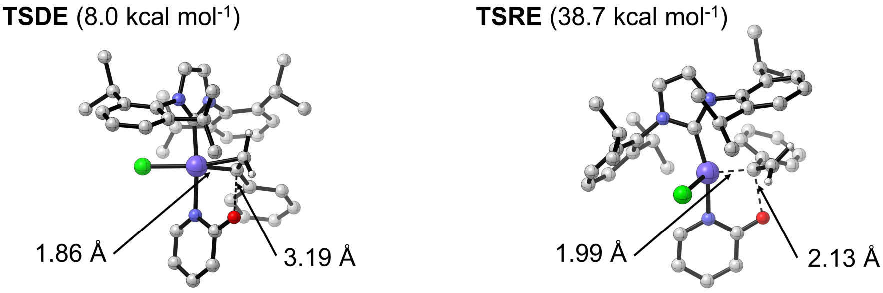

Figure 5.14. Representations of **TSDE** and **TSRE** with relevant distances.

Moreover, the chemoselectivity for this reaction is caused by the C—O coupling being favored over the C—N coupling. This can be correlated to the preferred coordination of the pyridinic N to the *trans* position of the IPr over that of the alkoxy O,[242] as well as the more stabilizing Rh—N bond compared to the Rh—O one, resulting in the 2.8 kcal mol^{-1} difference between **TSDE** and **TSDE'**.

For the catalytic cycle to be completed, the afforded alkenylated pyridone has to be decoordinated and new substrate molecules coordinated, regenerating the initial species, **A**. Since the product is coordinated through two distinct moieties to the Rh, and two different substrate molecules have to be coordinated to the metal, a wide variety of reaction pathways can lead to the release of the product and regeneration of **A**. Figure 5.15 presents the determined operating mechanism for this process.

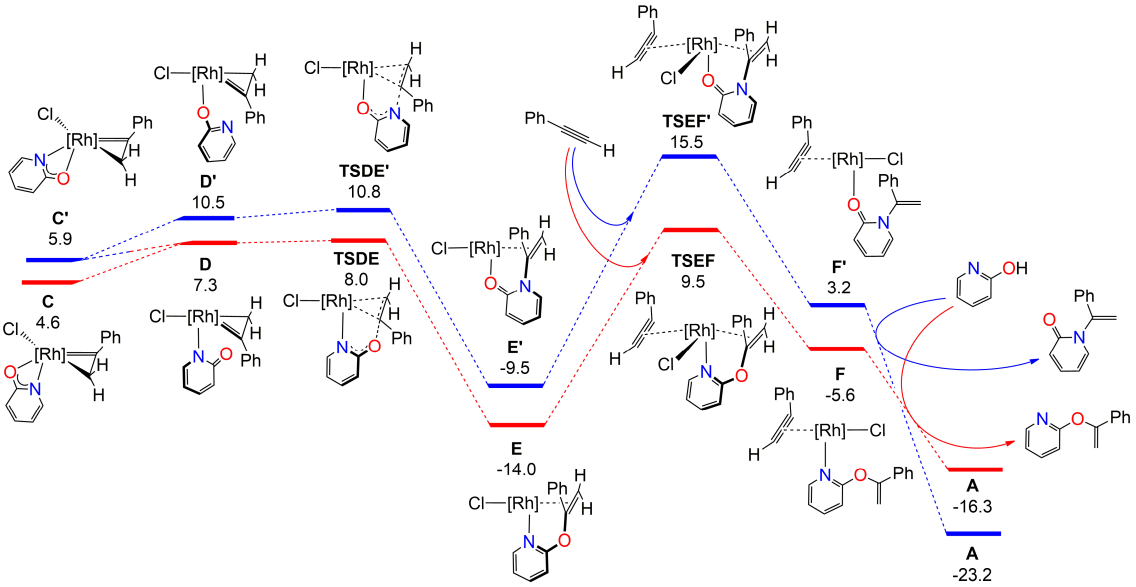

Figure 5.15. DFT calculated free energy profile (in kcal mol^{-1} relative to **A** and isolated molecules) for the release of the C—O and coupling product (red pathway) and the profile for the release of C—N and coupling product (blue pathway) via an associative pathway.

The mechanism presenting the lowest energy barrier for the release of the *O*-alkenylated pyridone goes through the concerted coordination of a phenylacetylene molecule and release of the product alkenyl ether as characterized by **TSEF** at a relative energy of 9.5 kcal mol^{-1}. This results in the formation of intermediate **F** (-5.6 kcal mol^{-1}) presenting the product exclusively bonded through its pyridinic N in the *trans* position to the IPr and the π-coordinated phenylacetylene in the *trans* position to the Cl. Subsequently, the product can be exchanged by a 2-hydroxypyridyne regenerating **A** and releasing the product.

Therefore, the reaction rate determining species for the formation of the *O*-alkenylated product are **E** and **TSEF**, yielding an energy span of 23.5 kcal mol^{-1}. This barrier aligns well with the fact that the catalysis requires moderate heating to occur. The formation of this product is exothermic by 16.3 kcal mol^{-1} whereas that of the *N*-alkenylated product is exothermic by 23.2 kcal mol^{-1}. Hence, the former is the kinetic product while the latter is the thermodynamic product. This conclusion was experimentally proven by heating the isolated *O*-alkenylated product with a catalytic amount of **preA** for 72h at 90°C, which resulted in the *N*-alkenylated product formation. It is essential to note that, this transformation does not occur in the absence of catalyst. However, it should also be noted that the *N*-alkenylated product formation through heating the catalytic crude for prolonged periods is not a viable strategy due to the decomposition of the active species.

Furthermore, other pathways for the product release starting with either the dissociation of the pyridone heteroatom or dissociation of the product alkenyl group were explored, with the former being the most favorable for the *N*-alkenylated product release. Figure 5.16 presents the energy profile this mechanism.

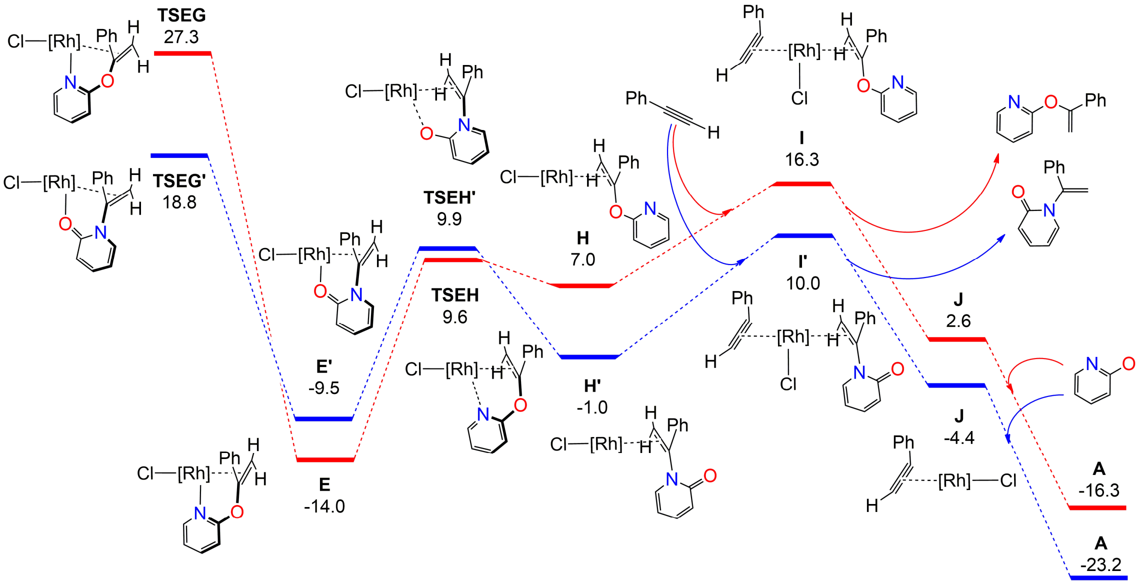

Figure 5.16. DFT calculated free energy profile (in kcal mol^{-1} relative to **A** and isolated molecules) for the release of the C—O and coupling product (red pathway) and the profile for the release of C—N and coupling product (blue pathway) via dissociative pathways.

The decoordination of the alkenyl group of **E** and **E'** is carried out via **TSEG** (27.3 kcal mol^{-1}) and **TSEG'** (18.8 kcal mol^{-1}) respectively. However, both these transition states are significantly more destabilized than those present in competing pathways for product release. Alternatively, the decoordination of the pyridone groups of **E** and **E'** are characterized by the transition states **TSEH** (9.6 kcal mol^{-1}) and **TSEH'** (9.9 kcal mol^{-1}), respectively. Nevertheless, the less stabilized species in these pathways are the intermediates formed after phenylacetylene coordination *trans* to the product alkenyl group, **I** (16.3 kcal mol^{-1}) and **I'** (10.0 kcal mol^{-1}). The former is significantly more stabilized than **TSEF'**, facilitating a more energetically favored pathway for the *N*-alkenylated product release.

Thus, whereas the associative pathway is the most favored for the *O*-alkenylated product release, the *N*-alkenylated product is released via this dissociative mechanism. While the former occurs through **TSEF** and the latter takes places through the slightly more destabilized **I'**. Nevertheless, the selectivity towards *O*-alkenylated product formation originates in the more destabilized transition state for the C—N coupling (**TSDE'** at 10.8 kcal mol^{-1}).

As the species with their pyridinic N coordinated to the Rh are remarkably more stable, the most energetically favored mechanism for **E’** formation goes through the previous formation of **E**. Thereafter it is possible, albeit kinetically and thermodynamically disfavored, for the C—O bond to be cleaved (**TSDE**), for the pyridonate coordination mode to change to a less energetically favored configuration that allows the pyridinic N attack (**C** to **D’**) and then for the C—N coupling to occur (**TSDE’**). Although pyridone hemilability allows **C**, **D**, **C’** and **D’** to be in quasi-equilibrium, and therefore for **E** to be transformed into **E’** by surmounting an effective energy barrier of 24.8 kcal mol^{-1}, this reaction is less favored than the *O*-alkenylated product release via the associative pathway.

Nevertheless, while this process is kinetically disfavored when compared to the direct *O*-alkenylated product formation, this behavior opens the possibility for the transformation of the *O*-alkenylated product into the *N*-alkenylated one. The *O*-alkenylated product formation can be reverted up to **E**, and from that point lead to the *N*-alkenylated product formation through the previously mentioned process. Hence, this isomerization presents and effective energy barrier of 27.1 kcal mol^{-1} defined by the energy liberated with the formation of the *O*-alkenylated product and **TSDE’**. This barrier aligns well with the reaction requiring heating of 90°C for days, as experimentally noted.

The reaction for other substrates was explored in order to further validate the mechanism. The reaction between 1-hexyne and 2-pyridone with both at 0.4M concentration, and 0.001M of the catalyst, reached 10% conversion of after 20h at 50°C. The reaction of phenylacetylene with 2-pyridone reached 96% conversion in that time under these same conditions. Conversely, the reaction of phenylacetylene with 6-chloro-2-pyridone achieved full conversion within two hours under these conditions. The mechanisms for these reactions were studied, with the rate-limiting species for the formation of the *O*-alkenylated product for these substrates depicted in Figure 5.17.

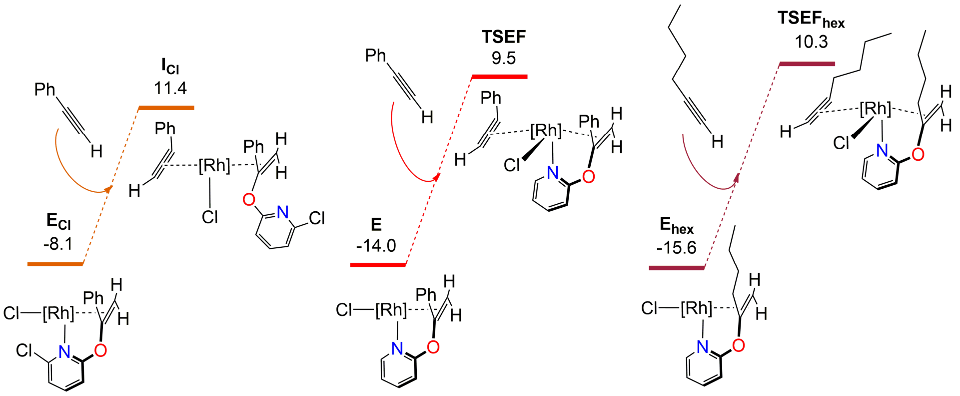

Figure 5.17. DFT calculated relative free energies (kcal mol^{-1}) to compare the rate-limiting species to yield the *O*-alkenylated product, for a selection of susbtrates.

Therefore, the reaction utilizing 6-chloro-2-pyridone presents an energy span of 19.5 kcal mol^{-1}, whereas the one employing 1-hexyne presents an energy span of 25.9 kcal mol^{-1}. These results match the trend observed for the catalytic rates with the former presenting a significantly higher reaction rate than the reaction between 2-pyridone and phenylacetylene, and the latter exhibiting a significantly lower one.

To recapitulate, the selective alkyne hydropyridonation catalyzed by the studied Rh-IPr complex presents many points of interest throughout its determined mechanism. The first transition state in the catalytic cycle corresponds to the selective proton donation of the pyridone to the π-coordinated alkyne terminal position (**TSAB**), which yields the *gem*-alkenyl. This selectivity is due to the terminal carbons of most terminal alkynes displaying a significantly more negative atomic charge than the internal carbon. The ethynyltrimethylsilane is known to be one of the few exceptions to this rule, exhibiting a more negative charge on its internal carbon than on the external one. Experiments with this alkyne selectively afforded the *trans*-product, proving the relevance of the proton transfer towards the selectivity of the process.

Following that, the alkenyl is isomerized into a metallacyclopropene (**TSBC**), facilitating the pyridonate nucleophilic attack. Although this transformation is generally highly energetically disfavored, effects such as the strong electron-donation and bulkiness of the IPr, can stabilize these species. Figure 5.18 compares the relative stability of these species and for the analogue complexes containing a PPh_3 instead of the IPr.

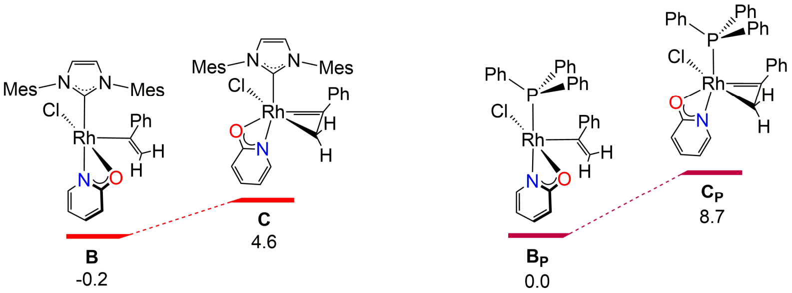

Figure 5.18. DFT calculated relative free energies (kcal mol^{-1}) to compare the effect of IPr and PPh_3 in the alkenyl-metallacyclopropene isomerization.

Similar to the IPr, the PPh_3 is a strong electron density donor. However, the configuration of the PPh_3 leads to its phenyl groups extending outward from the other ligands, whereas in the case of IPr, its bulky Mes groups are oriented inward. This difference generally results in greater interactions between the IPr and the ligands. These interactions can favor processes such as this isomerization, because the metallocycle and the *gem*-alkenyl interact differently with the IPr via steric hinderance and dispersion interactions.

Subsequently, the pyridonate ligand attacks the metallocycle carbenic carbon, leading to the formation of either the *O*-alkenylated or *N*-alkenylated product. The selectivity for this process is defined by the strong preference of the pyridinic N to be coordinated to the Rh, and in *trans*-position to the IPr. This favors the C—O coupling (**TSDE**) over the C—N coupling (**TSDE’**), which makes this process chemoselective.

Lastly, the product release can occur through diverse pathways. The associative pathway begins with the concerted association of a new alkyne molecule and release of the product alkenyl group (e.g., **TSEF**). The dissociative pathways begin with the decoordination of one of the product moieties, its alkenyl (e.g., **TSEG**) or its pyridone moiety (e.g., **TSEH**). For the reaction between phenylacetylene and 2-pyridone, the *O*-alkenylated product is released through the associative pathway, with this process (**E** to **TSEF**) defining the catalytic rate for the obtention of this product. The interplay between the great steric hindrance of IPr and its high *trans* effect might promote the product release. In opposition, the *N*-alkenylated product for these substrates is released via the dissociative pathway starting with the pyridone decoordination. This can be related with the less stabilizing coordination between the Rh and the carbonylic O in *trans* position to the IPr, when compared to the coordination of the pyridinic N to this position (see the difference between **C** and **C’**). This pathway is also favored for the release of the *O*-alkenylated product for phenylacetylene and 6-chloro-2-pyridone, likely due to steric effects experimented by the halogen in the pyridone.

Hence, the IPr ligand can influence the product release through both steric hindrance and electronic effects, such as the *trans* effect. This is especially relevant as the product release is the rate-limiting process for every studied system. Experimental tests indicated that the presence of an NHC was essential to the observed activity, as reactions with $RhCl(PPh_3)_3$ or $[Rh(\mu\text{-}Cl)(BINAP)]_2$ favored the alkyne dimerization over the alkyne hydropyridonation. Other catalytic tests were carried out substituting the 2-pyridone derivatives by similar compounds, namely phenol, N-methyl-2-aminopyridine, 2-thiopyridine, or 2-(hydroxymethyl)pyridine with none of them being productive. This indicated the requirement of both N and O atoms located at the 1,2-positions of the substrate for this reaction to be feasible.

Therefore, the mechanisms for the generation of the *O*-alkenylated and *N*-alkenylated products have been determined. Moreover, the factors that define the selectivity for these processes have been outlined. Lastly, these results have been validated using a diverse series of experimental tests and observations.

Chapter 6:
Conclusions

"You know how they say that youth is wasted on the young? Well, I say don't let the wisdom of age be wasted on you."

Ted Lasso

Conclusions

This Thesis is dedicated to the computational determination of catalytic reaction mechanisms. These results, as well as other insights specific to each system have been explored along the dissertation. Presented below are the summarized main findings derived for each system:

4.1 The activity of this catalytic system hinges on the Lewis acidity of the $B(C_6F_5)_3$. In this mechanism, the H—Si bond of the hydrosilanes is cleaved via a S_N2-type reaction in which this cocatalyst captures the leaving hydride and subsequently transfers it to the C atom of the substrate being reduced. The competition between the two determined mechanisms respectively leading to the formation of the silylformate and the bis(silyl)acetal rationalizes the dependence of the selectivity on the CO_2 pressure and temperature of the reaction.

4.2 The catalytic rate is enhanced by the additive NEt_3, which maintains a significant and constant concentration of the formate in the system as it is consumed in the rate-determining process. KIE experiments revealed that the microsolvation of this system was necessary to a correct representation of the reactivity.

4.3 The dehydrogenation is determined to be catalyzed by a cationic Rh^{III} complex generated through the oxidative addition of a FA molecule by the starting Rh^{I} complex. The catalytic reaction continues with the hydride abstraction from the afforded formate while the remaining hydride is not directly involved in the reaction at any point. The catalysis was evaluated for both the aforementioned complexes with the decomposition of the formate being the rate-limiting process for both of them, with that Rh^{III} complex presenting a lower effective energy barrier. This result also proves the beneficial role of the HCOONa additive towards the reactivity.

5.1 The dimerization is determined to occur through a Ligand Assisted Proton Shuttle (LAPS) reaction enabled by the hemilability of the 2-pyridonate. The selectivity of this process is determined by the favored protonation of the external carbons of terminal alkynes, making it highly selective for a vast range of substrates.

5.2 This reaction is facilitated by the 2-pyridone hemilability, with the operating mechanism involving the formation and subsequent attack of a metallacycle. However, the rate-limiting process consists of the release of the product which occurs through different mechanism depending on the formed product.

Conclusiones

Esta tesis está dedicada a la determinación computacional del mecanismo de reacciones catalíticas. Estos resultados, así como otros hallazgos específicos de cada sistema, han sido explorados en el desarrollo de esta Tesis Doctoral. A continuación, se presentan resumidos los principales resultados de cada sistema:

4.1 La actividad de este sistema catalítico depende de la acidez de Lewis del $B(C_6F_5)_3$. En el mecanismo determinado, el enlace H—Si de los hidrosilanos se rompe mediante una reacción de tipo S_N2, en la cual este cocatalizador captura el hidruro liberado y posteriormente lo transfiere al átomo de C del sustrato que está siendo reducido. La competición entre los dos mecanismos estudiados que conducen respectivamente a la formación del sililformiato y del bis(silil)acetal explica la dependencia de la selectividad en la presión de CO_2 y la temperatura de la reacción.

4.2 La velocidad de reacción incrementa debido al efecto del aditivo NEt_3, que mantiene una concentración significativa y constante del formiato en el sistema a medida que se consume en el proceso determinante de la velocidad. Los experimentos de KIE revelaron que la microsolvatación de este sistema era necesaria para una representación correcta de la reactividad.

4.3 Se determinó que la deshidrogenación está catalizada por un complejo catiónico de Rh^{III} generado mediante la adición oxidativa de una molécula de FA del complejo inicial de Rh^{I}. La reacción catalítica continúa con la abstracción de hidruro del formiato resultante, mientras que el hidruro restante no participa directamente en la reacción en ningún momento. La catálisis se evaluó para ambos complejos mencionados, con la descomposición del formiato siendo el proceso limitante para ambos, y el complejo Rh^{III} presentando una barrera de energía efectiva más baja. Este resultado también demuestra el papel beneficioso del aditivo HCOONa para la reacción

5.1 Se determinó que la dimerización ocurre a través de una reacción *Ligand Assisted Proton Shuttle* (LAPS) posibilitada por la hemilabilidad del 2-piridonato. La selectividad de este proceso está causada por la protonación preferencial de los carbonos externos de alquinos terminales, lo que lo hace altamente selectivo para una amplia gama de substratos.

5.2 Esta reacción se basa en la hemilabilidad de la 2-piridona, que permite la formación y el subsiguiente ataque de del metalaciclo que forma parte del mecanismo operativo. Sin embargo, el proceso limitante de la velocidad consiste en la liberación del producto, lo cual ocurre a través de un mecanismo diferente dependiendo del producto formado.

Bibliography

(1) Anastas, P. T.; Warner, J. C. *Green Chemistry: Theory and Practice*; Oxford University Press: Oxford, 1998.

(2) Warner, J. C.; Cannon, A. S.; Dye, K. M. Green Chemistry. *Environ Impact Assess Rev* **2004**, *24* (7–8), 775–799. https://doi.org/10.1016/j.eiar.2004.06.006.

(3) Anastas, P.; Nolasco, M.; Kerton, F.; Kirchhoff, M.; Licence, P.; Pradeep, T.; Subramaniam, B.; Moores, A. The Power of the United Nations Sustainable Development Goals in Sustainable Chemistry and Engineering Research. *ACS Sustain Chem Eng* **2021**, *9* (24), 8015–8017. https://doi.org/10.1021/acssuschemeng.1c03762.

(4) Anastas, P. T.; Kirchhoff, M. M.; Williamson, T. C. Catalysis as a Foundational Pillar of Green Chemistry. *Appl Catal A Gen* **2001**, *221*, 3–13.

(5) Bochmann, M. *Organometallics and Catalysis: An Introduction*; Oxford University Press: Oxford, 2014.

(6) Trost, B. M. The Atom Economy-A Search for Synthetic Efficiency. *Science (1979)* **1991**, *254*, 1471–1477.

(7) Arndtsen, B. A.; Bergman, R. G.; Mobley, T. A.; Peterson, T. H. Selective Intermolecular Carbon-Hydrogen Bond Activation by Synthetic Metal Complexes in Homogeneous Solution. *Acc. Chem. Res* **1995**, *28*, 154–162.

(8) Kang, X.; Qian, C.; Yang, H.; Shi, J.; Claverie, J.; Tang, W. Protecting-Group-Free Enantioselective Tandem Allylic Substitution of o-Phenylenediamines and o-Aminophenols. *Green Synthesis and Catalysis* **2022**, *3* (2), 185–189. https://doi.org/10.1016/j.gresc.2022.01.002.

(9) Calvo-Flores, F. G. Parámetros Para El Análisis de Las Reacciones En Química Sostenible. *Anales de Química* **2009**, *105*, 42–49.

(10) Houk, K. N.; Liu, F. Holy Grails for Computational Organic Chemistry and Biochemistry. *Acc Chem Res* **2017**, *50* (3), 539–543. https://doi.org/10.1021/acs.accounts.6b00532.

(11) Young, D. *Computational Chemistry: A Practical Guide for Applying Techniques to Real World Problems*; Wiley-Interscience: Hoboken, 2002.

(12) Lledós, A. Computational Organometallic Catalysis: Where We Are, Where We Are Going. *Eur J Inorg Chem* **2021**, *2021* (26), 2547–2555. https://doi.org/10.1002/ejic.202100330.

(13) Lan, Y. Elementary Reactions in Organometallic Chemistry; 2021; pp 51–123. https://doi.org/10.1002/9783527346028.ch3.

(14) Simm, G. N.; Vaucher, A. C.; Reiher, M. Exploration of Reaction Pathways and Chemical Transformation Networks. *Journal of Physical Chemistry A* **2019**, *123* (2), 385–399. https://doi.org/10.1021/acs.jpca.8b10007.

(15) Poli, R. The Elucidation of Mechanisms in Homogeneous Catalysis. *Comments on Inorganic Chemistry* **2009**, *30*, 177–228. https://doi.org/10.1080/02603590903423942ï.

(16) Kozuch, S.; Martin, J. M. L. "Turning over" Definitions in Catalytic Cycles. *ACS Catalysis*. December 7, 2012, pp 2787–2794. https://doi.org/10.1021/cs3005264.

(17) Ivančič, A.; Košmrlj, J.; Gazvoda, M. Elucidating the Reaction Mechanism of a Palladium-Palladium Dual Catalytic Process through Kinetic Studies of Proposed Elementary Steps. *Commun Chem* **2023**, *6* (1). https://doi.org/10.1038/s42004-023-00849-x.

(18) Sawatlon, B.; Wodrich, M. D.; Corminboeuf, C. Probing Substrate Scope with Molecular Volcanoes. *Org Lett* **2020**, *22* (20), 7936–7941. https://doi.org/10.1021/acs.orglett.0c02862.

(19) Lupp, D.; Christensen, N. J.; Fristrup, P. Synergy between Experimental and Theoretical Methods in the Exploration of Homogeneous Transition Metal Catalysis. *Dalton Transactions*. Royal Society of Chemistry August 7, 2014, pp 11093–11105. https://doi.org/10.1039/c4dt00342j.

(20) Gazvoda, M.; Virant, M.; Pinter, B.; Košmrlj, J. Mechanism of Copper-Free Sonogashira Reaction Operates through Palladium-Palladium Transmetallation. *Nat Commun* **2018**, *9* (1). https://doi.org/10.1038/s41467-018-07081-5.

(21) Weinhold, F.; Landis, C. R. Natural Bond Orbitals And Extensions Of Localized Bonding Concepts. *Chem. Educ. Res. Pract.* **2001**, *2*, 91–104. https://doi.org/10.1039/B1RP90011K.

(22) Bader, R. F. W. A Quantum Theory of Molecular Structure and Its Applications. *Chem Rev* **1991**, *91* (5), 893–928. https://doi.org/10.1021/cr00005a013.

(23) Munarriz, J.; Velez, E.; Casado, M. A.; Polo, V. Understanding the Reaction Mechanism of the Oxidative Addition of Ammonia by (PXP)Ir(i) Complexes: The Role of the X Group. *Physical Chemistry Chemical Physics* **2018**, *20* (2), 1105–1113. https://doi.org/10.1039/C7CP07453K.

(24) Santoro, S.; Kalek, M.; Huang, G.; Himo, F. Elucidation of Mechanisms and Selectivities of Metal-Catalyzed Reactions Using Quantum Chemical Methodology. *Acc Chem Res* **2016**, *49* (5), 1006–1018. https://doi.org/10.1021/acs.accounts.6b00050.

(25) Ahn, S.; Hong, M.; Sundararajan, M.; Ess, D. H.; Baik, M. H. Design and Optimization of Catalysts Based on Mechanistic Insights Derived from Quantum Chemical Reaction Modeling. *Chemical Reviews*. American Chemical Society June 12, 2019, pp 6509–6560. https://doi.org/10.1021/acs.chemrev.9b00073.

(26) Simm, G. N.; Vaucher, A. C.; Reiher, M. Exploration of Reaction Pathways and Chemical Transformation Networks. *Journal of Physical Chemistry A* **2019**, *123* (2), 385–399. https://doi.org/10.1021/acs.jpca.8b10007.

(27) Baxter, R. D.; Sale, D.; Engle, K. M.; Yu, J. Q.; Blackmond, D. G. Mechanistic Rationalization of Unusual Kinetics in Pd-Catalyzed C-H Olefination. *J Am Chem Soc* **2012**, *134* (10), 4600–4606. https://doi.org/10.1021/ja207634t.

(28) Sperger, T.; Sanhueza, I. A.; Schoenebeck, F. Computation and Experiment: A Powerful Combination to Understand and Predict Reactivities. *Acc Chem Res* **2016**, *49* (6), 1311–1319. https://doi.org/10.1021/acs.accounts.6b00068.

(29) Ziegler, T. Approximate Density Functional Theory as a Practical Tool in Molecular Energetics and Dynamics. *Chem. Rev* **1991**, *91*, 651–667.

(30) Cramer, C. J.; Truhlar, D. G. Density Functional Theory for Transition Metals and Transition Metal Chemistry. *Physical Chemistry Chemical Physics* **2009**, *11* (46), 10757–10816. https://doi.org/10.1039/b907148b.

(31) Tsipis, A. C. DFT Flavor of Coordination Chemistry. *Coord Chem Rev* **2014**, *272*, 1–29. https://doi.org/10.1016/j.ccr.2014.02.023.

(32) Bursch, M.; Mewes, J.-M.; Hansen, A.; Grimme, S. Best-Practice DFT Protocols for Basic Molecular Computational Chemistry**. *Angew. Chem. Int. Ed.* **2022**, *61* (42), e202205735. https://doi.org/10.26434/chemrxiv-2022-n304h.

(33) Lin, Z. Interplay between Theory and Experiment: Computational Organometallic and Transition Metal Chemistry. *Acc Chem Res* **2010**, *43* (5), 602–611. https://doi.org/10.1021/ar9002027.

(34) Jones, R. O. Density Functional Theory: Its Origins, Rise to Prominence, and Future. *Rev Mod Phys* **2015**, *87* (3). https://doi.org/10.1103/RevModPhys.87.897.

(35) Hartree, D. R.; Hartree, W. Self-Consistent Field, with Exchange, for Beryllium. *Proc R Soc Lond A Math Phys Sci* **1935**, *150* (869), 9–33. https://doi.org/10.1098/rspa.1935.0085.

(36) Møller, C.; Plesset, M. S. Note on an Approximation Treatment for Many-Electron Systems. *Phys. Rev.* **1934**, *46* (7), 618–622.

(37) Head-Gordon, M.; Pople, J. A.; Frisch, M. J. MP2 Energy Evaluation by Direct Methods. *Chem Phys Lett* **1988**, *153* (6), 503–506.

(38) Krishnan, R.; Pople, J. A. *Approximate Fourth-Order Perturbation Theory of the Electron Correlation Energy*; 1978; Vol. XIV.

(39) Jiȓ, I.; Ĉíẑ, E. K. On the Correlation Problem in Atomic and Molecular Systems. Calculation of Wavefunction Components in Ursell-Type Expansion Using Quantum-Field Theoretical Methods. *J Chem Phys* **1966**, *45* (11), 4256–4266. https://doi.org/10.1063/1.1727484.

(40) Scuseria, G. E.; Janssen, C. L.; Schaefer, H. F. An Efficient Reformulation of the Closed-Shell Coupled Cluster Single and Double Excitation (CCSD) Equations. *J Chem Phys* **1988**, *89* (12), 7382–7387. https://doi.org/10.1063/1.455269.

(41) Raghavachari, K.; Trucks, G. W.; Pople, J. A.; Head-Gordon, M. A Fifth-Order Perturbation Comparison of Electron Correlation Theories. *Chem Phys Lett* **1989**, *157* (6), 479–483.

(42) Burke, K. Perspective on Density Functional Theory. *Journal of Chemical Physics* **2012**, *136* (15). https://doi.org/10.1063/1.4704546.

(43) Becke, A. D. Perspective: Fifty Years of Density-Functional Theory in Chemical Physics. *Journal of Chemical Physics* **2014**, *140* (18). https://doi.org/10.1063/1.4869598.

(44) Hohenberg, P.; Kohn, W. Inhomogeneous Electron Gas. *Phys. Rev.* **1964**, *136*, B864–B871.

(45) Kohn, W.; Sham, L. J. Self-Consistent Equations Including Exchange and Correlation Effects*. *Phys. Rev.* **1965**, *140*, A1133–A1137.

(46) Peverati, R.; Truhlar, D. G. Quest for a Universal Density Functional: The Accuracy of Density Functionals across a Broad Spectrum of Databases in Chemistry and Physics. *Philosophical Transactions of the Royal Society A: Mathematical, Physical and Engineering Sciences* **2014**, *372* (2011). https://doi.org/10.1098/rsta.2012.0476.

(47) Lehtola, S.; Steigemann, C.; Oliveira, M. J. T.; Marques, M. A. L. Recent Developments in LIBXC — A Comprehensive Library of Functionals for Density Functional Theory. *SoftwareX* **2018**, *7*, 1–5. https://doi.org/10.1016/j.softx.2017.11.002.

(48) Perdew, J. P. Jacob's Ladder of Density Functional Approximations for the Exchange-Correlation Energy. *AIP Conf Proc* **2001**, *577*, 1–20. https://doi.org/10.1063/1.1390175.

(49) Sperger, T.; Sanhueza, I. A.; Kalvet, I.; Schoenebeck, F. Computational Studies of Synthetically Relevant Homogeneous Organometallic Catalysis Involving Ni, Pd, Ir, and Rh: An Overview of Commonly Employed DFT Methods and Mechanistic Insights. *Chem Rev* **2015**, *115* (17), 9532–9586. https://doi.org/10.1021/acs.chemrev.5b00163.

(50) Dirac, P. A. M. Note on Exchange Phenomena in the Thomas Atom. *Mathematical Proceedings of the Cambridge Philosophical Society* **1930**, *26* (3), 376–385. https://doi.org/10.1017/S0305004100016108.

(51) Goerigk, Lars.; Grimme, Stefan. Double-hybrid Density Functionals. *WIREs Comput Mol Sci* **2014**, *4*, 576–600.

(52) Cohen, A. J.; Mori-Sánchez, P.; Yang, W. Challenges for Density Functional Theory. *Chem Rev* **2012**, *112* (1), 289–320. https://doi.org/10.1021/cr200107z.

(53) Rappoport, D.; Crawford, N. R. M.; Furche, F.; Burke, K. Which Functional Should I Choose? In *Encyclopedia of Inorganic Chemistry*; 2009.

(54) Perdew, J. P.; Burke, K.; Ernzerhof, M. Generalized Gradient Approximation Made Simple. *Phys Rev Lett* **1997**, *77* (18), 3865–3868.

(55) Perdew, J. P.; Burke, K.; Ernzerhof, M. ERRATA Generalized Gradient Approximation Made Simple [Phys. Rev. Lett. 77, 3865 (1996)]. *Phys Rev Lett* **1997**, *78* (7), 1396.

(56) Grimme, S.; Ehrlich, S.; Goerigk, L. Effect of the Damping Function in Dispersion Corrected Density Functional Theory. *J Comput Chem* **2011**, *32* (7), 1456–1465. https://doi.org/10.1002/jcc.21759.

(57) Tao, J.; Perdew, J. P.; Staroverov, V. N.; Scuseria, G. E. Climbing the Density Functional Ladder: Nonempirical Meta–Generalized Gradient Approximation Designed for Molecules

and Solids. *Phys Rev Lett* **2003**, *91* (14), 146401. https://doi.org/10.1103/PhysRevLett.91.146401.

(58) Zhao, Y.; Truhlar, D. G. A New Local Density Functional for Main-Group Thermochemistry, Transition Metal Bonding, Thermochemical Kinetics, and Noncovalent Interactions. *Journal of Chemical Physics* **2006**, *125* (19). https://doi.org/10.1063/1.2370993.

(59) Becke, A. D. A New Mixing of Hartree-Fock and Local Density-Functional Theories. *J Chem Phys* **1993**, *98* (2), 1372–1377. https://doi.org/10.1063/1.464304.

(60) Adamo, C.; Barone, V. Toward Reliable Density Functional Methods without Adjustable Parameters: The PBE0 Model. *Journal of Chemical Physics* **1999**, *110* (13), 6158–6170. https://doi.org/10.1063/1.478522.

(61) Perdew, J. P.; Ruzsinszky, A.; Tao, J.; Staroverov, V. N.; Scuseria, G. E.; Csonka, G. I. Prescription for the Design and Selection of Density Functional Approximations: More Constraint Satisfaction with Fewer Fits. *Journal of Chemical Physics* **2005**, *123* (6). https://doi.org/10.1063/1.1904565.

(62) Zhao, Y.; Truhlar, D. G. The M06 Suite of Density Functionals for Main Group Thermochemistry, Thermochemical Kinetics, Noncovalent Interactions, Excited States, and Transition Elements: Two New Functionals and Systematic Testing of Four M06-Class Functionals and 12 Other Functionals. *Theor Chem Acc* **2008**, *120* (1–3), 215–241. https://doi.org/10.1007/s00214-007-0310-x.

(63) Tao, J.; Perdew, J. P.; Staroverov, V. N.; Scuseria, G. E. Climbing the Density Functional Ladder: Nonempirical Meta–Generalized Gradient Approximation Designed for Molecules and Solids. *Phys Rev Lett* **2003**, *91* (14). https://doi.org/10.1103/PhysRevLett.91.146401.

(64) Staroverov, V. N.; Scuseria, G. E.; Tao, J.; Perdew, J. P. Comparative Assessment of a New Nonempirical Density Functional: Molecules and Hydrogen-Bonded Complexes. *Journal of Chemical Physics* **2003**, *119* (23), 12129–12137. https://doi.org/10.1063/1.1626543.

(65) Staroverov, V. N.; Scuseria, G. E.; Tao, J.; Perdew, J. P. Erratum: Comparative Assessment of a New Nonempirical Density Functional: Molecules and Hydrogen-Bonded Complexes(Journal of Chemical Physics (2003) 119 (12129)). *Journal of Chemical Physics* **2004**, *121* (22), 11507. https://doi.org/10.1063/1.1795692.

(66) Yanai, T.; Tew, D. P.; Handy, N. C. A New Hybrid Exchange-Correlation Functional Using the Coulomb-Attenuating Method (CAM-B3LYP). *Chem Phys Lett* **2004**, *393* (1–3), 51–57. https://doi.org/10.1016/j.cplett.2004.06.011.

(67) Baer, R.; Livshits, E.; Salzner, U. Tuned Range-Separated Hybrids in Density Functional Theory. *Annu Rev Phys Chem* **2010**, *61*, 85–109. https://doi.org/10.1146/annurev.physchem.012809.103321.

(68) Rohrdanz, M. A.; Martins, K. M.; Herbert, J. M. A Long-Range-Corrected Density Functional That Performs Well for Both Ground-State Properties and Time-Dependent Density

Functional Theory Excitation Energies, Including Charge-Transfer Excited States. *Journal of Chemical Physics* **2009**, *130* (5). https://doi.org/10.1063/1.3073302.

(69) Mester, D.; Kállay, M. Charge-Transfer Excitations within Density Functional Theory: How Accurate Are the Most Recommended Approaches? *J Chem Theory Comput* **2022**, *18* (3), 1646–1662. https://doi.org/10.1021/acs.jctc.1c01307.

(70) Zhang, I. Y.; Su, N. Q.; Brémond, É. A. G.; Adamo, C.; Xu, X. Doubly Hybrid Density Functional XDH-PBE0 from a Parameter-Free Global Hybrid Model PBE0. *Journal of Chemical Physics* **2012**, *136* (17). https://doi.org/10.1063/1.3703893.

(71) Grimme, S. Semiempirical Hybrid Density Functional with Perturbative Second-Order Correlation. *Journal of Chemical Physics* **2006**, *124* (3). https://doi.org/10.1063/1.2148954.

(72) Goerigk, L.; Grimme, S. A Thorough Benchmark of Density Functional Methods for General Main Group Thermochemistry, Kinetics, and Noncovalent Interactions. *Physical Chemistry Chemical Physics* **2011**, *13* (14), 6670–6688. https://doi.org/10.1039/c0cp02984j.

(73) Goerigk, L.; Grimme, S. Double-Hybrid Density Functionals. *Wiley Interdiscip Rev Comput Mol Sci* **2014**, *4* (6), 576–600. https://doi.org/10.1002/wcms.1193.

(74) Korth, M. Dichtefunktionaltheorie: Noch Nicht Ganz Die Richtige Antwort Aus Den Richtigen Gründen. *Angewandte Chemie* **2017**, *129* (20), 5482–5484. https://doi.org/10.1002/ange.201701894.

(75) Morgante, P.; Peverati, R. The Devil in the Details: A Tutorial Review on Some Undervalued Aspects of Density Functional Theory Calculations. *Int J Quantum Chem* **2020**, *120* (18), e26332. https://doi.org/10.1002/qua.26332.

(76) Plata, R. E.; Singleton, D. A. A Case Study of the Mechanism of Alcohol-Mediated Morita Baylis-Hillman Reactions. the Importance of Experimental Observations. *J Am Chem Soc* **2015**, *137* (11), 3811–3826. https://doi.org/10.1021/ja5111392.

(77) Wagner, J. P.; Schreiner, P. R. London’sche Dispersionswechselwirkungen in Der Molekülchemie - Eine Neubetrachtung Sterischer Effekte. *Angewandte Chemie* **2015**, *127* (42), 12446–12471. https://doi.org/10.1002/ange.201503476.

(78) Bursch, M.; Caldeweyher, E.; Hansen, A.; Neugebauer, H.; Ehlert, S.; Grimme, S. Understanding and Quantifying London Dispersion Effects in Organometallic Complexes. *Acc Chem Res* **2019**, *52* (1), 258–266. https://doi.org/10.1021/acs.accounts.8b00505.

(79) Rodriguez-Reyes, J. C. F.; Siler, C. G. F.; Liu, W.; Tkatchenko, A.; Friend, C. M.; Madix, R. J. Van Der Waals Interactions Determine Selectivity in Catalysis by Metallic Gold. *J Am Chem Soc* **2014**, *136* (38), 13333–13340. https://doi.org/10.1021/ja506447y.

(80) Grimme, S.; Hansen, A.; Brandenburg, J. G.; Bannwarth, C. Dispersion-Corrected Mean-Field Electronic Structure Methods. *Chem Rev* **2016**, *116* (9), 5105–5154. https://doi.org/10.1021/acs.chemrev.5b00533.

(81) Grimme, S. Accurate Description of van Der Waals Complexes by Density Functional Theory Including Empirical Corrections. *J Comput Chem* **2004**, *25* (12), 1463–1473. https://doi.org/10.1002/jcc.20078.

(82) Kümmel, S.; Kronik, L. Orbital-Dependent Density Functionals: Theory and Applications. *Rev Mod Phys* **2008**, *80* (1), 3–60. https://doi.org/10.1103/RevModPhys.80.3.

(83) Langreth, D. C.; Lundqvist, B. I.; Chakarova-Käck, S. D.; Cooper, V. R.; Dion, M.; Hyldgaard, P.; Kelkkanen, A.; Kleis, J.; Kong, L.; Li, S.; Moses, P. G.; Murray, E.; Puzder, A.; Rydberg, H.; Schröder, E.; Thonhauser, T. A Density Functional for Sparse Matter. *Journal of Physics Condensed Matter* **2009**, *21* (8). https://doi.org/10.1088/0953-8984/21/8/084203.

(84) Berland, K.; Cooper, V. R.; Lee, K.; Schröder, E.; Thonhauser, T.; Hyldgaard, P.; Lundqvist, B. I. Van Der Waals Forces in Density Functional Theory: A Review of the VdW-DF Method. *Reports on Progress in Physics* **2015**, *78* (6). https://doi.org/10.1088/0034-4885/78/6/066501.

(85) Grimme, S.; Huenerbein, R.; Ehrlich, S. On the Importance of the Dispersion Energy for the Thermodynamic Stability of Molecules. *ChemPhysChem* **2011**, *12* (7), 1258–1261. https://doi.org/10.1002/cphc.201100127.

(86) Grimme, S. Semiempirical GGA-Type Density Functional Constructed with a Long-Range Dispersion Correction. *J Comput Chem* **2006**, *27* (15), 1787–1799. https://doi.org/10.1002/jcc.20495.

(87) Wu, Q.; Yang, W. Empirical Correction to Density Functional Theory for van Der Waals Interactions. *Journal of Chemical Physics* **2002**, *116* (2), 515–524. https://doi.org/10.1063/1.1424928.

(88) Goerigk, L. A Comprehensive Overview of the DFT-D3 London-Dispersion Correction. In *Non-Covalent Interactions in Quantum Chemistry and Physics: Theory and Applications*; Elsevier Inc., 2017; pp 195–219. https://doi.org/10.1016/B978-0-12-809835-6.00007-4.

(89) Grimme, S.; Antony, J.; Ehrlich, S.; Krieg, H. A Consistent and Accurate Ab Initio Parametrization of Density Functional Dispersion Correction (DFT-D) for the 94 Elements H-Pu. *Journal of Chemical Physics* **2010**, *132* (15). https://doi.org/10.1063/1.3382344.

(90) Johnson, E. R.; Becke, A. D. A Post-Hartree-Fock Model of Intermolecular Interactions. *Journal of Chemical Physics* **2005**, *123* (2). https://doi.org/10.1063/1.1949201.

(91) Van Voorhis, T.; Scuseria, G. E. A Novel Form for the Exchange-Correlation Energy Functional. *Journal of Chemical Physics* **1998**, *109* (2), 400–410. https://doi.org/10.1063/1.476577.

(92) Goerigk, L. Treating London-Dispersion Effects with the Latest Minnesota Density Functionals: Problems and Possible Solutions. *J. Phys. Chem. Lett.* **2015**, *6* (19), 3891–3896.

(93) Nagy, B.; Jensen, F. *Basis Sets in Quantum Chemistry*; 2017; Vol. 30.

(94) Check, C. E.; Faust, T. O.; Bailey, J. M.; Wright, B. J.; Gilbert, T. M.; Sunderlin, L. S. Addition of Polarization and Diffuse Functions to the LANL2DZ Basis Set for P-Block Elements. *Journal of Physical Chemistry A* **2001**, *105* (34), 8111–8116. https://doi.org/10.1021/jp011945l.

(95) Krauss, M.; Stevens, W. J. Effective Potentials in Molecular Quantum Chemistry. *Ann. Rev. Phys. Chern* **1984**, *35*, 357–385.

(96) Weigend, F.; Ahlrichs, R. Balanced Basis Sets of Split Valence, Triple Zeta Valence and Quadruple Zeta Valence Quality for H to Rn: Design and Assessment of Accuracy. *Physical Chemistry Chemical Physics* **2005**, *7* (18), 3297–3305. https://doi.org/10.1039/b508541a.

(97) Otero-De-La-Roza, A.; DiLabio, G. A. Transferable Atom-Centered Potentials for the Correction of Basis Set Incompleteness Errors in Density-Functional Theory. *J Chem Theory Comput* **2017**, *13* (8), 3505–3524. https://doi.org/10.1021/acs.jctc.7b00300.

(98) Witte, J.; Neaton, J. B.; Head-Gordon, M. Push It to the Limit: Characterizing the Convergence of Common Sequences of Basis Sets for Intermolecular Interactions as Described by Density Functional Theory. *Journal of Chemical Physics* **2016**, *144* (19). https://doi.org/10.1063/1.4949536.

(99) Balabin, R. M. Enthalpy Difference between Conformations of Normal Alkanes: Intramolecular Basis Set Superposition Error (BSSE) in the Case of n-Butane and n-Hexane. *Journal of Chemical Physics* **2008**, *129* (16). https://doi.org/10.1063/1.2997349.

(100) Van Duijneveldt, F. B.; Van Duijneveldt-Van De Rijdt, J. G. C. M.; Van Lenthe, J. H. State of the Art in Counterpoise Theory. *Chem. Rev.* **1994**, *94*, 1873–1885.

(101) Mardirossian, N.; Head-Gordon, M. How Accurate Are the Minnesota Density Functionals for Noncovalent Interactions, Isomerization Energies, Thermochemistry, and Barrier Heights Involving Molecules Composed of Main-Group Elements? *J Chem Theory Comput* **2016**, *12* (9), 4303–4325. https://doi.org/10.1021/acs.jctc.6b00637.

(102) Ochterski, J. W. *Thermochemistry in Gaussian*; 2000.

(103) Grimme, S. Supramolecular Binding Thermodynamics by Dispersion-Corrected Density Functional Theory. *Chemistry - A European Journal* **2012**, *18* (32), 9955–9964. https://doi.org/10.1002/chem.201200497.

(104) Ribeiro, R. F.; Marenich, A. V.; Cramer, C. J.; Truhlar, D. G. Use of Solution-Phase Vibrational Frequencies in Continuum Models for the Free Energy of Solvation. *Journal of Physical Chemistry B* **2011**, *115* (49), 14556–14562. https://doi.org/10.1021/jp205508z.

(105) Harvey, J. N.; Himo, F.; Maseras, F.; Perrin, L. Scope and Challenge of Computational Methods for Studying Mechanism and Reactivity in Homogeneous Catalysis. *ACS Catal* **2019**, *9* (8), 6803–6813. https://doi.org/10.1021/acscatal.9b01537.

(106) Amzel, L. M. *Loss of Translational Entropy in Binding, Folding, and Catalysis*; Wiley-Liss, Inc, 1997; Vol. 28.

(107) Huang, F.; Lu, G.; Zhao, L.; Li, H.; Wang, Z. X. The Catalytic Role of N-Heterocyclic Carbene in a Metal-Free Conversion of Carbon Dioxide into Methanol: A Computational Mechanism Study. *J Am Chem Soc* **2010**, *132* (35), 12388–12396. https://doi.org/10.1021/ja103531z.

(108) Besora, M.; Vidossich, P.; Lledós, A.; Ujaque, G.; Maseras, F. Calculation of Reaction Free Energies in Solution: A Comparison of Current Approaches. *Journal of Physical Chemistry A* **2018**, *122* (5), 1392–1399. https://doi.org/10.1021/acs.jpca.7b11580.

(109) Hopmann, K. H. How Accurate Is DFT for Iridium-Mediated Chemistry? *Organometallics* **2016**, *35* (22), 3795–3807. https://doi.org/10.1021/acs.organomet.6b00377.

(110) Courtemanche, M. A.; Légaré, M. A.; Maron, L.; Fontaine, F. G. Reducing CO2 to Methanol Using Frustrated Lewis Pairs: On the Mechanism of Phosphine-Borane-Mediated Hydroboration of CO2. *J Am Chem Soc* **2014**, *136* (30), 10708–10717. https://doi.org/10.1021/ja5047846.

(111) Tanaka, R.; Yamashita, M.; Chung, L. W.; Morokuma, K.; Nozaki, K. Mechanistic Studies on the Reversible Hydrogenation of Carbon Dioxide Catalyzed by an Ir-PNP Complex. *Organometallics* **2011**, *30* (24), 6742–6750. https://doi.org/10.1021/om2010172.

(112) Plata, R. E.; Singleton, D. A. A Case Study of the Mechanism of Alcohol-Mediated Morita Baylis-Hillman Reactions. the Importance of Experimental Observations. *J Am Chem Soc* **2015**, *137* (11), 3811–3826. https://doi.org/10.1021/ja5111392.

(113) Dyson, P. J.; Jessop, P. G. Solvent Effects in Catalysis: Rational Improvements of Catalysts: Via Manipulation of Solvent Interactions. *Catal Sci Technol* **2016**, *6* (10), 3302–3316. https://doi.org/10.1039/c5cy02197a.

(114) Cramer, C. J.; Truhlar, D. G. Implicit Solvation Models: Equilibria, Structure, Spectra, and Dynamics. *Chem Rev* **1999**, *99* (8), 2161–2200. https://doi.org/10.1021/cr960149m.

(115) Ryu, H.; Park, J.; Kim, H. K.; Park, J. Y.; Kim, S. T.; Baik, M. H. Pitfalls in Computational Modeling of Chemical Reactions and How to Avoid Them. *Organometallics* **2018**, *37* (19), 3228–3239. https://doi.org/10.1021/acs.organomet.8b00456.

(116) Houk, K. N.; Liu, F. Holy Grails for Computational Organic Chemistry and Biochemistry. *Acc Chem Res* **2017**, *50* (3), 539–543. https://doi.org/10.1021/acs.accounts.6b00532.

(117) Tomasi, J.; Mennucci, B.; Cammi, R. Quantum Mechanical Continuum Solvation Models. *Chem Rev* **2005**, *105* (8), 2999–3093. https://doi.org/10.1021/cr9904009.

(118) Mennucci, B.; Cammi, R.; Tomasi, J. Excited States and Solvatochromic Shifts within a Nonequilibrium Solvation Approach: A New Formulation of the Integral Equation Formalism Method at the Self-Consistent Field, Configuration Interaction, and Multiconfiguration Self-Consistent Field Level. *Journal of Chemical Physics* **1998**, *109* (7), 2798–2807. https://doi.org/10.1063/1.476878.

(119) Marenich, A. V.; Cramer, C. J.; Truhlar, D. G. Universal Solvation Model Based on Solute Electron Density and on a Continuum Model of the Solvent Defined by the Bulk Dielectric

Constant and Atomic Surface Tensions. *Journal of Physical Chemistry B* **2009**, *113* (18), 6378–6396. https://doi.org/10.1021/jp810292n.

(120) Stein, C. J.; Herbert, J. M.; Head-Gordon, M. The Poisson-Boltzmann Model for Implicit Solvation of Electrolyte Solutions: Quantum Chemical Implementation and Assessment via Sechenov Coefficients. *Journal of Chemical Physics* **2019**, *151* (22). https://doi.org/10.1063/1.5131020.

(121) Scalmani, G.; Frisch, M. J. Continuous Surface Charge Polarizable Continuum Models of Solvation. I. General Formalism. *Journal of Chemical Physics* **2010**, *132* (11). https://doi.org/10.1063/1.3359469.

(122) Cancès, E.; Mennucci, B.; Tomasi, J. A New Integral Equation Formalism for the Polarizable Continuum Model: Theoretical Background and Applications to Isotropic and Anisotropic Dielectrics. *Journal of Chemical Physics* **1997**, *107* (8), 3032–3041. https://doi.org/10.1063/1.474659.

(123) Bondi, A. Van Der Waals Volumes and Radii. *J Phys Chem* **1964**, *68* (3), 441–451. https://doi.org/10.1021/j100785a001.

(124) Ishikawa, S.; Hada, S.; Funasaki, N. Novel Method for Molecular Surface Area Calculation and Its Application for the Micelle Formation of Lecithins. *J. Phys. Chem* **1995**, *99*, 11508–11514.

(125) Hawkins, G. D.; Cramer, C. J.; Truhlar, D. G. Pairwise Solute Descreening of Solute Charges from a Dielectric Medium. *Chem Phys Lett* **1995**, *246*, 122–129.

(126) Mennucci, B. Polarizable Continuum Model. *Wiley Interdiscip Rev Comput Mol Sci* **2012**, *2* (3), 386–404. https://doi.org/10.1002/wcms.1086.

(127) Funes-Ardoiz, I.; Blanco-Lomas, M.; Campos, P. J.; Sampedro, D. Benzylidene-Oxazolones as Photoswitches: Photochemistry and Theoretical Calculations. *Tetrahedron* **2013**, *69* (46), 9766–9771. https://doi.org/10.1016/j.tet.2013.09.009.

(128) Sure, R.; el Mahdali, M.; Plajer, A.; Deglmann, P. Towards a Converged Strategy for Including Microsolvation in Reaction Mechanism Calculations. *J Comput Aided Mol Des* **2021**, *35* (4), 473–492. https://doi.org/10.1007/s10822-020-00366-2.

(129) Truhlar, D. G.; Klippenstein, S. J. Current Status of Transition-State Theory. *Journal of Physical Chemistry* **1996**, *100*, 12771–12800.

(130) Ferro-Costas, D.; Truhlar, D. G.; Fernández-Ramos, A. Pilgrim: A Thermal Rate Constant Calculator and a Chemical Kinetics Simulator. *Comput Phys Commun* **2020**, *256*. https://doi.org/10.1016/j.cpc.2020.107457.

(131) Bryantsev, V. S.; Diallo, M. S.; Goddard, W. A. Calculation of Solvation Free Energies of Charged Solutes Using Mixed Cluster/Continuum Models. *Journal of Physical Chemistry B* **2008**, *112* (32), 9709–9719. https://doi.org/10.1021/jp802665d.

(132) Gómez-Gallego, M.; Sierra, M. A. Kinetic Isotope Effects in the Study of Organometallic Reaction Mechanisms. *Chem Rev* **2011**, *111* (8), 4857–4963. https://doi.org/10.1021/cr100436k.

(133) Weinhold, F. Chemical Bonding as a Superposition Phenomenon. *J. Chem. Educ.* **1999**, *76* (8), 1141–1145.

(134) Reed, A. E.; Weinstock, R. B.; Weinhold, F. Natural Population Analysis. *J Chem Phys* **1985**, *83* (2), 735–746. https://doi.org/10.1063/1.449486.

(135) Mulliken, R. S. Electronic Population Analysis on LCAO-MO Molecular Wave Functions. I. *J Chem Phys* **1955**, *23* (10), 1833–1840. https://doi.org/10.1063/1.1740588.

(136) Frisch, M. J.; Trucks, G.; Schlegel, H. B.; Scuseria, G. E.; Robb, M. A.; Cheeseman, J.; Scalmani, G.; Barone, V.; Mennucci, B.; Petersson, G. A.; Nakatsuji, H.; Caricato, M.; Li, X.; Hratchian, H. P.; Izmaylov, A. F.; Bloino, J.; Zheng, G.; Sonnenberg, J.; Hada, M.; Ehara, M.; Toyota, K.; Fukuda, R.; Hasegawa, J.; Ishida, M.; Nakajima, T.; Honda, Y.; Kitao, O.; Nakai, H.; Vreven, J. A.; Montgomery, J. E.; Peralta, J. E.; Ogliaro, F.; Bearpark, M.; Heyd, J. J.; Brothers, E.; Kudin, K. N.; Staroverov, V. N.; Keith, T.; Kobayashi, R.; Normand, J.; Raghavachari, K.; Rendell, A.; Burant, J. C.; Iyengar, S. S.; Tomasi, J.; Cossi, M.; Rega, N.; Milliam, J. M.; Klene, M.; Knox, J. E.; Cross, J. B.; Bakken, V.; Adamo, C.; Jaramillo, J.; Gomperts, R.; Stratmann, R. E.; Yazyev, O.; Austin, A. J.; Cammi, R.; Pomelli, C.; Ochterski, J. W.; Martin, R. L.; Morokuma, K.; Zakrewski, O.; Voth, G. A.; Salvador, P.; Dannenberg, J. J.; Dapproch, S.; Daniels, A. D.; Farkas, O.; Foresman, J. B.; Ortiz, J. V; Cioslowski, J.; Fox, D. J. Gaussian 09 Revision D.01. Gaussian Inc 2014.

(137) Aresta, M.; Galia, A.; Filardo, G.; Berg, I. A.; Kockelkorn, D.; Ramos-Vera, H. W.; Say, R.; Zarzycki, J.; Fuchs, G.; Mascetti, J.; Zevaco, T.; Dinjus, E.; Quaranta, E.; Ballivet-Tkatchenko, D.; Dibenedetto, A.; Darensbourg, D. J.; Andreatta, J. R.; Moncada, A. I.; Pan, W.; Song, C.; Zou, J.-J.; Liu, C.-J.; Emily Cole, B.; Bocarsly, A. B.; Silvestri, G.; Scialdone, O.; Dibenedetto, A.; Zevenhoven, R.; Fagerlund, J. *Carbon Dioxide as Chemical Feedstock*; Aresta, M., Ed.; Wiley-VCH: Weinheim, 2010.

(138) D'Alessandro, D. M.; Smit, B.; Long, J. R. Carbon Dioxide Capture: Prospects for New Materials. *Angewandte Chemie - International Edition* **2010**, *49* (35), 6058–6082. https://doi.org/10.1002/anie.201000431.

(139) International Energy Agency. *Putting CO2 to Use - Creating Value from Emissions*; Paris, 2019.

(140) Yao, B.; Xiao, T.; Makgae, O. A.; Jie, X.; Gonzalez-Cortes, S.; Guan, S.; Kirkland, A. I.; Dilworth, J. R.; Al-Megren, H. A.; Alshihri, S. M.; Dobson, P. J.; Owen, G. P.; Thomas, J. M.; Edwards, P. P. Transforming Carbon Dioxide into Jet Fuel Using an Organic Combustion-Synthesized Fe-Mn-K Catalyst. *Nat Commun* **2020**, *11* (1). https://doi.org/10.1038/s41467-020-20214-z.

(141) Hepburn, C.; Adlen, E.; Beddington, J.; Carter, E. A.; Fuss, S.; Mac Dowell, N.; Minx, J. C.; Smith, P.; Williams, C. K. The Technological and Economic Prospects for CO2 Utilization and Removal. *Nature* **2019**, *575* (7781), 87–97. https://doi.org/10.1038/s41586-019-1681-6.

(142) Dabral, S.; Schaub, T. The Use of Carbon Dioxide (CO2) as a Building Block in Organic Synthesis from an Industrial Perspective. *Advanced Syntheis & Catalysis* **2019**, *361*, 223–246. https://doi.org/10.1002/adsc.201801215.

(143) Gulzar, A.; Gulzar, A.; Ansari, M. B.; He, F.; Gai, S.; Yang, P. Carbon Dioxide Utilization: A Paradigm Shift with CO2 Economy. *Chemical Engineering Journal Advances* **2020**, *3*. https://doi.org/10.1016/j.ceja.2020.100013.

(144) Aresta, M.; Dibenedetto, A.; Angelini, A. Catalysis for the Valorization of Exhaust Carbon: From CO2 to Chemicals, Materials, and Fuels. Technological Use of CO2. *Chem Rev* **2014**, *114* (3), 1709–1742. https://doi.org/10.1021/cr4002758.

(145) Burkart, M. D.; Hazari, N.; Tway, C. L.; Zeitler, E. L. Opportunities and Challenges for Catalysis in Carbon Dioxide Utilization. *ACS Catal* **2019**, *9*, 7973–7956. https://doi.org/10.1021/acscatal.9b02113.

(146) Artz, J.; Müller, T. E.; Thenert, K.; Kleinekorte, J.; Meys, R.; Sternberg, A.; Bardow, A.; Leitner, W. Sustainable Conversion of Carbon Dioxide: An Integrated Review of Catalysis and Life Cycle Assessment. *Chem Rev* **2018**, *118* (2), 434–504. https://doi.org/10.1021/acs.chemrev.7b00435.

(147) Li, Y.; Cui, X.; Dong, K.; Junge, K.; Beller, M. Utilization of CO2 as a C1 Building Block for Catalytic Methylation Reactions. *ACS Catal* **2017**, *7* (2), 1077–1086. https://doi.org/10.1021/acscatal.6b02715.

(148) Grignard, B.; Gennen, S.; Jérôme, C.; Kleij, A. W.; Detrembleur, C. Advances in the Use of CO2 as a Renewable Feedstock for the Synthesis of Polymers. *Chem Soc Rev* **2019**, *48* (16), 4466–4514. https://doi.org/10.1039/c9cs00047j.

(149) Das Neves Gomes, C.; Jacquet, O.; Villiers, C.; Thuéry, P.; Ephritikhine, M.; Cantat, T. A Diagonal Approach to Chemical Recycling of Carbon Dioxide: Organocatalytic Transformation for the Reductive Functionalization of CO2. *Angew. Chemie Int. Ed.* **2012**, *51*, 187–190. https://doi.org/10.1002/ANIE.201105516.

(150) Sakakura, T.; Choi, J. C.; Yasuda, H. Transformation of Carbon Dioxide. *Chem Rev* **2007**, *107* (6), 2365–2387. https://doi.org/10.1021/cr068357u.

(151) Liu, Q.; Wu, L.; Jackstell, R.; Beller, M. Using Carbon Dioxide as a Building Block in Organic Synthesis. *Nat Commun* **2015**, *6*. https://doi.org/10.1038/ncomms6933.

(152) Pesti, J.; Larson, G. L. Tetramethyldisiloxane: A Practical Organosilane Reducing Agent. *Org Process Res Dev* **2016**, *20* (7), 1164–1181. https://doi.org/10.1021/acs.oprd.6b00124.

(153) Heim, L. E.; Konnerth, H.; Prechtl, M. H. G. Future Perspectives for Formaldehyde: Pathways for Reductive Synthesis and Energy Storage. *Green Chemistry* **2017**, *19* (10), 2347–2355. https://doi.org/10.1039/c6gc03093a.

(154) Desmons, S.; Fauré, R.; Bontemps, S. Formaldehyde as a Promising C1 Source: The Instrumental Role of Biocatalysis for Stereocontrolled Reactions. *ACS Catal* **2019**, *9* (10), 9575–9588. https://doi.org/10.1021/acscatal.9b03128.

(155) Häggblad, R.; Wagner, J. B.; Hansen, S.; Andersson, A. Oxidation of Methanol to Formaldehyde over a Series of Fe1-XAlx-V-Oxide Catalysts. *J Catal* **2008**, *258* (2), 345–355. https://doi.org/10.1016/j.jcat.2008.06.029.

(156) Klankermayer, J.; Wesselbaum, S.; Beydoun, K.; Leitner, W. Selective Catalytic Synthesis Using the Combination of Carbon Dioxide and Hydrogen: Catalytic Chess at the Interface of Energy and Chemistry. *Angewandte Chemie* **2016**, *128* (26), 7416–7467. https://doi.org/10.1002/ange.201507458.

(157) Mitton, S. J.; Turculet, L. Mild Reduction of Carbon Dioxide to Methane with Tertiary Silanes Catalyzed by Platinum and Palladium Silyl Pincer Complexes. *Chemistry - A European Journal* **2012**, *18* (48), 15258–15262. https://doi.org/10.1002/chem.201203226.

(158) Ríos, P.; Rodríguez, A.; López-Serrano, J. Mechanistic Studies on the Selective Reduction of CO2 to the Aldehyde Level by a Bis(Phosphino)Boryl (PBP)-Supported Nickel Complex. *ACS Catal* **2016**, *6* (9), 5715–5723. https://doi.org/10.1021/acscatal.6b01715.

(159) Rauch, M.; Parkin, G. Zinc and Magnesium Catalysts for the Hydrosilylation of Carbon Dioxide. *J Am Chem Soc* **2017**, *139* (50), 18162–18165. https://doi.org/10.1021/jacs.7b10776.

(160) Leblanc, F. A.; Piers, W. E.; Parvez, M. Selective Hydrosilation of CO2 to a Bis(Silylacetal) Using an Anilido Bipyridyl-Ligated Organoscandium Catalyst. *Angewandte Chemie - International Edition* **2014**, *53* (3), 789–792. https://doi.org/10.1002/anie.201309094.

(161) Berkefeld, A.; Piers, W. E.; Parvez, M. Tandem Frustrated Lewis Pair/Tris(Pentafluorophenyl)Borane-Catalyzed Deoxygenative Hydrosilylation of Carbon Dioxide. *J Am Chem Soc* **2010**, *132* (31), 10660–10661. https://doi.org/10.1021/ja105320c.

(162) Cramer, H. H.; Das, S.; Wodrich, M. D.; Corminboeuf, C.; Werlé, C.; Leitner, W. Theory-Guided Development of Homogeneous Catalysts for the Reduction of CO2 to Formate, Formaldehyde, and Methanol Derivatives. *Chem Sci* **2023**, *14* (11), 2799–2807. https://doi.org/10.1039/d2sc06793e.

(163) Zhao, S.; Liang, H. Q.; Hu, X. M.; Li, S.; Daasbjerg, K. Challenges and Prospects in the Catalytic Conversion of Carbon Dioxide to Formaldehyde. *Angewandte Chemie - International Edition* **2022**, *61* (46). https://doi.org/10.1002/anie.202204008.

(164) Matsuo, T.; Kawaguchi, H. From Carbon Dioxide to Methane: Homogeneous Reduction of Carbon Dioxide with Hydrosilanes Catalyzed by Zirconium-Borane Complexes. *J Am Chem Soc* **2006**, *128* (38), 12362–12363. https://doi.org/10.1021/ja0647250.

(165) Chen, J.; Falivene, L.; Caporaso, L.; Cavallo, L.; Chen, E. Y. X. Selective Reduction of CO2 to CH4 by Tandem Hydrosilylation with Mixed Al/B Catalysts. *J Am Chem Soc* **2016**, *138* (16), 5321–5333. https://doi.org/10.1021/jacs.6b01497.

(166) Rendler, S.; Oestreich, M. Conclusive Evidence for an SN2-Si Mechanism in the B(C 6F5)3-Catalyzed Hydrosilylation of Carbonyl Compounds: Implications for the Related Hydrogenation. *Angewandte Chemie - International Edition* **2008**, *47* (32), 5997–6000. https://doi.org/10.1002/anie.200801675.

(167) Midilli, A.; Ay, M.; Dincer, I.; Rosen, M. A. On Hydrogen and Hydrogen Energy Strategies I : Current Status and Needs. *Renewable and Sustainable Energy Reviews* **2005**, *9* (3), 255–271. https://doi.org/10.1016/j.rser.2004.05.003.

(168) Ritchie, H.; Roser, M.; Rosado, P. *Energy*; 2022.

(169) International Energy Agency. *Net Zero by 2050 - A Roadmap for the Global Energy Sector*; 2021. www.iea.org/t&c/.

(170) Zhang, S. S. Status, Opportunities, and Challenges of Electrochemical Energy Storage. *Front Energy Res* **2013**, *1* (DEC). https://doi.org/10.3389/fenrg.2013.00008.

(171) Eppinger, J.; Huang, K. W. Formic Acid as a Hydrogen Energy Carrier. *ACS Energy Lett* **2017**, *2* (1), 188–195. https://doi.org/10.1021/acsenergylett.6b00574.

(172) Armaroli, N.; Balzani, V. Towards an Electricity-Powered World. *Energy Environ Sci* **2011**, *4* (9), 3193–3222. https://doi.org/10.1039/c1ee01249e.

(173) Appleby, A. J. From Sir William Grove to Today: Fuel Cells and the Future. *J Power Sources* **1990**, *29* (1), 3–11. https://doi.org/https://doi.org/10.1016/0378-7753(90)80002-U.

(174) Ifkovits, Z. P.; Evans, J. M.; Meier, M. C.; Papadantonakis, K. M.; Lewis, N. S. Decoupled Electrochemical Water-Splitting Systems: A Review and Perspective. *Energy Environ. Sci.* **2021**, *14* (9), 4740–4759. https://doi.org/10.1039/D1EE01226F.

(175) Iulianelli, A.; Liguori, S.; Wilcox, J.; Basile, A. Advances on Methane Steam Reforming to Produce Hydrogen through Membrane Reactors Technology: A Review. *Catal Rev Sci Eng* **2016**, *58* (1), 1–35. https://doi.org/10.1080/01614940.2015.1099882.

(176) Abe, J. O.; Popoola, A. P. I.; Ajenifuja, E.; Popoola, O. M. Hydrogen Energy, Economy and Storage: Review and Recommendation. *Int J Hydrogen Energy* **2019**, *44* (29), 15072–15086. https://doi.org/10.1016/j.ijhydene.2019.04.068.

(177) Preuster, P.; Papp, C.; Wasserscheid, P. Liquid Organic Hydrogen Carriers (LOHCs): Toward a Hydrogen-Free Hydrogen Economy. *Acc Chem Res* **2017**, *50* (1), 74–85. https://doi.org/10.1021/acs.accounts.6b00474.

(178) Coffey, R. S. The Decomposition of Formic Acid Catalysed by Soluble Metal Complexes. *Chemical Communications (London)* **1967**, 923b–9924.

(179) Himeda, Y.; Onozawa-Komatsuzaki, N.; Sugihara, H.; Arakawa, H.; Kasuga, K. Transfer Hydrogenation of a Variety of Ketones Catalyzed by Rhodium Complexes in Aqueous Solution and Their Application to Asymmetric Reduction Using Chiral Schiff Base Ligands. *J Mol Catal A Chem* **2003**, *195*, 95–100.

(180) Loges, B.; Boddien, A.; Junge, H.; Beller, M. Controlled Generation of Hydrogen from Formic Acid Amine Adducts at Room Temperature and Application in H2/O2 Fuel Cells. *Angewandte Chemie - International Edition* **2008**, *47* (21), 3962–3965. https://doi.org/10.1002/anie.200705972.

(181) Fellay, C.; Dyson, P. J.; Laurenczy, G. A Viable Hydrogen-Storage System Based on Selective Formic Acid Decomposition with a Ruthenium Catalyst. *Angewandte Chemie - International Edition* **2008**, *47* (21), 3966–3968. https://doi.org/10.1002/anie.200800320.

(182) Mellmann, D.; Sponholz, P.; Junge, H.; Beller, M. Formic Acid as a Hydrogen Storage Material-Development of Homogeneous Catalysts for Selective Hydrogen Release. *Chem Soc Rev* **2016**, *45* (14), 3954–3988. https://doi.org/10.1039/c5cs00618j.

(183) Barnard, J. H.; Wang, C.; Berry, N. G.; Xiao, J. Long-Range Metal-Ligand Bifunctional Catalysis: Cyclometallated Iridium Catalysts for the Mild and Rapid Dehydrogenation of Formic Acid. *Chem Sci* **2013**, *4* (3), 1234–1244. https://doi.org/10.1039/c2sc21923a.

(184) Wang, Z.; Lu, S. M.; Wu, J.; Li, C.; Xiao, J. Iodide-Promoted Dehydrogenation of Formic Acid on a Rhodium Complex. *Eur J Inorg Chem* **2016**, *2016* (4), 490–496. https://doi.org/10.1002/ejic.201501061.

(185) Morris, D. J.; Clarkson, G. J.; Wills, M. Insights into Hydrogen Generation from Formic Acid Using Ruthenium Complexes. *Organometallics* **2009**, *28* (14), 4133–4140. https://doi.org/10.1021/om900099u.

(186) Zell, T.; Butschke, B.; Ben-David, Y.; Milstein, D. Efficient Hydrogen Liberation from Formic Acid Catalyzed by a Well-Defined Iron Pincer Complex under Mild Conditions. *Chemistry - A European Journal* **2013**, *19* (25), 8068–8072. https://doi.org/10.1002/chem.201301383.

(187) Wang, Z.; Lu, S. M.; Li, J.; Wang, J.; Li, C. Unprecedentedly High Formic Acid Dehydrogenation Activity on an Iridium Complex with an N,N′-Diimine Ligand in Water. *Chemistry - A European Journal* **2015**, *21* (36), 12592–12595. https://doi.org/10.1002/chem.201502086.

(188) Filonenko, G. A.; Van Putten, R.; Schulpen, E. N.; Hensen, E. J. M.; Pidko, E. A. Highly Efficient Reversible Hydrogenation of Carbon Dioxide to Formates Using a Ruthenium PNP-Pincer Catalyst. *ChemCatChem* **2014**, *6* (6), 1526–1530. https://doi.org/10.1002/cctc.201402119.

(189) Onishi, N.; Kanega, R.; Kawanami, H.; Himeda, Y. Recent Progress in Homogeneous Catalytic Dehydrogenation of Formic Acid. *Molecules*. MDPI January 1, 2022. https://doi.org/10.3390/molecules27020455.

(190) Iglesias, M.; Fernández-Alvarez, F. J. Catalysts Advances in Nonprecious Metal Homogeneously Catalyzed Formic Acid Dehydrogenation. **2021**. https://doi.org/10.3390/catal.

(191) Ashish, S. K.; Suryabhan, S.; Abhinav, K. Hydrogen Energy Future with Formic Acid: A Renewable Chemical Hydrogen Storage System. *Catal. Sci. Technol.* **2016**, *6*, 12–40. https://doi.org/10.1039/x0xx00000x.

(192) Onishi, N.; Kanega, R.; Kawanami, H.; Himeda, Y. Recent Progress in Homogeneous Catalytic Dehydrogenation of Formic Acid. *Molecules*. MDPI January 1, 2022. https://doi.org/10.3390/molecules27020455.

(193) Iturmendi, A.; Rubio-Pérez, L.; Pérez-Torrente, J. J.; Iglesias, M.; Oro, L. A. Impact of Protic Ligands in the Ir-Catalyzed Dehydrogenation of Formic Acid in Water. *Organometallics* **2018**, *37* (20), 3611–3618. https://doi.org/10.1021/acs.organomet.8b00289.

(194) Kar, S.; Rauch, M.; Leitus, G.; Ben-David, Y.; Milstein, D. Highly Efficient Additive-Free Dehydrogenation of Neat Formic Acid. *Nat Catal* **2021**, *4* (3), 193–201. https://doi.org/10.1038/s41929-021-00575-4.

(195) Weber, S. M.; Queder, J.; Hilt, G. Ligand-Controlled Diastereoselective Cobalt-Catalysed Hydroalkynylation of Terminal Alkynes to E- or Z-1,3-Enynes. *Chemistry - A European Journal* **2020**, *26* (53), 12129–12133. https://doi.org/10.1002/chem.202001697.

(196) Torres, Ò.; Fernàndez, M.; Díaz-Jiménez, À.; Pla-Quintana, A.; Roglans, A.; Solà, M. Examining the Factors That Govern the Regioselectivity in Rhodium-Catalyzed Alkyne Cyclotrimerization. *Organometallics* **2019**, *38* (14), 2853–2862. https://doi.org/10.1021/acs.organomet.9b00347.

(197) Batrice, R. J.; McKinven, J.; Arnold, P. L.; Eisen, M. S. Selective Oligomerization and [2 + 2 + 2] Cycloaddition of Terminal Alkynes from Simple Actinide Precatalysts. *Organometallics* **2015**, *34* (16), 4039–4050. https://doi.org/10.1021/acs.organomet.5b00455.

(198) Wakatsuki, Y.; Yamazaki, H.; Kumegawa, N.; Satoh, T.; Satoh, J. Y. Regio- and Stereocontrolled Dimerization of Tert-Butylacetylene to (Z)-1,4-Di-Tert-Butylbutatriene by Ruthenium Catalysis. Reaction Mechanism Involving Alkynyl-Vinylidene Coupling and Rearrangement of the Metal-Bound C4 Unit. *J. Chem. Soc., Chem. Commun* **1991**, *113* (25), 9604–9610.

(199) Claus, V.; Schukin, M.; Harrer, S.; Rudolph, M.; Rominger, F.; Asiri, A. M.; Xie, J.; Hashmi, A. S. K. Direkter Zugang Zu Azulenen Über Eine Gold-katalysierte Dimerisierung von Diarylalkinen. *Angewandte Chemie* **2018**, *130* (39), 13148–13152. https://doi.org/10.1002/ange.201805918.

(200) Angoy, M.; Victoria Jiménez, M.; García-Orduña, P.; Oro, L. A.; Vispe, E.; Pé-Rez-Torrente, J. J. Dinuclear Phosphine-Amido [Rh2(Diene){μ-NH(CH2)3PPh2}2] Complexes as Efficient Catalysts Precursors for Phenylacetylene Polymerization. *Organometallics* **2019**, *38* (9), 1991–2006.

(201) Xue, F.; Song, X.; Lin, T. T.; Munkerup, K.; Albawardi, S. F.; Huang, K. W.; Hor, T. S. A.; Zhao, J. Dimerization of Terminal Aryl Alkynes Catalyzed by Iron(II) Amine-Pyrazolyl Tripodal Complexes with E/ Z Selectivity Controlled by Tert-Butoxide. *ACS Omega* **2018**, *3* (5), 5071–5077. https://doi.org/10.1021/acsomega.8b00539.

(202) Akita, M.; Yasuda, H.; Yasuda, H. Regioselective Homo- and Codimerzation of 1-Alkynes Leading to 2,4-Disubstitutes 1-Buten-3-Ynes by Catalysis of a (H5-C5Me5)2TiCl2/RMgX Sistem. *Bull. Chem. Soc. Jpn.* **1984**, *57*, 480–487.

(203) Sun, S.; Kroll, J.; Luo, Y.; Zhang, L. Gold-Catalyzed Regioselective Dimerization of Aliphatic Terminal Alkynes. *Synlett* **2012**, No. 1, 54–56. https://doi.org/10.1055/s-0031-1289567.

(204) Rubina, M.; Gevorgyan, V. Can Agostic Interaction Affect Regiochemistry of Carbopalladation? Reverse Regioselectivity in the Palladium-Catalyzed Dimerization of Aryl Acetylenes. *J Am Chem Soc* **2001**, *123* (44), 11107–11108. https://doi.org/10.1021/ja016934k.

(205) Kleinhans, G.; Guisado-Barrios, G.; Liles, D. C.; Bertrand, G.; Bezuidenhout, D. I. A Rhodium(i)-Oxygen Adduct as a Selective Catalyst for One-Pot Sequential Alkyne Dimerization-Hydrothiolation Tandem Reactions. *Chemical Communications* **2016**, *52* (17), 3504–3507. https://doi.org/10.1039/c6cc00029k.

(206) Geer, A. M.; Julián, A.; López, J. A.; Ciriano, M. A.; Tejel, C. Pseudo-Tetrahedral Rhodium and Iridium Complexes: Catalytic Synthesis of E-Enynes. *Chemistry – A European Journal* **2018**, *24* (66), 17545–17556. https://doi.org/https://doi.org/10.1002/chem.201803878.

(207) Żak, P.; Bołt, M.; Lorkowski, J.; Kubicki, M.; Pietraszuk, C. Platinum Complexes Bearing Bulky N-Heterocyclic Carbene Ligands as Efficient Catalysts for the Fully Selective Dimerization of Terminal Alkynes. *ChemCatChem* **2017**, *9* (19), 3627–3631. https://doi.org/10.1002/cctc.201700580.

(208) Ventre, S.; Derat, E.; Amatore, M.; Aubert, C.; Petit, M. Hydrido-Cobalt Catalyst as a Selective Tool for the Dimerisation of Arylacetylenes: Scope and Theoretical Studies. *Adv Synth Catal* **2013**, *355* (13), 2584–2590. https://doi.org/10.1002/adsc.201300486.

(209) Platel, R. H.; Schafer, L. L. Zirconium Catalyzed Alkyne Dimerization for Selective Z-Enyne Synthesis. *Chemical Communications* **2012**, *48* (86), 10609–10611. https://doi.org/10.1039/c2cc35913h.

(210) Gorgas, N.; Stöger, B.; Veiros, L. F.; Kirchner, K. Iron(II) Bis(Acetylide) Complexes as Key Intermediates in the Catalytic Hydrofunctionalization of Terminal Alkynes. *ACS Catal* **2018**, *8* (9), 7973–7982. https://doi.org/10.1021/acscatal.8b01942.

(211) Liang, Q.; Sheng, K.; Salmon, A.; Zhou, V. Y.; Song, D. Active Iron(II) Catalysts toward Gem-Specific Dimerization of Terminal Alkynes. *ACS Catal* **2019**, *9* (2), 810–818. https://doi.org/10.1021/acscatal.8b03552.

(212) Hasenbeck, M.; Müller, T.; Gellrich, U. Metal-Free: Gem Selective Dimerization of Terminal Alkynes Catalyzed by a Pyridonate Borane Complex. *Catal Sci Technol* **2019**, *9* (10), 2438–2444. https://doi.org/10.1039/c9cy00253g.

(213) Storey, C. M.; Gyton, M. R.; Andrew, R. E.; Chaplin, A. B. Terminal Alkyne Coupling Reactions through a Ring: Mechanistic Insights and Regiochemical Switching. *Angewandte Chemie* **2018**, *130* (37), 12179–12182. https://doi.org/10.1002/ange.201807028.

(214) Zatolochnaya, O. V.; Gordeev, E. G.; Jahier, C.; Ananikov, V. P.; Gevorgyan, V. Carboxylate Switch between Hydro- and Carbopalladation Pathways in Regiodivergent Dimerization of Alkynes. *Chemistry - A European Journal* **2014**, *20* (31), 9578–9588. https://doi.org/10.1002/chem.201402809.

(215) Khusnutdinova, J. R.; Milstein, D. Metall-Ligand-Cooperation. *Angewandte Chemie* **2015**, *127* (42), 12406–12445. https://doi.org/10.1002/ange.201503873.

(216) Kim, D. S.; Park, W. J.; Jun, C. H. Metal-Organic Cooperative Catalysis in C-H and C-C Bond Activation. *Chem Rev* **2017**, *117* (13), 8977–9015. https://doi.org/10.1021/acs.chemrev.6b00554.

(217) Higashi, T.; Kusumoto, S.; Nozaki, K. Cleavage of Si-H, B-H, and C-H Bonds by Metal-Ligand Cooperation. *Chem Rev* **2019**, *119* (18), 10393–10402. https://doi.org/10.1021/acs.chemrev.9b00262.

(218) Johnson, D. G.; Lynam, J. M.; Slattery, J. M.; Welby, C. E. Insights into the Intramolecular Acetate-Mediated Formation of Ruthenium Vinylidene Complexes: A Ligand-Assisted Proton Shuttle (LAPS) Mechanism. *Dalton Transactions* **2010**, *39* (43), 10432–10441. https://doi.org/10.1039/c0dt00431f.

(219) Amer, M. M. K.; Aziz, M. A.; Shehab, W. S.; Abdellattif, M. H.; Mouneir, S. M. Recent Advances in Chemistry and Pharmacological Aspects of 2-Pyridone Scaffolds. *Journal of Saudi Chemical Society* **2021**, *25* (6). https://doi.org/10.1016/j.jscs.2021.101259.

(220) Zhang, Y.; Pike, A. Pyridones in Drug Discovery: Recent Advances. *Bioorganic and Medicinal Chemistry Letters*. Elsevier Ltd April 15, 2021. https://doi.org/10.1016/j.bmcl.2021.127849.

(221) Mitscher, L. A. Bacterial Topoisomerase Inhibitors: Quinolone and Pyridone Antibacterial Agents. *Chem Rev* **2005**, *105* (2), 559–592. https://doi.org/10.1021/cr030101q.

(222) Rai, S. K.; Singh, P.; Khanam, S.; Tewari, A. K. Polymorphic Study and Anti-Inflammatory Activity of a 3-Cyano-2-Pyridone Based Flexible Model. *New Journal of Chemistry* **2016**, *40* (6), 5577–5587. https://doi.org/10.1039/c5nj03683f.

(223) Sayed, H. H.; Morsy, E. M. H.; Flefel, E. M. Synthesis and Reactions of Some Novel Nicotinonitrile, Thiazolotriazole, and Imidazolotriazole Derivatives for Antioxidant Evaluation. *Synth Commun* **2010**, *40* (9), 1360–1370. https://doi.org/10.1080/00397910903079631.

(224) Mahajan, P. S.; Burke, T. R. Synthetic Approaches to a Key Pyridone-Carboxylic Acid Precursor Common to the HIV-1 Integrase Strand Transfer Inhibitors Dolutegravir, Bictegravir, and Cabotegravir. *Org Process Res Dev* **2023**, *27* (5), 847–853. https://doi.org/10.1021/acs.oprd.3c00063.

(225) Manfroni, G.; Meschini, F.; Barreca, M. L.; Leyssen, P.; Samuele, A.; Iraci, N.; Sabatini, S.; Massari, S.; Maga, G.; Neyts, J.; Cecchetti, V. Pyridobenzothiazole Derivatives as New Chemotype Targeting the HCV NS5B Polymerase. *Bioorg Med Chem* **2012**, *20* (2), 866–876. https://doi.org/10.1016/j.bmc.2011.11.061.

(226) Torres, M.; Gil, S.; Parra, M. New Synthetic Methods to 2-Pyridone Rings. *Curr Org Chem* **2005**, *9*, 1757–1779.

(227) Imase, H.; Noguchi, K.; Hirano, M.; Tanaka, K. Convergent and Rapid Assembly of Substituted 2-Pyridones through Formation of N-Alkenyl Alkynylamides Followed by Gold-Catalyzed Cycloisomerization. *Org Lett* **2008**, *10* (16), 3563–3566. https://doi.org/10.1021/ol801466f.

(228) Hyster, T. K.; Rovis, T. An Improved Catalyst Architecture for Rhodium(Iii) Catalyzed C-H Activation and Its Application to Pyridone Synthesis. *Chem Sci* **2011**, *2* (8), 1606–1610. https://doi.org/10.1039/c1sc00235j.

(229) Feng, B.; Li, Y.; Li, H.; Zhang, X.; Xie, H.; Cao, H.; Yu, L.; Xu, Q. Specific N-Alkylation of Hydroxypyridines Achieved by a Catalyst- and Base-Free Reaction with Organohalides. *Journal of Organic Chemistry* **2018**, *83* (12), 6769–6775. https://doi.org/10.1021/acs.joc.8b00787.

(230) Khan, S.; Shah, B. H.; Khan, I.; Li, M.; Zhang, Y. J. Pd-Catalyzed Regio- And Enantioselective Allylic Substitution with 2-Pyridones. *Chemical Communications* **2019**, *55* (87), 13168–13171. https://doi.org/10.1039/c9cc07482a.

(231) Zhang, X.; Yang, Z. P.; Huang, L.; You, S. L. Highly Regio- And Enantioselective Synthesis of N-Substituted 2-Pyridones: Iridium-Catalyzed Intermolecular Asymmetric Allylic. *Angewandte Chemie - International Edition* **2015**, *54* (6), 1873–1876. https://doi.org/10.1002/anie.201409976.

(232) Breugst, M.; Mayr, H. Ambident Reactivities of Pyridone Anions. *J Am Chem Soc* **2010**, *132* (43), 15380–15389. https://doi.org/10.1021/ja106962u.

(233) Tasker, S. Z.; Brandsen, B. M.; Ryu, K. A.; Snapper, G. S.; Staples, R. J.; Dekock, R. L.; Anderson, C. E. Synthesis of a New Class of β-Iodo N-Alkenyl 2-Pyridones. *Org Lett* **2011**, *13* (23), 6224–6227. https://doi.org/10.1021/ol202679t.

(234) Mariano, P. S.; Krochmal, E.; Beamer, R.; Huesmann, P. J.; Dunaway-Mariano, D. General Synthetic Methods for the Preparation of 1-Substituted-Vinyl-2-Pyridones. *Tetrahedron* **1978**, *34*, 2069–2616.

(235) Lam, P. Y. S.; Vincent, G.; Bonne, D.; Clark, C. G. Copper-Promoted/Catalyzed C-N and C-O Bond Cross-Coupling with Vinylboronic Acid and Its Utilities. *Tetrahedron Lett* **2003**, *44* (26), 4927–4931. https://doi.org/10.1016/S0040-4039(03)01037-2.

(236) Bolshan, Y.; Batey, R. A. Enamide Synthesis by Copper-Catalyzed Cross-Coupling of Amides and Potassium Alkenyltrifluoroborate Salts. *Angewandte Chemie - International Edition* **2008**, *47* (11), 2109–2112. https://doi.org/10.1002/anie.200704711.

(237) Shivers, G. N.; Pigge, F. C. A Mild and Highly Diastereoselective Preparation of N-Alkenyl-2-Pyridones via 2-Halopyridinium Salts and Aldehydes. *Journal of Organic Chemistry* **2021**, *86* (18), 13134–13142. https://doi.org/10.1021/acs.joc.1c01566.

(238) Mola, L.; Font, J.; Bosch, L.; Caner, J.; Costa, A. M.; Etxebarría-Jardí, G.; Pineda, O.; De Vicente, D.; Vilarrasa, J. Nucleophile-Catalyzed Additions to Activated Triple Bonds. Protection of Lactams, Imides, and Nucleosides with MocVinyl and Related Groups. *Journal of Organic Chemistry* **2013**, *78* (12), 5832–5842. https://doi.org/10.1021/jo4006409.

(239) Yang, J.; Dudley, G. B. Pyridine-Directed Organolithium Addition to an Enol Ether. *Adv Synth Catal* **2010**, *352* (18), 3438–3442. https://doi.org/10.1002/adsc.201000495.

(240) Lingayya, R.; Vellakkaran, M.; Nagaiah, K.; Tadikamalla, P. R.; Nanubolu, J. B. Palladium(Ii)-Catalyzed Direct O-Alkenylation of 2-Arylquinazolinones with N-Tosylhydrazones: An Efficient Route to O-Alkenylquinazolines. *Chemical Communications* **2017**, *53* (10), 1672–1675. https://doi.org/10.1039/c6cc09445g.

(241) Singh, P.; Cairns, A. G.; Adolfsson, D. E.; Ådén, J.; Sauer, U. H.; Almqvist, F. Synthesis of Densely Functionalized N-Alkenyl 2-Pyridones via Benzyne-Induced Ring Opening of Thiazolino-Fused 2-Pyridones. *Org Lett* **2019**, *21* (17), 6946–6950. https://doi.org/10.1021/acs.orglett.9b02549.

(242) Palacios, L.; Di Giuseppe, A.; Castarlenas, R.; Lahoz, F. J.; Pérez-Torrente, J. J.; Oro, L. A. Pyridine versus Acetonitrile Coordination in Rhodium-N-Heterocyclic Carbene Square-Planar Complexes. *Dalton Transactions* **2015**, *44* (12), 5777–5789. https://doi.org/10.1039/c5dt00182j.

Annex:
Published papers

The work discussed in this Ph.D Thesis has been published in the following articles:

- Guzmán, J.; Urriolabeitia, A.; Padilla, M.; García-Orduña, P.; Polo, V.; Fernández-Alvarez, F. J. Mechanism Insights into the Iridium(III)- and $B(C_6F_5)_3$-Catalyzed Reduction of CO_2 to the Formaldehyde Level with Tertiary Silanes. *Inorg Chem* **2022**, *61* (50), 20216–20221. https://doi.org/10.1021/acs.inorgchem.2c03330
- Guzmán, J.; Urriolabeitia, A.; Polo, V.; Fernández-Buenestado, M.; Iglesias, M.; Fernández-Alvarez, F. J. Dehydrogenation of Formic Acid Using Iridium-NSi Species as Catalyst Precursors. *Dalton Transactions*. **2022**, *51* (11), 4386–4393. https://doi.org/10.1039/D1DT04335H
- Hermosilla, P.; Urriolabeitia, A.; Iglesias, M.; Polo, V.; Casado, M. A. Efficient Solventless Dehydrogenation of Formic Acid by a CNC-Based Rhodium Catalyst. *Inorg Chem Front* **2022**, *9* (17), 4538–4547. https://doi.org/10.1039/D2QI01056A
- Galiana-Cameo, M.; Urriolabeitia, A.; Barrenas, E.; Passarelli, V; Pérez-Torrente, J. J.; Di Giuseppe, A.; Polo, V.; Castarlenas, R. Metal−Ligand Cooperative Proton Transfer as an Efficient Trigger for Rhodium-NHC-Pyridonato Catalyzed *gem*-Specific Alkyne Dimerization. *ACS Catal.* **2021**, *11* (12), 7553–7567. https://doi.org/10.1021/acscatal.1c00602
- Galiana-Cameo, M.; Romeo, R.; Urriolabeitia, A.; Passarelli, V; Pérez-Torrente, J. J.; Polo, V.; Castarlenas, R. Rhodium-NHC-Catalyzed *gem*-Specific *O*-Selective Hydropyridonation of Terminal Alkynes. *Angew. Chem. Int. Ed.* **2022**, *61*, e202117006. https://doi.org/10.1002/anie.202117006

Inorganic Chemistry

pubs.acs.org/IC

Communication

Mechanism Insights into the Iridium(III)- and $B(C_6F_5)_3$-Catalyzed Reduction of CO_2 to the Formaldehyde Level with Tertiary Silanes

Jefferson Guzmán, Asier Urriolabeitia, Marina Padilla, Pilar García-Orduña, Víctor Polo, and Francisco J. Fernández-Alvarez*

Cite This: *Inorg. Chem.* 2022, 61, 20216−20221

Read Online

ACCESS | Metrics & More | Article Recommendations | Supporting Information

ABSTRACT: The catalytic system $[Ir(CF_3CO_2)(\kappa^2\text{-}NSi^{Me})_2]$ [**1**; NSi^{Me} = (4-methylpyridin-2-yloxy)dimethylsilyl]/$B(C_6F_5)_3$ promotes the selective reduction of CO_2 with tertiary silanes to the corresponding bis(silyl)acetal. Stoichiometric and catalytic studies evidenced that species $[Ir(CF_3COO\text{-}B(C_6F_5)_3)(\kappa^2\text{-}NSi^{Me})_2]$ (**3**), $[Ir(\kappa^2\text{-}NSi^{Me})_2][HB(C_6F_5)_3]$ (**4**), and $[Ir(HCOO\text{-}B(C_6F_5)_3)(\kappa^2\text{-}NSi^{Me})_2]$ (**5**) are intermediates of the catalytic process. The structure of **3** has been determined by X-ray diffraction methods. Theoretical calculations show that the rate-limiting step for the **1**/$B(C_6F_5)_3$-catalyzed hydrosilylation of CO_2 to bis(silyl)acetal is a boron-promoted Si−H bond cleavage via an iridium silylacetal borane adduct.

The potential of CO_2 as a renewable and cheap C1 carbon source has received increasing attention over recent years.[1] The major difficulties to achieve this goal are the kinetic and thermodynamic stability of CO_2, which hampers most of its chemical transformations. In this regard, catalysis has proven to be an essential tool for transforming CO_2 into value-added chemicals. Although great advances have been made in the field of the catalytic transformation of CO_2, there are still many challenges to overcome for its utilization as a raw material on an industrial scale.[2,3]

Formic acid, formaldehyde, methanol, and methane are C1 chemicals that can be obtained from the reduction of CO_2. In this work, we focus on formaldehyde, which is obtained industrially by the partial oxidation of methanol and has an annual demand of 30 million tons.[4] The catalytic hydrogenation of CO_2 to formaldehyde has been scarcely reported.[5] However, several examples of the catalytic reduction of CO_2 to the formaldehyde level with hydrosilanes[6−14] or hydroboranes[15] have been reported. Catalytic systems based on Zr,[6] Re,[7] Ru,[8] Co,[9] Ni,[10] Pd,[11] Pt,[11] Sc,[12] Mg,[13] and Zn[13] complexes and germylene-$B(C_6F_5)_3$ adducts[14] have proven to be effective for the selective reduction of CO_2 with hydrosilanes to the corresponding bis(silyl)acetal. It is noteworthy that all of these catalytic systems require the use of a Lewis acid, such as $B(C_6F_5)_3$, to selectively achieve the formation of the corresponding bis(silyl)acetal.[16] The selectivity of these processes depends on the metal/$B(C_6F_5)_3$ ratio. Thus, with an excess of borane, the formation of methane is facilitated.[6−14] Although the effectivity of $B(C_6F_5)_3$ as a hydrosilylation catalyst is well-known,[17] $B(C_6F_5)_3$ alone cannot catalyze the hydrosilylation of CO_2.[6a,18]

It has recently been proven that bis(silyl)acetal, $H_2C(OSiPh_3)_2$, provides a means to incorporate CH_n (n = 1 or 2) moieties into organic molecules.[19] Therefore, developing catalytic systems effective for the reduction of CO_2 to the bis(silyl)acetal level using hydrosilanes is of great interest.

To date, few studies have been reported on the mechanism of these processes. Indeed, the mechanistic discussion remains open. For example, two different mechanisms have been proposed for the bis(phosphino)borylnickel hydride/$B(C_6F_5)_3$-catalyzed reduction of CO_2 to the formaldehyde level with hydrosilanes. Thus, while Rodriguez et al. proposed a boron-promoted Si−H activation mechanism,[10a,b] Ke et al. proposed a nickel-promoted Si−H mechanism.[10c]

Understanding the mechanisms that operate in different transition-metal-catalyzed processes to reduce CO_2 with hydrosiloxanes is one of our aims.[20] We have recently reported that species $[Ir(CF_3CO_2)(\kappa^2\text{-}NSi^{Me})_2]$ [**1**; NSi^{Me} = (4-methylpyridin-2-yloxy)dimethylsilyl] catalyzes the selective reduction of CO_2 with $HSiMe(OSiMe_3)_2$ to the corresponding methoxysilane, $CH_3OSiMe(OSiMe_3)_2$, or silylformate, $HCO_2SiMe(OSiMe_3)_2$, under mild reaction conditions. The selectivity of this catalytic system can be easily tuned by controlling the pressure of CO_2.[21] It is noteworthy that the two active positions of the catalytic systems based on **1** are trans located to two silyl groups; in addition, the Ir−Si bond in such species is stronger than would be expected for a traditional Ir−silyl bond.[22] Hence, the positions trans to the Ir−Si bonds in $Ir(\kappa^2\text{-}NSi^{Me})_2$ complexes are highly activated.

We now report that using **1** as a catalyst precursor in the presence of catalytic amounts of $B(C_6F_5)_3$ allow achievement of the selective formation of bis(silyl)acetals by the reaction of CO_2 with hydrosilanes (Scheme 1).

^1H NMR studies of the **1**/$B(C_6F_5)_3$ (1:1 ratio; 1.0 mol %)-catalyzed reaction of CO_2 (1 bar) with $HSiMe(OSiMe_3)_2$

Received: September 19, 2022
Published: December 6, 2022

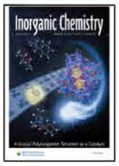

https://doi.org/10.1021/acs.inorgchem.2c03330
Inorg. Chem. 2022, 61, 20216−20221

Scheme 1. 1-Catalyzed (1.0 mol %) Reactions of CO_2 with Tertiary Silanes in the Presence of $B(C_6F_5)_3$ (1.0 mol %)

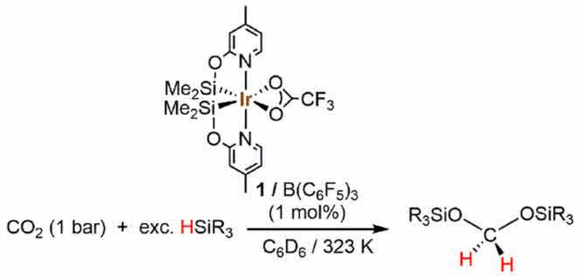

SiR_3 = $SiMe(OSiMe_3)_2$ (**2a**), $SiMe_2Ph$ (**2b**); $SiMePh_2$ (**2c**) $SiEt_3$ (**2d**)

(HMTS) in C_6D_6 at 323 K show the slow and selective formation of $H_2C\{OSiMe(OSiMe_3)_2\}_2$ (**2a**; Table 1, entry 1). To explore the scope of this catalytic process, we performed the reaction of CO_2 with different silicon hydrides ($HSiMe_2Ph$, $HSiMePh_2$, $HSiEt_3$, and $HSiMe(OSiMe_3)_2$) in the presence of **1**/$B(C_6F_5)_3$ (1:1) in C_6D_6. The best reaction conditions were found to be CO_2 (1 bar) and 323 K. The reactions are highly selective to the formation of the corresponding bis(silyl)acetal (Table 1, entries 1, 2, 4, and 5). The nature of silane influences the reaction performance. The best reaction rates were obtained using $HSiMe_2Ph$ and $HSiMePh_2$ (Table 1). The reactions with HMTS and $HSiEt_3$ were slower, which can be attributable to the higher hindrance of the Si−H bond in such compounds.

^1H NMR studies of the **1**/$B(C_6F_5)_3$ (1:1; 1.0 mol %)-catalyzed reaction of CO_2 with $HSiMe_2Ph$ in C_6D_6 at 323 K demonstrate the influence of CO_2 pressure on the reaction performance; at 3 bar, the reactions are faster but less selective than those at at 1 bar (Table 1, entries 2 and 6). The stoichiometry of borane is a key factor in the selectivity of these catalytic processes. Within the range of 1−3 bar of CO_2, if the load of $B(C_6F_5)_3$ is increased from 1.0 to 2.0 mol %, the reactions are selective toward the formation of methane[23] and $O(SiMe_2Ph)_2$, albeit at a lower rate (Table 1, entry 7). While reducing the amount of $B(C_6F_5)_3$ to 0.5 mol % does not alter the activity, the selectivity is affected, resulting in the formation of silylformate (82%) and bis(silyl)acetal (18%) as secondary products (Table 1, entry 8). In the absence of additives, the catalyst precursor **1** promotes the reduction of CO_2 (1 bar) with $HSiMe_2Ph$ to give silylformate (90%) as major reaction product (Table 1, entry 9).

^1H NMR studies of the **1**-catalyzed (1.0 mol %) reaction of CO_2 (1 bar) with $HSiMe_2Ph$ in the presence of BPh_3 (1.0 mol %), instead of $B(C_6F_5)_3$, show a slower and less selective reaction. After 24 h, a 73% conversion of hydrosilane is reached to give a mixture of the corresponding silylformate (81%), bis(silyl)acetal (12%), and methoxysilane (7%) (Table 1, entry 3). Therefore, BPh_3 plays a role in the activity and selectivity of the process, although to a lesser degree than $B(C_6F_5)_3$, which can be correlated to its lower Lewis acidic character.[24]

Scheme 2. NMR Monitoring of the Stepwise Stoichiometric Reaction

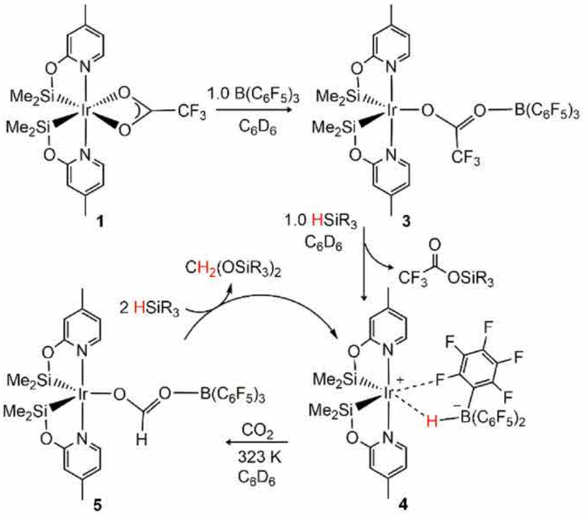

^1H NMR studies of the reaction of **1** with $B(C_6F_5)_3$ evidenced the quantitative formation of $[Ir(CF_3COO\text{-}B(C_6F_5)_3)(\kappa^2\text{-}NSi^{Me})_2]$ [**3** (CCDC 2218258); Scheme 2]. Contrarily, no reaction is observed between **1** and BPh_3 under the same conditions. The molecular structure of **3** has been confirmed by X-ray diffraction studies (Figure S38). The

Table 1. Results from the 1 (1.0 mol %)- and BR_3-Catalyzed Reaction of CO_2 with Hydrosilanes in C_6D_6 at 323 K

							ratio of the reaction products			
entry	silane	borane	equiv of BR_3	CO_2 (bar)	time (h)	conversion (%)[a]	OCHO (%)[b]	OCH_2O (%)[b]	CH_3O (%)[b]	CH_4 (%)
1	HMTS	$B(C_6F_5)_3$	1	1	16	28		>99	<1	
					40	74		>99	<1	
2	$HSiMe_2Ph$	$B(C_6F_5)_3$	1	1	16	93		>99	<1	
					40	>99		>99		
3	$HSiMe_2Ph$	BPh_3	1	1	24	73	81	12	7	
4	$HSiMePh_2$	$B(C_6F_5)_3$	1	1	16	78		>99	<1	
					40	>99		>99	<1	
5	$HSiEt_3$	$B(C_6F_5)_3$	1	1	16	12		>99	<1	
					40	25		>99	<1	
6	$HSiMe_2Ph$	$B(C_6F_5)_3$	1	3	8	>99	83	13	4	
7	$HSiMe_2Ph$	$B(C_6F_5)_3$	2	1	24	48				>99[c]
8	$HSiMe_2Ph$	$B(C_6F_5)_3$	0.5	1	24	93	82	18		
9	$HSiMe_2Ph$			1	24	50	90	2	8	

[a] Conversion and selectivity percentages are based on ^1H NMR integration using hexamethylbenzene (0.0525 mmol) as an internal standard. [b] Composition of the mixture of products. [c] On the basis of the ^1H NMR integral of $O(SiMe_2Ph)_2$, 12% CH_4 was formed.

https://doi.org/10.1021/acs.inorgchem.2c03330
Inorg. Chem. 2022, 61, 20216−20221

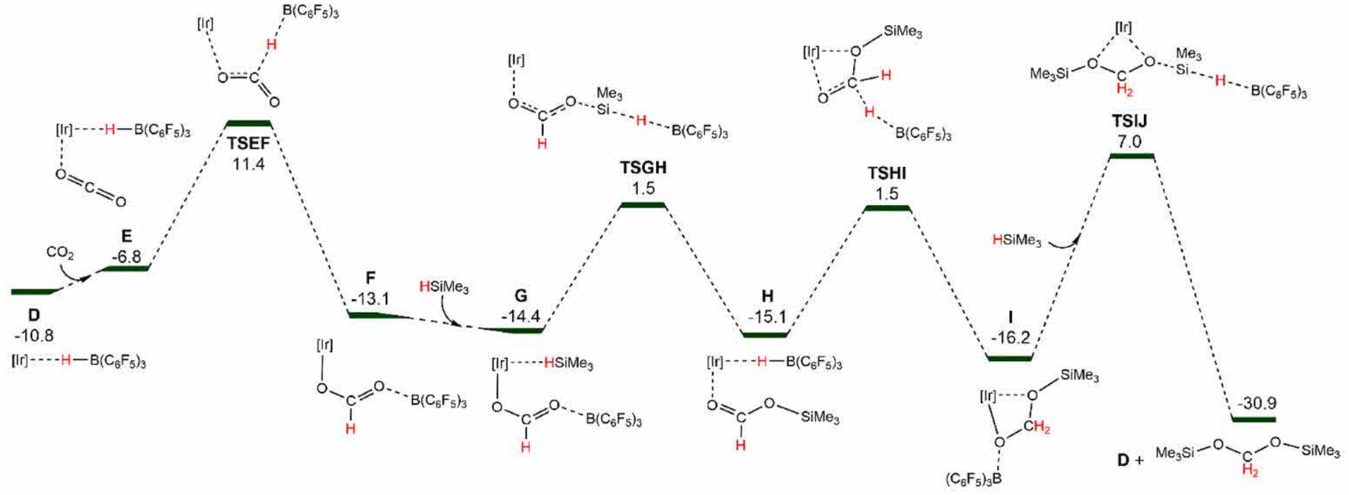

Figure 1. DFT-calculated Gibbs free energy profile for the catalytic formation of bis(silyl)acetal from **E** (kcal mol^{-1}) relative to **A**.

geometrical parameters of the [Ir(κ^2-NSi^{Me})$_2$] fragment (see the Supporting Information, SI) agree with those of **1**, with short Ir−Si bond lengths [2.2526(11) and 2.2599(11) Å]. The Ir−O bond length in **3** [2.285(3) Å] is shorter than those found in **1** [2.363(3) and 2.418(3) Å].[22a]

The ^{11}B{^{1}H} NMR spectra of **3** show a singlet at $\delta = -1.7$ ppm (Figure S18), in agreement with what is expected for the O−B(C_6F_5)$_3$ fragment[25] (Scheme 2). The absolute value of the difference between δ_{para} and δ_{meta} of the fluorine atoms $\Delta(\delta_{m,p})$ in the ^{19}F NMR spectra of **3** is 6.3 ppm (Figure S21), which agrees with the presence of a tetracoordinated borate anion.[26,27]

The addition of 1 equiv of HSiMe(OSiMe$_3$)$_2$, at room temperature (RT), to C_6D_6 solutions of **3** gives [Ir(κ^2-NSi^{Me})$_2$][HB(C_6F_5)$_3$] (**4**) and $CF_3CO_2SiR_3$. The ^{11}B NMR spectra of **4** show a doublet resonance at $\delta = -15.1$ ppm ($^1J_{B-H}$ = 53 Hz),[12b,15a] which in the ^{11}B{^{1}H} NMR spectra appears as a singlet (Figures S24 and S25). Moreover, the ^{19}F NMR spectra show a $\Delta(\delta_{m,p})$ value of ∼6 ppm, which is higher than the characteristic values found for noncoordinating [HB(C_6F_5)$_3$]$^-$ anions [$\Delta(\delta_{m,p}) < 3$ ppm], which indicates a certain degree of coordination of the [HB(C_6F_5)$_3$]$^-$ anion to the metallic center.[17b]

The addition of an excess of HSiMe(OSiMe$_3$)$_2$ to C_6D_6 solutions of **3** produces **4** and CF_3CH\{OSiMe(OSiMe$_3$)$_2$\}$_2$. Note that the overreduced product CF_3CH_2OSiMe(OSiMe$_3$)$_2$ is not obtained, which is reminiscent of the **1**/B(C_6F_5)$_3$ system selectivity toward the bis(silyl)acetal species. This evidences the effective entrapment of B(C_6F_5)$_3$ in the form of a hydridoborate ion pair because the free borane might promote activation of the Si−H bond toward reduction of the bis(silyl)acetal derivatives, as well as the direct participation of **4** in the catalytic reaction, because **4** not only promotes hydrosilylation of the TFA ligand or CO_2 but also catalyzes reduction of the R′COOSiR$_3$ species (R′ = H, CF_3).

The ^{1}H NMR spectra of **4** in C_6D_6 show no changes when pressurized with CO_2 (3 bar) at RT. However, after the reaction mixture is heated at 323 K, the formation of complex [Ir(HCOOB(C_6F_5)$_3$)(κ^2-NSi^{Me})$_2$] (**5**) is observed. The presence of a IrOC(H)OB(C_6F_5)$_3$ moiety in **5** has been demonstrated by means of ^{1}H, ^{13}C, ^{11}B, and ^{19}F NMR spectroscopies (Figures S32−S36). The addition of 2 equiv of HSiMe(OSiMe$_3$)$_2$ to a solution of **5**, in the absence of CO_2, produces the formation of **2a** and the regeneration of **4** within 1 h at RT (Scheme 2). Exposure of **5** to $^{13}CO_2$ (2.7 bar) at 353 K for 48 h did not result in the partial substitution of [Ir]OC(H)OB(C_6F_5)$_3$ to the ^{13}C-enriched [Ir]O^{13}C(H)OB(C_6F_5)$_3$, which suggests that, different from that reported for analogous MOC(H)OB(C_6F_5)$_3$ (M = Re,[8] Ni,[10] Pd,[11] Pt[11]) species, the CO_2 insertion step to give **5** is irreversible under the catalytic conditions.

Density functional theory (DFT) studies at the M06L-(SMD)/def2-TZVP//B3LYP-D3(BJ)/def2-SVP level have been performed to study in detail the reaction mechanism of CO_2 hydrosilylation catalyzed by **3** (see the SI). HSiMe$_3$ has been selected as a model system for the silanes. The Gibbs free energy energetic profile for the catalyst activation process, from **3** (**A**) to **4** (**D**) (Figure S39), is exoergic by 10.8 kcal mol^{-1}. Si−H bond activation occurs via boron-promoted Si−H cleavage **TSBC** (9.0 kcal mol^{-1}), which corresponds to a linear S_N2 nucleophilic attack of the terminal oxygen of the trifluoroacetate ligand to the silicon atom in which the leaving hydride is transferred to the boron moiety. A similar type of activation mechanism has been proposed for Lewis acid PBP−Ni hydrosilylation of CO_2 based on DFT calculations.[10b] An alternative mechanism for the Si−H activation step based on a nickel-promoted Si−H cleavage has been proposed.[10c] In our case, the iridium-promoted Si−H cleavage is energetically disfavored (see Figures S40 and S41 for a comparison of both pathways). Intermediate **D** can be described as a hydroborate moiety and a cationic metallic complex rather than a metal hydride interacting with the Lewis acid. Inspection of the natural bond orbitals reveals a σ(B−H) bonding orbital with an electron population of 1.76 electrons (Figure S42).

The coordination of CO_2 to **D** leads to the beginning of the catalytic cycle. The Gibbs free energy profile for this process is reported in Figure 1. The first step corresponds to hydride transfer from HB(C_6F_5)$_3$ to CO_2 via **TSEF** at an energy barrier of 22.2 kcal mol^{-1} from intermediate **D**. The obtained intermediate **F** is thermodynamically favored (−13.1 kcal mol^{-1}) and corresponds to complex **5** experimentally detected by NMR. Following that, the addition of silane leads to σ^1-*H*-(HSiMe$_3$) coordination to **F**, yielding **G**. Then, activation of the Si−H bond takes place via **TSGH**, like the previously reported **TSBC**, consisting of the linear S_N2 nucleophilic attack of the terminal oxygen atom of the formate to the silicon atom and transfer of the leaving hydride to the boron atom of the Lewis acid. The activation barrier of **TSGH** is 15.9 kcal mol^{-1}, leading to intermediate **H**. The subsequent hydride transfer from the hydroborate to the carbon atom of the silylformate coordinated to the metal takes place through **TSHI**, yielding intermediate **I**. Upon reaction with another molecule of $HSiMe_3$, the silylformate develops into the final bis(silyl)acetal product via **TSIJ**, with the activation energy for this step being 23.2 kcal mol^{-1}. This activation barrier for the boron-promoted Si−H bond cleavage is higher than those of the previously related processes, **TSBC** (9.0 kcal mol^{-1}) and **TSGH** (15.9 kcal mol^{-1}). It should be noted that, for **TSIJ**, the nucleophilic attack to the silane is performed by an alkoxy group,[10,17c,28] in contrast with previous steps, where the nucleophilic attack was performed by trifluoroacetate and formate groups.

The catalytic process is strongly exergonic (−30.9 kcal mol^{-1}), and the rate-limiting step is boron-promoted Si−H cleavage by the iridium silylacetal borane adduct **I** (23.2 kcal mol^{-1}) characterized by **TSIJ**. This activation barrier agrees with the experimental finding that the reaction proceeds slowly at RT. Indeed, the reaction of **4** with CO_2 (3 bar) to give **5** requires heating at 323 K. It should be noted that the intermediates proposed in the DFT-calculated catalytic cycle match the experimentally detected species (**4** and **5**; Scheme 2).

In conclusion, this is the first example of an iridium-based catalytic system effective for the selective reduction of CO_2 to the formaldehyde level with hydrosilanes. The selectivity of this catalytic system to the formation of bis(silyl)acetals is determined by the interaction between the active species and the Lewis acid $B(C_5F_6)_3$. In fact, any factor that affects that interaction influences the selectivity of the process. Thus, using a borane with a lower Lewis acidity such as BPh_3, high temperature, or CO_2 pressure higher than 1.0 bar inhibit the selectivity toward the bis(silyl)acetal. DFT calculations support a boron-promoted Si−H cleavage mechanism, with the rate-limiting step being boron-promoted Si−H cleavage by the iridium silylacetal borane adduct **I**.

■ ASSOCIATED CONTENT

Supporting Information

The Supporting Information is available free of charge at https://pubs.acs.org/doi/10.1021/acs.inorgchem.2c03330.

Experimental details, NMR spectra, crystallographic, and theoretical calculation data (PDF)

Accession Codes

CCDC 2218258 contains the supplementary crystallographic data for this paper. These data can be obtained free of charge via www.ccdc.cam.ac.uk/data_request/cif, or by emailing data_request@ccdc.cam.ac.uk, or by contacting The Cambridge Crystallographic Data Centre, 12 Union Road, Cambridge CB2 1EZ, UK; fax: +44 1223 336033.

■ AUTHOR INFORMATION

Corresponding Author

Francisco J. Fernández-Alvarez − *Facultad de Ciencias, Departamento de Química Inorgánica, Instituto de Síntesis Química y Catálisis Homogénea, Universidad de Zaragoza, CSIC, Zaragoza 50009, Spain*; orcid.org/0000-0002-0497-1969; Email: paco@unizar.es

Authors

Jefferson Guzmán − *Facultad de Ciencias, Departamento de Química Inorgánica, Instituto de Síntesis Química y Catálisis Homogénea, Universidad de Zaragoza, CSIC, Zaragoza 50009, Spain*

Asier Urriolabeitia − *Facultad de Ciencias, Departamento de Química Física, BIFI, Universidad de Zaragoza, Zaragoza 50009, Spain*; orcid.org/0000-0001-9352-6922

Marina Padilla − *Facultad de Ciencias, Departamento de Química Inorgánica, Instituto de Síntesis Química y Catálisis Homogénea, Universidad de Zaragoza, CSIC, Zaragoza 50009, Spain*

Pilar García-Orduña − *Facultad de Ciencias, Departamento de Química Inorgánica, Instituto de Síntesis Química y Catálisis Homogénea, Universidad de Zaragoza, CSIC, Zaragoza 50009, Spain*

Víctor Polo − *Facultad de Ciencias, Departamento de Química Física, BIFI, Universidad de Zaragoza, Zaragoza 50009, Spain*; orcid.org/0000-0001-5823-7965

Complete contact information is available at: https://pubs.acs.org/10.1021/acs.inorgchem.2c03330

Author Contributions

J.G., M.P., and F.J.F.-A., experimental studies; P.G.-O., X-ray diffraction; A.U. and V.P., theoretical calculations.

Notes

The authors declare no competing financial interest.

■ ACKNOWLEDGMENTS

Financial support from Projects PGC2018-099383-B-I00 (MCIU/AEI/FEDER, UE) and DGA/FSE Project E42_20R is gratefully acknowledged. A.U. thankfully acknowledges the Spanish MECD for a FPU fellowship (FPU 2017/05417). The authors acknowledge the resources from the supercomputers “Memento” and “Cierzo” and technical expertise and assistance provided by BIFI-ZCAM (Universidad de Zaragoza, Spain). M.P. thankfully acknowledges the resources cofinanced with the European Social Fund (ESF) and the Youth Employment Initiative assigned to the CSIC in the Youth Employment Operational Program ESF 2014-2020.

■ REFERENCES

(1) (a) Artz, J.; Müller, T. E.; Thenert, K.; Kleinekorte, J.; Meys, R.; Sternberg, A.; Bardow, A.; Leitner, W. Sustainable Conversion of Carbon Dioxide: An Integrated Review of Catalysis and Life Cycle Assessment. *Chem. Rev.* **2018**, *118*, 434−504. (b) Stahel, W. R. The circular economy. *Nature* **2016**, *531*, 435−438. (c) Clark, J. H.; Farmer, T. J.; Herrero-Davila, L.; Sherwood, J. Circular economy design considerations for research and process development in the chemical sciences. *Green Chem.* **2016**, *18*, 3914−3934. (d) Grignard, B.; Gennen, S.; Jérôme, C.; Kleij, A. W.; Detrembleur, C. Advances in the use of CO_2 as a renewable feedstock for the synthesis of polymers. *Chem. Soc. Rev.* **2019**, *48*, 4466−4514. (e) Martens, J. A.; Bogaerts, A.; De Kimpe, N.; Jacobs, P. A.; Marin, G. B.; Rabaey, K.; Saeys, M.; Verhelst, S. The Chemical Route to a Carbon Dioxide Neutral World. *ChemSusChem* **2017**, *10*, 1039−1055.

(2) For some reviews, see: (a) Liu, Q.; Wu, L.; Jackstell, R.; Beller, M. Using carbon dioxide as a building block in organic synthesis. *Nat. Commun.* **2015**, *6*, 5933. (b) Wang, W.-H.; Himeda, Y.; Muckerman, J. T.; Manbeck, G. F.; Fujita, E. CO_2 Hydrogenation to Formate and Methanol as an Alternative to Photo- and Electrochemical CO_2 Reduction. *Chem. Rev.* **2015**, *115*, 12936−12973. (c) Aresta, M.; Dibenedetto, A.; Angelini, A. Catalysis for the Valorization of Exhaust Carbon: from CO_2 to Chemicals, Materials, and Fuels. Technological

Use of CO_2. *Chem. Rev.* **2014**, *114*, 1709−1742. (d) Das Neves Gomes, C.; Jacquet, O.; Villiers, C.; Thuéry, P.; Ephritikhine, M.; Cantat, T. A Diagonal Approach to Chemical Recycling of Carbon Dioxide: Organocatalytic Transformation for the Reductive Functionalization of CO_2. *Angew. Chem., Int. Ed.* **2012**, *51*, 187−190. (e) Cokoja, M.; Bruckmeier, C.; Rieger, B.; Herrmann, W. A.; Kühn, F. E. Transformation of Carbon Dioxide with Homogeneous Transition-Metal Catalysts: A Molecular Solution to a Global Challenge? *Angew. Chem., Int. Ed.* **2011**, *50*, 8510−8537. (f) Peters, M.; Köhler, B.; Kuckshinrichs, W.; Leitner, W.; Markewitz, P.; Müller, T. E. Chemical Technologies for Exploiting and Recycling Carbon Dioxide into the Value Chain. *ChemSusChem* **2011**, *4*, 1216−1240. (g) Wang, W.; Wang, S.; Ma, X.; Gong, J. Recent advances in catalytic hydrogenation of carbon dioxide. *Chem. Soc. Rev.* **2011**, *40*, 3703−3727. (h) Sakakura, T.; Choi, J.-C.; Yasuda, H. Transformation of Carbon Dioxide. *Chem. Rev.* **2007**, *107*, 2365−2387. (i) Jessop, P. G.; Joó, F.; Tai, C.-C. Recent advances in the homogeneous hydrogenation of carbon dioxide. *Coord. Chem. Rev.* **2004**, *248*, 2425−2442. (j) Jessop, P. G.; Ikariya, T.; Noyori, R. Homogeneous Hydrogenation of Carbon Dioxide. *Chem. Rev.* **1995**, *95*, 259−272.

(3) For recent reviews on the catalytic hydrogenation of CO_2, see: (a) Ronda-Lloret, M.; Rothenberg, G.; Shiju, N. R. A Critical Look at Direct Catalytic Hydrogenation of Carbon Dioxide to Olefins. *ChemSusChem* **2019**, *12*, 3896−3914. (b) Onishi, N.; Laurenczy, G.; Beller, M.; Himeda, Y. Recent progress for reversible homogeneous catalytic hydrogen storage in formic acid and in methanol. *Coord. Chem. Rev.* **2018**, *373*, 317−332. (c) Jia, J.; Qian, C.; Dong, Y.; Li, Y. F.; Wang, H.; Ghoussoub, M.; Butler, K. T.; Walsh, A.; Ozin, G. A. Heterogeneous catalytic hydrogenation of CO_2 by metal oxides: defect engineering − perfecting imperfection. *Chem. Soc. Rev.* **2017**, *46*, 4631−4644.

(4) (a) Heim, L. E.; Konnerth, H.; Prechtl, M. H. G. Future perspectives for formaldehyde: pathways for reductive synthesis and energy storage. *Green Chem.* **2017**, *19*, 2347−2355. (b) Bahmanpour, A. M.; Hoadley, A.; Mushrif, S. H.; Tanksale, A. Hydrogenation of carbon monoxide into formaldehyde in liquid media. *ACS Sustainable Chem. Eng.* **2016**, *4*, 3970−3977. (c) Desmons, S.; Fauré, R.; Bontemps, S. Formaldehyde as a promising C1 source: The instrumental role of biocatalysis for stereocontrolled reactions. *ACS Catal.* **2019**, *9*, 9575−9588.

(5) Klankermayer, J.; Wesselbaum, S.; Beydoun, K.; Leitner, W. Selective catalytic synthesis using the combination of carbon dioxide and hydrogen: catalytic chess at the interface of energy and chemistry. *Angew. Chem., Int. Ed.* **2016**, *55*, 7296−7343.

(6) (a) Matsuo, T.; Kawaguchi, H. From Carbon Dioxide to Methane: Homogeneous Reduction of Carbon Dioxide with Hydrosilanes Catalyzed by Zirconium−Borane Complexes. *J. Am. Chem. Soc.* **2006**, *128*, 12362−12363. (b) Luconi, L.; Rossin, A.; Tuci, G.; Gafurov, Z.; Lyubov, D. M.; Trifonov, A. A.; Cicchi, S.; Ba, H.; Pham-Huu, C.; Yakhvarov, D.; Giambastiani, G. Benzoimidazole-Pyridylamido Zirconium and Hafnium Alkyl Complexes as Homogeneous Catalysts for Tandem Carbon Dioxide Hydrosilylation to Methane. *ChemCatChem.* **2019**, *11*, 495−510.

(7) (a) Jiang, Y.; Blacque, O.; Fox, T.; Berke, H. Catalytic CO_2 Activation Assisted by Rhenium Hydride/$B(C_6F_5)_3$ Frustrated Lewis Pairs—Metal Hydrides Functioning as FLP Bases. *J. Am. Chem. Soc.* **2013**, *135*, 7751−7760. (b) Morris, D. S.; Weetman, C.; Wennmacher, J. T. C.; Cokoja, M.; Drees, M.; Kühn, F. E.; Love, J. B. Reduction of carbon dioxide and organic carbonyls by hydrosilanes catalysed by the perrhenate anion. *Catal. Sci. Technol.* **2017**, *7*, 2838−2845.

(8) Metsänen, T. T.; Oestreich, M. Temperature-Dependent Chemoselective Hydrosilylation of Carbon Dioxide to Formaldehyde or Methanol Oxidation State. *Organometallics* **2015**, *34*, 543−546.

(9) (a) Cramer, H. H.; Chatterjee, B.; Weyhermüller, T.; Werlé, C.; Leitner, W. Controlling the Product Platform of Carbon Dioxide Reduction: Adaptive Catalytic Hydrosilylation of CO_2 Using a Molecular Cobalt(II) Triazine Complex. *Angew. Chem., Int. Ed.* **2020**, *59*, 15674−15681. (b) Cramer, H. H.; Ye, S.; Neese, F.; Werlé, C.; Leitner, W. Cobalt-Catalyzed Hydrosilylation of Carbon Dioxide to the Formic Acid, Formaldehyde, and Methanol Level-How to Control the Catalytic Network? *JACS Au* **2021**, *1*, 2058−2069.

(10) (a) Ríos, P.; Curado, N.; López-Serrano, J.; Rodríguez, A. Selective reduction of carbon dioxide to bis(silyl)acetal catalyzed by a PBP-supported nickel complex. *Chem. Commun.* **2016**, *52*, 2114−2117. (b) Ríos, P.; Rodriguez, A.; López-Serrano, J. Mechanistic Studies on the Selective Reduction of CO_2 to the Aldehyde Level by a Bis(phosphino)boryl (PBP)-Supported Nickel Complex. *ACS Catal.* **2016**, *6*, 5715−5723. (c) Huang, X.; Zhang, K.; Shao, Y.; Li, Y.; Gu, F.; Qu, L.-B.; Zhao, C.; Ke, Z. Mechanism of Si−H Bond Activation for Lewis Acid PBP-Ni-Catalyzed Hydrosilylation of CO_2: The Role of the Linear S_N2 Type Cooperation. *ACS Catal.* **2019**, *9*, 5279−5289.

(11) Mitton, S. J.; Turculet, L. Mild Reduction of Carbon Dioxide to Methane with Tertiary Silanes Catalyzed by Platinum and Palladium Silyl Pincer Complexes. *Chem. Eur. J.* **2012**, *18*, 15258−15262.

(12) (a) LeBlanc, F. A.; Piers, W. E.; Parvez, M. Selective Hydrosilation of CO_2 to a Bis(silylacetal) Using an Anilido Bipyridyl-Ligated Organoscandium Catalyst. *Angew. Chem., Int. Ed.* **2014**, *53*, 789−792. (b) Beh, D. W.; Piers, W. E.; Gelfand, B. S.; Lin, J.-B. Tanden deoxygenative hydrosilation of carbon dioxide with a cationic scandium hydridoborate and $B(C_6F_5)_3$. *Dalton Trans* **2020**, *49*, 95−101.

(13) Rauch, M.; Parkin, G. Zinc and Magnesium Catalysts for the Hydrosilylation of Carbon Dioxide. *J. Am. Chem. Soc.* **2017**, *139*, 18162−18165.

(14) Del Rio, N.; Lopez-Reyes, M.; Baceiredo, A.; Saffon-Merceron, N.; Lutters, D.; Müller, T.; Kato, T. *N,P*-Heterocyclic Germylene/$B(C_6F_5)_3$ Adducts: A Lewis Pair with Multi-reactive Sites. *Angew. Chem., Int. Ed.* **2017**, *56*, 1365−1370.

(15) For some recent examples of the catalytic hydroboration of CO_2, see: (a) Anker, M. D.; Arrowsmith, M.; Bellham, P.; Hill, M. S.; Kociok-Köhn, G.; Liptrot, D. J.; Mahon, M. F.; Weetman, C. Selective reduction of CO_2 to a methanol equivalent by $B(C_6F_5)_3$-activated alkaline earth catalysis. *Chem. Sci.* **2014**, *5*, 2826−2830. (b) Murphy, L. J.; Hollenhorst, H.; McDonald, R.; Ferguson, M.; Lumsden, M. D.; Turculet, L. Selective Ni-Catalyzed Hydroboration of CO_2 to the Formaldehyde Level Enabled by New PSiP Ligation. *Organometallics* **2017**, *36*, 3709−3720. (c) Espinosa, M. R.; Charboneau, D. J.; Garcia de Oliveira, A.; Hazari, N. Controlling Selectivity in the Hydroboration of Carbon Dioxide to the Formic Acid, Formaldehyde, and Methanol Oxidation Levels. *ACS Catal.* **2019**, *9*, 301−314. (d) Wang, X.; Chang, K.; Xu, X. Hydroboration of carbon dioxide enabled by molecular zinc dihydrides. *Dalton Trans* **2020**, *49*, 7324−7327. (e) Zhang, L.; Zhao, Y.; Liu, C.; Pu, M.; Lei, M.; Cao, Z. *Inorg. Chem.* **2022**, *61*, 5616−5625.

(16) (a) Ríos, P.; Rodríguez, A.; Conejero, S. Activation of Si−H and B−H bonds by Lewis acidic transition metals and p-block elements: same, but different. *Chem. Sci.* **2022**, *13*, 7392−7418. (b) Stahl, T.; Hrobárik, P.; Königs, C. D. F.; Ohki, Y.; Tatsumi, K.; Kemper, S.; Kaupp, M.; Klare, H. F. T.; Oestreich, M. Mechanism of the cooperative Si-H bond activation at Ru-S bonds. *Chem. Sci.* **2015**, *6*, 4324−4334.

(17) (a) Parks, D. J.; Piers, W. E. Tris(pentafluorophenyl)boron-Catalyzed Hydrosilylation of Aromatic Aldehydes, Ketones, and Esters. *J. Am. Chem. Soc.* **1996**, *118*, 9440−9441. (b) Parks, D. J.; Blackwell, J. M.; Piers, W. E. Studies on the Mechanism of $B(C_6F_5)_3$-Catalyzed Hydrosilation of Carbonyl Functions. *J. Org. Chem.* **2000**, *65*, 3090−3098. (c) Hog, D. T.; Oestreich, M. $B(C_6F_5)_3$-Catalyzed Reduction of Ketones and Imines Using Silicon-Stereogenic Silanes: Stereoinduction by Single-Point Binding. *Eur. J. Org. Chem.* **2009**, *2009*, 5047−5056. (d) Houghton, A. Y.; Hurmalainen, J.; Mansikkamäki, A.; Piers, W. A.; Tuononen, H. M. Direct observation of a borane-silane complex involved in frustrated Lewis-pair-mediated hydrosilylations. *Nat. Chem.* **2014**, *6*, 983−988. (e) Oestreich, M.; Hermeke, J.; Mohr, J. A unified survey of Si−H and H−H bond activation catalysed by electron-deficient boranes. *Chem. Soc. Rev.* **2015**, *44*, 2202−2220. (f) Keess, S.; Simonneau, A.; Oestreich, M. Direct and Transfer Hydrosilylation Reactions Catalyzed by Fully or

Partially Fluorinated Triarylboranes: A Systematic Study. *Organometallics* **2015**, *34*, 790−799.

(18) Berkefeld, A.; Piers, W. E.; Parvez, M. Tandem Frustrated Lewis Pair/Tris(pentafluorophenyl)borane-Catalyzed Deoxygenative Hydrosilylation of Carbon Dioxide. *J. Am. Chem. Soc.* **2010**, *132*, 10660−10661.

(19) Rauch, M.; Strater, Z.; Parkin, G. Selective Conversion of Carbon Dioxide to Formaldehyde via a Bis(silyl)acetal: Incorporation of Isotopically Labeled C1Moieties Derived from Carbon Dioxide into Organic Molecules. *J. Am. Chem. Soc.* **2019**, *141*, 17754−17762.

(20) (a) Lalrempuia, R.; Iglesias, M.; Polo, V.; Sanz Miguel, P. J.; Fernández-Alvarez, F. J.; Pérez-Torrente, J. J.; Oro, L. A. Effective Fixation of CO_2 by Iridium-Catalyzed Hydrosilylation. *Angew. Chem., Int. Ed.* **2012**, *51*, 12824−12827. (b) Julián, A.; Jaseer, E. A.; Garcés, K.; Fernández-Alvarez, F. J.; García-Orduña, P.; Lahoz, F. J.; Oro, L. A. Tuning the activity and selectivity of iridium-NSiN catalyzed CO_2 hydrosilylation processes. *Catal. Sci. Technol.* **2016**, *6*, 4410−4417. (c) Julián, A.; Guzmán, J.; Jaseer, E. A.; Fernández-Alvarez, F. J.; Royo, R.; Polo, V.; García-Orduña, P.; Lahoz, F. J.; Oro, L. A. Mechanistic Insights on the Reduction of CO_2 to Silylformates Catalyzed by Ir-NSiN Species. *Chem. Eur. J.* **2017**, *23*, 11898−11907.

(21) Guzmán, J.; García-Orduña, P.; Polo, V.; Lahoz, F. J.; Oro, L. A.; Fernández-Alvarez, F. J. Ir-catalyzed selective reduction of CO_2 to the methoxy or formate level with $HSiMe(OSiMe_3)_2$. *Catal. Sci. Technol.* **2019**, *9*, 2858−2867.

(22) (a) Guzmán, J.; Bernal, A. M.; García-Orduña, P.; Lahoz, F. J.; Polo, V.; Fernández-Alvarez, F. J. 2-Pyridone-stabilized iridium silylene/silyl complexes: structure and QTAIM analysis. *Dalton Trans* **2020**, *49*, 17665−17673. (b) García-Orduña, P.; Fernández, I.; Oro, L. A.; Fernández-Alvarez, F. J. Origin of the Ir−Si bond shortening in Ir−NSiN complexes. *Dalton Trans* **2021**, *50*, 5951−5959. (c) Gómez-España, A.; García-Ordua, P.; Guzmán, J.; Fernández, I.; Fernández-Alvarez, F. J. Synthesis and Characterization of Ir-(κ^2-NSi) Species Active toward the Solventless Hydrolysis of $HSiMe(OSiMe_3)_2$. *Inorg. Chem.* **2022**, *61*, 16282−16294.

(23) The selective formation of $^{13}CH_4$ was confirmed by ^{13}C labeling using $^{13}CO_2$ (Figure S37).

(24) Mayer, R. J.; Hampel, N.; Ofial, A. R. Lewis Acidic Boranes. Lewis bases, and Equilibrium Constants: A Reliable Scaffold for a Quantitative Lewis Acidity/Basicity Scale. *Chem. Eur. J.* **2021**, *27*, 4070−4080.

(25) Bibal, C.; Santini, C. C.; Chauvin, Y.; Vallée, C.; Olivier-Bourbigou, H. A selective synthesis of hydroxyborate anions as novel anchors for zirconocene catalysts. *Dalton Trans* **2008**, 2866−2870.

(26) (a) Hayes, P. G.; Xu, Z.; Beddie, C.; Keith, J. M.; Hall, M. B.; Tilley, T. D. The Osmium−Silicon Triple Bond: Synthesis, Characterization, and Reactivity of an Osmium Silylyne Complex. *J. Am. Chem. Soc.* **2013**, *135*, 11780−11783. (b) Berkefeld, A.; Piers, W. E.; Parvez, M.; Castro, L.; Maron, L.; Eisenstein, O. Decamethylscandocinium-hydrido-(perfluorophenyl)borate: fixation and tandem tris(perfluorophenyl)borane catalysed deoxygenative hydrosilation of carbon dioxide. *Chem. Sci.* **2013**, *4*, 2152−2162. (c) Horton, A. D. Direct Observation of β-Methyl Elimination in Cationic Neopentyl Complexes: Ligand Effects on the Reversible Elimination of Isobutene. *Organometallics* **1996**, *15*, 2675−2677.

(27) (a) Agnew, D. W.; Moore, C. E.; Rheingold, A. L.; Figueroa, J. S. Controlled *cis* Labilization of CO from Manganese(I) Mixed Carbonyl/Isocyanide Complexes: An Entry Point to Coordinatively Unsaturated Metallo-Lewis Acids. *Organometallics* **2017**, *36*, 363−371. (b) Beh, D. W.; Piers, W. E.; del Rosal, I.; Maron, L.; Gelfand, B. S.; Gendy, C.; Lin, J.-B. Scandium alkyl and hydride complexes supported by a pentadentate diborane ligand: reactions with CO_2 and N_2O. *Dalton Trans* **2018**, *47*, 13680−13688.

(28) (a) Robert, T.; Oestreich, M. Si-H Bond Activation: Bridging Lewis Acid Catalysis with Brookhart́s Iridium (III) Pincer Complex and $B(C_6F_5)_3$. *Angew. Chem., Int. Ed.* **2013**, *52*, 5216−5218. (b) Metsänen, T. T.; Hrobárik, P.; Klare, H. F. T.; Kaupp, M.; Oestreich, M. Insight into the Mechanism of Carbonyl Hydrosilylation Catalyzed by Brookhart́s Iridium (III) Pincer Complex. *J. Am. Chem. Soc.* **2014**, *136*, 6912−6915.

Dalton Transactions

ROYAL SOCIETY OF CHEMISTRY

PAPER

View Article Online
View Journal | View Issue

Cite this: *Dalton Trans.*, 2022, **51**, 4386

Dehydrogenation of formic acid using iridium-NSi species as catalyst precursors†

Jefferson Guzmán,[a] Asier Urriolabeitia,[b] Víctor Polo,[b] Marta Fernández-Buenestado,[a] Manuel Iglesias[a] and Francisco J. Fernández-Alvarez*[a]

Received 26th December 2021,
Accepted 3rd February 2022

DOI: 10.1039/d1dt04335h

rsc.li/dalton

Using a low loading of the iridium(III) complexes $[Ir(CF_3SO_3)(\kappa^2\text{-}NSi^{iPr})_2]$ (**1**) (NSi^{iPr} = (4-methylpyridin-2-yloxy)diisopropylsilyl) and $[\{Ir(\kappa^2\text{-}NSi^{Me})_2\}_2(\mu\text{-}CF_3SO_3)_2]$ (**2**) (NSi^{Me} = (4-methylpyridin-2-yloxy)dimethylsilyl) in the presence of Et_3N, it has been possible to achieve the solventless selective dehydrogenation of formic acid. The best catalytic performance ($TOF_{5\ min} \approx 2900\ h^{-1}$) has been achieved with **2** (0.1 mol%) and Et_3N (40 mol% to FA) at 373 K. Kinetic studies at variable temperatures show that the activation energy of the **2**-catalyzed process at 353 K is 22.8 ± 0.8 kcal mol^{-1}. KIE values of 1.33, 2.86, and 3.33 were obtained for the **2**-catalyzed dehydrogenation of HCOOD, DCOOH, and DCOOD, respectively, in the presence of 10 mol% of Et_3N at 353 K. These data show that the activation of the C–H bond of FA is the rate-determining step of the process. A DFT mechanistic study for the catalytic cycle involving hydride abstraction from the formate anion by the metal, assisted by a molecule of formic acid, and heterolytic H_2 formation has been performed. Moreover, the presence of Ir-formate intermediates was identified by means of NMR studies of the catalytic reactions in thf-d_8 at 323 K. In all the cases, the decomposition of the catalyst to give unactive crystalline iridium NPs was observed.

Introduction

The future implementation of the hydrogen economy on a global scale depends on achieving scientific and technological advances to overcome the difficulties related to its production, delivery, storage and transport.[1] In this context, liquid organic hydrogen carriers (LHCs) have become an alternative for the storage and transportation of H_2 in a safe and easy manner.[2] Among them, formic acid (FA) stands out as an interesting option since it can be easily prepared, stored and transported, and, in addition, it has a high volumetric concentration of H_2, which reaches 53 L^{-1}.[3]

Two competitive and thermodynamically accessible reaction pathways for the decomposition of FA can occur: the dehydrogenation to produce H_2 and CO_2, and the dehydration to give CO and H_2O (Scheme 1). In this regard, due to the CO poisoning of the Pt electrode in fuel cells,[4] the selective production of H_2 from FA is required to apply FA-based fuel cells in vehicles and other fuel cell-based technologies.[3h]

It is generally assumed that the first examples of homogeneous catalytic FA dehydrogenation (FADH) were reported by Coffey and co-workers in 1967.[5] They reported that Pt-, Rh-, Ru- and Ir-phosphane complexes catalyzed the FADH in acetic acid; particularly, the iridium(III) complex $[IrH_3(PPh_3)_3]$ was found to be a highly effective catalyst (TOF = 1187 h^{-1}).[5] Conversely, it was not until 2008 that Beller[6] and Laurenczy[7] and their respective co-workers reported the potential of the catalytic dehydrogenation of FA to supply hydrogen to fuel cells. Over recent decades, great advances have been made in this field.[3,4]

In this regard, it should be mentioned that several examples of highly active catalysts for FADH that operate in aqueous solution, such as the binuclear iridium-bipyridine catalysts described by Fujita and Himeda *et al.* (TOF = 228 000 h^{-1}),[8] the cationic species [IrClCp*(2,2′-bi-2-imidazo-

$$HCO_2H \xrightarrow{\text{dehydrogenation}} CO_2 + H_2$$

$$HCO_2H \xrightarrow{\text{dehydratation}} CO + H_2O$$

Scheme 1 Possible decomposition reactions for FA.

---

[a] *Departamento de Química Inorgánica – Instituto de Síntesis Química y Catálisis Homogénea (ISQCH). Universidad de Zaragoza, Facultad de Ciencias 50009, Zaragoza, Spain. E-mail: paco@unizar.es*

[b] *Departamento de Química Física – Instituto de Biocomputación y Física de Sistemas complejos (BIFI) – Universidad de Zaragoza, Facultad de Ciencias 50009, Zaragoza, Spain*

† Electronic supplementary information (ESI) available. See DOI: 10.1039/d1dt04335h

line)]Cl (TOF = 487 500 h^{-1}),[9] the Ir complex [IrCp*(H_2O)(DHBP)]$^{2+}$ (DHBP = 4,4′-dihydroxy-2,2′-bipyridine; (TOF = 14 000 h^{-1}),[10] the cationic ruthenium species [Ru(*p*-cymene)(2,2′-bi-2-imidazoline)Cl]Cl (TOF = 12 000 h^{-1})[11] and iridium compounds of general formula [IrClCp*(L)] (L = diphenylethylenediamine and derivatives; TOF ≈ 5000 h^{-1} and 11 000 h^{-1}),[12,13] have been reported in recent years. However, examples of catalytic solventless dehydrogenation of FA, which is of great interest since it allows one to reduce the reaction volume and avoids the use of organic solvents that could damage the fuel cell, are scarce.[14]

A pioneering example of solventless catalytic FADH was published by Williams *et al.* in 2016.[14d] They found that in the presence of catalytic amounts (0.005 mol%, 50 ppm) of the iridium(I) species [Ir(cod)(κ^2-NP^{tBu})][CF_3SO_3] (NP^{tBu} = 2-({di-*t*-butylphosphino}methyl)pyridine) and 5 mol% of the formate base it was possible to achieve the dehydrogenation of FA with a maximum TOF value of 13 300 h^{-1}. Recently, Fischmeister *et al.* (max. TOF ≈ 13 300 h^{-1}),[14a] Iglesias and Oro *et al.* (max. TOF ≈ 11 600 h^{-1})[14b] and Gelman *et al.* (TOF ≈ 11 800 h^{-1})[14c] have also reported examples of highly active iridium catalysts for solventless FADH.

In this work, as a continuation of our studies on the catalytic properties of iridium[15] and rhodium[16] species with pyridin-2-yloxy-silyl based ligands in catalysis, we have explored the potential of iridium(III) complexes with monoanionic bidentate (κ^2-NSi^R; R = Me, {4-methylpyridine-2-yloxy}dimethylsilyl; R = ^{i}Pr, {4-methylpyridine-2-yloxy}diisopropylsilyl) ligands as catalysts for the dehydrogenation of FA in the presence of Et_3N.

Results and discussion

NMR studies of the iridium-NSi^R catalyzed FADH in thf-d_8 in the presence of Et_3N

The first examples of transition-metal catalyzed generation of H_2 from FA–amine adducts were reported by Beller *et al.* in 2008.[6] Since then, a number of catalytic systems effective for the hydrogen generation from FA–amine adducts have been reported, including Ru,[6,18] Fe,[19] and Mn[20] complexes and organocatalysts.[21] These systems usually operate with 2 equiv. of amine per 5 equiv. of formic acid (40 mol% of amine to FA). In this regard, Beller *et al.* found that a reduction of the catalytic performance was observed when using a lower amine loading.[6] Moreover, it has been reported that the nature of the amine influences the potential of the FA–amine adducts as a hydrogen source, the best results have commonly been obtained using the FA–Et_3N system.[6,18–21]

To explore the potential of the iridium-NSi^R species as catalyst precursors for the dehydrogenation of FA, ^{1}H NMR studies of FADH in thf-d_8 using complexes [Ir(CF_3SO_3)(κ^2-NSi^{iPr})$_2$] (**1**)[17] and [{Ir(κ^2-NSi^{Me})$_2$}$_2$(μ-CF_3SO_3)$_2$] (**2**)[15c] as catalyst precursors (Scheme 2) and NEt_3 (40 mol% to FA) as the base have been performed (Fig. S1–S8†).

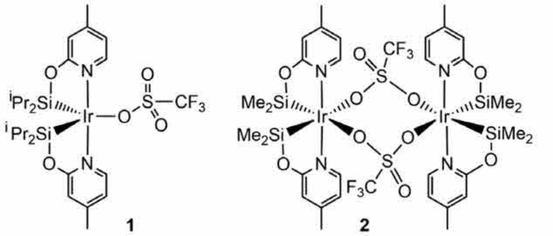

Scheme 2 Catalyst precursors **1** and **2**.

We have found that the thf-d_8 solutions of complexes **1** (or **2**) and FA (20 equiv. of FA to Ir) are stable at 323 K for at least 3 hours. Under these conditions only traces of H_2 (δ 4.56 ppm) were observed in the ^{1}H NMR spectra of such solutions (Fig. S1 and S2†). The ^{1}H NMR spectra of the thf-d_8 solutions of **1**, FA (20 equiv. to Ir) and Et_3N (40 mol% to FA) show no changes at RT, and it is necessary to heat at 323 K for 30 min to observe the full transformation of **1** into the species [Ir(OCHO)(κ^2-NSi^{iPr})$_2$] (**3**) and the formation of H_2 (Scheme 3). All the attempts to isolate **3** were unsuccessful. However, it has been characterized in solution by means of ^{1}H, ^{13}C and ^{29}Si NMR spectroscopy (Fig. S4, S5 and S6†). The most noticeable resonance in the ^{1}H NMR spectra of **3** is a singlet at δ 10.11 ppm, which correlates in the ^{1}H–^{13}C HSQC spectra with a singlet that appears at δ 175.7 ppm in the ^{13}C APT spectra. ^{29}Si{^{1}H} NMR shows a single resonance centered at δ 41.4 ppm, which correlates in the ^{1}H–^{29}Si HMBC spectra with the resonances due to the Si–^{i}Pr protons in the ^{1}H NMR. This value compares well with the values reported for [Ir(X)(κ^2-NSi^{iPr})$_2$] (X = Cl, CF_3SO_3) species. Moreover, the ^{1}H NMR spectra show the resonances corresponding to H_2 and to the [HEt_3N]$^+$ cation. Moreover, the ^{13}C NMR spectra evidenced the presence of CO_2 (Fig. S8†) and no traces of CO were observed. These outcomes show that the Ir–Si bond in **3** is stronger than a normal Ir–silyl bond, which agrees with the silyl/base-stabilized silylene character reported for such bonds.[17]

On the other hand, ^{1}H NMR studies of the behavior of the thf-d_8 solutions of **2** and FA (20 equiv. to Ir) and Et_3N (40 mol% to FA) show that at RT the catalytic process is slow, and it is necessary to heat at 323 K to achieve a reasonable activity. These studies showed the transformation of **2** into a mixture of complexes. Although, in this case, it has not been

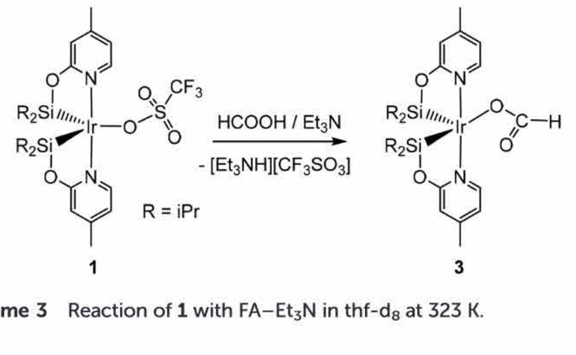

Scheme 3 Reaction of **1** with FA–Et_3N in thf-d_8 at 323 K.

possible to characterize the components of these mixtures. It has been observed that two components of these mixtures are Ir–(OC*H*O) (δ 10.25 ppm), related to **3**, and Ir–(*H*) (δ −24.88 ppm) species (Fig. S7†). Moreover, the formation of H_2 and the disappearance of the resonances of FA during the catalytic process were observed.

Therefore, these NMR studies evidenced that the thf-d_8 solutions of both complexes, **1** and **2**, promote the FADH in the presence of Et_3N.

Ir-NSi^R catalyzed dehydrogenation of FA using Et_3N as the base

The outcomes of the NMR studies prompted us to overcome the challenges of using the systems based on **1** (or **2**) and Et_3N as the catalyst precursor, for the solventless catalytic FADH. In all the experiments, the gas evolution was measured using a *man on the moon*™ reactor ($H_2 : CO_2 = 1 : 1$).[22]

A comparative study of the activity of complexes **1** and **2** as catalyst precursors for the hydrogen generation from FA–Et_3N (10 mol% of Et_3N to FA) at 353 K under neat conditions shows that complex **2** ($TOF_{10\ min} = 190\ h^{-1}$) is a more effective catalyst precursor than **1** ($TOF_{10\ min} = 6\ h^{-1}$) (Fig. S9†). This result agrees with the outcomes of the NMR studies. Therefore, we decided to further explore the **2**-catalyzed FADH processes.

To shed light on the effect of the Et_3N concentration on the reaction performance, we have performed experiments varying the concentration of Et_3N from 1.0 to 40 mol% (to FA) using **2** (0.1 mol% to Ir) as the catalyst precursor under neat conditions and at 353 K. The outcomes of these studies, which are shown in Fig. 1, revealed that the experiments performed with an initial concentration of Et_3N of 40 mol% to FA (FA : Et_3N ratio of 5 : 2) show higher catalytic performance. Reducing the amine concentration results in a decrease in the activity. Consequently, in agreement with this, a lower concentration of Et_3N (1.0 to 5.0 mol%) results in lower catalytic performances. It should be mentioned that when using an initial concentration of Et_3N of 20 mol% to FA an acceleration of the reaction rate is observed after one hour, which could be a consequence of the gradual increase of the relative amine–FA ratio due to the consumption of FA.

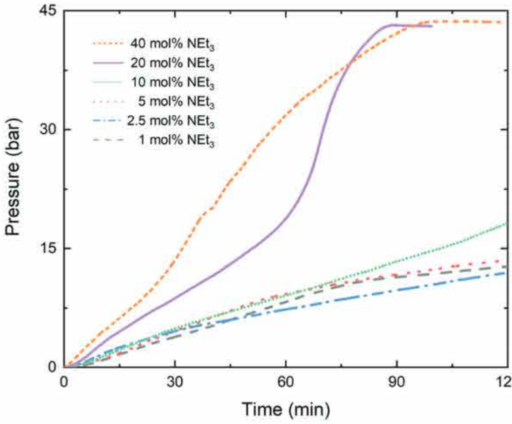

Fig. 1 Pressure of H_2 (bar) *vs.* time observed during the **2**-catalyzed (0.1 mol% referred to Ir) solventless dehydrogenation of formic acid–Et_3N adducts at 353 K (concentration of Et_3N referred to FA.

Next, we have studied the effect of the temperature on the performance of the catalytic FADH using **2** as the catalyst precursor. In this study, we decided to use an initial concentration of Et_3N of 10 mol% and a catalyst loading of 0.1 mol% referred to iridium (**2** contains two Ir atoms). These studies revealed that as expected the temperature provides a positive effect on the reaction performance (Fig. 2). In all cases, after 20–30 minutes, the slow formation of a gray precipitate due to the decomposition of the catalyst was observed.

The highest activity of this system has been found using **2** (0.10 mol% referred to Ir) and Et_3N (40 mol%) at 373 K, resulting in a TOF value of 2900 h^{-1} calculated at 5 min (Fig. 3). Under these conditions, the activity of complex **2** is in the range of those reported for transition metal base catalyzed dehydrogenation of the FA–Et_3N (5 : 2) adduct under neat conditions (Table 1).[6,14d,20]

It should be mentioned that **2** catalyzes the FADH selectively (Scheme 1). The FT-IR spectra of the gas obtained from the FADH reactions evidenced the presence of CO_2, and no

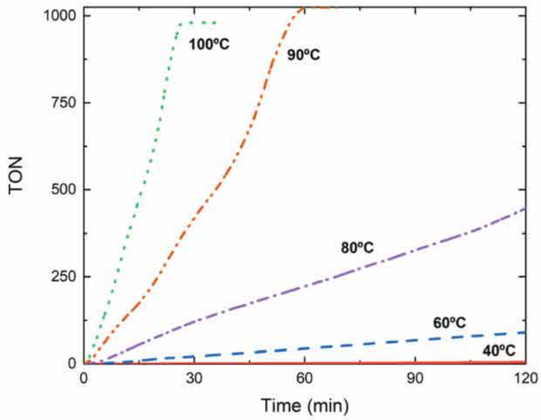

Fig. 2 TON (mol of H_2 per mol of Ir) *vs.* time representation of the **2**-catalyzed (0.1 mol%) solvent-free FA dehydrogenation in the presence of Et_3N (10 mol% to FA) at different temperatures.

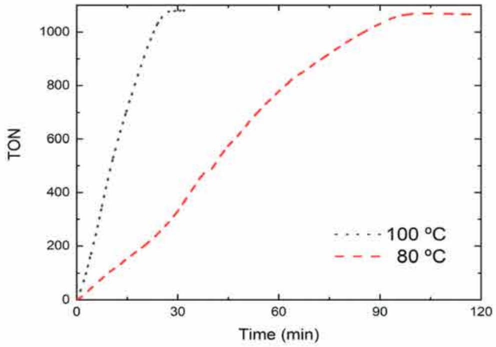

Fig. 3 TON (mol of H_2 per mol of Ir) *vs.* time representation of the **2**-catalyzed (0.1 mol%) solventless FA dehydrogenation in the presence of Et_3N (40 mol% to FA) at 353 K and 373 K.

Table 1 Comparison of the activity of **2** (0.1 mol%) as the catalyst precursor for the solventless dehydrogenation of FA with other metal base catalysts

Catalyst	*T* (K)	TOF (h^{-1})	Base	Ref.
Compound **2**	373	2900	Et_3N (5 : 2)	This work
$[Mn(CO)_2(^{tBu}PNNOP)]^a$	353	8500	Et_3N (5 : 2)	21
$[RuCl_2(PPh_3)_3]$	313	240	Et_3N (5 : 2)	6
$[Ir(COD)(NP^{tBu})]^{+\,b}$	363	3000	NaO_2CH (5 mol%)	14*d*

[a] ^{tBu}PNNOP = 2,6-(ditertbutylphosphinito)(ditertbutylphosphineamine).pyridine. [b] NP^{tBu} = 2-({di-*t*-butylphosphino}methyl)pyridine.

detectable amounts of CO were observed (Fig. S13†). We have also analysed the resulting gas using a GC column of type HP PLOT Molesieve 5A (30 m × 0.32 mm, 25 μm), which excludes molecules by molecular size, so it allows CO to be observed even in ppm amounts (Fig. 4). This study confirms that no CO is present in the obtained gas, which is of great importance for fuel cell applications due to CO poisoning of the Pt electrode and compares well with the selectivity found for other iridium based FADH catalysts.[3,4]

Kinetic and mechanistic studies

A catalytic study of the **2**-catalyzed (0.10 mol% to Ir) FA dehydrogenation using Et_3N (10 mol% to FA) at different temperatures, from 313 to 373 K, (Fig. 2) allowed one to calculate the initial $TOF_{5\ min}$ values (Fig. S15†). The Arrhenius plot for these data yields an apparent activation energy of 27.50 ± 0.88 kcal mol^{-1} (Fig. S16†).[9,14,23] The Eyring analysis of these data shows activation parameters of $\Delta H^{\ddagger} = 26.8 \pm 0.4$ kcal mol^{-1} and $\Delta S^{\ddagger} = 12.0 \pm 1.5$ cal K^{-1} mol^{-1}, which implies an activation barrier $\Delta G^{\ddagger} = 22.6 \pm 0.8$ kcal mol^{-1} at 353 K (Fig. S17†).[14a,b,24] These activation values are in the range of the activation barriers recently reported for other iridium-catalyzed solventless FA dehydrogenation processes,[14b,d] and slightly higher than the values found for iridium-catalyzed FA dehydrogenation processes in water.[9,24]

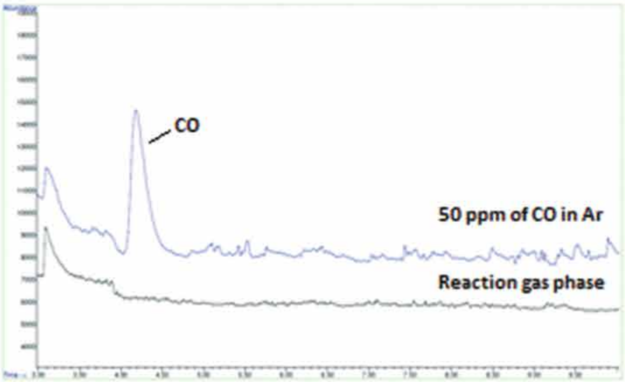

Fig. 4 Top: GC of the gaseous mixture of CO (50 ppm) in Ar. Down: GC of the gas phase formed in the **2**-catalyzed (0.1 mol%) solventless FA dehydrogenation at 353 K in the presence of Et_3N (40 mol% to FA).

Table 2 Kinetic isotope effect experiments on the **2**-catalyzed dehydrogenation of FA using 10 mol% of Et_3N at 353 K

Entry	Substrate	TOF^a (h^{-1})	KIE^b
1	HCOOH	400	—
2	HCOOD	300	1.33
3	DCOOH	140	2.86
4	DCOOD	120	3.33

[a] Calculated at 5 min. [b] KIE = entry 1/the corresponding entry (2, 3 or 4).

To shed light on the rate-limiting step of the **2**-catalyzed dehydrogenation process, H/D kinetic isotope experiments were performed at 353 K using 10 mol% of Et_3N. The results from these studies show that the initial TOF values (calculated after 5 min) dropped from 400 to 300 and 140 h^{-1} when HCOOH was replaced with HCOOD and DCOOH, respectively (Table 2 and Fig. S18†). These TOF values correspond to KIE values of 1.33 and 2.86, respectively. It is remarkable that using DCOOD a high isotopic effect was observed (KIE = 3.33, entry 4 in Table 2). These data evidenced that the C–H bond activation of FA is the rate-determining step of the process.[25]

Computational DFT studies

To gain better insight into the operative pathway on the dehydrogenation of formic acid catalyzed by the Ir-NSi species, a thorough DFT computational study was performed for the catalytic cycle enabled by **2**. Our model refers to the first 5 minutes of reaction when the active species has not yet been transformed into other possible species or decomposed to give metallic iridium particles. According to the obtained experimental results, we have considered as the active catalyst the monomer resulting from replacing the triflate ligand with a formate anion in **2**. Fig. 5 shows the energetic profile obtained for this catalytic cycle.

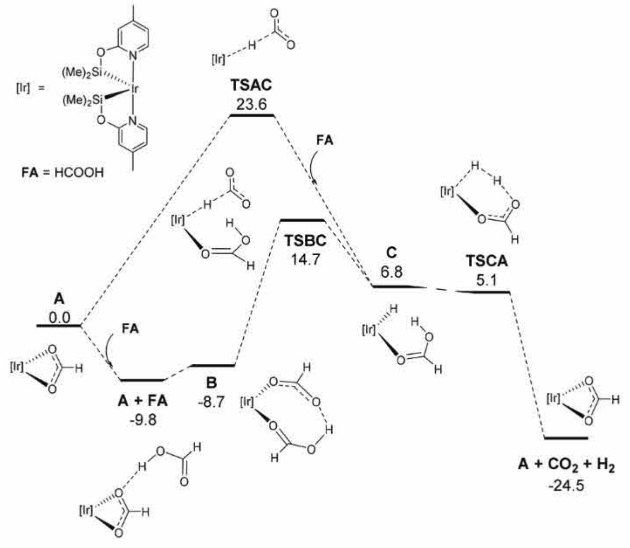

Fig. 5 DFT energetic profile (ΔG in kcal mol^{-1}, relative to A and isolated molecules) for formic acid dehydrogenation.

The catalytic cycle starts with **A** in which the formate is coordinated as a chelate, occupying both vacancies of the metal. The addition of a molecule of formic acid to **A** leads to the formation of **A + FA** which is 9.8 kcal mol^{-1} lower in energy. Following that, the formic acid coordinates to the metal developing into intermediate **B**, stabilized by an intramolecular hydrogen bond between the acid and the formate, at a relative energy of −8.7 kcal mol^{-1}. Next, the formate changes its coordination mode to the metal, allowing the interaction between the Ir and hydrogen atom of the formate. Then, the hydride can be transferred by means of **TSBC**, which exhibits a relative energy of 14.7 kcal mol^{-1}. Interestingly, this transition state is favored by the electrostatic interaction between the positively charged acidic proton of the formic acid and the hydride being transferred from the formate to the metal center (see Fig. 6). Comparatively, the hydride abstraction from the formate anion by the metallic complex without explicit participation of the solvent media takes place *via* **TSAC** at a significantly higher energy of 23.6 kcal mol^{-1}. The calculation of a β-elimination pathway was attempted but unsuccessful because the strong effect of the implicit solvent favors conformations with the negatively charged formate oxygens separated from the positively charged metal. The metal hydride intermediate **C** shows a high relative energy (6.8 kcal mol^{-1}) due to the unfavorable *trans* influence of the silyl ligand. The release of molecular hydrogen can be achieved *via* **TSCA** (5.1 kcal mol^{-1}) corresponding to heterolytic H–H bond formation from the negatively charged hydride and the positively charged proton (Fig. 6).

The DFT calculated overall energetic barrier is 24.5 kcal mol^{-1}, defined by the difference between **A + FA** and **TSBC**, which is in between the experimental values of 27.50 ± 0.88 kcal mol^{-1} and 22.8 ± 0.8 kcal mol^{-1} obtained from the Arrhenius and Eyring analysis, respectively. Moreover, the KIE calculated from the DFT structures for the rate determining species showed values comparable to those shown in Table 2 (3.08, 1.18 and 3.60 for DCOOH, HCOOD, and DCOOD, respectively). It is noteworthy that, according to the DFT calculations, the hydride abstraction step (**TSBC**) is assisted by the interaction between the proton of the coordinated FA and the formate hydrogen. These results correspond to a primary KIE for the C–H bond breaking and a secondary KIE for the O–H bond stretching in the rate limiting step.

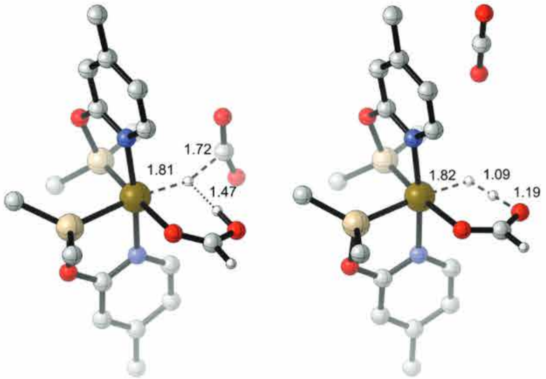

Fig. 6 Geometrical representation of the **TSBC** (left) and **TSCA** (right) DFT optimized structures. Key distances in Å; hydrogen atoms omitted for clarity.

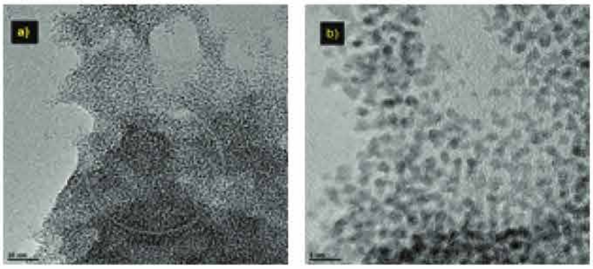

Fig. 7 Transmission electronic microscopy images of the dark iridium nanoparticles. (a) TEM image (20 nm). (b) Closer image showing lattice fringes (5 nm).

Catalyst decomposition

In all the studied reactions the formation of a black precipitate during the reaction was observed. These precipitates were isolated and characterized as iridium crystalline nanoparticles (NPs) by TEM (Fig. 7) and EDX (Fig. S20†). The formation of these Ir-NPs shows that the homogeneous catalyst slowly decomposes under the reaction conditions.

These Ir-NPs show no activity as FA–Et_3N dehydrogenation catalysts, which has been demonstrated by using them as the catalyst in the presence of 10 mol% of Et_3N and at 353 K. Moreover, a mercury poisoning test[26] was performed by the addition of mercury drops to the **2**-catalyzed (0.10 mol%) dehydrogenation of formic acid in the presence of 10 mol% of Et_3N. Under these conditions no change in the reaction rate was observed (Fig. S21†). This agrees with the homogeneous nature of the catalytic reaction.

To check if catalyst decomposition was caused by the evolving pressure of H_2 during the reaction, we have performed the reactions in an open system connected to a bubbler. However, catalyst decomposition was also observed. Consequently, we can conclude that the decomposition of the catalyst is not related to a buildup of H_2 pressure within the reactor during the catalysis.

Experimental

General information

Complexes **1**[17] and **2**[15c] were prepared according to the reported method. Formic acid and Sodium formate were purchased from commercial sources and used without further purifications. Et_3N was purchased from commercial sources and distilled prior to use.

General procedure for the formic acid dehydrogenation

Catalytic reactions were carried out on a microreactor (Man on the Moon series X102 Kit)[18] with a total volume of 19 mL.

Under an argon atmosphere, the reactor was filled with the desired amount of base (sodium formate or Et_3N) and 450 μL of formic acid. The reactor was then closed and heated to the desire temperature in an oil bath, and when the temperature and pressure of the system are stabilized, a solution of the corresponding catalyst precursor in 50 μL of formic acid is injected with a microsyringe.

Conditions for specific catalytic experiments

NMR studies of 1 (or 2) and FA solutions in thf-d_8. In a Young cap NMR tube, **1** (0.011 mmol) or **2** (5.5×10^{-3} mmol) was dissolved in thf-d_8 (0.4 mL). To this solution FA (40 equiv., 16.6 μL, 0.441 mmol) was added. The solutions were studied by ^{1}H NMR after several hours at RT. After this they were heated at 323 K for 1 more hour and monitored by ^{1}H NMR.

NMR studies of 1 (or 2), FA and Et_3N solutions in thf-d_8. In a Young cap NMR tube, **1** (0.011 mmol) or **2** (5.5×10^{-3} mmol) was dissolved in thf-d_8 (0.4 mL). To this solution FA (40 equiv., 16.6 μL, 0.441 mmol) and Et_3N (16 equiv., 24.5 μL, 0.176 mmol) were added. The solutions were analysed by ^{1}H NMR at RT. After this they were heated at 323 K and monitored by ^{1}H NMR.

Data for complex [Ir(OCHO)(κ^2-NSi^{iPr})$_2$] (3). ^{1}H NMR (300 MHz, thf-d_8, 298 K): δ 10.12 (s. 1H, OC*H*O), 8.39 (d, 2H, J_{H-H} = 6.2 Hz, 2H, py), 6.78 (m, 2H, py), 6.67 (dd, J_{HH} = 6.3 and 1.5 Hz, 2H, py), 2.26 (s, 6H, CH_3-py), 1.53 (septet, 2H, J_{H-H} = 7.5 Hz, CH-^{i}Pr), 1.22 (septet, 2H, J_{H-H} = 7.2 Hz, CH-^{i}Pr), 1.08 (d, 6H, CH_3-^{i}Pr, J_{H-H} = 7.5 Hz), 0.98 (d, 6H, CH_3-^{i}Pr, J_{H-H} = 7.3 Hz), 0.75 (d, 6H, CH_3-^{i}Pr, J_{H-H} = 7.3 Hz), 0.53 (d, 6H, CH_3-iPr, J_{H-H} = 7.5 Hz); ^{13}C{^{1}H} NMR plus APT plus HSQC ^{1}H–^{13}C (75 MHz, CD_2Cl_2, 298 K): δ 175.7 (s, O*C*HO), 170.8 (s, C_{ipso}-py), 152.7 (s, C_{ipso}-py), 149.2 (s, CH-py), 118.4 (s, CH-py), 112.1 (s, CH-py), 21.1 (s, CH_3-py), 19.1 (s, CH_3-iPr), 18.7 (s, CH_3-iPr), 18.0 (s, CH_3-iPr), 17.9 (s, CH_3-^{i}Pr), 17.5 (s, CH-^{i}Pr), 16.9 (s, CH-^{i}Pr); ^{29}Si{^{1}H} NMR plus HMBC ^{29}Si–^{1}H (298 K, thf-d_8): δ 41.4 ppm.

Comparative study of the activity of 1 and 2 in the presence of Et_3N. The *man on the moon* reactor was charged with 500 μL of FA, 10 mol% of Et_3N (186 μL, 1.32 mmol), and **1** (10.4 mg, 0.013 mmol, 0.1 mol%) or **2** (9 mg, 6.5×10^{-3} mmol, 0.1 mol% to Ir) at 353 K.

Study of the Et_3N concentration effect. The reactor was charged with 500 μL of FA, **2** (9 mg, 6.5×10^{-3} mmol, 0.1 mol% to Ir) and the corresponding amount of Et_3N: 1.0 mol% (18.6 μL, 0.13 mmol), 2.5 mol% (46.5 μL, 0.32 mmol), 5.0 mol% (93 μL, 0.65 mmol) 10 mol% (186 μL, 1.32 mmol), 20 mol% (372 μL, 2.64 mmol) or 40 mol% (744 μL, 5.28 mmol) at 353 K.

Study of the temperature effect. The reactor was charged with 500 μL of FA, **2** (9 mg, 6.5×10^{-3} mmol, 0.1 mol% to Ir) and 10 mol% (186 μL, 1.32 mmol) of Et_3N at different temperatures (from 313 to 373 K).

KIE experiments

250 μL of FA (HCOOH, HCOOD, DCOOH or DCOOD), **2** (4,5 mg, 3.25×10^{-3} mmol, 0.1 mol% to Ir) and 40 mol% (372 μL, 2.64 mmol) of Et_3N at 353 K.

FT-IR of the gaseous product. The gas phase from the dehydrogenation reaction of 500 μL of FA in the presence of **2** (9 mg, 6.5×10^{-3} mmol, 0.1 mol% to Ir) and 10 mol% of Et_3N (186 μL, 1.32 mmol) at 353 K was collected in a rubber balloon. The gas sample was transferred to the cell and the FT-IR spectrum was recorded GC-MS: the gas samples were taken directly from the microreactor and injected into the GC-MS.

Mercury drop test. A drop of mercury was added to the microreactor together with 450 μL of FA, and 10 mol% (186 μL, 1.32 mmol) of Et_3N, and the system was heated at 353 K. When the system was stabilized, a solution of **2** (9 mg, 6.5×10^{-3} mmol, 0.1 mol% to Ir) in 50 μL of FA was injected.

Computational details. All DFT theoretical calculations were carried out using the Gaussian program package.[27] The B3LYP-D3 [28] method with solvent corrections using the PCM[29] method for formic acid as implemented in G09 was used for energy and gradient calculations. All atoms were treated with the def2-SVP basis set together with the corresponding core potential for Ir for geometry optimizations. Energies were further refined by single point calculations using the def2-TZVP basis set.[30] The "ultrafine" grid was employed in all calculations. All reported energies are Gibbs free energies referred to a 1 atm standard state at 353 K including the basis set and solvent corrections. Gibbs free energies were corrected by suppressing the translational entropy term of the solvent molecules (formic acid) following the approach of Morokuma and co-workers.[31] The nature of the stationary points was confirmed by analytical frequency analysis, and the transition states were characterized by a single imaginary frequency corresponding to the expected motion of the atoms. Calculations of KIE from the DFT data were performed by replacing the mass of the selected hydrogen atom with deuterium using the keyword readisotopes in G09 and calculating the vibrational frequencies at the transition state and the corresponding intermediate.

Conclusions

Complexes **1** and **2** are active catalyst precursors for the selective solventless dehydrogenation of formic acid (FA) in the presence of Et_3N. Species **2** has been found to be more active than **1**, which could be attributed to the higher steric hindrance caused by the isopropyl substituents of the silicon atoms in **1**.

The highest activity ($TOF_{5\ min}$ = 2900 h^{-1}) for the solventless dehydrogenation of FA has been achieved using complex **2** (0.1 mol% to Ir) as the catalyst precursor and Et_3N 40 mol% (to FA) as a base at 373 K. The DFT calculated overall energetic barrier is 24.5 kcal mol^{-1}, which is in between the experimental values of 27.50 ± 0.88 kcal mol^{-1} and 22.8 ± 0.8 kcal mol^{-1} obtained from the Arrhenius and Eyring analysis, respectively. KIE values of 1.33, 2.86, and 3.33 were obtained for HCOOD, DCOOH, and DCOOD, respectively. These data show that the C–H bond activation of FA is the rate-determining step of the process and agree with the mechanistic calculations using DFT.

The information about the nature of the active species under solventless conditions remains scarce. However, ^{1}H and ^{13}C NMR studies of the catalytic reactions in thf-d$_8$ evidenced the formation of the $[Ir(OCHO)(\kappa^2\text{-NSi}^R)_2]$ (R = Me; ^{i}Pr) intermediates during the catalytic process.

It should be mentioned that catalyst decomposition to give Ir-NPs has been observed in all cases under study. However, the possible activity of such Ir-NPs has been discarded based on experimental evidence.

Conflicts of interest

There are no conflicts to declare.

Acknowledgements

The financial support from projects PGC2018-099383-B-I00 (MCIU/AEI/FEDER, UE), RTI2018-099136-A-I00 (MCIU/AEI/FEDER, UE), CSIC project 202080I024 and DGA/FSE project E42_20R is gratefully acknowledged. A. U. thankfully acknowledges the Spanish MECD for a FPU fellowship (FPU 2017/05417).

Notes and references

1 For recent reviews see: (*a*) Z. Abdin, A. Zafaranloo, A. Rafiee, W. Mérida, W. Lipiński and K. R. Khalilpour, *Renewable Sustainable Energy Rev.*, 2020, **120**, 109620; (*b*) F. Dawood, M. Anda and G. M. Shafiullah, *Int. J. Hydrogen Energy*, 2020, **45**, 3847–3869; (*c*) J. O. Abe, A. P. I. Popoola, E. Ajenifuja and O. M. Popoola, *Int. J. Hydrogen Energy*, 2019, **44**, 15072–15086; (*d*) S. Z. Baykara, *Int. J. Hydrogen Energy*, 2018, **43**, 10605–10614; (*e*) J.O'M. Bockris, *Int. J. Hydrogen Energy*, 2013, **38**, 2579–2588; (*f*) N. Armaroli and V. Balzani, *ChemSusChem*, 2011, **4**, 21–36.

2 T. He, P. Pachfule, H. Wu, Q. Xu and P. Chen, *Nat. Rev. Mater.*, 2016, 16059.

3 For recent reviews see: (*a*) M. Iglesias and F. J. Fernández-Alvarez, *Catalysts*, 2021, **11**, 1288, DOI: 10.3390/catal11111288; (*b*) K. Grubel, H. Jeong, C. W. Yoon and T. Autrey, *J. Energy Chem.*, 2020, **41**, 216–224; (*c*) C. Guan, Y. Pan, T. Zhang, M. J. Ajitha and K.-W. Huang, *Chem. – Asian J.*, 2020, **15**, 937–946; (*d*) P. Stathi, M. Solakidou, M. Louloudi and Y. Deligiannakis, *Energies*, 2020, **13**, 733; (*e*) M. Iglesias and L. A. Oro, *Eur. J. Inorg. Chem.*, 2018, 2125–2138; (*f*) K. Sordakis, C. Tang, L. K. Vogt, H. Junge, P. J. Dyson, M. Beller and G. Laurenczy, *Chem. Rev.*, 2018, **118**, 372–433; (*g*) N. Onishi, G. Laurenczy, M. Beller and Y. Himeda, *Coord. Chem. Rev.*, 2018, **373**, 317–332; (*h*) P. Preuster, C. Papp and P. Wasserscheid, *Acc. Chem. Res.*, 2017, **50**, 74–85; (*i*) J. Eppinger and K.-W. Huang, *ACS Energy Lett.*, 2017, **2**, 188–195; (*j*) D. Mellmann, P. Sponholz, H. Junge and M. Beller, *Chem. Soc. Rev.*, 2016, **45**, 3954–3988; (*k*) A. K. Singh, S. Singh and A. Kumar, *Catal. Sci. Technol.*, 2016, **6**, 12–40.

4 (*a*) G. Kim and S.-H. Jhi, *ACS Nano*, 2011, **5**, 805–810; (*b*) S. K. Das, A. Reis and K. J. Berry, *J. Power Sources*, 2009, **193**, 691–698; (*c*) J. J. Baschuk and X. Li, *Int. J. Energy Res.*, 2001, **25**, 695–713.

5 R. S. Coffey, *Chem. Commun.*, 1967, 923–924.

6 B. Loges, A. Boddien, H. Junge and M. Beller, *Angew. Chem., Int. Ed.*, 2008, **47**, 3962–3965.

7 C. Fellay, P. J. Dyson and G. Laurenczy, *Angew. Chem., Int. Ed.*, 2008, **47**, 3966–3968.

8 J. F. Hull, Y. Himeda, W.-H. Wang, B. Hashiguchi, R. Periana, D. J. Szalda, J. T. Muckerman and E. Fujita, *Nat. Chem.*, 2012, **4**, 383–388.

9 Z. Wang, S.-M. Lu, J. Li, J. Wang and C. Li, *Chem. – Eur. J.*, 2015, **21**, 12592–12595.

10 Y. Himeda, *Green Chem.*, 2009, **11**, 2018–2022.

11 C. Guan, D.-D. Zhang, Y. Pan, M. Iguchi, M. J. Ajitha, J. Hu, H. Li, C. Yao, M.-H. Huang, S. Min, J. Zheng, Y. Himeda, H. Kawanami and K.-W. Huang, *Inorg. Chem.*, 2017, **56**, 438–445.

12 A. Matsunami, Y. Kayaki and T. Ikariya, *Chem. – Eur. J.*, 2015, **21**, 13513–13517.

13 A. Matsunami, S. Kuwata and Y. Kayaki, *ACS Catal.*, 2017, **7**, 4479–4484.

14 (*a*) S. Wang, H. Huang, T. Roisnel, C. Bruneau and C. Fischmeister, *ChemSusChem*, 2019, **12**, 179–184; (*b*) A. Iturmendi, M. Iglesias, J. Munarriz, V. Polo, V. Passarelli, J. J. Pérez-Torrente and L. A. Oro, *Green Chem.*, 2018, **20**, 4875–4879; (*c*) S. Cohen, V. Borin, I. Schapiro, S. Musa, S. De-Botton, N. V. Belkova and D. Gelman, *ACS Catal.*, 2017, **7**, 8139–8146; (*d*) J. J. A. Celaje, Z. Lu, E. A. Kedzie, N. J. Terrile, J. N. Lo and T. J. Williams, *Nat. Commun.*, 2016, **7**, 11308; (*e*) A. Luque-Gómez, S. García-Abellán, J. Munarriz, V. Polo, V. Passarelli and M. Iglesias, *Inorg. Chem.*, 2021, **60**, 15497–15508.

15 (*a*) J. Guzmán, P. García-Orduña, V. Polo, F. J. Lahoz, L. A. Oro and F. J. Fernández-Alvarez, *Catal. Sci. Technol.*, 2019, **9**, 2858–2867; (*b*) J. Guzmán, A. M. Bernal, P. García-Orduña, F. J. Lahoz, L. A. Oro and F. J. Fernández-Alvarez, *Dalton Trans.*, 2019, **48**, 4255–4262; (*c*) J. Guzmán, P. García-Orduña, F. J. Lahoz and F. J. Fernández-Alvarez, *RSC Adv.*, 2020, **10**, 9582–9586.

16 J. Guzmán, A. Torguet, P. García-Orduña, F. J. Lahoz, L. A. Oro and F. J. Fernández-Alvarez, *J. Organomet. Chem.*, 2019, **897**, 50–56.

17 J. Guzmán, A. M. Bernal, P. García-Orduña, F. J. Lahoz, V. Polo and F. J. Fernández-Alvarez, *Dalton Trans.*, 2020, **49**, 17665–17673.

18 N. H. Anderson, J. M. Boncella and A. M. Tondreau, *Chem. – Eur. J.*, 2017, **23**, 13617–13622.

19 (*a*) T. Zell, B. Butschke, Y. Ben-David and D. Milstein, *Chem. – Eur. J.*, 2013, **19**, 8068–8072; (*b*) E. A. Bielinski,

P. O. Lagaditis, Y. Zhang, B. Q. Mercado, C. Würtele, W. H. Bernskoetter, N. Hazari and S. Schneider, *J. Am. Chem. Soc.*, 2014, **136**, 10234–10237.

20 N. H. Anderson, J. Boncella and A. M. Tondreau, *Chem. – Eur. J.*, 2019, **25**, 10557–10560.

21 C. Chauvier, A. Tlili, C. Das Neves Gomes, P. Thuéry and T. Cantat, *Chem. Sci.*, 2015, **6**, 2938–2942.

22 https://www.manonthemoontech.com.

23 For recent examples of catalytic FADH activation parameters obtained from Arrhenius plot using initial TOF values see: (*a*) M. Iguchi, H. Zhong, Y. Himeda and H. Kawanami, *Chem. – Eur. J.*, 2017, **23**, 17017–17021; (*b*) Y. Manaka, W.-H. Wang, Y. Suna, H. Kambayashi, J. T. Muckerman, E. Fujita and Y. Himeda, *Catal. Sci. Technol.*, 2014, **4**, 34–37; (*c*) H. Junge, M. Beller and H. Grützmacher, *ChemSusChem*, 2018, **11**, 3092–3095; (*d*) W.-H. Wang, H. Wang, Y. Yang, X. Lai, Y. Li, J. Wang, Y. Himeda and M. Bao, *ChemSusChem*, 2020, **13**, 5015–5022.

24 P. M. Morse, M. D. Spencer, S. R. Wilson and G. S. Girolami, *Organometallics*, 1994, **13**, 1646–1655.

25 G. Menendez Rodriguez, F. Zaccaria, L. Tensi, C. Zuccaccia, P. Belanzoni and A. Macchioni, *Chem. – Eur. J.*, 2021, **27**, 2050–2064.

26 D. Gärtner, S. Sandl and A. J. von Wangelin, *Catal.: Sci. Technol.*, 2020, **10**, 3502–3514.

27 M. J. Frisch, G. W. Trucks, H. B. Schlegel, G. E. Scuseria, M. A. Robb, J. R. Cheeseman, G. Scalmani, V. Barone, B. Mennucci, G. A. Petersson, H. Nakatsuji, M. Caricato, X. Li, H. P. Hratchian, A. F. Izmaylov, J. Bloino, G. Zheng, J. L. Sonnenberg, M. Hada, M. Ehara, K. Toyota, R. Fukuda, J. Hasegawa, M. Ishida, T. Nakajima, Y. Honda, O. Kitao, H. Nakai, T. Vreven, J. A. Montgomery Jr., J. E. Peralta, F. Ogliaro, M. Bearpark, J. J. Heyd, E. Brothers, K. N. Kudin, V. N. Staroverov, R. Kobayashi, J. Normand, K. Raghavachari, A. Rendell, J. C. Burant, S. S. Iyengar, J. Tomasi, M. Cossi, N. Rega, J. M. Millam, M. Klene, J. E. Knox, J. B. Cross, V. Bakken, C. Adamo, J. Jaramillo, R. Gomperts, R. E. Stratmann, O. Yazyev, A. J. Austin, R. Cammi, C. Pomelli, J. W. Ochterski, R. L. Martin, K. Morokuma, V. G. Zakrzewski, G. A. Voth, P. Salvador, J. J. Dannenberg, S. Dapprich, A. D. Daniels, ö. Farkas, J. B. Foresman, J. V. Ortiz, J. Cioslowski and D. J. Fox, *Gaussian 09, revision D.01*, Gaussian, Inc., Wallingford CT, 2009.

28 (*a*) A. D. Becke, *J. Chem. Phys.*, 1993, **98**, 1372–1377; (*b*) C. Lee, W. Yang and R. G. Parr, *Phys. Rev. B: Condens. Matter Mater. Phys.*, 1988, **37**, 785–789; (*c*) S. Grimme, J. Antony, S. Ehrlich and H. Krieg, *J. Chem. Phys.*, 2010, **132**, 154104; (*d*) E. R. Johnson and A. D. Becke, *J. Chem. Phys.*, 2006, **124**, 174104.

29 (*a*) S. Miertuš, E. Scrocco and J. Tomasi, *Chem. Phys.*, 1981, **55**, 117–129; (*b*) S. Miertuš, E. Scrocco and J. Tomasi, *Chem. Phys.*, 1982, **65**, 239–245.

30 F. Weigend and R. Ahlrichs, *Phys. Chem. Chem. Phys.*, 2005, **7**, 3297–3305.

31 R. Tanaka, M. Yamashita, L. W. Chung, K. Morokuma and K. K. Nozaki, *Organometallics*, 2011, **30**, 6742–6750.

INORGANIC CHEMISTRY
FRONTIERS

Cite this: *Inorg. Chem. Front.*, 2022, **9**, 4538

Efficient solventless dehydrogenation of formic acid by a CNC-based rhodium catalyst†

Pablo Hermosilla, [a] Asier Urriolabeitia,[b] Manuel Iglesias, [a] Víctor Polo [b] and Miguel A. Casado *[a]

Received 14th May 2022,
Accepted 9th July 2022

DOI: 10.1039/d2qi01056a

rsc.li/frontiers-inorganic

The complex $[(\mathrm{CNC})^{Mes}\mathrm{Rh}(\mathrm{PMe_2Ph})]\mathrm{PF_6}$ (**1**) has been found to be an effective catalyst for solventless formic acid (FA) dehydrogenation, affording exclusively H_2 and CO_2 as decomposition products. The effect of the addition of a base as a co-catalyst was studied, and it was found that HCOONa was the most efficient additive in terms of catalyst efficiency with a catalyst loading of 0.016 mol%, reaching $\mathrm{TOF_{max}}$ values up to 5869 h^{-1}. Additionally, we observed that the addition of water dramatically increased the catalytic activity in FA dehydrogenation, yielding $\mathrm{TOF_{max}}$ values up to 10 150 h^{-1}. Additionally, VT kinetic NMR experiments allowed us to estimate the activation energy ($\Delta G^{\ddagger}$ = 18.12 ± 1.17 kcal $\mathrm{mol^{-1}}$) of the FA dehydrogenation catalysed by **1**. Stoichiometric NMR experiments, aimed to shed light on the nature of possible catalytic intermediates, allowed us to detect and further isolate the $\mathrm{Rh^{III}}$ hydrido formate complex $[(\mathrm{CNC})^{Mes}\mathrm{Rh}(\kappa^{O}\text{-}\mathrm{OC(O)H})(\mathrm{PMe_2Ph})\mathrm{H}]\mathrm{PF_6}$ (**2**), which originates from an oxidative addition of FA to **1**; additionally, we could detect a bis(hydrido) $\mathrm{Rh^{III}}$ complex $[(\mathrm{CNC})^{Mes}\mathrm{Rh}(\mathrm{PMe_2Ph})\mathrm{H_2}]\mathrm{PF_6}$ (**1-H₂**), which is another operative intermediate in the catalytic FA dehydrogenation by **1**. DFT calculations performed on the catalytic FA dehydrogenation perfectly accounted for the gathered experimental data; the approach of a FA molecule to **1** leads to O–H oxidative addition producing the κ^{O}-formate intermediate **2**, which subsequently undergoes a FA-assisted isomerization to the κ^{H}-formate species. Further hydride abstraction generates the dihydrido intermediate **1-H₂**, which releases H_2 upon interaction with another FA molecule closing the catalytic cycle. The rate-limiting step in the catalytic process corresponds to the hydride abstraction step, which agrees with the KIE values estimated by NMR experiments.

Introduction

The use of hydrogen as an energy vector has received increasing attention in recent years, mainly due to the need for an urgent transition from a fossil fuel-based energy system to more sustainable alternatives. The energy surplus generated by renewable sources during low-demand periods can be stored as hydrogen by water electrolysis, which is considered a viable solution to the problems related to their intermittent nature.[1] However, the low volumetric energy density of H_2 raises concerns over its storage and transportation. On these grounds, the use of hydrogen carriers has been proposed as a means to circumvent the storage and safety issues associated with H_2. Among the hydrogen carriers proposed in the literature, formic acid (FA) offers great promise due to the fact that its gravimetric and volumetric energy densities are higher than those of compressed hydrogen, it presents low toxicity and flammability, it is environmentally benign and it is a liquid under atmospheric conditions.[2] Moreover, FA can be obtained from renewable sources, namely, CO_2 hydrogenation,[3] biomass oxidation,[4] and as a by-product of the synthesis of acetic acid.[5]

Formic acid dehydrogenation (FADH) has been extensively studied in the presence of solvents and in the FA/Et_3N azeotropic mixture, with Ir and Ru homogeneous catalysts being the most successful.[6] However, in these cases, the gravimetric and volumetric energy densities of the reaction mixtures are intrinsically lower than those of pure FA and, consequently, solvent-free conditions are desirable for FADH. To date, only Ir[7] and Ru[8] catalysts for solvent-free FADH have been reported. Catalysts **A** and **B** reported by Gelman (TOF = 11 760 h^{-1}) and Fischmeister (TOF = 5122 h^{-1}), respectively, contain participative ligands able to interact with FA *via* hydrogen bond interactions. On the other hand, Ir complexes **C** and **D** described by

---

[a] *Instituto de Síntesis Química y Catálisis Homogénea ISQCH, Universidad de Zaragoza-CSIC, C/Pedro Cerbuna, 12, 50009 Zaragoza, Spain.*
E-mail: mcasado@unizar.es; Fax: +34 976 761 187; Tel: +34 876 553 502

[b] *Departamento de Química Física e Instituto de Biocomputación y Física de Sistemas Complejos (BIFI), Universidad de Zaragoza, 50009 Zaragoza, Spain*

† Electronic supplementary information (ESI) available: Experimental methods, figures for NMR spectra, IR and GC analyses, deuterium labelling studies and full computational details. See DOI: **https://doi.org/10.1039/d2qi01056a**

Williams (TOF = 13 320 h^{-1}) and us (TOF = 11 590 h^{-1}), respectively, and the Ru complex (**E**) recently reported by Milstein (TOF = 3067 h^{-1} without additives or solvent, TON: over 1.7 million) are able to efficiently carry out the dehydrogenation of FA without the participation of ancillary ligands (Fig. 1).

Regardless of whether the ligand plays an active or a passive role in the reaction mechanism, its design is key to tuning the activity of the catalyst. In the case of non-participative ligands, although less conspicuous, their architecture defines the stability and activity of the catalyst. A common feature in complexes **A–E** is the presence of pincer or chelate ligands that confer stability to the system, while providing electron density to the metal center by means of strongly donating wingtip groups—*e.g.*, phosphanes, a tertiary alkyl in **A**, an N-heterocyclic olefin in D, or an amido moiety in E—or co-ligands, namely, a Cp* ligand in **B**.

The presence of an electron-rich metal center facilitates the oxidative addition of FA's O–H bond, while rendering more nucleophilic hydrides, which consequently undergo protonation to generate H_2 straightforwardly.

On these grounds, we set off to study the impact on the catalytic activity of pincer ligands featuring strongly donating N-heterocyclic carbenes (NHCs) as wingtip groups.[9] More specifically, we were interested in the chemistry of a pincer ligand based on a lutidine core bearing two NHC moieties in combination with rhodium, namely complex [(CNC)^{Mes}Rh(PMe$_2$Ph)]PF$_6$ (**1**) (Scheme 1).[10] Herein we report the catalytic activity of complex **1** in FA dehydrogenation under solvent-free conditions at 353 K to yield exclusively carbon dioxide and dihydrogen. The catalytic efficiency can be tuned by the addition of sodium formate and also by the presence of water. DFT calculations in combination with NMR techniques provided valuable insights into the operative FA dehydrogenation mechanism.

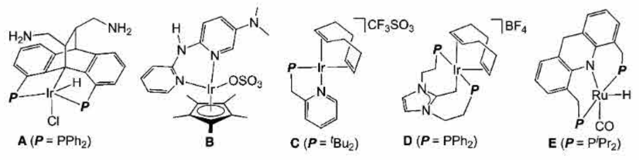

Fig. 1 Selected examples of catalysts for FA dehydrogenation.

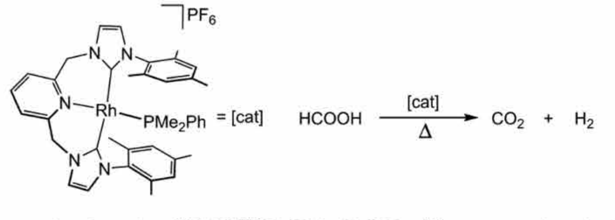

Scheme 1 Complex [(CNC)^{Mes}Rh(PMe$_2$Ph)]PF$_6$ (**1**) as a catalyst in FA dehydrogenation.

Results and discussion

Complex **1** was evaluated as a catalyst for the dehydrogenation of FA under base-free conditions in acetonitrile. However, we did not observe any transformation when FA (0.53 mmol) was dissolved in acetonitrile (1 mL) at 353 K for 1 h in the presence of **1** (1 mol%). Then we studied the effect of a base in order to assess whether **1** could act as a catalyst in FA dehydrogenation;[11] in this line, the addition of bases such as triethylamine, KHDMS or Na_2CO_3 under similar conditions did not alter the results in a remarkable way. However, upon addition of HCOONa (10 mol%), catalyst **1** decomposed FA (20 μL, 0.53 mmol) at 353 K in less than one minute, resulting in the production of a gaseous mixture. It is worth mentioning that the related complexes [(CNC)^{Mes}Rh(L)]PF$_6$ (L = CO, NCCH$_3$),[10] bearing non-phosphine ligands, did not show any catalytic activity on FA dehydrogenation under the same conditions.

Due to these encouraging preliminary results in catalytic FA dehydrogenation in acetonitrile, we aimed at exploring the activity of complex **1** on FA dehydrogenation under solventless conditions. For this reason, we carried out some catalytic runs with variable amounts of HCOONa as a co-catalyst (Table 1). In this context, the use of a base is a common feature in many catalytic systems in FA dehydrogenation, because it may play a role as a buffer solution to control the pH of the medium and also it may be able to cleave FA dimers formed by hydrogen bonds in solution.[12] In this regard, a number of reports have proved that the activity of the catalyst strongly depends on the pH of the solution, with optimum values usually observed between pH 3 and 4.[13,14] Moreover, recent reports show that variable amounts of HCOONa and water in the catalytic system may help improve the catalytic activity in both homogeneous[15] and heterogeneous approaches.[16]

Catalyst **1** is air stable, although the activities in FA dehydrogenation are lower if the catalytic experiments are carried out under air. Therefore, the catalytic experiments are best performed in a high-pressure reaction vessel, which is charged with the rhodium catalyst **1** (0.016%) and sodium formate under an argon atmosphere. Complex **1** decomposed FA (2 mL, 53.01 mmol) with HCOONa as a co-catalyst (5–40 mol%) at 353 K (Table 1). A catalytic run resulted in the production of 27.1 mmol of H_2 (51% conversion, TON: 3195) after 1 h with 40 mol% of HCOONa (Table 1, entry 5).

Table 1 Catalytic dehydrogenation of FA by **1** in the presence of variable amounts of HCOONa[a]

Entry	Mol% HCOONa	TON	TOF$_{max}$ (h^{-1})
1	5	150	849
2	10	235	3329
3	20	586	5182
4	30	2014	4634
5	40	3195	5869

[a] General conditions: FA (2 mL, 53.01 mmol), complex **1** (7.5 mg, 0.016 mol%) and the specified amount of HCOONa, at 353 K.

When **1** was dissolved in a FA/HCOONa mixture, the initial red solution turned yellow. When the reaction was finished, a yellow solution remained in the flask when low base loadings were used (5–10 mol%); however, when HCOONa concentrations exceeded 10 mol%, solid HCOONa remained at the bottom of the reactor at the end of the reaction. When HCOONa reaches 20 mol%, the solution becomes saturated and a yellow suspension is formed during FA dehydrogenation, which may lead to diffusion problems throughout the reaction. Although TON values are not very high (TON = 3195), when the amount of HCOONa is between 5 and 40 mol%, TOF values indicate good catalytic activities, reaching 5869 h^{-1} when operating at 40 mol% of HCOONa (Fig. 2; Table 1, entry 5).

The overall catalytic activity increases with co-catalyst concentrations higher than 20 mol%. As Fig. 2 shows, the rate of hydrogen production is linear at the beginning of the reactions, and their slope increases with higher HCOONa concentrations, reaching its maximum close to 20 min when 40 mol% of HCOONa is used. After this point, the activity of the catalyst decreases with time. Additionally, we studied the dependence of the catalytic activity on the H_2O concentration in the catalytic media. These experiments showed that, not only the catalyst is stable under a wet environment, but also the presence of water increases the catalytic efficiency (see Fig. S3†). In this way, the addition of increasing amounts of water into the catalytic reactions (5 to 40 mol% H_2O) enhanced the catalytic activity (Fig. 3). With 5 to 10 mol% of water, a fast increase of the catalytic activity was observed, which becomes slower upon reaching a maximum TOF value at 40 mol% of water.

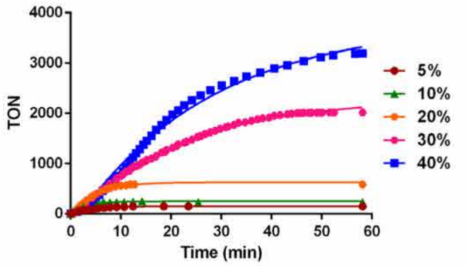

Fig. 2 Reaction profiles of FA dehydrogenation of neat FA by **1** under different HCOONa concentrations at 353 K.

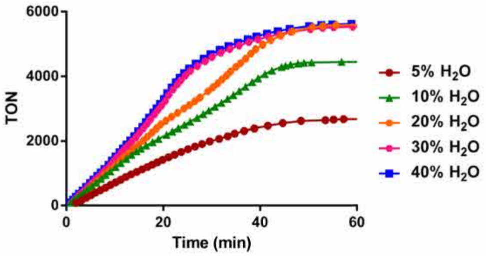

Fig. 3 Reaction profiles of FA dehydrogenation of neat FA by **1** under different H_2O concentrations at 353 K.

Table 2 Catalytic activity dependence on the addition of variable mol% of H_2O in FA dehydrogenation by **1**[a]

Entry	Mol% H_2O	TON	TOF_{max} (h^{-1})
1	5	2673	4319
2	10	4454	7034
3	20	5589	7740
4	30	5525	9784
5	40	5625	10 150

[a] General conditions: 0.016 mol% of **1**, 30 mol% HCOONa and FA (2 mL, 53.01 mmol), and the specified amount of H_2O at 353 K.

Table 2 and Fig. 3 show the TON values obtained at different water loadings. In particular, a catalytic run produced 47.7 mmol of H_2 (94% conversion) with a TON number of 5625, and reaching a TOF value of 10 150 h^{-1} (Table 2, entry 5). This is the highest TOF value reported for a Rh-based catalyst to date.[17] Moreover, the TOF values obtained with and without the addition of catalytic amounts of water compare well with those of most active catalysts hitherto reported for the solventless dehydrogenation of FA (**A–D**).[7,8]

The enhancement of the catalytic efficiency induced by water can be understood from different perspectives; on one hand, it may favor dissociation of FA dimers and increase co-catalyst solubility; in this line, it is known that FA molecules arrange as dimers *via* hydrogen bonds, where the presence of water may help dissociate such dimers leading to an easier accessibility of FA molecules to the catalytic species, therefore increasing the catalytic activity.[12] On the other hand, H_2O molecules may play an active role in the stabilization of catalytic intermediates, act as proton shuttles or even participate in hydrogen bonding with FA.[18] Fig. 4 shows comparative graphs of the dependence of the catalytic activity of **1** (0.016 mol%) on HCOONa and water, respectively. The graph on the left shows the variation of the catalytic activity of **1** with variable amounts of HCOONa without water, while the graph on the right shows its variation under 30 mol% of HCOONa with variable amounts of water. Note that although a 20 mol% loading of HCOONa leads to a higher initial TOF than at 30 mol%, the TON values are significantly higher in the case of the latter (Fig. 2), which prompted us to optimize the H_2O loading employing 30 mol% HCOONa. The variation of both

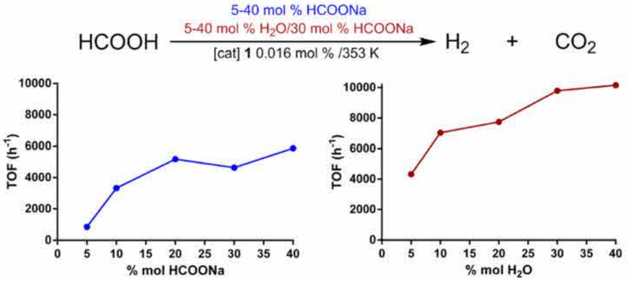

Fig. 4 TOF_{max} value variation as a function of mol% HCOONa (left, blue line) and mol% H_2O (right, red line).

parameters has similar effects on the catalytic activity, as shown in Fig. 4.

It is important to stress that decreasing the catalyst **1** loading to 0.005 mol% (2.16 mg, 2.6 μmol) led to a remarkable increase of the TOF value up to 11 164 h^{-1} when working with 30 mol% of HCOONa and 30 mol% of water at 353 K. However, this high TOF value is encompassed with a reduction in the TON number (850). A rather important aspect associated with catalytic FA dehydrogenation is that it is desirable that FA decomposition is selective toward H_2 and CO_2 production, therefore avoiding the formation of carbon monoxide, which has been reported to damage fuel cells. In order to assess this issue, the gaseous mixture obtained under optimized conditions (neat FA, 40 mol% HCOONa, 0.016 mol% of **1**) was subjected to IR spectroscopy and GC-MS analyses, showing no traces of CO. Therefore, under our experimental conditions, the CO gas produced in the catalysis is below the detection limit (Fig. S5–S6†).

We also studied the effect of temperature in the catalytic performance of **1** on FA dehydrogenation; as Fig. 5 shows, increasing the temperature leads to enhanced reaction rates. The activation energy ($\Delta G^{\ddagger}$) for solventless FA dehydrogenation catalyzed by complex **1** was estimated experimentally between 333 and 353 K using the Eyring plot ($\Delta G^{\ddagger} = 18.12 \pm 1.17$ kcal mol^{-1}; Fig. S26†).

Interestingly, we observed that there is a strong dependence of the catalyst's activity and durability on temperature. Even though the catalytic activity and TON values remain low at 333 K, when the temperature reaches 343 K the life of the catalyst increases considerably, reaching a TON value of 3400, which is a greater value than that achieved at 353 K; however, under these conditions catalyst **1** presents a moderate activity in FA dehydrogenation associated with a TOF value of 3559 h^{-1}. When the temperature reaches 363 K, TON values are quite similar to those observed at 353 K (TOF = 4984 h^{-1}); such catalytic activity, in spite of being greater than that observed at 353 K, shows a loss of the linear progression of the FA dehydrogenation activity with the temperature in the Eyring plot (see Fig. S27†), which indicates that high temperatures may compromise the stability of **1** in the catalytic media. This statement becomes evident at 373 K, where TON and TOF values fall, which indicates that despite the fact that temperature is a key parameter to improving the catalyst's activity and life, high temperatures boost catalyst decomposition.

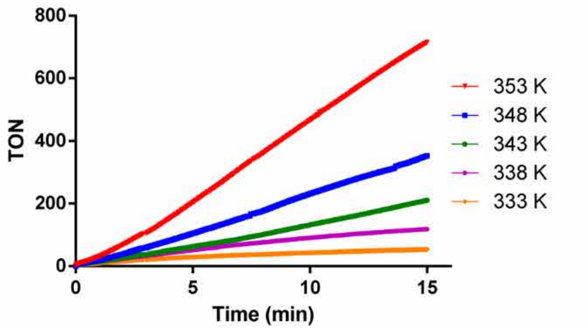

Fig. 5 Representation of TON (mol of H_2 per mol of Rh) *vs.* time of the solventless FA dehydrogenation catalysed by **1** (0.016 mol%) in the presence of HCOONa (30 mol%) at different temperatures.

NMR studies

In order to gain more insight into the operative mechanism of FA dehydrogenation performed with the cationic complex **1**, we carried out a series of NMR experiments in combination with DFT theoretical studies. Firstly, we monitored the direct interaction of **1** with variable amounts of FA in CD_3CN by NMR techniques; in this way, addition of neat FA to a solution of **1** in CD_3CN in a 1 : 1 ratio at RT resulted in a quick reaction that allowed observing for a short time a monohydrido species, along with unreacted **1**. Furthermore, a typical signal of molecular hydrogen is observed at $\delta(^1H)$ 4.56 ppm along with two weak signals in the hydride area at $\delta(^1H)$ −9.43 and −17.18 ppm. Then, a variable temperature NMR study was carried out. When **1** was treated with FA in a 1 : 3 molar ratio in CD_3CN at low temperatures (268–282 K) in a sealed J Young NMR tube, the initial deep red colour changed to yellow (which agrees with the colour change observed under catalytic conditions), and the ^1H NMR spectrum of the mixture showed, upon 5 min of standing, a clean transformation to monohydrido species, further characterized as the formate hydrido Rh^{III} complex $[(CNC)^{Mes}Rh(\kappa^{O}\text{-}OC(O)H)(PMe_2Ph)H]PF_6$ (**2**; Scheme 2). Interestingly, when **1** was reacted with FA in a 1 : 3 molar ratio at room temperature, only the bis(hydrido) species **1-H₂** and starting complex **1** were detected in the NMR spectra, while no monohydrido **2** was observed in the mixture (Fig. S11 and S12†). All these results suggest that there is an dynamic equilibrium in solution between **1**, **2** and **1-H₂** throughout the FA dehydrogenation process.

Interestingly, we were able to isolate the formate complex **2** as a yellow solid by reacting complex **1** with 3 molar-equiv. of neat FA at 253 K in acetonitrile (see the Experimental section). The intermediate formate complex **2** has been characterized through a combination of NMR techniques (Fig. S13–S19†).

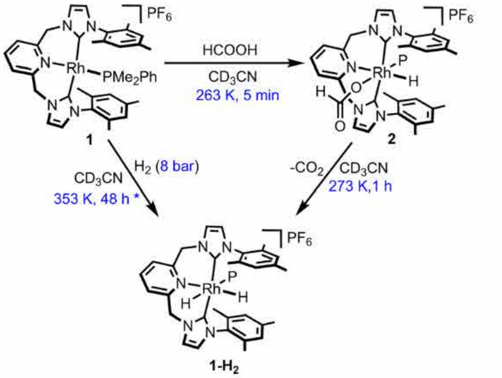

Scheme 2 Reactivity of complex **1** with FA and H_2, giving rise to species **2** and **1-H₂** (P = PMe_2Ph). *This reaction never proceeded to completion, even under harsher conditions.

The ^1H NMR spectrum of **2** in CD_3CN showed a pseudo-triplet at $\delta(^1H)$ −15.62 ppm (J = 21.2 Hz), signalling the presence of a hydrido ligand bound to the metal, *cis* to the phosphane ligand ($\delta(^{31}P)$ 37.0 ppm, $^1J_{P-Rh}$ = 135 Hz). The presence of the formate ligand in **2** was evident from the resonance observed at $\delta(^1H)$ 8.32 ppm, assigned to the formate proton, which correlated with a singlet observed at $\delta(^{13}C)$ 166.2 ppm in the $^{13}C\{^1H\}$-APT NMR spectrum corresponding to the carboxylic C atom. The ligand skeleton in **2** reflected an averaged C_{2h} symmetry in solution, due to the observation of a sole signal (dd) for the carbenic atoms in the $^{13}C\{^1H\}$-APT NMR spectrum of **2** ($\delta(^{13}C)$ 171.9 ppm, $^1J_{C-Rh}$ = 35 Hz, $^2J_{C-P}$ = 14 Hz). Also, the =CH protons of both imidazolium moieties were observed as two separated doublets in the ^1H NMR spectrum of **2**, which correlated with signals at $\delta(^{13}C)$ 125.9 and 125.8 ppm in the $^{13}C\{^1H\}$-APT NMR spectrum, respectively.

The stereochemistry of compound **2** was well established by ^1H–^1H NMR NOESY experiments; more specifically, we observed a strong NOE effect between the hydrido ligand and the *meta* protons of the phenyl group of the phosphane ligand, and also with one methyl moiety from the mesityl group, which located the hydrido ligand *trans* to the pyridinic N atom (Fig. 6). Species **2** is well depicted in Scheme 2; the hydrido and formate ligands are mutually *cis* as a consequence of an oxidative addition of the O–H bond of a FA molecule to the Rh^I centre, in agreement with DFT calculations (see below).

Once the nature of complex **2** was well established, we continued monitoring the reaction of **1** with 3 molar-equiv. of FA by NMR techniques in CD_3CN by gradually increasing the temperature.

Upon formation of **2** after 5 min at 268 K, the temperature was increased to 278 K; after 10 min, two incipient signals of hydrido ligands were detected, which became more intense after 30 min of standing at 282 K. At 1 h, the ^1H NMR spectrum of the reaction showed the presence of two different species, hydrido formate **2** and a new bis(hydrido) complex, further characterized as $[(CNC)^{Mes}Rh(PMePh_2)H_2]PF_6$ (**1-H₂**, Scheme 2). Fig. 7 shows the hydride area of the ^1H NMR spectra of the reaction between **1** and FA in CD_3CN at variable temperatures. Complex **1-H₂** is characterized by two hydrido resonances: a doublet of doublets at $\delta(^1H)$ −9.43 ppm ($^2J_{H-P}$ = 173.4 Hz; $^1J_{H-Rh}$ = 24.8 Hz) and another doublet of doublets at $\delta(^1H)$ −17.18 ppm ($^3J_{H-P}$ = 17.4 Hz; $^1J_{H-Rh}$ = 28.9 Hz), while the $^{31}P\{^1H\}$ NMR spectrum showed a broad doublet at $\delta(^{31}P)$ −8.4 ppm ($^1J_{P-Rh}$ = 153 Hz). The location and integration of the hydrido signals clearly indicate a complex with two hydrido ligands in mutual *cis* disposition. Another diagnostic resonance of the bis(hydrido) complex **1-H₂** was observed with an AB system centred at 5.03 ppm due to the CH_2 arms of the CNC^{Mes} ligand.

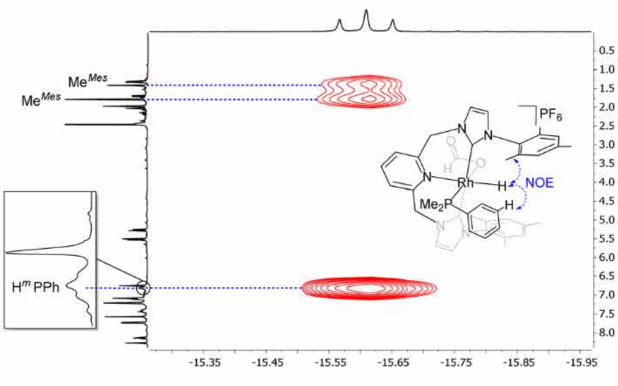

Fig. 6 Selected region of the ^1H–^1H NOESY NMR spectrum of $[(CNC)^{Mes}Rh(\kappa^O\text{-}OC(O)H)(PMe_2Ph)H]PF_6$ (**2**) in CD_3CN at 263 K.

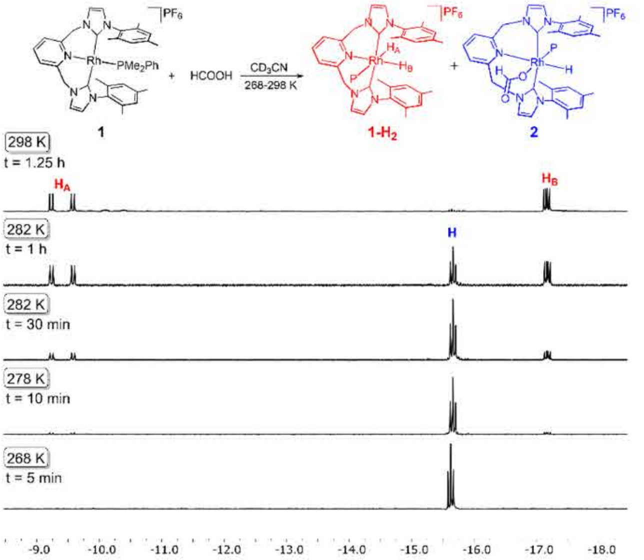

Fig. 7 Selected hydride region of the ^1H NMR spectra of the evolution of the reaction of **1** with 3 molar-equiv. of FA in CD_3CN at variable temperatures (268–298 K).

Given the nature and composition of the bis(hydrido) complex **1-H₂**, we tried its synthesis through direct hydrogenation of complex **2**. For this purpose, a J Young NMR tube was charged with **1**, dissolved in CD_3CN and pressurized with H_2 (8 bar). The NMR tube was sealed and heated at 353 K for 45 min. At this point, the ^1H NMR of the mixture showed incipient hydride signals. Upon heating overnight at 353 K, the initial red solution of **1** eventually transformed to a yellowish mixture containing the bis(hydrido) complex, tentatively characterized as $[(CNC)^{Mes}Rh(PMePh_2)H_2]PF_6$ (**1-H₂**, Scheme 2), along with some unreacted **1** (Fig. S20†). From this experiment it is clear that access to **1-H₂** by oxidative addition of H_2 to **2** is a difficult process when compared to its formation *via* hydride abstraction of the hydrido formate complex **2**. The difficulty in achieving net addition of dihydrogen to **1** is in contrast to the behaviour observed for the related deprotonated amido complex $[(CNC)^{Mes*}Rh(PMe_2Ph)]$, which easily adds dihydrogen to afford the corresponding bis(hydrido) Rh^{III} complex $[(CNC)^{Mes*}Rh(PMe_2Ph)H_2]$.[10]

Deuterium labelling and KIE experiments

In order to gain a deeper insight into the **2**-catalysed FA dehydrogenation process, we performed some deuterium labelling experiments. We monitored the reaction of **1** with HCOOD in $CDCN_3$ at 253 K by ^2H NMR techniques, observing the formation of a broad resonance in the ^2H NMR spectrum at $\delta(^2H)$ −16.0 ppm. This signal corresponded to the Rh–D bond formed by oxidative addition of HCOO–D to **1**, affording an isotopomer of **2**, namely $[(CNC)^{Mes}Rh(\kappa^O\text{-}OC(O)H)(PMe_2Ph)D]PF_6$ (2-D; Fig. S21 and S22†). Additionally, the ^1H NMR spectrum of the *in situ* reaction of fully deuterated FA (DCOOD) with **1** allowed us to observe, together with a signal of dihydrogen ($\delta(^1H)$ 4.56 ppm), a pattern of H–D coupling due to released gaseous HD (Fig. S23†), which indicates that throughout the catalysis there is an exchange with the sodium formate of the medium. When the same experiment is carried out without sodium formate in the catalytic mixture, the formation of HD is not observed (absence of the H–D pattern in the ^1H NMR spectrum). These observations agreed with the KIE effect estimated where the use of DCOONa affects the reaction rate $(K_{HCOONa}/K_{DCOONa}) = 1.51$, Table 3.

In order to gain insight into the rate-limiting step of the FA dehydrogenation by complex **1**, we performed H/D kinetic isotopic effect (KIE) experiments with **1** as a catalyst (Table 3). The KIE obtained upon changing HCOOH to DCOOD (2.58) and that from HCOOH to DCOOH (2.44) firmly suggests that the rate-limiting step in the proposed mechanism involves the C–H bond cleavage of a formate ligand, a process that may occur through β-hydride elimination or hydride abstraction. Interestingly, the experiment with deuterated sodium formate (DCOONa) has a slope that falls right in the middle of both groups, which supports the postulation that the C–H bond cleavage is the rate-limiting step. Furthermore, the H/D kinetic isotopic effects measured from HCOOH/HCOOD and DCOOD/DCOOH experiments (1.05 and 1.17, respectively) suggest that O–H cleavage is not involved in the turnover limiting step.

Table 3 Kinetic isotope effect data

FA derivative	K	K_{rel}	KIE effect (observed)
HCOOH	240.14	1	$k_{DCOOD}/k_{DCOOH} = 1.05$
DCOOD	92.79	2.58	$k_{DCOOD}/k_{HCOOD} = 2.21$
DCOOH	98.06	2.44	$k_{HCOOH}/k_{HCOOD} = 1.17$
HCOOD	204.78	1.17	$k_{HCOOH}/k_{DCOOD} = 2.58$
30% DCOONa/HCOOH	158.19	1.51	$k_{HCOOH}/k_{DCOOH} = 2.44$ $k_{HCOONa}/k_{DCOONa} = 1.51$

DFT studies on catalytic FA dehydrogenation by 1

DFT studies were performed in order to gain better insight into the operative mechanism of FA dehydrogenation catalysed by complex **1**. Two alternative pathways have been considered, the first of them starting with the activation of the formate and the second one from the activation of the formic acid. The former path would start by the hydride abstraction step from the formate by the metal complex. However, the calculated activation energy for this step is energetically unaffordable (TSBC' 27.4 kcal mol^{-1}, see Fig. S27†) while the second pathway yields lower energetic barriers. The relative Gibbs energy profile calculated using DFT methodology is provided in Fig. 8. As the reaction takes place in FA media, microsolvation of strong hydrogen donors and acceptors is considered in the proposed species throughout the catalytic cycle.

The initial step in FA dehydrogenation involves the *O*-coordination of a FA molecule to **1**. This coordination to the metal induces decoordination of the pyridinic N atom generating intermediate **B**, in which Rh^I maintains a square planar geometry. This is an endergonic process where the energy increases to 9.1 kcal mol^{-1} and induces a conformational change within the bulky $(CNC)^{Mes*}$ and PMe_2Ph ligands. Following this, intramolecular O–H oxidative addition of coordinated FA proceeds through **TSBC** (9.4 kcal mol^{-1}), affording the Rh^{III} hydrido formate intermediate **C**, in which the hydrido ligand is located *trans* to the pyridinic N atom.

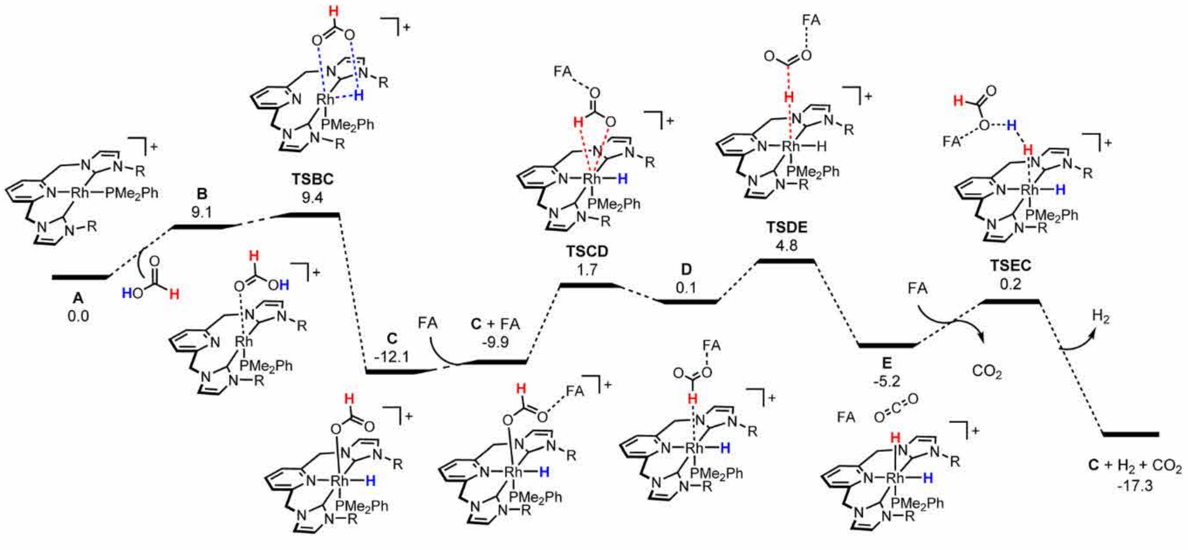

Fig. 8 DFT energetic profile (ΔG in kcal mol^{-1}, relative to A and isolated molecules) for formic acid dehydrogenation catalysed by **1**.

Intermediate C presents a relative energy of −12.1 kcal mol^{-1} and its stereochemistry agrees with the NMR data obtained for intermediate **2**. Subsequent addition of a second FA molecule leads to adduct **C** + FA stabilized by hydrogen bonding with the formate ligand. At this point, protonation of the hydride intermediate **C** by formic acid yields a Rh^{III} bis(formate) intermediate, **F**, and molecular H_2, which could be a viable pathway to close the catalytic cycle. However, the calculated relative energy of **F** amounts to 14.7 kcal mol^{-1} (see Fig. S28†), being energetically unaffordable. Instead, the κ-*O*-formate ligand switches its coordination mode from κ-*O* to κ-*H* *via* the transition state **TSCD**, with a relative energy of 1.7 kcal mol^{-1}. Then, hydrogen abstraction from the formate anion to the metal is characterized by **TSDE**, showing an overall energy barrier of 16.9 kcal mol^{-1} (from intermediate **C**) leading to the dihydride intermediate **E** and releasing a CO_2 molecule (−5.2 kcal mol^{-1}). Finally, a H_2 molecule can be formed by heterolytic bond formation between the negatively charged hydride and the positively charged proton of a FA molecule. This process is characterized by **TSEC** with a relative energy of 0.2 kcal mol^{-1}. The release of H_2 is exergonic (−17.3 kcal mol^{-1}) and leads to the intermediate **C** + **FA**, closing the catalytic cycle.

Based on this DFT study, complex **1** is activated by oxidative addition of the O–H bond of FA to the metal. Then, the catalytic cycle comprises three steps: (i) change in the coordination mode of the formate ligand, (ii) hydrogen abstraction to yield the dihydride and release of CO_2 and (iii) H_2 formation between hydride and a proton from an external FA molecule. The rate determining step for the DFT calculated mechanism is the hydride abstraction step presenting an overall energetic barrier of 16.9 kcal mol^{-1} in good agreement with the obtained experimental data of 18.12 ± 1.17 kcal mol^{-1}. It should be noted that for other FA dehydrogenation catalysts the formation of the hydride intermediates takes place by a β-elimination process, which resultantly becomes the rate determining step.[19] In the present case, the lack of vacant sites at the metal impedes such a mechanism similar to other catalysts reported in the literature.[20]

The KIEs have been calculated using DFT methodology for a direct comparison with experimental KIEs. According to the calculated energetic profile, the rate determinant structures are C and TSCE and the calculated KIE for DCOOH is 2.63, while for HCOOD it is **1**. This is in good agreement with the experimental values of 2.44 and 1.17 obtained in the previous section.

Conclusions

In summary, we have shown that the Rh complex **1** behaves as an efficient catalyst for the dehydrogenation of FA under solvent-free conditions. The TOF values obtained for **1** are amongst the highest so far reported in the absence of solvent, which is in contrast with the modest catalytic activities reported for Rh-complexes in the dehydrogenation of FA. The astounding performance of **1** could be attributed to the bis-NHC scaffold of the pincer ligand and also to the presence of the P-donor PMe_2Ph ligand. NHC ligands give rise to electron-rich metal centres and strong C–metal bonds; therefore, the presence of the $(CNC)^{Mes}$ pincer ligand chosen by us for this study plausibly eases the formation of the active species **2** and stabilises the Rh^{III} intermediates of the catalytic cycle. The DFT calculations support a catalytic cycle that involves a hydride abstraction step, which converts monohydride **C** into bis(hydrido) **E**, followed by protonation of the bis(hydrido) **E** to regenerate **C**. The formation of the active species, **C** (**2**), takes place *via* oxidative addition of FA to **A** (**1**). The calculated reaction mechanism agrees well with experimental data: (i) key intermediates of the catalytic cycle, **C** (**2**) and **E** (**1-H$_2$**), were observed and characterised *in situ* by NMR by means of stoichiometric reactions; (ii) KIE measurements suggest that the hydride abstraction is the rate-limiting step; (iii) the activation energies calculated with the Eyring model compare well with the theoretical value obtained from DFT calculations; and (iv) labelling experiments confirm that the active species is formed by oxidative addition of the O–H bond of FA to the Rh(I) center in **1**.

Experimental

Procedure for FA dehydrogenation

FA dehydrogenation catalytic experiments were carried out as follows. The catalyst **1** (0.016 mol%) and sodium formate were weighted on an analytic balance placed into a drybox, and then transferred to a microreactor (*Man on the moon* series X102 kit), which was pre-heated at 353 K. Then, under an argon atmosphere, 2 mL of neat formic acid was injected into the reactor *via* a syringe and left under stirring until complete dehydrogenation of FA. Pressure measurements were monitored by a manometer connected to the reactor.

Computational details

All DFT calculations were carried out using the Gaussian program package.[21] Geometrical optimizations and analytical frequency calculations were performed using the B3LYP-D3 method[22] including solvent corrections using the PCM method[23] for formic acid and the def2-SVP basis set,[24] together with the corresponding core potential for Rh atoms. Energies were refined by single point calculations using the M06L functional[25] combined with the SMD solvation model[26] and the def2-TZVP basis set. The "ultrafine" grid was employed in all calculations. All reported energies are Gibbs free energies referred to a 1 M standard state at 353 K and quasi-harmonic corrections[27] calculated using the Goodvibes program.[28]

The nature of the stationary points was confirmed by analytical frequency analysis, and transition states were characterized by a single imaginary frequency corresponding to the expected motion of the atoms. Calculations of KIE from DFT data are performed by replacing the mass of the selected hydrogen atom with deuterium using the keyword readisotopes in G09 and calculating the vibrational frequencies at the transition state and the corresponding intermediate.

Preparation of $[(CNC)^{Mes}Rh(\kappa^{O}\text{-}OC(O)H)(PMe_2Ph)H]PF_6$ (2)

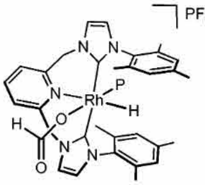

A Schlenk tube was charged with **1** (120 mg, 0.148 mmol) and dissolved in CH_3CN (5 mL). Then, 2 mol-equiv. of neat FA (11.2 μL, 0.202 mmol) were added *via* a microsyringe and the resulting yellow solution was stirred for 10 min at 253 K. Evaporation of the volatiles by reduced pressure left a yellow residue, which was washed with hexanes and then vacuum-dried. Yield: 115 mg (86%).

^1H NMR (400 MHz, CD_3CN, 253 K): δ 8.32 (s, 1H; HC(O)O–Rh), 8.13 (t, $^3J_{H-H}$ = 7.9 Hz, 1H; H^p py), 7.73 (d, $^3J_{H-H}$ = 7.7 Hz, 1H; H^m py), 7.56 (d, $^3J_{H-H}$ = 1.9 Hz, 2H; =CH Im), 7.48 (m, 2H; H^o Ph), 7.20 (d, $^3J_{H-H}$ = 1.9 Hz, 2H; =CH Im), 7.10 (m, 2H; H^m Ph), 7.08 (br s, 2H; CH Mes), 6.80 (m, 1H; H^m Ph), 6.74 (br s, 2H; CH Mes), 5.51 (d, $^3J_{H-H}$ = 16.5 Hz, 2H), 5.26 (d, $^3J_{H-H}$ = 16.5 Hz, 2H) (CH_2N), 2.55 (s, 6H), 1.78 (s, 6H), 1.41 (s, 6H) (Me Mes), 1.32 (d, $^2J_{H-P}$ = 10.4 Hz, 6H; CH_3P), −15.62 (t, $^1J_{H-Rh}$ = 21.2 Hz, $^2J_{H-P}$ = 21.2 Hz, 1H; Rh–H). ^{31}P {^1H} NMR (162 MHz, CD_3CN, 253 K): δ 27.0 (d, $^2J_{P-Rh}$ = 135 Hz). ^{13}C {^1H}-APT NMR (100 MHz, CD_3CN, 253 K): δ 171.9 (dd, $^1J_{C-Rh}$ = 35 Hz, $^2J_{C-P}$ = 14 Hz; Rh–C Im), 166.2 (s; HCOO–Rh), 156.8 (s; C^o py), 142.7 (C^p py), 136.9, 136.7, 135.8 (C_q Mes), 132.1, 131.9 (P*Ph*), 131.0, 130.4 (CH Mes), 129.9, 129.8 (P*Ph*), 127.7 (C^m py), 125.9, 125.8 (=CH Im), 55.7 (CH_2N), 21.5 (Me Mes), 171.9 (d, $^1J_{C-P}$ = 36 Hz; PMe), 19.1, 19.0 (Me Mes). Mass Calcd for $C_{40}H_{46}N_5O_2PRh$: 762.7048; HRMS (ESI^+): *m/z* 716.2408 (100%; M^+ − HCOOH).

Conflicts of interest

There are no conflicts to declare.

Acknowledgements

Grants PGC2018-099383-B-I00 and RTI2018-099136-A-I00 funded by MCIN/AEI/10.13039/501100011033 and by "ERDF A way of making Europe", DGA/FSE (group E42_20R) and CSIC project 202080I024 are gratefully acknowledged. The co-author V. P. thankfully acknowledges the resources from the supercomputers "Memento" and the technical expertise and assistance provided by the Institute for Biocomputation and Physics of Complex Systems (BIFI)–Universidad de Zaragoza. A. U. thankfully acknowledges the Spanish MECD for an FPU fellowship (FPU 2017/05417).

Notes and references

1 N. P. Brandon and Z. Kurban, Clean energy and the hydrogen economy, *Philos. Trans. R. Soc., A*, 2017, **375**, 20160400.

2 (*a*) S. Enthaler, Carbon Dioxide—The hydrogen–storage material of the future?, *ChemSusChem*, 2008, **1**, 801–804; (*b*) J. Eppinger and K.-W. Huang, Formic acid as a hydrogen energy carrier, *ACS Energy Lett.*, 2017, **2**, 188–195; (*c*) F. Joó, Breakthroughs in hydrogen storage—formic acid as a sustainable storage material for hydrogen, *ChemSusChem*, 2008, **1**, 805–808.

3 (*a*) S. Thomas, CO_2-based hydrogen storage: CO_2 hydrogenation to formic acid, formaldehyde and methanol, *Phys. Sci. Rev.*, 2018, 20170015; (*b*) U. Praveenkumar and S. Vivek, Carbon sequestration: hydrogenation of CO_2 to Formic acid, *Present Environ. Sustainable Dev.*, 2016, **10**, 13–34.

4 (*a*) F. Valentini, V. Kozell, C. Petrucci, A. Marrocchi, Y. Gu, D. Gelman and L. Vaccaro, Formic acid, a biomass-derived source of energy and hydrogen for biomass upgrading, *Energy Environ. Sci.*, 2019, **12**, 2646–2664; (*b*) D. A. Bulushev and J. R. H. Ross, Towards sustainable production of formic acid, *ChemSusChem*, 2018, **11**, 821–836.

5 D. J. Drury, in *FA and Derivatives. Kirk-Othmer Encyclopedia of Chemical Technology*, ed. J. I. Kroschwitz and M. Howe-Grant, John Wiley & Sons, Inc., New York, 2013, vol. 27.

6 (*a*) K. Sordakis, C. Tang, L. K. Vogt, H. Junge, P. J. Dyson, M. Beller and G. Laurenczy, Homogeneous catalysis for sustainable hydrogen storage in formic acid and alcohols, *Chem. Rev.*, 2018, **118**, 372–433; (*b*) P. Stathi, M. Solakidou, M. Louloudi and Y. Deligiannakis, From homogeneous to heterogenized molecular catalysts for H2 production by formic acid dehydrogenation: mechanistic aspects, role of additives, and co-Catalysts, *Energies*, 2020, **13**, 733; (*c*) M. Grasemann and G. Laurenczy, Formic acid as a hydrogen source—recent developments and future trends, *Energy Environ. Sci.*, 2012, **5**, 8171–8181; (*d*) A. Luque-Gómez, S. García-Abellán, J. Munarriz, V. Polo, V. Passarelli and M. Iglesias, Impact of green cosolvents on the catalytic dehydrogenation of formic acid: the case of iridium catalysts bearing NHC-phosphane ligands, *Inorg. Chem.*, 2021, **60**, 15497–15508.

7 (*a*) J. J. A. Celaje, Z. Lu, E. A. Kedzie, N. J. Terrile, J. N. Lo and T. J. Williams, A prolific catalyst for dehydrogenation of neat formic acid, *Nat. Commun.*, 2016, **7**, 11308; (*b*) A. Iturmendi, M. Iglesias, J. Munarriz, V. Polo, V. Passarelli, J. J. Pérez-Torrente and L. A. Oro, A highly efficient Ir-catalyst for the solventless dehydrogenation of formic acid: the key role of an N-heterocyclic olefin, *Green Chem.*, 2018, **20**, 4875–4879; (*c*) S. Cohen, V. Borin, I. Schapiro, S. Musa, S. De-Botton, N. V. Belkova and D. Gelman, Ir(III)-PC(sp^3)P bifunctional catalysts for production of H_2 by dehydrogenation of formic acid: experimental and theoretical study, *ACS Catal.*, 2017, **7**, 8139–8146; (*d*) S. Wang, H. Huang, T. Roisnel, C. Bruneau and C. Fischmeister, Base-free dehydrogenation of aqueous and

neat formic acid with iridium(III) Cp*(dipyridylamine) catalysts, *ChemSusChem*, 2019, **12**, 179–184.

8 S. Kar, M. Rauch, G. Leitus, Y. Ben-Davis and D. Milstein, Highly efficient additive-free dehydrogenation of neat formic acid, *Nat. Catal.*, 2021, **4**, 193–201.

9 (*a*) M. Albrecht, *Chem. Rev.*, 2010, **110**, 576–623; (*b*) K. R. Jain, W. A. Herrmann and F. E. Kühn, High oxidation state transition metal complexes ligated with N-heterocyclic carbenes, *Curr. Org. Chem.*, 2008, **12**, 1468–1478; (*c*) M. Iglesias and L. A. Oro, A leap forward in iridium–NHC catalysis: new horizons and mechanistic insights, *Chem. Soc. Rev.*, 2018, **47**, 2772–2808.

10 P. Hermosilla, P. García-Orduña, F. J. Lahoz, V. Polo and M. A. Casado, Rh complexes with pincer carbene CNC lutidine-based ligands: reactivity studies toward H_2 addition, *Organometallics*, 2021, **40**, 3720–3732.

11 (*a*) J. B. Curley, N. E. Smith, W. H. Bernskoetter, N. Hazari and B. Q. Mercado, Catalytic formic acid dehydrogenation and CO_2 hydrogenation using iron PN^RP pincer complexes with isonitrile ligands, *Organometallics*, 2018, **37**, 3846–3853; (*b*) S. Oldenhof, J. I. van der Vlugt and J. N. H. Reek, Hydrogenation of CO_2 to formic acid with iridium^{III} (bisMETAMORPhos) (hydride): the role of a dormant *fac*-Ir^{III} (trihydride) and an active *trans*-Ir^{III} (dihydride) species, *Catal. Sci. Technol.*, 2016, **6**, 404–408.

12 P. Rodziewicz and N. L. Doltsinis, Formamide dimers: a computational and matrix isolation study, *J. Phys. Chem. A*, 2009, **113**, 6266–6274.

13 S. Fukuzumi, T. Kobayashi and T. Suenobu, Unusually large tunneling effect on highly efficient generation of hydrogen and hydrogen isotopes in pH-selective decomposition of formic acid catalyzed by a heterodinuclear iridium–ruthenium complex in water, *J. Am. Chem. Soc.*, 2010, **132**, 1496–1497.

14 (*a*) S. Siek, D. B. Burks, D. L. Gerlach, G. Liang, J. M. Tesh, C. R. Thompson, F. Qu, J. E. Shankwitz, R. M. Vasquez, N. Chambers, G. J. Szulczewski, D. B. C. Grotjahn, E. Webster and E. T. Papish, Iridium and ruthenium complexes of N-heterocyclic carbene- and pyridinol-derived chelates as catalysts for aqueous carbon dioxide hydrogenation and formic acid dehydrogenation: the role of the alkali metal, *Organometallics*, 2017, **36**, 1091–1106; (*b*) J. F. Hull, Y. Himeda, W.-H. Wang, B. Hashiguchi, R. Periana, D. J. Szalda, J. T. Muckerman and E. Fujita, Reversible hydrogen storage using CO_2 and a proton-switchable iridium catalyst in aqueous media under mild temperatures and pressures, *Nat. Chem.*, 2012, **4**, 383–388; (*c*) S. Fukuzumi, T. Kobayashi and T. Suenobu, Efficient catalytic decomposition of formic acid for the selective generation of H_2 and H/D exchange with a water-soluble rhodium complex in aqueous solution, *ChemSusChem*, 2008, **1**, 827–834; (*d*) Y. Himeda, Highly efficient hydrogen evolution by decomposition of formic acid using an iridium catalyst with 4,4′-dihydroxy-2,2′-bipyridine, *Green Chem.*, 2009, **11**, 2018–2022; (*e*) W.-H. Wang, M. Z. Ertem, S. Xu, N. Onishi, Y. Manaka, Y. Suna, H. Kambayashi, J. T. Muckerman, E. Fujita and Y. Himeda, Highly robust hydrogen generation by bioinspired Ir complexes for dehydrogenation of formic acid in water: experimental and theoretical mechanistic investigations at different pH, *ACS Catal.*, 2015, **5**, 5496–5504.

15 S. Patra, M. K. Awasthi, R. K. Rai, H. Deka, S. M. Mobin and S. K. Singh, Dehydrogenation of formic acid catalyzed by Water-soluble ruthenium complexes: X-ray crystal structure of a diruthenium complex, *Eur. J. Inorg. Chem.*, 2019, 1046–1053.

16 X.-T. Guo, J. Zhang, J.-C. Chi, Z.-H. Li, Y.-C. Liu, X.-R. Liu and S.-Y. Zhang, Efficient dehydrogenation of a formic Acid–ammonium formate mixture over Au_3Pd_1 catalyst, *RSC Adv.*, 2019, **9**, 5995–6002.

17 C. Fink and G. Laurenczy, A precious catalyst: rhodium-catalyzed formic acid dehydrogenation in water, *Eur. J. Inorg. Chem.*, 2019, 2381–2387.

18 N. J. Britto and M. Jaccob, Deciphering the mechanistic details of manganese-catalyzed formic acid dehydrogenation: insights from DFT calculations, *Inorg. Chem.*, 2021, **60**, 11038–11047.

19 M. Iglesias and L. A. Oro, Mechanistic considerations on homogeneously catalyzed formic acid dehydrogenation, *Eur. J. Inorg. Chem.*, 2018, 2125–2138.

20 (*a*) T. Zell, B. Butschke, Y. Ben-David and D. Milstein, Efficient hydrogen liberation from formic acid catalyzed by a well-defined iron pincer complex under mild conditions, *Chem. – Eur. J.*, 2013, **19**, 8068–8072; (*b*) I. Mellone, N. Gorgas, F. Bertini, M. Peruzzini, K. Kirchner and L. Gonsalvi, Selective formic acid dehydrogenation catalyzed by Fe-PNP pincer complexes based on the 2,6-diaminopyridine scaffold, *Organometallics*, 2016, **35**, 3344–3349; (*c*) E. A. Bielinski, P. O. Lagaditis, Y. Zhang, B. Q. Mercado, C. Würtele and W. H. N. Bernskoetter, Hazari and S. Schneider. Lewis acid-assisted formic acid dehydrogenation using a pincer-supported iron catalyst, *J. Am. Chem. Soc.*, 2014, **136**, 10234–10237; (*d*) S. Oldenhof, M. Lutz, B. de Bruin, J. I. van der Vlugt and J. N. H. Reek, Dehydrogenation of formic acid by Ir–bisMETAMORPhos complexes: experimental and computational insight into the role of a cooperative ligand, *Chem. Sci.*, 2015, **6**, 1027–1034.

21 *Gaussian 09, revision D.01*, Gaussian, Inc., Wallingford CT, 2016. See ESI for full citation.†

22 (*a*) A. D. Becke, A new mixing of Hartree–Fock and local density–functional theories, *J. Chem. Phys.*, 1993, **98**, 1372–1377; (*b*) C. Lee, W. Yang and R. G. Parr, Development of the Colle-Salvetti correlation-energy formula into a functional of the electron density, *Phys. Rev. B: Condens. Matter Mater. Phys.*, 1988, **37**, 785–789; (*c*) S. Grimme, J. Antony, S. Ehrlich and H. Krieg, A consistent and accurate ab initio parametrization of density functional dispersion correction (DFT-D) for the 94 elements H-Pu, *J. Chem. Phys.*, 2010, **132**, 154104; (*d*) E. R. Johnson and A. D. Becke, A post-Hartree-Fock model of intermolecular interactions: inclusion of higher-order corrections, *J. Chem. Phys.*, 2006, **124**, 174104.

23 (*a*) S. Miertuš, E. Scrocco and J. Tomasi, Electrostatic interaction of a solute with a continuum. A direct utilizaion of AB initio molecular potentials for the prevision of solvent effects, *Chem. Phys.*, 1981, **55**, 117–129; (*b*) S. Miertuš, E. Scrocco and J. Tomasi, Approximate evaluations of the electrostatic free energy and internal energy changes in solution processes, *J. Chem. Phys.*, 1982, **65**, 239–245.

24 F. Weigend and R. Ahlrichs, Balanced basis sets of split valence, triple zeta valence and quadruple zeta valence quality for H to Rn: Design and assessment of accuracy, *Phys. Chem. Chem. Phys.*, 2005, **7**, 3297–3305.

25 Y. Zhao and D. G. Truhlar, A new local density functional for main-group thermochemistry, transition metal bonding, thermochemical kinetics, and noncovalent interactions, *J. Chem. Phys.*, 2006, **125**, 194101.

26 A. V. Marenich, C. J. Cramer and D. G. Truhlar, Universal solvation model based on solute electron density and a continuum model of the solvent defined by the bulk dielectric constant and atomic surface tensions, *J. Phys. Chem. B*, 2009, **113**, 6378–6396.

27 S. Grimme, Supramolecular Binding Thermodynamics by Dispersion-Corrected Density Functional Theory, *Chem. – Eur. J.*, 2012, **18**, 9955–9964.

28 G. Luchini, J. V. Alegre-Requena, I. Funes-Ardoiz and R. S. Paton, *F1000Research*, 2020, **9**, 291, DOI: **10.12688/f1000research.22758.1**. GoodVibes version 3.1.1.

ACS Catalysis

pubs.acs.org/acscatalysis

Research Article

Metal–Ligand Cooperative Proton Transfer as an Efficient Trigger for Rhodium-NHC-Pyridonato Catalyzed *gem*-Specific Alkyne Dimerization

María Galiana-Cameo, Asier Urriolabeitia, Eduardo Barrenas, Vincenzo Passarelli, Jesús J. Pérez-Torrente, Andrea Di Giuseppe, Víctor Polo,* and Ricardo Castarlenas*

Cite This: *ACS Catal.* 2021, 11, 7553–7567

ABSTRACT: The mononuclear square-planar Rh{κ^2-*X*,*N*-(Xpy)}(η^2-coe)(IPr) (X = O, NH, NMe, S) complexes have been synthesized from the dinuclear precursor $[\mathrm{Rh}(\mu\text{-Cl})(\mathrm{IPr})(\eta^2\text{-coe})]_2$ and the corresponding 2-heteroatom-pyridinate salts. The Rh-NHC-pyridinato derivatives are highly efficient catalysts for *gem*-specific alkyne dimerization. Particularly, the chelating N,O-pyridonato complex displays turnover frequency levels of up 17 000 h^{-1} at room temperature. Mechanistic investigations and density functional theory calculations suggest a pyridonato-based metal–ligand cooperative proton transfer as responsible for the enhancement of catalytic activity. The initial deprotonation of a Rh-π-alkyne complex by the oxo-functionality of a κ^1-N-pyridonato moiety has been established to be the rate-limiting step, whereas the preferential protonation of the terminal position of a π-coordinated alkyne accounts for the exclusive observation of head-to-tail enynes. The catalytic cycle is closed by a very fast alkenyl–alkynyl reductive elimination.

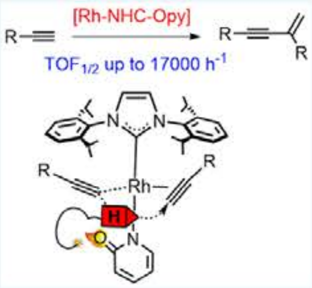

KEYWORDS: *metal–ligand cooperation, ligand assisted proton shuttle, alkyne dimerization, N-heterocyclic carbene, DFT calculations, hemilability*

INTRODUCTION

Organometallic catalysis is nowadays at the central core of the preparation of elaborated organic structures owing to a continuous design of new metal–ligand architectures.[1] Undoubtedly, the high levels of catalytic efficiency have been achieved due to a precise control of reactivity through detailed determination of mechanistic issues. In this context, the concept of metal–ligand cooperation (MLC) has emerged as an essential piece in organometallic-mediated bond cleavage and formation, particularly for dihydrogen activation and related reactions.[2] The synergic effect arising from MLC generally triggers an enhancement of catalytic activity and provides better control of selectivity. A particular case of MLC arises when a ligand acts as a carrier for a proton from one substrate to the other for which the term ligand assisted proton shuttle (LAPS) has been coined (Scheme 1).[3] Besides its competence in the originally proposed alkyne–vinylidene tautomerization,[4] LAPS pathways have been proposed in catalytic intramolecular cyclizations[5] and stoichiometric intermolecular reactions,[6] but scarcely applied to catalytic intermolecular transformations.[7]

Alkyne dimerization is a practical and atom economical access to 1,3-enynes as key structural elements in a variety of biologically active molecules and functional organic materials.[8] Efficient catalysts spread across the periodic table, from f-block,[9] early[10] or late transition metals,[11] to main group elements.[12] Moreover, earth-abundant transition metals of the first row[13] or organocatalysts[14] have recently emerged. Due to the inherent rich chemistry of alkynes, the formation of head-to-tail (*gem*) or head-to-head (*E*/*Z*) enynes is commonly in competition with the formation of a myriad of oligomeric, polymeric, or cyclic organic structures. Therefore, despite the fact that remarkable advances in the selective preparation of *E*,[11b,g,13b] *Z*,[9c,10b,13c,e] or *gem*-enynes,[13d,f,i,14a] further research effort is still desirable, particularly in mechanism elucidation.

Four general pathways have been proposed for transition-metal mediated alkyne dimerizations:[11i] (i) external attack on the coordinated π-alkyne; (ii) oxidative addition of a terminal alkyne; (iii) nonoxidative base-mediated formation of metal-alkynyl species; and (iv) dimerization via a vinylidene intermediate. It has been rationalized that the nonoxidative route iii would be the preferred approach for the selective preparation of *gem*-enynes (Scheme 2).[11i] Initial deprotonation of the alkyne leads to metal-alkynyl species. Noteworthy, an MLC effect has been claimed in the case of an internal base.[11f,13d,f,g,i] Then, the pathway continues by an insertion of another alkyne into metal-alkynyl bond and subsequent

Received: February 9, 2021
Revised: May 21, 2021
Published: June 9, 2021

https://doi.org/10.1021/acscatal.1c00602
ACS Catal. 2021, 11, 7553–7567

Scheme 1. Catalytic Ligand Assisted Proton Shuttle

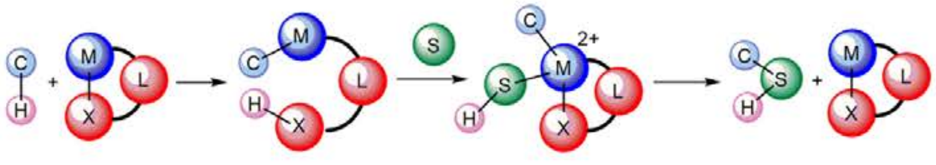

Scheme 2. Metal-Ligand Cooperative Alkyne Dimerization

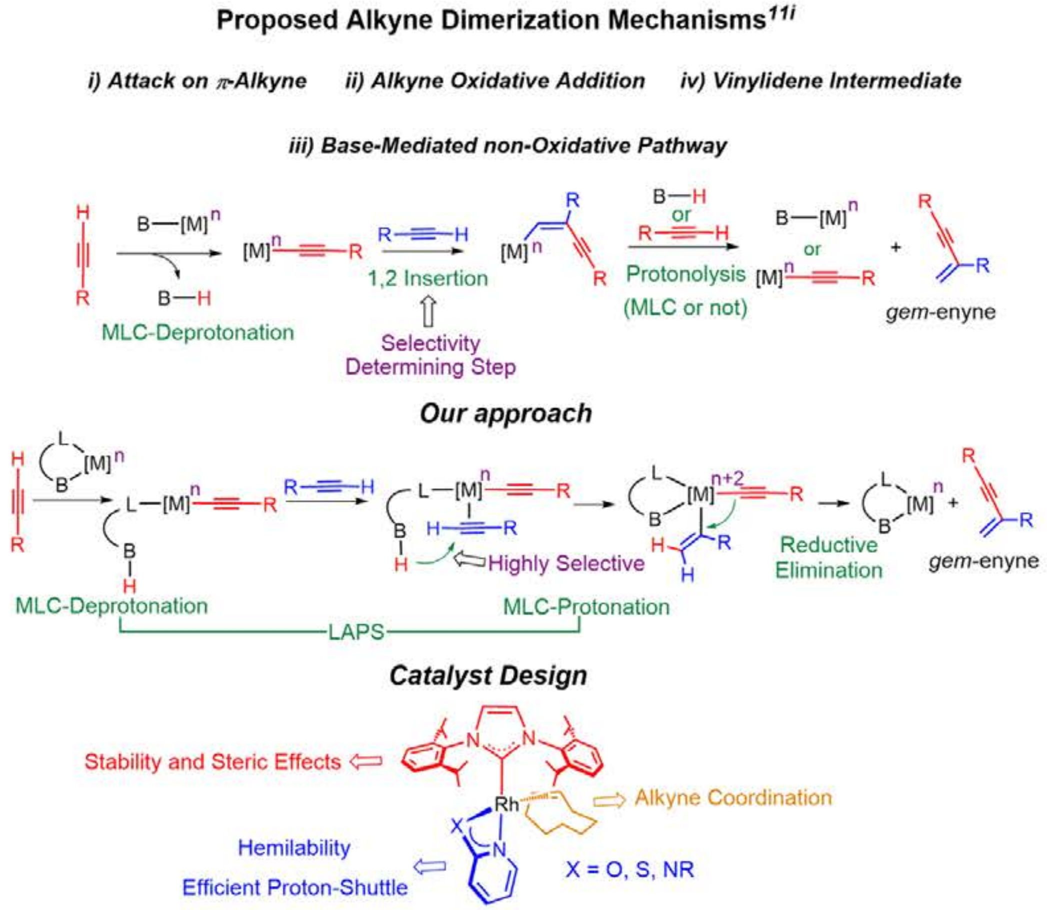

protonolysis by the conjugated acid of the initial base (MLC or not) or an alkyne itself. Although this pathway takes advantage of the benefits of MLC in deprotonation or protonolysis, the key insertion step, which determines the selectivity and is usually rate-limiting, remains excluded from the metal–ligand cooperative influence. An alternative approach can be envisaged in which metal and ligand would act in cooperation throughout the whole catalytic cycle. After the initial deprotonation of an alkyne molecule, the resulting protonated ligand could transfer the hydrogen atom to a second molecule of the alkyne in an oxidatively manner that yields a $\mathrm{Rh^{III}}$-alkenyl-alkynyl species. Subsequent reductive elimination will close the catalytic cycle. An MLC effect is expected to result in lowering the key energetic barriers. Indeed, the selectivity determining step changes from a mainly sterically ligand-controlled carbometalation in iii to a Markovnikov-type electronically and sterically favored protonation on a coordinated alkyne, therefore enhancing specific *gem*-enyne formation.

Recent results from our laboratories have revealed that coordination of an *N*-heterocyclic carbene (NHC) ligand to rhodium complexes resulted in efficient alkyne dimerization catalysts.[11i,15] Several chelate 1,3-bis-hetereoatomic acidato (BHetA) ligands, such as carboxylato, thioacidato, or amidato, have demonstrated their utility as internal bases to selectively promote the formation of head-to-tail enynes. Now, along this line, we hypothesize that increasing the robustness of the chelate interaction should allow the anionic ligand to act not only as a base but also as an efficient proton shuttle. In this regard, pyridine-like moieties have previously been efficiently anchored to Rh-NHC platforms.[16] Thus, 2-heteroatom-substituted pyridine ligands appear to be promising candidates to fulfill the requirements of a BHetA structure with tight chelate coordination.[17] Particularly, 2-pyridonate moieties have been shown to act as versatile proton-responsive ligands[18] which can behave as powerful internal bases[19] as well as efficient proton shuttles.[20] Moreover, its proven hemilability[21] would be key for the generation of vacant sites and the proton transfer process. Herein, we report on the preparation of $\mathrm{Rh^{I}}$-

Scheme 3. Preparation of Rh-IPr 2-Heteroatom-Pyridinato Complexes

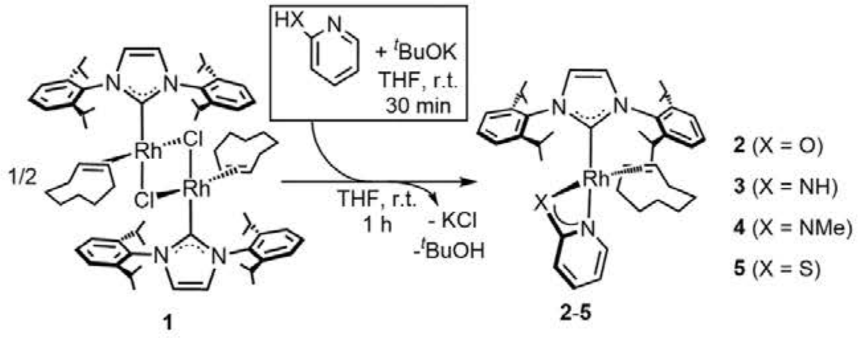

NHC-pyridinato derivatives and their application as catalysts for *gem*-specific alkyne dimerization. Experimental and theoretical studies have revealed a rhodium-pyridonato LAPS process as responsible for the enhancement of catalytic activity.

■ RESULTS AND DISCUSSION

Preparation of Rh-Pyridinato Catalysts. The dinuclear precursor $[\mathrm{Rh}(\mu\text{-Cl})(\eta^2\text{-coe})(\mathrm{IPr})]_2$ (**1**) {IPr = 1,3-bis(2,6-diisopropylphenyl)imidazolin-2-carbene; coe = cyclooctene} reacts with a THF solution of deprotonated 2-heteroatom-pyridine compounds to yield BHetA derivatives Rh{κ^2-*X,N*-(Xpy)}(η^2-coe)(IPr) {py = C_5H_4N, X = O (**2**), NH (**3**), NMe (**4**), S (**5**)} (Scheme 3). The new complexes were obtained as yellow−orange solids with 55−72% yields. It is worth mentioning that complex **2** can be directly obtained by reaction of **1** with 2-pyridone in the absence of an external base, although in low yield and purity. Moreover, in contrast to related 8-quinoline derivatives,[16a] no O−H oxidative addition to yield $\mathrm{Rh^{III}}$-hydride species was observed. On the contrary, the reaction of **1** with the more acidic 2-mercapto-pyridine resulted in the formation of several $\mathrm{Rh^{III}}$-hydride species, as reflected in the appearance of ^{1}H NMR highly shielded doublets. As far as we know, the coordination of the 2-heteroatom-pyridinato moiety into an Rh-NHC framework is unprecedented.[22−25]

The solid-state structure of the pyridonato complex **2** was elucidated by X-ray diffraction analysis. An ORTEP view of the molecule with selected bond lengths and angles is displayed in Figure 1. A mononuclear structure with a rare chelate arrangement[22] of the 2-pyridonato ligand is observed instead of the more typical μ-bridge dinuclear assembly.[23] The crystal structure exhibits a distorted square planar geometry at the metal center with the IPr in a *cis* arrangement with respect to coe [C(1)−Rh−ct 94.32(6)°], and the oxygen atom in a *trans* disposition to the latter [ct−Rh−O(44) 168.82(4)°]. The Rh−C(1) bond length [1.947(2) Å] is similar to those already reported for $\mathrm{Rh^{I}}$−IPr complexes.[16] The imidazolinyl ring deviates from the typical perpendicular *out-of-plane* configuration [N(5)−C(1)−Rh−O(44) −68.0(2)°] and the calculated pitch (θ 10.1°) and yaw (ψ 1.5°) angles[16e] indicate a distorted coordination with respect to the Rh−C(1) bond. As for the chelate ligand, it exhibits a reduced bite angle [O(44)−Rh−N(38) 62.85(7)°] and a relatively small pitch angle (θ 2.9°), bringing about a severely distorted κ^2-*N,O* coordination mode.[22] In addition, the O(44)−C(39)−N(38) angle [113.8(2)°] is smaller than that reported for the free 2-pyridone[26] (121.3°). Finally, the short C(39)−O(44) bond length [1.297(3) Å] suggests a major contribution of the 2-pyridonato carbon−oxygen double bond tautomer.

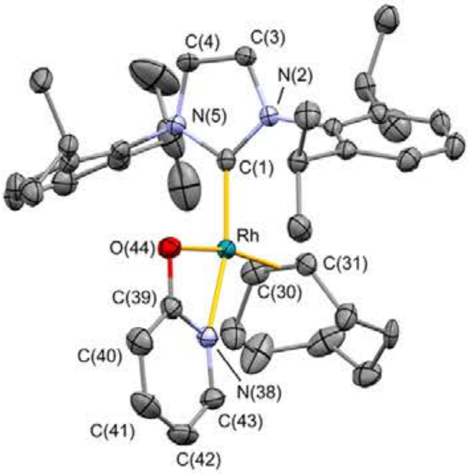

Figure 1. Solid-state crystal structure of **2**. For clarity, all hydrogen atoms are omitted. Selected bond lengths (Å) and angles (deg) are N(38)−Rh 2.1536(19), O(44)−Rh 2.1245(16), C(1)−Rh 1.947(2), Rh−ct 1.9655(2), C(30)−C(31) 1.393(4), C(39)−N(38) 1.366(3), C(39)−O(44) 1.297(3), C(1)−Rh−ct 94.32(6), ct−Rh−O(44) 168.82(4), ct−Rh−N(38) 106.02(5), C(1)−Rh−O(44) 96.78(8), C(1)−Rh−N(38) 159.59(8), O(44)−Rh−N(38) 62.85(7), O(44)−C(39)−N(38) 113.8(2), ct: centroid of C(30) and C(31).

The NMR spectra of **2** is in agreement with the solid-state structure; thus, we assume a related mononuclear square-planar configuration also for **3**−**5**. The $^{13}\mathrm{C}\{^1\mathrm{H}\}$-APT NMR spectra corroborates the presence of IPr, coe, and 2-heteroatom-pyridyl ligands in **2**−**5** by the appearance of three carbon−rhodium coupled doublets, with a coupling constant $J_{\mathrm{C-Rh}}$ of around 60, 15, and 3 Hz, respectively. The ^{1}H NMR spectra display the characteristic feature of a pyridinato moiety, namely, a deshielded doublet of doublets between δ 7.71 and 7.19 ppm, corresponding to the $H_{6\text{-py}}$ proton, in addition to shielded resonances around 6 ppm, ascribed to $H_{3\text{-py}}$ and $H_{5\text{-py}}$ atoms. Also of note is the observation of only one septuplet around 3 ppm for **2**, **3**, and **5**, ascribed to the four CH-isopropyl protons of the wingtips of carbene. This fact is explained by the occurrence of a symmetry plane and a rotational process of the IPr ligand,[27] whose rate slows down as a function of temperature resulting in the observation of two broad signals at 203 K (See Figure S1 in the Supporting Information for **2**). The carbene rotation is hindered in **4** by the methyl group of the amino-pyridinato ligand. The presence of both nitrogenated ligands in **2**−**5** was

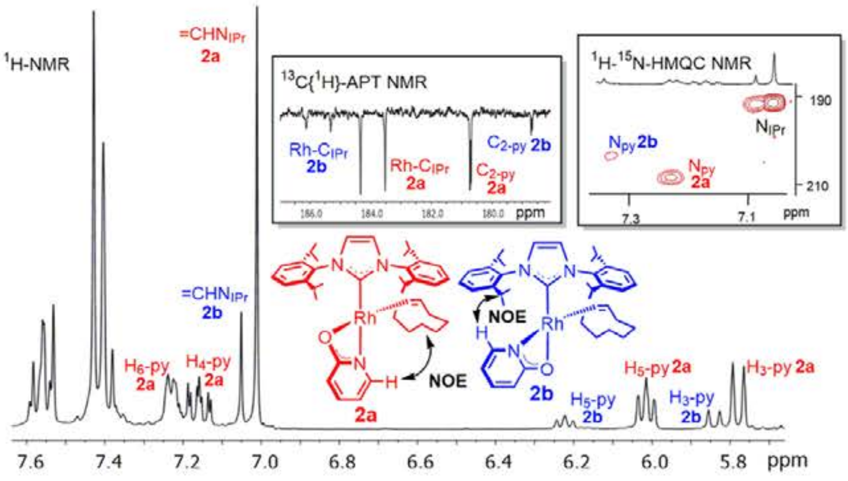

Figure 2. Selected regions of the ^{1}H,^{13}C{^{1}H}-APT and ^{1}H−^{15}N-HMQC NMR spectra in CD_2Cl_2 at 298 K for the equilibrium mixture of **2a**−**2b**.

further confirmed by ^{1}H−^{15}N HMQC NMR experiments. ^{15}N pyridyl resonances are in the expected range for metal-coordinated ligands (δ 198−235 ppm),[15a] whereas ^{15}N signals of the IPr and amine functionalities in **3**−**4** appear around 192 and 105 ppm, respectively.

Interestingly, complex **2** appears as a unique species in C_6D_6 solutions but as two isomers in CD_2Cl_2, **2a**:**2b** in 3:1 ratio, displaying opposite disposition of the chelating pyridonato ligand (Figure 2). A ^{1}H−^{1}H NOE NMR experiment (see Figure S15 in the Supporting Information) confirms that the major isomer (**2a**) presents the chelate ligand in the same disposition as that determined in the solid state, whereas the nitrogen atom is located *cis* to IPr in the minor isomer (**2b**). Both isomers are in a thermodynamic equilibrium with similar ratios in the temperature range 203−298 K, displaying fast exchange at room temperature. DFT calculations show that these isomers display a energy difference of 0.37 kcal·mol^{-1} (see Figure S2 in the Supporting Information). Larger separation of 0.96 and 1.41 kcal·mol^{-1} were computed for the amino- and mercapto-pyridinato derivatives, respectively, which is agreement the observation of a single isomer in solution.

Dimerization of Alkynes. The new Rh$^{\mathrm{I}}$-NHC-pyridinato complexes **2**−**5** were evaluated as catalysts for alkyne dimerization. Phenylacetylene was initially studied as a benchmark substrate (Scheme 4, Table 1). The course of the reaction was monitored by NMR using 2 mol % of catalyst loading in C_6D_6 at 25 °C. Rh-pyridonato complex **2** is extremely active and selective. Total conversion to the head-to-tail enyne, 1,3-diphenylbut-3-en-1-yne, was observed in the first ^{1}H NMR experiment recorded, after less than 5 min (entry 1). A TOF$_{1/2}$ value of 16 000 h^{-1} was calculated, which is, as far as we know, the highest value reported for alkyne dimerization at room temperature.[11i] Catalytic activity remained very high after reducing catalyst loading to 0.5 mol %, with complete phenylacetylene conversion after only 6 min of reaction (entry 2). Catalyst **2** was also efficient at 0.1 mol % catalyst loading (entry 3). Further decrease of the catalyst loading to a 1:2000 catalyst:substrate ratio resulted in a 54% conversion in 4 h, still maintaining complete selectivity for the *gem*-enyne product (entry 4). In contrast, amino-pyridine-based catalyst precursors **3**−**4** are much less efficient and selective (entries 5−6). Moreover, although Rh-mercapto-pyridine catalyst **5** was able to fully transform phenylacetylene in 5 h, it showed poor selectivity (entry 7).

Scheme 4. Alkyne Dimerization Products

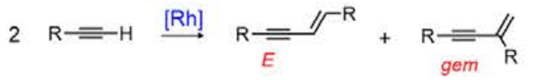

Table 1. Catalyst Evaluation for Dimerization of Phenylacetylene[a]

entry	catalyst	mol %	*t* (h)	conv (%)	*gem/E*	TOF$_{1/2}$ (h^{-1})[b]
1	**2**	2	<0.1	>99	>99	16000
2	**2**	0.5	0.1	>99	>99	8300
3	**2**	0.1	3	>99	>99	11000
4	**2**	0.05	4	54	>99	6900[c]
5	**3**	2	22	29	95/5	
6	**4**	2	25	55	96/4	1
7	**5**	2	5	>99	54/46	11

[a] Reaction conditions: 0.5 mL of C_6D_6, 0.5 mmol of phenylacetylene, 25 °C. [b] Turnover frequency at 50% conversion. [c] Calculated at 40% conversion.

The catalytic activity of **2** was studied for different alkynes (Table 2). Electronic modification on the aromatic ring of phenylacetylene resulted in only slight changes in catalytic activity (entries 3−4). Aliphatic alkynes were also efficiently transformed with high selectivity (entries 5−7). Catalyst **2** tolerates the presence of heteroatoms well (entries 8−10). Particularly, the hydroxy group in 3-butynol did not affect significantly the catalytic activity with regard to an ether functionality (entries 8 vs 10). It is interesting to note that this alcohol is involved for the first time in an alkyne dimerization process.[28] Increasing of bulkiness in the substrate is detrimental to catalytic activity. Thus, trimethylphenylacetylene reacted very slowly but maintaining the head-to-tail selectivity (entry 11). In contrast, no regioselectivity was observed for trimethylsilylacetylene (entry 12), whereas (*Z*)-(1,3,5-tri*tert*-butyl)hexa-3,5-dien-1-yne trimer was found to be the major product when *tert*-butylacetylene was used (entry 13). Finally, catalyst **2** was ineffective for the transformation of 2-pyridylacetylene.

Table 2. Screening of Alkynes Catalyzed by **2**[a]

Entry	Substrate	t(h)	Conv(%)	*gem*/*E*	$TOF_{1/2}(h^{-1})$[b]
1	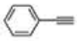	<0.1	>99	>99	16000
2[c]	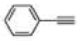	3	>99	>99	11000
3[c]	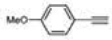	1	96	>99	12000
4[c]	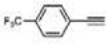	2.5	73	>99	17000
5		0.3	>99	>99	900
6		<0.1	>99	>99	700
7	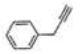	<0.1	>99	>99	800
8	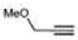	21	95	>99	15
9	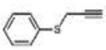	4	98	>99	100
10		16	94	>99	6
11	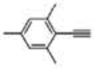	21	40	>99	-
12	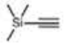	96	>99	48/52	2
13	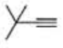	48	65	21/8/71[d]	1
14	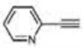	48	-	-	-

[a]Reaction conditions: 0.5 mL of C_6D_6, 0.5 mmol of alkyne, 0.01 mmol of **2**, 25 °C. [b]Turnover frequency at 50% conversion. [c]0.1 mol % of **2**. [d](*Z*)-(1,3,5-tri*tert*-butyl)hexa-3,5-dien-1-yne trimer was also obtained.

Mechanistic Investigation. In order to shed light on the operative mechanism for the Rh-NHC-pyridinato catalyzed alkyne dimerization, low temperature reactivity studies were made. Unfortunately, catalyst **2** dimerized phenylacetylene very fast, even at 213 K, thwarting the detection of catalytic intermediates. In view of this, reactivity studies were carried out with a less efficient catalyst or a less reactive alkyne (Scheme 5). Thus, the addition of phenylacetylene to the mercaptopyridine complex **5** at 233 K gave the π-phenylacetylene complex $Rh\{\kappa^2\text{-}S,N\text{-}(Spy)\}(\eta^2\text{-}HC{\equiv}CPh)(IPr)$ (**6**)[11i] by alkyne-coe exchange, which can be proposed as the first step of the catalytic cycle. Warming the solution led to the smooth formation of the head-to-head and head-to-tail enynes, according to the selectivity observed in the catalytic experiments (entry 7, Table 1), and a mixture of unidentified complexes. In contrast, addition of the bulky trimethylphenylacetylene to **2** afforded $Rh\{\kappa^2\text{-}O,N\text{-}(Opy)\}\{\eta^2\text{-}H_2C{=}C(Mes)\text{-}C{\equiv}C(Mes)\}(IPr)$ (**7**), that results from the η^2-C=C coordination of the enyne reaction product formed by fast dimerization of the alkyne. This uncommon coordination mode for an enyne[29] is reflected in the appearance in the $^{13}C\{^1H\}$-APT NMR spectrum of two doublets at δ 50.3 and 41.0 ppm with J_{C-Rh} around 18.8 Hz, corresponding to the coordinated olefin. Most likely, the presence of the bulky substituents in the proximity of the alkynyl moiety hinders the coordination of the triple bond.

Scheme 5. Reactivity of Pyridinato Complexes with Alkynes

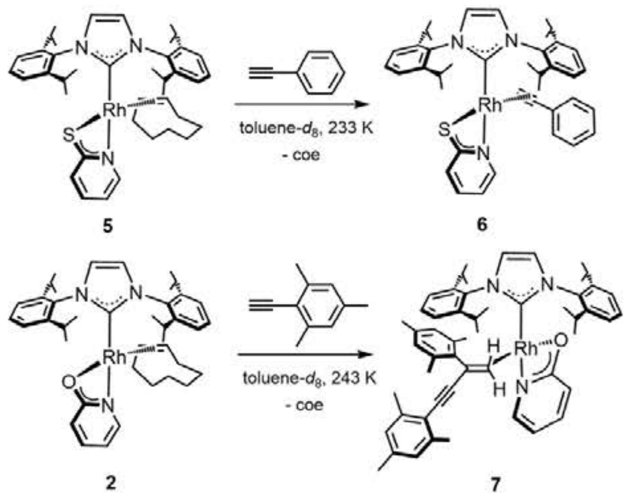

Based on previous investigations in our group,[11i] the pyridinato ligand must play a role in the deprotonation of the rather acidic terminal proton of the alkyne. Thus, addition of triflic acid to a CD_2Cl_2 solution of **2** at 223 K resulted in the formation of $Rh[\kappa^1\text{-}O\text{-}\{O{=}C({-}CH{=}CH{-}CH{=}CH{-})\text{-}NH\}]\{\kappa^1\text{-}O\text{-}(CF_3O_3S)\}(\eta^2\text{-coe})(IPr)$ as a mixture of two isomers in a 1:1 ratio, tentatively assigned to **8a** and **8b**, where the nitrogen atom of the pyridonato ligand has been protonated (Scheme 6) (see Theoretical Calculations on the Mechanism section). The $^1H-^{15}N$ HMQC NMR spectrum shows two NH cross-peaks at δ 174.0 and 170.3 which correlate with δ 11.73 and 10.97 ppm proton signals, respectively, thereby confirming the presence of pyridin-2(1*H*)-one ligands in both isomers. Moreover, the ^{19}F NMR spectrum displays the typical broad signal of a coordinated triflate ligand.

Deuterium-labeling experiments using phenylacetylene-d_1 were performed with the aim of gaining information about the turnover limiting step (Scheme 7). First, the H/D kinetic isotopic effect (KIE) was measured by performing separate NMR experiments using 0.4 mol % of catalyst **2**. A KIE of 1.67 ± 0.12 was found. This relatively small value suggests that a X−H cleavage or formation event is not likely involved in the turnover limiting step.[30] Further, a catalytic test with a mixture of natural and phenylacetylene-d_1 in a 1:1 ratio resulted in a different deuteration degree of the geminal positions of the enyne. The calculated H/D ratios show the overdeuteration of the vinyl proton *cis* to the phenyl group (0.37 vs 0.63 H). Taking into consideration a *syn* addition process and no preference between natural and deuterated alkyne as the acceptor partner, this result suggests that the cleavage of the C−H bond is 1.7 times faster than that of the C−D bond, which is in concordance with the calculated KIE. Moreover, the ability of the pyridonato ligand to act as an efficient shuttle was analyzed. The mixture resulting from a catalytic test with phenylacetylene-d_1 and **2** in the presence of natural pyridin-2-one resulted in the clean formation of *gem*-enyne-d_2. The lack of incorporation of protons from the heterocycle indicates that

Scheme 6. Protonation of 2 with Triflic Acid

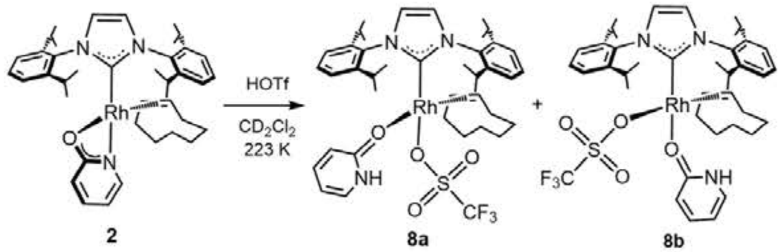

Scheme 7. Deuterium Labeling Experiments

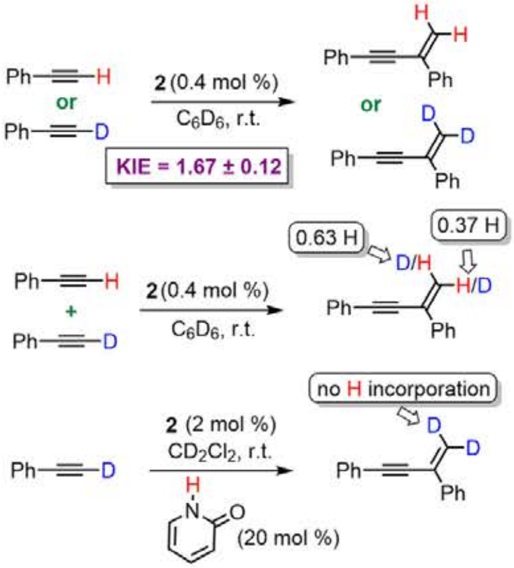

hydrogen transfer is faster than the metal-pyridone ligand coordination exchange.

Theoretical Calculations on the Mechanism. To further clarify the operating pathway leading to the observed *gem*-enyne selectivity, a detailed density functional theory (DFT) computational analysis on the dimerization of phenylacetylene promoted by the Rh-NHC-pyridinato complexes has been carried out. All plausible mechanistic pathways have been thoroughly examined (ΔG in kcal·mol^{-1}), excluding the external attack on coordinated π-alkyne and vinylidene-mediated dimerization pathways as these usually do not result in *gem*-selectivity.

The first step considered in this study is the preactivation of catalyst **2** by phenylacetylene-coe exchange via an associative mechanism. This exergonic process (−6.1 kcal·mol^{-1}) has an energetic barrier of 13.7 kcal·mol^{-1} (see Figure S103 in the Supporting Information). The resulting complex Rh{κ^2-*O*,*N*-(Opy)}(η^2-HC≡CPh)(IPr) (**A**) can be considered as the active species, and hence, it has been selected as the energetic reference for all DFT calculations in this section.

First, we have analyzed the pathway starting by oxidative addition of the alkyne to form a Rh^{III}-hydride-alkynyl intermediate.[15] The energy profile of this cycle is shown in Figure 3. The initial step is the slippage of the η^2-(C≡C)-alkyne bond in **A** rendering the η^2-(C−H) agostic interaction in **B**. This process presents an energetic barrier characterized by **TSAB** of 19.9 kcal·mol^{-1}, and it is endergonic by 10.4 kcal·mol^{-1}. The formation of the σ-complex **B** is essential in the cleavage of the C−H bond.[10a,13b,d,f,h] From that point, the oxidative addition takes place by a negligible energy barrier, characterized by **TSBC**, leading to the Rh^{III}-hydride-alkynyl **C**, which presents a relative free energy of 8.3 kcal·mol^{-1}. The reaction continues by coordination of a second alkyne to the metal center and subsequent hydrometalation. The two possible orientations of the alkyne toward its insertion on the Rh−H bond are characterized by the transition states **TSCDg** (leading to the *gem* product) and **TSCDt** (leading to the *E* product), with free energies of 20.2 and 23.7 kcal·mol^{-1}, respectively. It should be noted that, although **Dt** is more stable than **Dg**, the reaction is under kinetic control and **Dt** is not accessible. The insertion of the alkyne into the Rh−C bond has been discarded based on previous studies on similar systems.[11e,15a] The obtained alkynyl-alkenyl complexes **D** evolve to the final products via reductive elimination via **TSDAg** and **TSDAt**, showing energetic barriers of 7.4 and 12.4 kcal·mol^{-1}, respectively. This mechanistic proposal presents an overall activation energy of 20.2 kcal·mol^{-1} for the *gem*-enyne, which is preferentially obtained due to the significantly higher barrier for the *E* product (23.7 kcal·mol^{-1}).

For the sake of comparison, a classical mechanism alternative to alkyne oxidative addition is a base-mediated nonoxidative pathway. In our case the pyridonato ligand may play this role via a concerted metalation-deprotonation (CMD) process. The energetic profile is shown in Figure 4. The reaction starts by coordination of a second alkyne to **A**, allowed by the hemilabile behavior of the pyridonato ligand.[21] As a result, a switch to a {κ^1-*N*-(Opy)} coordination mode of this molecule is observed.[31] This process is characterized by **TSAE** (energetic barrier of 14.2 kcal·mol^{-1}) leading to the intermediate **E** Rh{κ^1-*N*-(Opy)}(η^2-HC≡CPh)$_2$(IPr), displaying a mutually *trans* disposition for the two π-alkyne molecules.[32] Since the pyridonato ligand is now coordinated to the metal only by the nitrogen atom, free rotation about the Rh−N bond becomes possible thus enabling the easy approach of the basic oxo group to any terminal hydrogen of the η^2-coordinated alkynes of **E**. Therefore, the subsequent CMD step is characterized by the **TSEF** transition state, which has an energetic barrier of 15.9 kcal·mol^{-1}, leading to the intermediate **F** Rh(-C≡CPh){κ^1-*N*-{HOpy}(η^2-HC≡CPh)(IPr). The possible deprotonation of the alkyne by the nitrogen atom of the pyridonato was also computed revealing a higher energetic barrier of 20.7 kcal·mol^{-1} (**TSEG** see Figure S104 in the Supporting Information). However, the resulting pyridin-2-one intermediate **G** is almost isoenergetic to **F**, in accordance to the experimental observation that **8** forms after the protonation of **2** with triflic acid.

Once the Rh^{I}-alkynyl intermediate **F** is obtained, carbometalation is available via **TSFHg** (30.2 kcal·mol^{-1}) or **TSFHt** (26.5 kcal·mol^{-1}) depending on the orientation of the alkyne

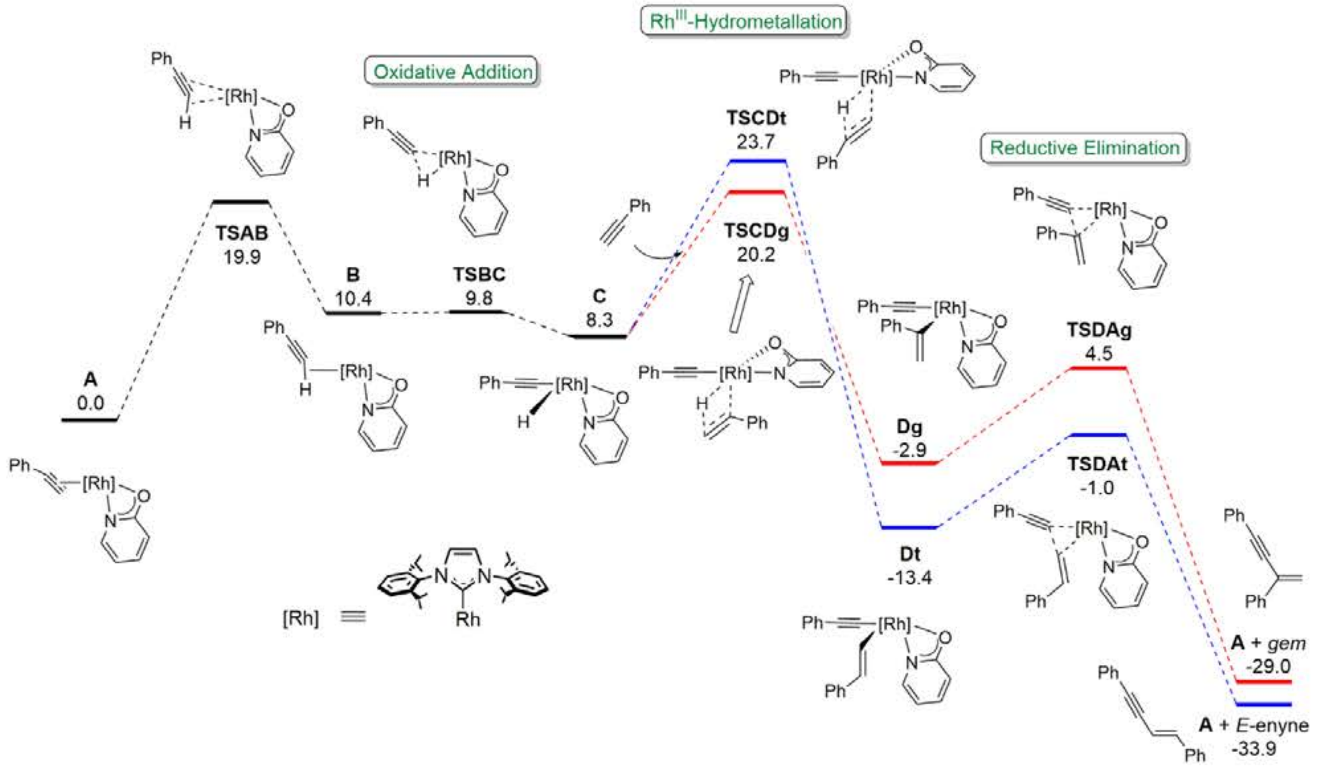

Figure 3. DFT calculations (ΔG in kcal·mol^{-1}, relative to **A** and isolated molecules) along phenylacetylene dimerization following the oxidative addition, migratory insertion, and reductive elimination steps.

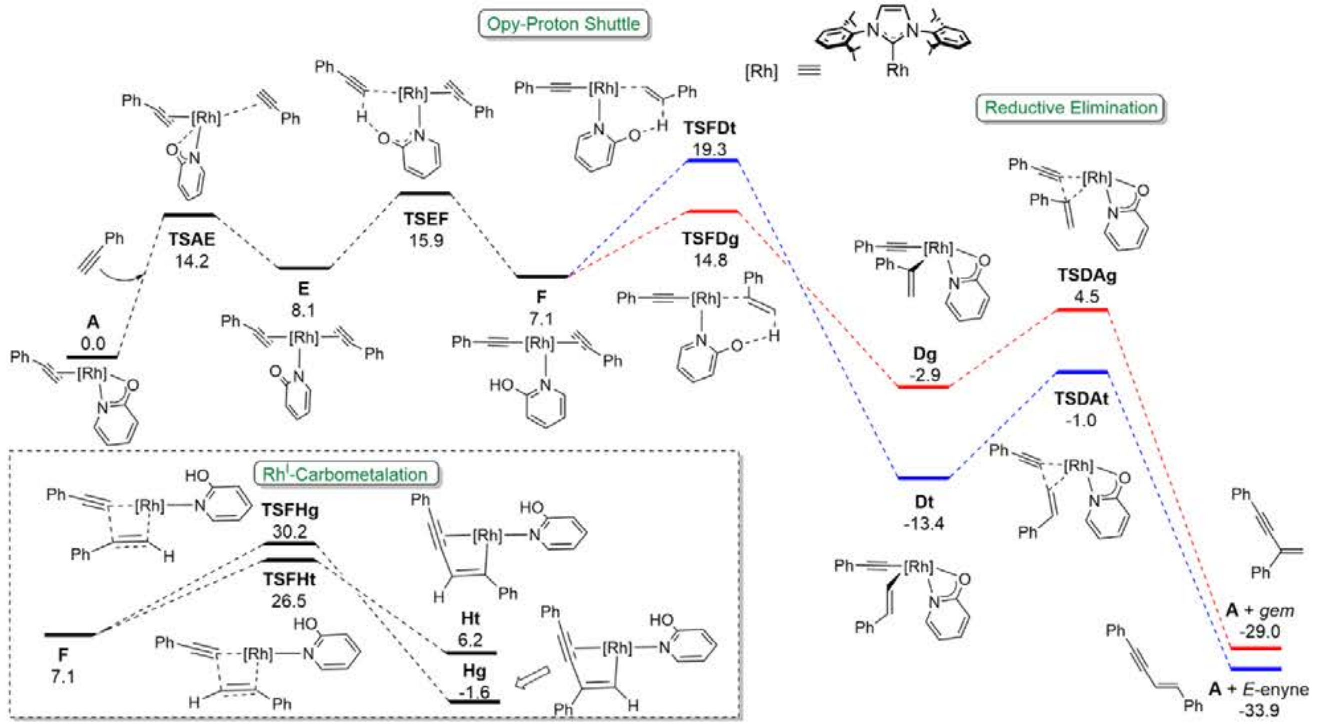

Figure 4. DFT calculations (ΔG in kcal·mol^{-1}, relative to **A** and isolated molecules) along phenylacetylene dimerization following the pyridonato-mediated proton shuttle and reductive elimination steps.

(Figure 4). However, these energetic barriers are higher than that computed for the oxidative route. An alternative pathway can be envisaged starting from the Rh^{I}-alkynyl intermediate **F**.

The κ^1-*N*-hydroxypyridine ligand can now act as an intramolecular Brønsted acid able to transfer the proton to the remaining η^2-alkyne of **F** to yield **D**.[33] Two possibilities arise for this selectivity-determining step as the proton can be transferred to either the terminal or the substituted carbon atoms of phenylacetylene. Protonation of the external position via **TSFDg** (14.8 kcal·mol^{-1}), which ultimately leads to *gem*-enynes, is much more favored than the protonation of the internal one (**TSFDt**, 19.3 kcal·mol^{-1}). Alternative protonation reactions by the κ^1-*O*- pyridin-2-one ligand in complex **G** are considerably more disfavored (see Figure S104 in the Supporting Information). The catalytic cycle ends via alkenyl-alkynyl reductive elimination within **D** as previously analyzed. The concurrence of the **E** → **F** and **F** → **D** steps shows a very efficient cooperative Rh-pyridonato-mediated LAPS process. Figure 4 shows that the higher energetic barrier corresponds to the CMD event (**TSEF**, 15.9 kcal·mol^{-1}), although those of the associative coordination of a second molecule of alkyne (**TSAE**, 14.2 kcal·mol^{-1}) or proton transfer (**TSFDg**, 14.8 kcal·mol^{-1}) are very close in energy, and thus, its contribution to the overall kinetics of the catalytic cycle might be not negligible. In order to evaluate the proposed mechanism for aliphatic alkynes, key structures were calculated considering propyne as a model system. An increment in the overall energy barrier from 15.9 to 17.7 kcal mol^{-1} is observed which is in accordance with a lower catalytic activity (see Table S3 in the Supporting Information).

As extracted from Figure 4, the regioselectivity is controlled by the proton transfer to the alkyne, determined by a difference of 4.5 kcal·mol^{-1} between the energetic barriers for the *gem*- and *E*-enynes. The origin of this selectivity can be explained by inspecting the NBO atomic charges in the intermediate **F** and the transition states **TSFDg** and **TSFDt** (Figure 5). Polarization of the coordinated alkyne in **F** was observed, showing a negative charge at the terminal carbon atom (−0.243e) larger than that at the internal position (−0.042e). Since the atomic charge of the hydrogen is +0.378e in **TSFDg** and +0.410e in **TSFDt**, the hydrogen migration can be considered formally a proton transfer, and not surprisingly, it will take place preferentially on the carbon bearing a larger negative charge, in this case the terminal carbon atom.

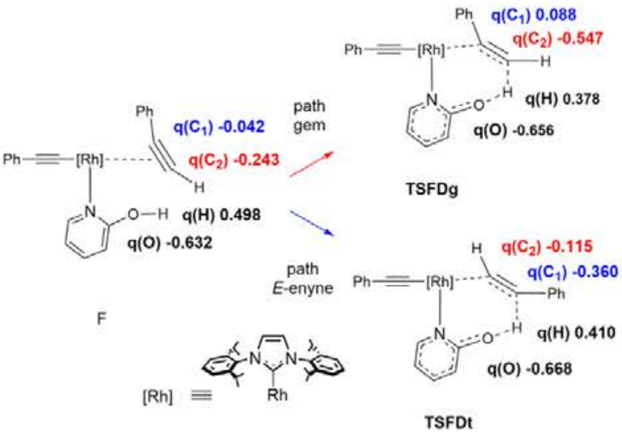

Figure 5. NBO atomic charges of atoms (in a.u.) involved in the proton transfer in structures **F**, **TSFDg**, and **TSFDt**.

In order to understand the excellent catalytic performance of pyridonato complex **2** in comparison to similar amino-pyridinato (**3**) and mercapto-pyridinato derivatives (**5**), the energetic barrier for the CMD step has been calculated. Deprotonation by an oxygen atom is more efficient (15.9 kcal·mol^{-1}) since the energetic barrier increases up to 22.5 and 26.5 kcal·mol^{-1} for the NH or S substituents, respectively, in agreement with the experimental results (see Figure S106 in the Supporting Information).

Mechanistic Considerations. Experimental and computational studies on the phenylacetylene dimerization catalyzed by **2** have revealed an operative metal−ligand cooperative mechanism as an alternative to the classical alkyne-C−H oxidative-addition or base mediated nonoxidative pathways (Scheme 8). The key point of this mechanism is the role of the Rh-pyridonato motif in the cooperative LAPS process. Initially, the hemilability of the ligand[21] is essential to promote a κ^1-*N* coordination mode which triggers the CMD step. Then, the proton is transferred selectively to the terminal position of a coordinated alkyne to finally close the cycle via a fast alkynyl-alkenyl reductive elimination. Indeed, the step determining the selectivity also changes. The orientation of the alkyne relative to the Rh−X bond in the insertion step generally directs the selectivity in conventional pathways, although reductive elimination is essential in some cases.[11h,j] Thus, the difficult stereoelectronic control on π-alkyne coordination usually results in a mixture of isomers. However, the selectivity in the LAPS mechanism is directed by a protonation event. Thus, the attack to the terminal position of the alkyne is favored by 4.5 kcal·mol^{-1} due to the formation of the more stable substituted carbocation intermediate, therefore enhancing specific *gem*-enyne formation. The combination of nitrogen−oxygen atoms within a pyridinato framework seems essential, since amino or thio functionalities show a lower ability for the CMD step.

As far as the deuterium labeling experiments are concerned, the relative small KIE value of 1.67 ± 0.12 discards, in principle, a C−H bond cleavage in the rate-determining step. However, DFT calculations have revealed that the CMD step is the one with the higher energetic barrier. A rational explanation for this, at first view paradoxical result, arises from the analysis of the CMD transition state **TSEF** (Figure 6). Inspection of the geometrical parameters reveals an early transition state character, as indicated by the distances $d(\mathrm{C, H})$ and $d(\mathrm{O, H})$ of 1.14 and 1.66 Å, respectively. Hence, the η^2-(C−H) agostic interaction component in this transition state is prevalent over the C−H cleavage, therefore explaining its moderate effect in the KIE value. In fact, the theoretically computed KIE for this step is 1.57, which agrees with the experimentally determined value (see Table S1 in the Supporting Information).

■ CONCLUSION

A series of mononuclear square-planar Rh{κ^2-*X*,*N*-(Xpy)}(η^2-coe)(IPr) (X = O, NH, NMe, S) BHetA complexes have been prepared. Among them, the N,O-pyridonato derivative displays an outstanding catalytic activity for *gem*-specific alkyne dimerization reaching TOF$_{1/2}$ values of up to 17 000 h^{-1} at room temperature. The proposed mechanism entails a cooperative LAPS process followed by fast alkenyl-alkynyl reductive elimination, which boosts the catalytic activity by lowering the energy barrier from 5 to 10 kcal·mol^{-1} compared to Rh$^{\mathrm{III}}$-hydrometalation or Rh$^{\mathrm{I}}$-carbometalation conventional pathways. Hemilability of the pyridonato moiety has been revealed to be essential for an efficient CMD rate-limiting step. Moreover, the change in the selectivity-determining step from insertion to protonation is responsible for the exclusive formation of *gem*-enynes. These results prompt us to extend

Scheme 8. Rh-Pyridonato Cooperative Mechanism for *gem*-Specific Alkyne Dimerization

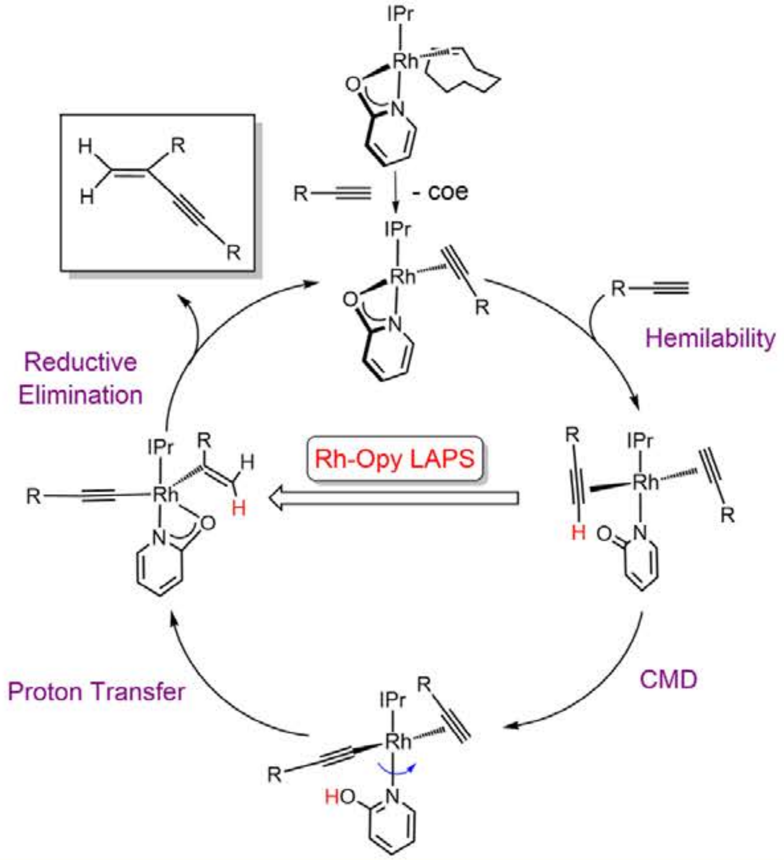

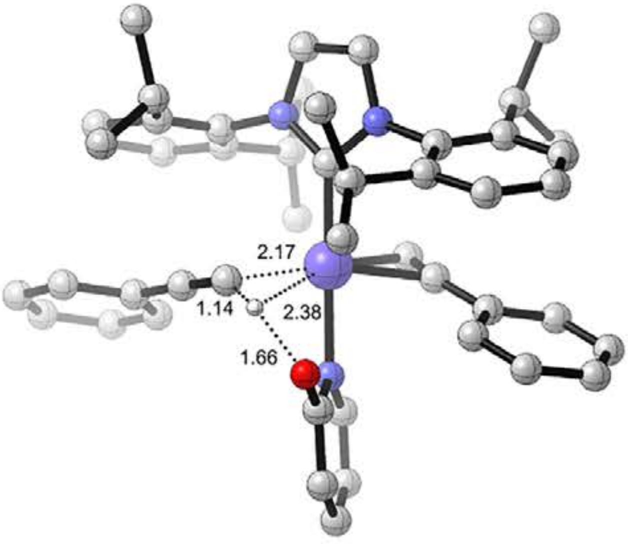

Figure 6. DFT optimized geometrical representation of **TSEF**. Key geometrical parameters (in Å) are indicated.

the underlying principles described herein to related C−C and C−heteroatom bond forming catalytic reactions via C−H activation.

■ EXPERIMENTAL SECTION

General Considerations. All reactions were performed with rigorous exclusion of air and moisture using Schlenk-tube techniques and drybox when necessary. The organometallic precursor [Rh(μ-Cl)(IPr)(η^2-coe)]$_2$ (**1**) was prepared as previously described.[34] Chemical shifts (expressed in parts per million) are referenced to residual solvent peaks (^{1}H and ^{13}C{^{1}H}), NH$_3$ (^{15}N), or CFCl$_3$ (^{19}F). Coupling constants, *J*, are given in Hz. Spectral assignments were achieved by combination of ^{1}H−^{1}H correlation spectroscopy (COSY), ^{13}C{^{1}H} attached proton test (APT), and ^{1}H−^{13}C heteronuclear single quantum correlation/heteronuclear multiple bond correlation (HSQC/HMBC) experiments.

Preparation of Rh{κ^2-*O,N*-(Opy)}(η^2-coe)(IPr) (2a,b). A mixture of 2-hydroxypyridine (49 mg, 0.52 mmol) and ^{t}BuOK (58 mg, 0.52 mmol) in 5 mL of THF was stirred for 30 min at r.t. Then, a solution of dinuclear complex **1** (300 mg, 0.24 mmol) in 10 mL of THF was added, and the resulting mixture was stirred for an additional 1 h at r.t. After removing the solvent in vacuo, the residue was dissolved in toluene (10 mL) and was filtered through celite. Then, the filtrate was evaporated to dryness. The addition of hexane at −40 °C induced the precipitation of a yellow solid, which was washed with cold hexane (3 × 2 mL) and dried in vacuo. Yield: 236 mg (72%). Satisfactory elemental analysis could not be obtained. HRMS (ESI$^+$): m/z calc for $C_{40}H_{54}N_3RhO$ (M^+ − coe − H) 583.2180 exp 583.2173. IR (cm^{-1}, ATR): 1598 $\nu(OCN_{sym})$, 1471 $\nu(OCN_{asym})$. NMR data evidenced the presence of two isomers **2a** and **2b** (80:20), in equilibrium. Data for complex **2a**: ^{1}H NMR (500.1 MHz, CD$_2$Cl$_2$, 298 K): δ 7.51 (t, J_{H-H} = 8.0, 2H, $H_{p\text{-}Ph\text{-}IPr}$), 7.38 (d, J_{H-H} = 8.0, 4H, $H_{m\text{-}Ph\text{-}IPr}$), 7.19 (dd, J_{H-H} = 5.2, 1.9, 1H, $H_{6\text{-}py}$), 7.11 (ddd, J_{H-H} = 8.6, 6.9, 1.9, 1H, $H_{4\text{-}py}$), 6.97 (s, 2H, $=CHN_{IPr}$), 5.97

(ddd, J_{H-H} = 6.9, 5.2, 1.1, 1H, $H_{5\text{-}py}$), 5.74 (dd, J_{H-H} = 8.6, 1.1, 1H, $H_{3\text{-}py}$), 2.98 (sept, J_{H-H} = 6.8, 4H, $\mathrm{C\underline{H}Me_{IPr}}$), 2.57 (m, 2H, $=\mathrm{CH_{coe}}$), 1.6−1.0 (12H, $\mathrm{CH_{2\text{-}coe}}$), 1.42 and 1.12 (both d, J_{H-H} = 6.8, 24H, $\mathrm{CH\underline{Me}_{IPr}}$). ^{13}C{^{1}H}-APT NMR (125.8 MHz, CD_2Cl_2, 298 K): δ 184.5 (d, J_{C-Rh} = 61.1, Rh−C_{IPr}), 181.3 (d, J_{C-Rh} = 3.0, $C_{2\text{-}py}$), 147.5 (s, $C_{q\text{-}IPr}$), 144.7 (s, $C_{6\text{-}py}$), 138.9 (s, $C_{4\text{-}py}$), 137.4 (s, C_qN), 129.9 (s, $\mathrm{CH_{p\text{-}Ph\text{-}IPr}}$), 124.9 (d, J_{C-Rh} = 1.2, $=\mathrm{CHN_{IPr}}$), 124.1 (s, $\mathrm{CH_{m\text{-}Ph\text{-}IPr}}$), 110.7 (d, J_{C-Rh} = 1.2, $C_{3\text{-}py}$), 108.4 (s, $C_{5\text{-}py}$), 57.8 (d, J_{C-Rh} = 16.0, $=\mathrm{CH_{coe}}$), 30.4, 30.3, and 27.8 (both s, $\mathrm{CH_{2\text{-}coe}}$), 29.3 (s, $\mathrm{\underline{C}HMe_{IPr}}$), 26.6 and 23.2 (both s, $\mathrm{CH\underline{Me}_{IPr}}$). ^{1}H−^{15}N HMQC NMR (50.7 MHz, CD_2Cl_2, 298 K): δ 207.8 (N_{py}), 191.8 (N_{IPr}). Data for complex **2b**: ^{1}H NMR (500.1 MHz, CD_2Cl_2, 298 K): δ 7.52 (t, J_{H-H} = 8.0, 2H, $H_{p\text{-}Ph\text{-}IPr}$), 7.38 (d, J_{H-H} = 8.0, 4H, $H_{m\text{-}Ph\text{-}IPr}$), 7.32 (dd, J_{H-H} = 5.2, 1.9, 1H, $H_{6\text{-}py}$), 7.17 (ddd, J_{H-H} = 8.7, 6.9, 1.9, 1H, $H_{4\text{-}py}$), 7.01 (s, 2H, $=\mathrm{CHN_{IPr}}$), 6.18 (ddd, J_{H-H} = 6.9, 5.2, 1.1, 1H, $H_{5\text{-}py}$), 5.80 (dd, J_{H-H} = 8.7, 1.1, 1H, $H_{3\text{-}py}$), 2.84 (m, 6H, $\mathrm{C\underline{H}Me_{IPr}}$ and $=\mathrm{CH_{coe}}$), 1.6−1.0 (12H, $\mathrm{CH_{2\text{-}coe}}$), 1.18 and 1.13 (both d, J_{H-H} = 6.8, 24H, $\mathrm{CH\underline{Me}_{IPr}}$). ^{13}C{^{1}H}-APT NMR (125.8 MHz, CD_2Cl_2, 298 K): δ 186.2 (d, J_{C-Rh} = 61.7, Rh−C_{IPr}), 179.2 (d, J_{C-Rh} = 3.0, $C_{2\text{-}py}$), 147.1 (s, $C_{q\text{-}IPr}$), 144.8 (d, J_{C-Rh} = 1.8, $C_{6\text{-}py}$), 138.5 (s, $C_{4\text{-}py}$), 137.4 (s, C_qN), 130.1 (s, $\mathrm{CH_{p\text{-}Ph\text{-}IPr}}$), 125.3 (s, d, J_{C-Rh} = 1.2, $=\mathrm{CHN_{IPr}}$), 124.3 (s, $\mathrm{CH_{m\text{-}Ph\text{-}IPr}}$), 112.3 (s, $C_{3\text{-}py}$), 108.2 (d, J_{C-Rh} = 1.5, $C_{5\text{-}py}$), 62.1 (d, J_{C-Rh} = 15.5, $=\mathrm{CH_{coe}}$), 30.0 and 28.2 (both d, J_{C-Rh} = 1.7, $\mathrm{CH_{2\text{-}coe}}$), 29.3 (s, $\mathrm{\underline{C}HMe_{IPr}}$), 27.1 (s, $\mathrm{CH_{2\text{-}coe}}$), 26.6 and 22.7 (both s, $\mathrm{CH\underline{Me}_{IPr}}$). ^{1}H−^{15}N HMQC NMR (50.7 MHz, CD_2Cl_2, 298 K): δ 203.0 (N_{py}), 192.2 (N_{IPr}).

Preparation of Rh{κ^2-*N,N*-(NHpy)}(η^2-coe)(IPr) (3). This compound was prepared as described for **2** starting from 2-aminopyridine (30 mg, 0.32 mmol), ^{t}BuOK (37 mg, 0.33 mmol), and **1** (200 mg, 0.16 mmol). Yellow solid. Yield: 130 mg (59%). Satisfactory elemental analysis could not be obtained. HRMS (ESI$^+$): *m/z* calcd for $RhC_{40}H_{55}N_4$ (M$^+$ − coe − H) 583.2314 exp 583.2303. IR (cm^{-1}, ATR): 1595 $\nu(\mathrm{NCN_{sym}})$, 1447 $\nu(\mathrm{NCN_{asym}})$. ^{1}H NMR (400.2 MHz, C_6D_6, 298 K): δ 7.37 (dd, J_{H-H} = 5.5, 1.8, 1H, $H_{6\text{-}py}$), 7.29 (t, J_{H-H} = 7.2, 2H, $H_{p\text{-}Ph\text{-}IPr}$), 7.18 (d, J_{H-H} = 7.2, 4H, $H_{m\text{-}Ph\text{-}IPr}$), 6.76 (ddd, J_{H-H} = 8.7, 6.9, 1.8, 1H, $H_{4\text{-}py}$), 6.47 (s, 2H, $=\mathrm{CHN_{IPr}}$), 5.63 (ddd, J_{H-H} = 6.9, 5.5, 1.0, 1H, $H_{5\text{-}py}$), 5.51 (dd, J_{H-H} = 8.7, 1.0, 1H, $H_{3\text{-}py}$), 3.67 (d, J_{H-Rh} = 6.6, 1H, NH), 3.11 (sept, J_{H-H} = 6.8, 4H, $\mathrm{C\underline{H}Me_{IPr}}$), 2.73 (m, 2H, $=\mathrm{CH_{coe}}$), 2.0−1.2 (m, 12H, $\mathrm{CH_{2\text{-}coe}}$), 1.50 and 1.04 (both d, J_{H-H} = 6.8, 24H, $\mathrm{CH\underline{Me}_{IPr}}$). ^{13}C{^{1}H}-APT NMR (100 MHz, C_6D_6, 298 K): δ 187.6 (d, J_{C-Rh} = 63.8, Rh−C_{IPr}), 177.8 (d, J_{C-Rh} = 4.2, $C_{2\text{-}py}$), 146.6 (s, $C_{q\text{-}IPr}$), 145.9 (s, $C_{6\text{-}py}$), 137.8 (s, C_qN), 137.0 (s, $C_{4\text{-}py}$), 129.6 (s, $\mathrm{CH_{p\text{-}Ph\text{-}IPr}}$), 123.9 (s, $\mathrm{CH_{m\text{-}Ph\text{-}IPr}}$), 123.9 ($=\mathrm{CHN_{IPr}}$), 107.5 (d, J_{C-Rh} = 1.3, $C_{3\text{-}py}$), 104.7 (s, $C_{5\text{-}py}$), 59.7 (d, J_{C-Rh} = 14.5, $=\mathrm{CH_{coe}}$), 30.6 (d, J_{C-Rh} = 1.0, $\mathrm{CH_{2\text{-}coe}}$), 29.9 (d, J_{C-Rh} = 1.7, $\mathrm{CH_{2\text{-}coe}}$), 27.1 (s, $\mathrm{CH_{2\text{-}coe}}$), 29.1 (s, $\mathrm{\underline{C}HMe_{IPr}}$), 26.2 and 23.0 (both s, $\mathrm{CH\underline{Me}_{IPr}}$). ^{1}H−^{15}N HMQC NMR (40.5 MHz, C_6D_6, 298 K): δ 198.8 (N_{py}), 190.8 (N_{IPr}), 105.0 (NH).

Preparation of Rh[κ^2-*N,N*-{N(Me)py}](η^2-coe)(IPr) (4). This compound was prepared as described for **2** starting from *N*-methyl-2-aminopyridine (29 mg, 0.26 mmol), ^{t}BuOK (29 mg, 0.26 mmol), and **1** (150 mg, 0.12 mmol). Yellow solid. Yield: 102 mg (61%). Anal. calcd for $C_{41}H_{57}N_4Rh$: C, 69.47; H, 8.11; N, 7.90. Found: C, 69.35; H, 8.06; N, 7.53. IR (cm^{-1}, ATR): 1594 $\nu(\mathrm{NCN_{sym}})$, 1487 $\nu(\mathrm{NCN_{asym}})$. ^{1}H NMR (300.1 MHz, C_6D_6, 298 K): δ 7.38 (dd, J_{H-H} = 5.4, 1.8, 1H, $H_{6\text{-}py}$), 7.4−7.1 (m, 6H, $H_{Ph\text{-}IPr}$), 7.02 (ddd, J_{H-H} = 8.8, 6.9, 1.8, 1H, $H_{4\text{-}py}$), 6.48 (s, 2H, $=\mathrm{CHN_{IPr}}$), 5.7−5.6 (m, 2H, $H_{5\text{-}py}$ and $H_{3\text{-}py}$), 3.99 and 2.05 (both sept, J_{H-H} = 6.7, 4H, $\mathrm{C\underline{H}Me_{IPr}}$), 2.73 (s, 3H, NMe), 2.66 (m, 2H, $=\mathrm{CH_{coe}}$), 1.8−1.0 (m, 12H, $\mathrm{CH_{2\text{-}coe}}$), 1.53, 1.29, 1.16, and 0.98 (all d, J_{H-H} = 6.7, 24H, $\mathrm{CH\underline{Me}_{IPr}}$). ^{13}C{^{1}H}-APT NMR (75.5 MHz, C_6D_6, 298 K): δ 192.3 (d, J_{C-Rh} = 60.0, Rh−C_{IPr}), 177.1 (d, J_{C-Rh} = 4.0, $C_{2\text{-}py}$), 147.5 and 146.4 (both s, $C_{q\text{-}IPr}$), 145.9 (s, $C_{6\text{-}py}$), 137.7 (s, C_qN), 137.6 (s, $C_{4\text{-}py}$), 129.7, 124.8, and 123.6 (all s, $\mathrm{CH_{Ph\text{-}IPr}}$), 124.5 (d, J_{C-Rh} = 1.3, $=\mathrm{CHN_{IPr}}$), 104.1 (s, $C_{5\text{-}py}$), 100.7 (s, $C_{3\text{-}py}$), 57.9 (d, J_{C-Rh} = 14.6, $=\mathrm{CH_{coe}}$), 36.0 (d, J_{C-Rh} = 3.5, N-Me), 30.6 and 29.7 (both d, J_{C-Rh} = 1.0, $\mathrm{CH_{2\text{-}coe}}$), 29.0 and 28.8 (both s, $\mathrm{\underline{C}HMe_{IPr}}$), 27.2 (s, $\mathrm{CH_{2\text{-}coe}}$), 26.9, 26.0, 23.3, and 22.7 (all s, $\mathrm{CH\underline{Me}_{IPr}}$). ^{1}H−^{15}N HMQC NMR (40.5 MHz, C_6D_6, 298 K): δ 200.1 (N_{py}), 191.7 (N_{IPr}), 106.0 (NMe).

Preparation of Rh{κ^2-*S,N*-(Spy)}(η^2-coe)(IPr) (5). This compound was prepared as described for **2** starting from 2-mercaptopyridine (38 mg, 0.35 mmol), ^{t}BuOK (39 mg, 0.35 mmol), and **1** (200 mg, 0.16 mmol). Orange solid. Yield: 123 mg (55%). Anal. calcd for $C_{40}H_{54}N_3SRh$: C, 67.49; H, 7.65; N, 5.90; S, 4.50. Found: C, 67.19; H, 7.44; N, 6.22; S, 4.45. IR (cm^{-1}, ATR): 1579 and 1444 ν(SCN). ^{1}H NMR (400.2 MHz, C_6D_6, 298 K): δ 7.71 (dd, J_{H-H} = 5.5, 1.7, 1H, $H_{6\text{-}py}$), 7.3−7.2 (m, 6H, $H_{Ph\text{-}IPr}$), 6.56 (dd, J_{H-H} = 8.1, 1.4, 1H, $H_{3\text{-}py}$), 6.54 (s, 2H, $=\mathrm{CHN_{IPr}}$), 6.47 (ddd, J_{H-H} = 8.1, 7.2, 1.7, 1H, $H_{4\text{-}py}$), 5.85 (ddd, J_{H-H} = 7.2, 5.5, 1.4, 1H, $H_{5\text{-}py}$), 3.4−3.2 (m, 6H, $\mathrm{C\underline{H}Me_{IPr}}$ and $=\mathrm{CH_{coe}}$), 2.0−1.2 (m, 12H, $\mathrm{CH_{2\text{-}coe}}$), 1.64 and 1.05 (both d, J_{H-H} = 6.8, 24H, $\mathrm{CH\underline{Me}_{IPr}}$). ^{13}C{^{1}H}-APT NMR (100 MHz, C_6D_6, 298 K): δ 185.2 (d, J_{C-Rh} = 60.9, Rh−C_{IPr}), 184.7 (d, J_{C-Rh} = 4.1, $C_{2\text{-}py}$), 146.8 (s, $C_{q\text{-}IPr}$), 146.5 (s, $C_{6\text{-}py}$), 138.0 (s, C_qN), 135.1 (s, $C_{4\text{-}py}$), 129.7 and 124.1 (both s, $\mathrm{CH_{Ph\text{-}IPr}}$), 126.7 (s, $C_{3\text{-}py}$), 124.6 (d, J_{C-Rh} = 1.2, $=\mathrm{CHN_{IPr}}$), 114.9 (s, $C_{5\text{-}py}$), 64.1 (d, J_{C-Rh} = 14.1, $=\mathrm{CH_{coe}}$), 30.5 and 29.7 (both d, J_{C-Rh} = 1.0, $\mathrm{CH_{2\text{-}coe}}$), 29.3 (s, $\mathrm{\underline{C}HMe_{IPr}}$), 27.0 (s, $\mathrm{CH_{2\text{-}coe}}$), 26.5 and 23.5 (both s, $\mathrm{CH\underline{Me}_{IPr}}$). ^{1}H−^{15}N HMQC NMR (40.5 MHz, C_6D_6, 298 K): δ 235.7 (N_{py}), 191.9 (N_{IPr}).

In Situ Formation of Rh{κ^2-*S,N*-(Spy)}(η^2-HC≡CPh)(IPr) (6). A solution of **5** (25 mg, 0.035 mmol) in toluene-d_8 at 233 K (0.5 mL, NMR tube) was treated with phenylacetylene (6 μL, 0.053 mmol). NMR spectra were recorded immediately at low temperature. ^{1}H NMR (400.2 MHz, toluene-d_8, 233 K): δ 7.64 (d, J_{H-H} = 6.8, 2H, $H_{o\text{-}Ph}$), 7.3−6.9 (9H, H_{Ph}), 6.73 (dd, J_{H-H} = 5.1, 1.7, 1H, $H_{6\text{-}py}$), 6.49 (s, 2H, $=\mathrm{CHN_{IPr}}$), 6.33 (dd, J_{H-H} = 7.8, 1.7, 1H, $H_{3\text{-}py}$), 6.24 (ddd, J_{H-H} = 7.8, 7.1, 1.7, 1H, $H_{4\text{-}py}$), 5.55 (ddd, J_{H-H} = 7.1, 5.1, 1.7, 1H, $H_{5\text{-}py}$), 4.54 (d, J_{H-Rh} = 2.3, 1H, η^2-$\mathrm{\underline{H}C{\equiv}CPh}$), 3.63 and 2.82 (both sept, J_{H-H} = 6.8, 4H, $\mathrm{C\underline{H}Me_{IPr}}$), 1.75, 1.48, 1.08, and 1.04 (all d, J_{H-H} = 6.8, 24H, $\mathrm{CH\underline{Me}_{IPr}}$). ^{13}C{^{1}H}-APT NMR (100.4 MHz, toluene-d_8, 233 K): δ 184.9 (d, J_{C-Rh} = 56.8, Rh−C_{IPr}), 181.9 (d, J_{C-Rh} = 4.0, $C_{2\text{-}py}$), 145.8 and 145.3 (both s, $C_{q\text{-}IPr}$), 142.3 (s, $C_{6\text{-}py}$), 137.0 (s, C_qN), 135.8 (s, $C_{4\text{-}py}$), 130.8, 129.3, 128.7, 128.6, 128.4, and 127.1 (all s, $\mathrm{CH_{Ph}}$), 125.2 (s, $C_{3\text{-}py}$), 123.9 (s, = $\mathrm{CHN_{IPr}}$), 123.2 (s, $C_{q\text{-}Ph}$), 115.0 (s, $C_{5\text{-}py}$), 89.2 (d, J_{C-Rh} = 15.6, $\mathrm{HC{\equiv}\underline{C}Ph}$), 81.9 (d, J_{C-Rh} = 14.1, $\mathrm{H\underline{C}{\equiv}CPh}$), 29.1 and 28.9 (both s, $\mathrm{\underline{C}HMe_{IPr}}$), 26.5, 25.7, 23.3, and 22.8 (all s, $\mathrm{CH\underline{Me}_{IPr}}$).

In Situ Formation of Rh{κ^2-*O,N*-(Opy)}{η^2-H_2C=C-(Mes)C≡C(Mes)}(IPr) (7). A solution of **2** (30 mg, 0.043 mmol) in toluene-d_8 at 243 K (0.5 mL, NMR tube) was treated with 2-ethynyl-1,3,5-trimethylbenzene (21 μL, 0.129 mmol). NMR spectra were recorded immediately at low temperature. ^{1}H NMR (300.1 MHz, toluene-d_8, 298 K): δ 7.5−6.5 (m, 10H, H_{Ph}), 6.80 (m, 1H, $H_{5\text{-}py}$), 6.65 and 6.62 (both br, 2H, = $\mathrm{CHN_{IPr}}$), 5.76 (dt, J_{H-H} = 8.5, 1.1, 1H, $H_{6\text{-}py}$), 5.54 (ddd, J_{H-H} = 6.8, 5.3, 1.0, 1H, $H_{4\text{-}py}$), 5.25 (dt, J_{H-H} = 5.3, 1.1, 1H, $H_{3\text{-py}}$), 3.97, 3.95, 3.50, and 2.85 (all sept, J_{H-H} = 6.7, 4H, $C\underline{H}Me_{IPr}$), 3.27 and 3.07 (both dd, J_{H-H} = 2.2, J_{H-Rh} = 1.0, 2H, $CH_{2\text{-}\pi\text{-enyne}}$), 2.3−2.0 (18H, $Me_{\pi\text{-enyne}}$), 1.80, 1.57, 1.55, 1.30, 1.14, 1.11, 1.08, and 1.02 (all d, J_{H-H} = 6.7, 24H, $CH\underline{Me}_{IPr}$). $^{13}C\{^1H\}$-APT NMR (75.5 MHz, toluene-d_8, 243 K): δ 185.0 (d, J_{C-Rh} = 60.1, Rh−C_{IPr}), 181.4 (d, J_{C-Rh} = 2.7, $C_{2\text{-py}}$), 150.0, 148.2, 146.6, and 145.3 (all s, $C_{q\text{-IPr}}$), 142.4 (s, $C_{3\text{-py}}$), 142−134 (all s, $C_{q\text{-Ph-}\pi\text{-enyne}}$), 139.0 (s, $C_{5\text{-py}}$), 138.9 and 137.1 (both s, C_qN), 131−123 (all s, CH_{Ph}), 128.4 (s, $=CHN_{IPr}$), 110.1 (s, $PhC{\equiv}\underline{C}C(Ph){=}CH_2$), 109.8 (s, $C_{6\text{-py}}$), 109.0 (s, $C_{4\text{-py}}$), 83.2 (s, $Ph\underline{C}{\equiv}CC(Ph){=}CH_2$), 50.3 (d, J_{C-Rh} = 17.9, $=CH_2$), 41.0 (d, J_{C-Rh} = 17.8, $\underline{C}{=}CH_2$), 30.3, 29.4, 28.8, and 28.7 (all s, $\underline{C}HMe_{IPr}$), 29−20 (all s, $Me_{\pi\text{-enyne}}$), 28.4, 28.3, 26.8, 26.6, 24.0, 23.5, 23.4, and 21.6 (all s, $CH\underline{Me}_{IPr}$).

In Situ Formation of Rh[κ^1-*O*-{O=C(−CH=CH−CH=CH−)NH}]{κ^1-*O*-(CF_3O_3S)}(η^2-coe)(IPr) (8a,b). A solution of **2** (23 mg, 0.033 mmol) in CD_2Cl_2 at 223 K (0.5 mL, NMR tube) was treated with trifluoromethanesulfonic acid (3 μL, 0.033 mmol). NMR spectra were recorded immediately at low temperature. NMR data evidenced the presence of an equilibrium mixture of two isomers, **8a** and **8b** (50:50). Data for complex **8a**: ^1H NMR (400.1 MHz, CD_2Cl_2, 223 K): δ 11.73 (s, 1H, NH), 7.8−7.1 (m, 6H, $H_{Ph,IPr}$), 7.67 (m, 1H, $H_{6\text{-py}}$), 7.52 (m, 1H, $H_{4\text{-py}}$), 7.06 (s, 2H, $=CHN_{IPr}$), 6.85 (d, J_{H-H} = 9.0, 1H, $H_{3\text{-py}}$), 6.43 (m, 1H, $H_{5\text{-py}}$), 3.55 and 2.75 (both sept, J_{H-H} = 6.8, 4H, $C\underline{H}Me_{IPr}$), 2.9−2.7 (m, 2H, $=CH_{coe}$), 1.6−1.0 (m, 36H, $CH_{2\text{-coe}}$ and $CH\underline{Me}_{IPr}$). $^{13}C\{^1H\}$-APT NMR (100.6 MHz, CD_2Cl_2, 223 K): δ 177.0 (d, J_{C-Rh} = 62.1, Rh−C_{IPr}), 165.2 (s, $C_{2\text{-py}}$), 147.0 and 146.9 (both s, $C_{q\text{-IPr}}$), 142.7 (s, $C_{4\text{-py}}$), 136.1 (s, C_qN), 135.9 (s, $C_{6\text{-py}}$), 130−123 (all s, $CH_{Ph\text{-IPr}}$), 120.0 (s, $C_{3\text{-py}}$), 109.7 (s, $C_{5\text{-py}}$), 66.9 (d, J_{C-Rh} = 14.0, $=CH_{coe}$), 33−25 (all s, $CH_{2\text{-coe}}$), 29.0 and 28.4 (both s, $\underline{C}HMe_{IPr}$), 26.2, 22.5, 22.2, and 22.0 (all s, $CH\underline{Me}_{IPr}$). $^1H-^{15}N$ HMQC NMR (40.5 MHz, C_6D_6, 233 K): δ 174.0 (NH_{py}). ^{19}F NMR (282.3 MHz, CD_2Cl_2, 223 K): δ −77.9 and −79.2 (both br, CF_3). Data for complex **8b**: ^1H NMR (400.1 MHz, CD_2Cl_2, 223 K): δ 10.97 (s, 1H, NH), 7.8−7.1 (m, 6H, $H_{Ph,IPr}$), 7.37 (m, 1H, $H_{6\text{-py}}$), 7.30 (m, 1H, $H_{4\text{-py}}$), 7.06 (s, 2H, $=CHN_{IPr}$), 6.45 (m, 1H, $H_{3\text{-py}}$), 6.43 (m, 1H, $H_{5\text{-py}}$), 2.66 and 2.27 (both br, 4H, $C\underline{H}Me_{IPr}$), 2.9−2.7 (m, 2H, $=CH_{coe}$), 1.6−1.0 (m, 36H, $CH_{2\text{-coe}}$ and $CH\underline{Me}_{IPr}$). $^{13}C\{^1H\}$-APT NMR (100.6 MHz, CD_2Cl_2, 223 K): δ 177.0 (d, J_{C-Rh} = 62.1, Rh−C_{IPr}), 164.6 (s, $C_{2\text{-py}}$), 146.0 (s, $C_{q\text{-IPr}}$), 142.5 (s, $C_{4\text{-py}}$), 135.5 (s, C_qN), 135.1 (s, $C_{6\text{-py}}$), 130−123 (all s, $CH_{Ph\text{-IPr}}$), 119.9 (s, $C_{3\text{-py}}$), 108.6 (s, $C_{5\text{-py}}$), 66.9 (d, J_{C-Rh} = 14.0, $=CH_{coe}$), 33−25 (all s, $CH_{2\text{-coe}}$), 29.0 and 28.4 (both s, $\underline{C}HMe_{IPr}$), 26.2, 22.5, 22.2, and 22.0 (all s, $CH\underline{Me}_{IPr}$). $^1H-^{15}N$ HMQC NMR (40.5 MHz, CD_2Cl_2, 223 K): δ 170.3 (NH_{py}). ^{19}F NMR (282.3 MHz, CD_2Cl_2, 223 K): δ −77.9 and −79.2 (both br, CF_3).

Standard Conditions for the Catalytic Alkyne Dimerization. To a C_6D_6 solution (0.5 mL) in a NMR tube under argon atmosphere, 0.01 mmol of catalyst and 0.17 mmol of toluene as internal standard were added. The solution was frozen by means of a dewar flask containing isopropanol at 195 K. Then, 0.50 mmol of alkyne were added and the NMR tube was sealed under argon. The solution was allowed to warm up to room temperature just before the first NMR spectrum was recorded. The reaction course was monitored by ^1H NMR spectroscopy, and the conversion was determined by integration of the corresponding resonances of the internal standard and the products. In case of 0.5, 0.1, or 0.05 mol % of catalyst loading, a 20 mM solution of catalyst in C_6D_6 was prepared, and then, the corresponding amount of solution was added to the reaction mixture and it was proceeded as described above.

Crystal Structure Determination. Single crystals of **2** suitable for the X-ray diffraction studies were grown by slow diffusion of hexane into a toluene solution of the compound. X-ray diffraction data were collected at 100(2) K on a Bruker APEX SMART CCD diffractometer with graphite-monochromated Mo−Kα radiation (λ = 0.71073 Å) using 0.6° ω rotations. Intensities were integrated and corrected for absorption effects with SAINT-PLUS[35] and SADABS[36] programs, both included in the APEX2 package. The structures were solved by the Patterson method with SHELXS-97[37] and refined by full matrix least-squares on F^2 with SHELXL-2014,[38] under WinGX.[39]

Crystal Data and Structure Refinement for 2. $C_{40}H_{54}N_3ORh$, 695.77 g mol^{-1}, Monoclinic, $P2_1/c$, a = 11.2672(10) Å, b = 10.7013(10) Å, c = 29.775(3) Å, b = 90.3070(10)°, V = 3590.0(6) Å^3, Z = 4, D_{calc} = 1.287 g cm^{-3}, μ = 0.510 mm^{-1}, $F(000)$ = 1472, $\theta_{min}/\theta_{max}$ = 1.807/25.680°, index ranges $-13 \le h \le 13$, $-13 \le k \le 13$, $-36 \le l \le 36$, reflections collected/independent 36521/6806 [R(int) = 0.0410], data/restraints/parameters 6806/13/452, GooF(F^2) 1.041, R_1 = 0.0282 [$I > 2\sigma(I)$], wR_2 = 0.0635 (all data), largest diff. peak/hole 0.350/−0.422 e·Å^{-3}. CCDC deposition number 2015873.

Computational Details. All DFT theoretical calculations were carried out using the Gaussian program package.[40] The B97D3 exchange correlation functional[41] has been employed for the calculation of energies, gradients, and frequencies in combination to the def2-SVP basis set[42] which considers effective core potentials for Rh. Single point calculations at the M06L/def-TZVP level of theory,[43] including also the SMD approach[44] for benzene to simulate solvation effects were performed to refine the energetic values. All calculations were done using the "ultrafine" grid. Relative energies are Gibbs free energies referred to a 1 M standard state using the approximation of Goddard et al.[45] at 25 °C. Analytical frequency analyses were employed to confirm the nature of the stationary points. An intrinsic reaction path or coordinate scan calculations connecting both minima were performed for flat or unclear transition states.

ASSOCIATED CONTENT

Supporting Information

The Supporting Information is available free of charge at https://pubs.acs.org/doi/10.1021/acscatal.1c00602.

> Miscellaneous information including NMR data of complexes and organic products, deuterium labeling experiments, and DFT calculation data (PDF)
>
> Crystallographic information file for CCDC 2015873 (CIF)
>
> Optimized coordinates for the computed compounds (XYZ)

AUTHOR INFORMATION

Corresponding Authors

Ricardo Castarlenas − *Departamento de Química Inorgánica−Instituto de Síntesis Química y Catálisis Homogénea (ISQCH), Universidad de Zaragoza−CSIC, 50009 Zaragoza, Spain;* orcid.org/0000-0003-4460-8678; Email: rcastar@unizar.es

Víctor Polo − *Departamento de Química Física, Universidad de Zaragoza, 50009 Zaragoza, Spain;* orcid.org/0000-0001-5823-7965; Email: vipolo@unizar.es

Authors

María Galiana-Cameo − *Departamento de Química Inorgánica−Instituto de Síntesis Química y Catálisis Homogénea (ISQCH), Universidad de Zaragoza−CSIC, 50009 Zaragoza, Spain;* orcid.org/0000-0002-2043-4864

Asier Urriolabeitia − *Departamento de Química Física, Universidad de Zaragoza, 50009 Zaragoza, Spain*

Eduardo Barrenas − *Departamento de Química Inorgánica−Instituto de Síntesis Química y Catálisis Homogénea (ISQCH), Universidad de Zaragoza−CSIC, 50009 Zaragoza, Spain*

Vincenzo Passarelli − *Centro Universitario de la Defensa, 50090 Zaragoza, Spain; Departamento de Química Inorgánica−Instituto de Síntesis Química y Catálisis Homogénea (ISQCH), Universidad de Zaragoza−CSIC, 50009 Zaragoza, Spain;* orcid.org/0000-0002-1735-6439

Jesús J. Pérez-Torrente − *Departamento de Química Inorgánica−Instituto de Síntesis Química y Catálisis Homogénea (ISQCH), Universidad de Zaragoza−CSIC, 50009 Zaragoza, Spain;* orcid.org/0000-0002-3327-0918

Andrea Di Giuseppe − *Departamento de Química Inorgánica−Instituto de Síntesis Química y Catálisis Homogénea (ISQCH), Universidad de Zaragoza−CSIC, 50009 Zaragoza, Spain; Dipartimento di Scienze Fisiche e Chimiche, Università dell'Aquila, I-67100 Coppito, AQ, Italy;* orcid.org/0000-0002-3666-5800

Complete contact information is available at: https://pubs.acs.org/10.1021/acscatal.1c00602

Notes

The authors declare no competing financial interest.

ACKNOWLEDGMENTS

Financial support from the Spanish Ministerio de Ciencia e Innovación (MICINN/FEDER) under the Projects PID2019-103965GB-I00 and PGC2018-099383-B-I00, and the Diputación General de Aragón (FEDER 2014-2020 "Building Europe from Aragón", group E42_20R) are gratefully acknowledged. A.D.G. thanks the Spanish Ministerio de Economía y Competitividad (MINECO) for the postdoctoral grant Juan de la Cierva - Incorporación 2015 (IJCI-2015-27029). A.U. thankfully acknowledges the Spanish MECD for a FPU fellowship (FPU 2017/05417). The authors would like to acknowledge the use of Servicio General de Apoyo a la Investigación-SAI, Universidad de Zaragoza and the computational resources provided by the Institute for Biocomputation and the Physics of Complex Systems (BIFI)−Universidad de Zaragoza.

DEDICATION

Dedicated to Prof. Pierre H. Dixneuf, a very active species who initiated the catalytic cycles of many researchers.

REFERENCES

(1) Hayler, J. D.; Leahy, D. K.; Simmons, E. M. A. Pharmaceutical Industry Perspective on Sustainable Metal Catalysis. *Organometallics* **2019**, *38*, 36−46.

(2) (a) Ikariya, T.; Murata, K.; Noyori, R. Bifunctional Transition Metal-Based Molecular Catalysts for Asymmetric Syntheses. *Org. Biomol. Chem.* **2006**, *4*, 393−406. (b) Grotjahn, D. B. Bifunctional Catalysts and Related Complexes: Structures and Properties. *Dalton Trans.* **2008**, 6497−6508. (c) Khusnutdinova, J. R.; Milstein, D. Metal-Ligand Cooperation. *Angew. Chem., Int. Ed.* **2015**, *54*, 12236−12273. (d) Kim, D.-S.; Park, W.-J.; Jun, C.-H. Metal-Organic Cooperative Catalysis in C-H and C-C Bond Activation. *Chem. Rev.* **2017**, *117*, 8977−9015. (e) Higashi, T.; Kusumoto, S.; Nozaki, K. Cleavage of Si-H, B-H, and C-H bonds by Metal-Ligand cooperation. *Chem. Rev.* **2019**, *119*, 10393−10402.

(3) Johnson, D. G.; Lynam, J. M.; Slattery, J. M.; Welby, C. E. Insights into the Intramolecular Acetate-Mediated Formation of Ruthenium Vinylidene Complexes: a Ligand-Assisted Proton Shuttle (LAPS) Mechanism. *Dalton Trans.* **2010**, *39*, 10432−10441.

(4) (a) Breit, B.; Gellrich, U.; Li, T.; Lynam, J. M.; Milner, L. M.; Pridmore, N. E.; Slattery, J. M.; Whitwood, A. C. Mechanistic Insight into the Ruthenium-Catalysed anti-Markovnikov Hydration of Alkynes Using a Self-Assembled Complex: a Crucial Role for Ligand-Assisted Proton Shuttle Processes. *Dalton Trans.* **2014**, *43*, 11277−11285. (b) Leeb, N. M.; Drover, M. W.; Love, J. A.; Schafer, L. L.; Slattery, J. M. Phosphoramidate-Assisted Alkyne Activation: Probing the Mechanism of Proton Shuttling in a N,O-Chelated Cp*Ir(III) Complex. *Organometallics* **2018**, *37*, 4630−4638. (c) Zafar, M.; Ramalakshmi, R.; Pathak, K.; Ahmad, A.; Roisnel, T.; Ghosh, S. Five-Membered Ruthenacycles: Ligand-Assisted Alkyne Insertion into 1,3-N,S-Chelated Ruthenium Borate Species. *Chem. - Eur. J.* **2019**, *25*, 13537−13546.

(5) (a) Monot, J.; Brunel, P.; Kefalidis, C. E.; Espinosa-Jalapa, N. A.; Maron, L.; Martin-Vaca, B.; Bourissou, D. A Case Study of Proton Shuttling in Palladium Catalysis. *Chem. Sci.* **2016**, *7*, 2179−2187. (b) El-Sepelgy, O.; Brzozowska, A.; Azofra, L. M.; Jang, Y. K.; Cavallo, L.; Rueping, M. Experimental and Computational Study of an Unexpected Iron-Catalyzed Carboetherification by Cooperative Metal and Ligand Substrate Interaction and Proton Shuttling. *Angew. Chem., Int. Ed.* **2017**, *56*, 14863−14867.

(6) de Aguirre, A.; Díez-González, S.; Maseras, F.; Martín, M.; Sola, E. The Acetate Proton Shuttle between Mutually Trans Ligands. *Organometallics* **2018**, *37*, 2645−2651.

(7) (a) Crawford, L.; Cole-Hamilton, D. J.; Drent, E.; Bühl, M. Mechanism of Alkyne Alkoxycarbonylation at a Pd Catalyst with P,N Hemilabile Ligands: A Density Functional Study. *Chem. - Eur. J.* **2014**, *20*, 13923−13926. (b) Virant, M.; Mihelač, M.; Gazvoda, M.; Cotman, A. E.; Frantar, A.; Pinter, B.; Košmrlj. Pyridine Wingtip in $[Pd(Py\text{-}tzNHC)_2]_2^+$ Complex Is a Proton Shuttle in the Catalytic Hydroamination of Alkynes. *Org. Lett.* **2020**, *22*, 2157−2161. (c) Zhu, L.; Liu, L.-J.; Jiang, Y.-Y.; Liu, P.; Fan, X.; Zhang, Q.; Zhao, Y.; Bi, S. Mechanism and Origin of Ligand-Controlled Chemo- and Regioselectivities in Palladium-Catalyzed Methoxycarbonylation of Alkynes. *J. Org. Chem.* **2020**, *85*, 7136−7151.

(8) (a) García-Garrido, S. E. *Modern Alkyne Chemistry: Catalytic and Atom-Economic Transformations*; Trost, B. M., Li, C.-J., Eds.; Wiley-VCH: Weinheim, Germany, 2015; pp 301−334. (b) Trost, B. M.; Masters, J. T. Transition Metal-Catalyzed Couplings of Alkynes to 1,3-Enynes: Modern Methods and Synthetic Applications. *Chem. Soc. Rev.* **2016**, *45*, 2212−2238. (c) Temkin, O. N. Golden Age" of Homogeneous Catalysis Chemistry of Alkynes: Dimerization and Oligomerization of Alkynes. *Kinet. Catal.* **2019**, *60*, 689−732. (d) Liang, Q.; Hayashi, K.; Song, D. Catalytic Alkyne Dimerization without Noble Metals. *ACS Catal.* **2020**, *10*, 4895−4905.

(9) (a) Duchateau, R.; van Wee, C. T.; Teuben, J. H. Insertion and C-H Bond Activation of Unsaturated Substrates by Bis(benzamidinato)yttrium Alkyl, $[PhC(NSiMe_3)_2]_2YR$ (R = $CH_2Ph.THF$, $CH(SiMe_3)_2$), and Hydrido, $\{[PhC(NSiMe_3)_2]_2Y(\mu\text{-}H)\}_2$, Compounds. *Organometallics* **1996**, *15*, 2291−2302. (b) Haskel,

A.; Straub, T.; Dash, A. K.; Eisen, M. S. Oligomerization and Cross-Oligomerization of Terminal Alkynes Catalyzed by Organoactinide Complexes. *J. Am. Chem. Soc.* **1999**, *121*, 3014−3024. (c) Nishiura, M.; Hou, Z.; Wakatsuki, Y.; Yamaki, T.; Miyamoto, T. Novel Z-Selective Head-to-Head Dimerization of Terminal Alkynes Catalyzed by Lanthanide Half-Metallocene Complexes. *J. Am. Chem. Soc.* **2003**, *125*, 1184−1185. (d) Batrice, R. J.; McKinven, J.; Arnold, P. L.; Eisen, M. S. Selective Oligomerization and [2 + 2 + 2] Cycloaddition of Terminal Alkynes from Simple Actinide Precatalysts. *Organometallics* **2015**, *34*, 4039−4050.

(10) (a) Oshovsky, G. V.; Hessen, B.; Reek, J. N. H.; De Bruin, B. Electronic Selectivity Tuning in Titanium(III)-Catalyzed Acetylene Cross-Dimerization Reactions. *Organometallics* **2011**, *30*, 6067−6070. (b) Platel, R. H.; Schafer, L. L. Zirconium Catalyzed Alkyne Dimerization for Selective Z-Enyne Synthesis. *Chem. Commun.* **2012**, *48*, 10609−10611.

(11) (a) Trost, B. M.; Sorum, M. T.; Chan, C.; Ruhter, G. Palladium-Catalyzed Additions of Terminal Alkynes to Acceptor Alkynes. *J. Am. Chem. Soc.* **1997**, *119*, 698−708. (b) Rubina, M.; Gevorgyan, V. Can Agostic Interaction Affect Regiochemistry of Carbopalladation? Reverse Regioselectivity in the Palladium-Catalyzed Dimerization of Aryl Acetylenes. *J. Am. Chem. Soc.* **2001**, *123*, 11107−11108. (c) Katagiri, T.; Tsurugi, H.; Satoh, T.; Miura, M. Rhodium-Catalyzed (*E*)-Selective Cross-Dimerization of Terminal Alkynes. *Chem. Commun.* **2008**, 3405−3407. (d) Chen, T.; Guo, C.; Goto, M.; Han, L.-B. A Brønsted Acid-Catalyzed Generation of Palladium Complexes: Efficient Head-to-Tail Dimerization of Alkynes. *Chem. Commun.* **2013**, *49*, 7498−7500. (e) Zatolochnaya, O. V.; Gordeev, E. G.; Jahier, C.; Ananikov, V. P.; Gevorgyan, V. Carboxylate Switch between Hydro- and Carbopalladation Pathways in Regiodivergent Dimerization of Alkynes. *Chem. - Eur. J.* **2014**, *20*, 9578−9588. (f) Salvio, R.; Juliá-Hernández, F.; Pisciottani, L.; Mendoza-Meroño, R.; García-Granda, S.; Bassetti, M. Kinetics and Mechanistic Insights into the Acetate-Assisted Dimerization of Terminal Alkynes under Ruthenium- and Acid-Promoted (RAP) Catalysis. *Organometallics* **2017**, *36*, 3830−3840. (g) Żak, P.; Bołt, M.; Lorkowski, J.; Kubicki, M.; Pietraszuk, C. Platinum Complexes Bearing Bulky N-Heterocyclic Carbene Ligands as Efficient Catalysts for the Fully Selective Dimerization of Terminal Alkynes. *ChemCatChem* **2017**, *9*, 3627−3631. (h) Storey, C. M.; Gyton, M. R.; Andrew, R. E.; Chaplin, A. B. Terminal Alkyne Coupling Reactions through a Ring: Mechanistic Insights and Regiochemical Switching. *Angew. Chem., Int. Ed.* **2018**, *57*, 12003−12006. (i) Galiana-Cameo, M.; Borraz, M.; Zelenkova, Y.; Passarelli, V.; Lahoz, F. J.; Pérez-Torrente, J. J.; Oro, L. A.; Di Giuseppe, A.; Castarlenas, R. Rhodium(I)-NHC Complexes Bearing Bidentate Bis-Heteroatomic Acidato Ligands as *gem*-Selective Catalysts for Alkyne Dimerization. *Chem. - Eur. J.* **2020**, *26*, 9598−9608. (j) Storey, C. M.; Gyton, M. R.; Andrew, R. E.; Chaplin, A. B. Terminal Alkyne Coupling Reactions Through a Ring: Effect of Ring Size on Rate and Regioselectivity. *Chem. - Eur. J.* **2020**, *26*, 14715−14723.

(12) (a) Dash, A. K.; Eisen, M. S. Chemo- and Regioselective Dimerization of Terminal Alkynes Promoted by Methylaluminoxane. *Org. Lett.* **2000**, *2*, 737−740. (b) Brar, A.; Mummadi, S.; Unruh, D. K.; Krempner, C. Verkade Base in FLP Chemistry-From Stoichiometric C-H Bond Cleavage to the Catalytic Dimerization of Alkynes. *Organometallics* **2020**, *39*, 4307−4311.

(13) (a) Midya, G. C.; Paladhi, S.; Dhara, K.; Dash, J. Iron Catalyzed Highly Regioselective Dimerization of Terminal Aryl Alkynes. *Chem. Commun.* **2011**, *47*, 6698−6700. (b) Ventre, S.; Derat, E.; Amatore, M.; Aubert, C.; Petit, M. Hydrido-Cobalt Catalyst as a Selective Tool for the Dimerisation of Arylacetylenes: Scope and Theoretical Studies. *Adv. Synth. Catal.* **2013**, *355*, 2584−2590. (c) Rivada-Wheelaghan, O.; Chakraborty, S.; Shimon, L. J. W. Y.; Ben-David, Y.; Milstein, D. Z-Selective (Cross-)Dimerization of Terminal Alkynes Catalyzed by an Iron Complex. *Angew. Chem., Int. Ed.* **2016**, *55*, 6942−6945. (d) Liang, Q.; Osten, K. M.; Song, D. Iron-Catalyzed gem-Specific Dimerization of Terminal Alkynes. *Angew. Chem., Int. Ed.* **2017**, *56*, 6317−632. (e) Gorgas, N.; Stöger, B.; Veiros, L. F.; Kirchner, K. Iron(II) Bis(acetylide) Complexes as Key Intermediates in the Catalytic Hydrofunctionalization of Terminal Alkynes. *ACS Catal.* **2018**, *8*, 7973−7982. (f) Liang, Q.; Sheng, K.; Salmon, A.; Zhou, V. Y.; Song, D. Active Iron(II) Catalysts toward gem-Specific Dimerization of Terminal Alkynes. *ACS Catal.* **2019**, *9*, 810−818. (g) Zhuang, X.; Chen, J.-Y.; Yang, Z.; Jia, M.; Wu, C.; Liao, R.-Z.; Tung, C.-H.; Wang, W. Sequential Transformation of Terminal Alkynes to 1,3-Dienes by a Cooperative Cobalt Pyridonate Catalyst. *Organometallics* **2019**, *38*, 3752−3759. (h) Ueda, Y.; Tsurugi, H.; Mashima, K. Cobalt-Catalyzed E-Selective Cross-Dimerization of Terminal Alkynes: A Mechanism Involving Cobalt(0/II) Redox Cycles. *Angew. Chem., Int. Ed.* **2020**, *59*, 1552−1556. (i) Chen, J.-F.; Li, C. Cobalt-Catalyzed gem-Cross-Dimerization of Terminal Alkynes. *ACS Catal.* **2020**, *10*, 3881−3889.

(14) (a) Hasenbeck, M.; Müller, T.; Gellrich, U. Metal-free gem Selective Dimerization of Terminal Alkynes Catalyzed by a Pyridonate Borane Complex. *Catal. Sci. Technol.* **2019**, *9*, 2438−2444. (b) Ahmed, J.; Swain, A. K.; Das, A.; Govindarajan, R.; Bhunia, M.; Mandal, S. K. A K-Arylacetylide Complex for Catalytic Terminal Alkyne Functionalization Using KOtBu as a Precatalyst. *Chem. Commun.* **2019**, *55*, 13860−13863.

(15) (a) Rubio-Pérez, L.; Azpíroz, R.; Di Giuseppe, A.; Polo, V.; Castarlenas, R.; Pérez-Torrente, J. J.; Oro, L. A. Pyridine-Enhanced Head-to-Tail Dimerization of Terminal Alkynes by a Rhodium-N-Heterocyclic-Carbene Catalyst. *Chem. - Eur. J.* **2013**, *19*, 15304−15314. (b) Azpíroz, R.; Rubio-Pérez, L.; Castarlenas, R.; Pérez-Torrente, J. J.; Oro, L. A. gem-Selective Cross-Dimerization and Cross-Trimerization of Alkynes with Silylacetylenes Promoted by a Rhodium-Pyridine-N-Heterocyclic Carbene Catalyst. *ChemCatChem* **2014**, *6*, 2587−2592.

(16) (a) Di Giuseppe, A.; Castarlenas, R.; Pérez-Torrente, J. J.; Lahoz, F. J.; Polo, V.; Oro, L. A. Mild and Selective H/D Exchange at the β Position of Aromatic α-Olefins by N-Heterocyclic Carbene-Hydride-Rhodium Catalysts. *Angew. Chem., Int. Ed.* **2011**, *50*, 3938−3942. (b) Kwak, J.; Ohk, Y.; Jung, Y.; Chang, S. Rollover Cyclometalation Pathway in Rhodium Catalysis: Dramatic NHC Effects in the C-H Bond Functionalization. *J. Am. Chem. Soc.* **2012**, *134*, 17778−17788. (c) Keske, E. C.; Moore, B. D.; Zenkina, O. V.; Wang, R.; Schatte, G.; Crudden, C. M. Highly Selective Directed Arylation Reactions via Back-to-Back Dehydrogenative C-H Borylation/Arylation Reactions. *Chem. Commun.* **2014**, *50*, 9883−9886. (d) Palacios, L.; Meheut, Y.; Galiana-Cameo, M.; Artigas, M. J.; Di Giuseppe, A.; Lahoz, F. J.; Polo, V.; Castarlenas, R.; Pérez-Torrente, J. J.; Oro, L. A. Design of Highly Selective Alkyne Hydrothiolation Rh^{I}-NHC Catalysts: Carbonyl-Triggered Nonoxidative Mechanism. *Organometallics* **2017**, *36*, 2198−2207. (e) Azpíroz, R.; Di Giuseppe, A.; Passarelli, V.; Pérez-Torrente, J. J.; Oro, L. A.; Castarlenas, R. Rhodium-N-Heterocyclic Carbene Catalyzed Hydroalkenylation Reactions with 2-Vinylpyridine and 2-Vinylpyrazine: Preparation of Nitrogen-Bridgehead Heterocycles. *Organometallics* **2018**, *37*, 1695−1707. (f) Azpíroz, R.; Di Giuseppe, A.; Urriolabeitia, A.; Passarelli, V.; Polo, V.; Pérez-Torrente, J. J.; Oro, L. A.; Castarlenas, R. Hydride-Rhodium(III)-N-Heterocyclic Carbene Catalyst for Tandem Alkylation/Alkenylation via C-H Activation. *ACS Catal.* **2019**, *9*, 9372−9386.

(17) (a) Rawson, J. M.; Winpenny, R. E. P. The Coordination Chemistry of 2-pyridone and its Derivatives. *Coord. Chem. Rev.* **1995**, *139*, 313−374. (b) Oro, L. A.; Ciriano, M. A.; Pérez-Torrente, J. J.; Villarroya, E. Controlling the Molecular Architecture of Low Nuclearity Rhodium and Iridium Complexes using Bridging N-C-X (X = N, O, S) Ligands. *Coord. Chem. Rev.* **1999**, *193−195*, 941−975. (c) Kempe, R. The Strained η^2-*N*-Amido-*N*-Pyridine Coordination of Aminopyridinato Ligands. *Eur. J. Inorg. Chem.* **2003**, *2003*, 791−803.

(18) (a) Breit, B.; Seiche, W. Hydrogen Bonding as a Construction Element for Bidentate Donor Ligands in Homogeneous Catalysis: Regioselective Hydroformylation of Terminal Alkenes. *J. Am. Chem. Soc.* **2003**, *125*, 6608−6609. (b) Kawahara, R.; Fujita, K.-i.; Yamaguchi, R. Cooperative Catalysis by Iridium Complexes with a Bipyridonate Ligand: Versatile Dehydrogenative Oxidation of

Alcohols and Reversible Dehydrogenation-Hydrogenation between 2-Propanol and Acetone. *Angew. Chem., Int. Ed.* **2012**, *51*, 12790−12794. (c) Siek, S.; Burks, D. B.; Gerlach, D. L.; Thompson, C. R.; Qu, F.; Shankwitz, J. E.; Vasquez, R. M.; Chambers, N.; Szulczewski, G. J.; Grotjahn, D. B.; Webster, C. E.; Papish, E.; et al. Iridium and Ruthenium Complexes of N-Heterocyclic Carbene- and Pyridinol-Derived Chelates as Catalysts for Aqueous Carbon Dioxide Hydrogenation and Formic Acid Dehydrogenation: The Role of the Alkali Metal. *Organometallics* **2017**, *36*, 1091−1106.

(19) (a) Chong, E.; Brandt, J. W.; Schafer, L. L. 2-Pyridonate Tantalum Complexes for the Intermolecular Hydroaminoalkylation of Sterically Demanding Alkenes. *J. Am. Chem. Soc.* **2014**, *136*, 10898−10901. (b) Wang, P.; Verma, P.; Xia, G.; Shi, J.; Qiao, J. X.; Tao, S.; Cheng, P. T. W.; Poss, M. A.; Farmer, M. E.; Yeung, K.-S.; Yu, J.-Q. Ligand-Accelerated non-Directed C-H Functionalization of Arenes. *Nature* **2017**, *551*, 489−494. (c) Salamanca, V.; Toledo, A.; Albéniz, A. C. [2,2′-Bipyridin]-6(1H)-one, a Truly Cooperating Ligand in the Palladium-Mediated C-H Activation Step: Experimental Evidence in the Direct C-3 Arylation of Pyridine. *J. Am. Chem. Soc.* **2018**, *140*, 17851−17856. (d) Li, F.; Zhou, Y.; Yang, H.; Wang, Z.; Yu, Q.; Zhang, F. L. Monodentate Transient Directing Group Enabled Pd-Catalyzed Ortho-C-H Methoxylation and Chlorination of Benzaldehydes. *Org. Lett.* **2019**, *21*, 3692−3695. (e) Xiao, L. J.; Hong, K.; Luo, F.; Hu, L.; Ewing, W. R.; Yeung, K. S.; Yu, J. Q. Pd^{II}-Catalyzed Enantioselective $C(sp^3)$-H Arylation of Cyclobutyl Ketones Using a Chiral Transient Directing Group. *Angew. Chem., Int. Ed.* **2020**, *59*, 9594−9600.

(20) (a) Wang, R.; Ma, J.; Li, F. Synthesis of α-Alkylated Ketones via Tandem Acceptorless Dehydrogenation/α-Alkylation from Secondary and Primary Alcohols Catalyzed by Metal-Ligand Bifunctional Iridium Complex [Cp*Ir(2,2′-bpyO)(H_2O)]. *J. Org. Chem.* **2015**, *80*, 10769−10766. (b) Yan, X.; Ge, H.; Yang, X. Unexpected Concerted Two-Proton Transfer for Amination of Formic Acid to Formamide Catalysed by Mn Bipyridinol Complexes. *Catal. Sci. Technol.* **2018**, *8*, 5735−5739. (c) Griffin, S. E.; Schafer, L. L. Vanadium Pyridonate Catalysts: Isolation of Intermediates in the Reductive Coupling of Alcohols. *Inorg. Chem.* **2020**, *59*, 5256−5260.

(21) (a) Flood, T. C.; Lim, J. K.; Deming, M. A. Generation of Coordinative Unsaturation at Osmium via Ring-Opening Equilibration of a 2-Pyridonato Chelate Complex. *Organometallics* **2000**, *19*, 2310−2317. (b) Royer, A. M.; Rauchfuss, T. B.; Gray, D. L. *Organometallics* **2010**, *29*, 6763−6768. (c) Clarkson, J. M.; Schafer, L. L. Bis(tert-butylimido)bis(N,O-chelate)tungsten(VI) Complexes: Probing Amidate and Pyridonate Hemilability. *Inorg. Chem.* **2017**, *56*, 5553−5566.

(22) (a) Wang, N.; Li, B.; Song, H.; Xu, S.; Wang, B. Investigation and Comparison of the Mechanistic Steps in the $[(Cp^*MCl_2)_2]$ ($Cp^*=C_5Me_5$; M = Rh, Ir)-Catalyzed Oxidative Annulation of Isoquinolones with Alkynes. *Chem. - Eur. J.* **2013**, *19*, 358−364. (b) Munjanja, L.; Yuan, H.; Brennessel, W. W.; Jones, W. D. Synthesis, Characterization, and Reactivity of Cp*Rh(III) Complexes Having Functional N,O Chelate Ligands. *J. Organomet. Chem.* **2017**, *847*, 28−32.

(23) (a) Boyd, D. C.; Szalapski, R.; Mann, K. R. Preparation, Characterization, and Structural Analyses of $[Rh(chp)(NBD)]_2$ and $[Rh(chp)(NBD)]_2(PF_6)$. Isolation of a Paramagnetic d^7-d^8 Binuclear Radical and Its d^8-d^8 Precursor. *Organometallics* **1989**, *8*, 790−795. (b) Fandos, R.; Hernández, C.; Otero, A.; Rodríguez, A.; Ruiz, M. J.; García Fierro, J. L.; Terreros, P. Rhodium and Iridium Hydroxide Complexes $[M(\mu\text{-OH})(COD)]_2$ (M = Rh, Ir) as Versatile Precursors of Homo and Early-Late Heterobimetallic Compounds. X-ray Crystal Structures of $Cp^*Ta(\mu_3\text{-O})_4[Rh(COD)]_4$ ($Cp^*= \eta^5\text{-}C_5Me_5$) and $[Ir(2\text{-O-3-CN-4,6-Me}_2\text{-}C_5HN)(COD)]_2$. *Organometallics* **1999**, *18*, 2718−2723. (c) Li, Z.; David, A.; Albani, B. A.; Pellois, J.-P.; Turro, C.; Dunbar, K. R. Optimizing the Electronic Properties of Photoactive Anticancer Oxypyridine-Bridged Dirhodium(II,II) Complexes. *J. Am. Chem. Soc.* **2014**, *136*, 17058−17070.

(24) (a) Spannenberg, A.; Oberthur, M.; Noss, H.; Tillack, A.; Arndt, P.; Kempe, R. Metal-Metal Communication of Rh or Pd with Nd in Novel Heterobinuclear Complexes. *Angew. Chem., Int. Ed.* **1998**, *37*, 2079−2082. (b) Zamorano, A.; Rendón, N.; Valpuesta, J. E. V.; Álvarez, E.; Carmona, E. Synthesis and Reactivity toward H_2 of (η^5-C_5Me_5)Rh(III) Complexes with Bulky Aminopyridinate Ligands. *Inorg. Chem.* **2015**, *54*, 6573−6581.

(25) (a) Deeming, A. J.; Hardcastle, K. I.; Meah, M. N.; Bates, P. A.; Dawes, H. M.; Hursthouse, M. B. Rhodium(III) Complexes with Pyridine-2-thiol (pySH) and Pyridine-2-thiolato (pyS) as the only Ligands: Crystal Structures of mer-[Rh(pyS),], [Rh(pyS)(pySH)]Cl·0.5$H_2$0 and [Rh(pyS),(pySH)]. *J. Chem. Soc., Dalton Trans.* **1988**, 227−233. (b) Seino, H.; Yoshikawa, T.; Hidai, M.; Mizobe, Y. Preparation of Mononuclear and Dinuclear Rh Hydrotris(pyrazolyl)-borato Complexes Containing Arenethiolato Ligands and Conversion of the Mononuclear Complexes into Dinuclear Rh-Rh and Rh-Ir Complexes with Bridging Arenethiolato Ligands. *Dalton Trans.* **2004**, 3593−3600. (c) Wang, H.; Guo, X.-Q.; Zhong, R.; Lin, Y.; Zhang, P.-C.; Hou, X.-F. Reactions of Half-Sandwich Rhodium(III) and Iridium(III) Compounds with Pyridinethiolate Ligands: Mono-, di-, and tri-Nuclear Complexes. *J. Organomet. Chem.* **2009**, *694*, 3362−3368.

(26) Penfold, B. R. The Electronic Distribution in Crystalline α-pyridone. *Acta Crystallogr.* **1953**, *6*, 591−600.

(27) Palacios, L.; Di Giuseppe, A.; Castarlenas, R.; Lahoz, F. J.; Pérez-Torrente, J. J.; Oro, L. A. Pyridine versus Acetonitrile Coordination in Rhodium-N-Heterocyclic Carbene Square-Planar Complexes. *Dalton Trans.* **2015**, *44*, 5777−5789.

(28) Feuerstein, M.; Chahen, L.; Doucet, H.; Santelli, M. Efficient Synthesis of Enynes by Tetraphosphine-Palladium Catalysed Reaction of Vinyl Bromides with Terminal Alkynes. *Tetrahedron* **2006**, *62*, 112−120.

(29) (a) Timpa, S. D.; Zhou, J.; Bhuvanesh, N.; Ozerov, O. V. Potential Carbon-Fluorine Reductive Elimination from Pincer-Supported Rh(III) and Dominating Side Reactions: Theoretical and Experimental Examination. *Organometallics* **2014**, *33*, 6210−6217. (b) Jurt, P.; Salnikov, O. G.; Gianetti, G. L.; Chukanov, N. V.; Baker, M. G.; Le Corre, G.; Borger, J. E.; Verel, R.; Gauthier, S.; Fuhr, O.; Kovtunov, K. V.; Fedorov, A.; Fenske, D.; Koptyug, V.; Grützmacher, H. Low-Valent Homobimetallic Rh Complexes: Influence of Ligands on the Structure and the Intramolecular Reactivity of Rh-H Intermediates. *Chem. Sci.* **2019**, *10*, 7937−7945.

(30) Gómez-Gallego, M.; Sierra, M. A. Kinetic Isotope Effects in the Study of Organometallic Reaction Mechanisms. *Chem. Rev.* **2011**, *111*, 4857−4963.

(31) (a) Royer, A. M.; Rauchfuss, T. B.; Wilson, S. R. Coordination Chemistry of a Model for the GP Cofactor in the Hmd Hydrogenase: Hydrogen-Bonding and Hydrogen-Transfer Catalysis. *Inorg. Chem.* **2008**, *47*, 395−397.

(32) A Rh^I square-planar intermediate **E′**, similar to **E** but bearing mutually *cis* π-alkyne molecules, was found to be more stable. However, the CMD step originated from the new isomer **E′**, presents a transition state **TSEF′** of 26.3 kcal mol^{-1}, significantly higher than **TSEF** (15.9 kcal mol^{-1}) (see Figure S107 in the Supporting Information).

(33) (a) Gellrich, U.; Mei*ß*ner, A.; Steffani, A.; Kähny, M.; Drexler, H.-J.; Heller, D.; Plattner, D. A.; Breit, B. Mechanistic Investigations of the Rhodium Catalyzed Propargylic CH Activation. *J. Am. Chem. Soc.* **2014**, *136*, 1097−1104. (b) Zhang, H.; Bao, X. Computational insight into the mechanism of the Pd(0)-Brønsted acid cooperatively catalysed head-to- tail dimerization of terminal alkynes. *RSC Adv.* **2015**, *5*, 84636−84642.

(34) Yu, X.-Y.; Patrick, B. O.; James, B. R. Rhodium(III) Peroxo Complexes Containing Carbene and Phosphine Ligands. *Organometallics* **2006**, *25*, 4870−4877.

(35) *SAINT+: Area-Detector Integration Software*, version 6.01; Bruker AXS: Madison, WI, 2001.

(36) Sheldrick, G. M. *SADABS Program*; University of Götingen: Göttingen, Germany, 1999.

(37) Sheldrick, G. M. *SHELXS 97, Program for the Solution of Crystal Structure*; University of Göttingen: Göttingen, Germany, 1997.

(38) Sheldrick, G. M. Crystal Structure Refinement with SHELXL. *Acta Crystallogr., Sect. C: Struct. Chem.* **2015**, *71*, 3−8.

(39) Farrugia, L. J. WinGX and ORTEP for Windows: an Update. *J. Appl. Crystallogr.* **2012**, *45*, 849−854.

(40) Firsch, M. J.; Trucks, G. W.; Schlegel, H. B.; Scuseria, G. E.; Robb, M. A.; Cheeseman, J. R.; Scalmani, G.; Barone, V.; Mennucci, B.; Petersson, G. A.; Nakatsuji, H.; Caricato, M.; Li, X.; Hratchian, H. P.; Izmaylov, A. F.; Bloino, J.; Zheng, G.; Sonnenberg, J. L.; Hada, M.; Ehara, M.; Toyota, K.; Fukuda, R.; Hasegawa, J.; Ishida, M.; Nakajima, T.; Honda, Y.; Kitao, O.; Nakai, H.; Vreven, T.; Montgomery, J. A., Jr.; Peralta, J. E.; Ogliaro, F.; Bearpark, M.; Heyd, J. J.; Brothers, E.; Kudin, K. N.; Staroverov, V. N.; Kobayashi, R.; Normand, J.; Raghavachari, K.; Rendell, A.; Burant, J. C.; Iyengar, S. S.; Tomasi, J.; Cossi, M.; Rega, N.; Millam, J. M.; Klene, M.; Knox, J. E.; Cross, J. B.; Bakken, V.; Adamo, C.; Jaramillo, J.; Gomperts, R.; Stratmann, R. E.; Yazyev, O.; Austin, A. J.; Cammi, R.; Pomelli, C.; Ochterski, J. W.; Martin, R. L.; Morokuma, K.; Zakrzewski, V. G.; Voth, G. A.; Salvador, P.; Dannenberg, J. J.; Dapprich, S.; Daniels, A. D.; Farkas, Ö.; Foresman, J. B.; Ortiz, J. V.; Cioslowski, J.; Fox, D. J. *Gaussian 09*, revision D.1; Gaussian, Inc., Wallingford, CT, 2004.

(41) (a) Becke, A. D. Density-Functional Thermochemistry. V. Systematic Optimization of Exchange-Correlation Functionals. *J. Chem. Phys.* **1997**, *107*, 8554−8560. (b) Grimme, S.; Ehrlich, S.; Goerigk, L. Effect of the Damping Function in Dispersion Corrected Density Functional Theory. *J. Comput. Chem.* **2011**, *32*, 1456−1465.

(42) Weigend, F. R.; Ahlrichs, R. Balanced Basis Sets of Split Valence, Triple Zeta Valence and Quadruple Zeta Valence Quality for H to Rn: Design and Assessment of Accuracy. *Phys. Chem. Chem. Phys.* **2005**, *7*, 3297−3305.

(43) Zhao, Y.; Truhlar, D. G. A New Local Density Functional for Main-group Thermochemistry, Transition Metal Bonding, Thermochemical Kinetics, and Noncovalent Interactions. *J. Chem. Phys.* **2006**, *125*, 194101.

(44) Marenich, A. V.; Cramer, C. J.; Truhlar, D. G. Universal Solvation Model Based on Solute Electron Density and on a Continuum Model of the Solvent Defined by the Bulk Dielectric Constant and Atomic Surface Tensions. *J. Phys. Chem. B* **2009**, *113*, 6378−6396.

(45) Bryantsev, V. S.; Diallo, M. S.; Goddard, W. A., III Calculation of Solvation Free Energies of Charged Solutes Using Mixed Cluster/Continuum Models. *J. Phys. Chem. B* **2008**, *112*, 9709−9719.

https://doi.org/10.1021/acscatal.1c00602
ACS Catal. 2021, 11, 7553−7567

How to cite: *Angew. Chem. Int. Ed.* **2022,** *61,* e202117006
International Edition: doi.org/10.1002/anie.202117006
German Edition: doi.org/10.1002/ange.202117006

Rhodium Catalysis

Rhodium-NHC-Catalyzed *gem*-Specific *O*-Selective Hydropyridonation of Terminal Alkynes

María Galiana-Cameo, Raúl Romeo, Asier Urriolabeitia, Vincenzo Passarelli, Jesús J. Pérez-Torrente, Victor Polo, and Ricardo Castarlenas**

Abstract: The dinuclear complex [Rh(μ-Cl)(η^2-coe)(IPr)]$_2$ is an efficient catalyst for the *O*-selective Markovnikov-type addition of 2-pyridones to terminal alkynes. DFT calculations support a hydride-free pathway entailing intramolecular oxidative protonation of a π-alkyne by a κ^1*N*-hydroxypyridine ligand. Subsequent *O*-nucleophilic attack on a metallacyclopropene species affords an *O*-alkenyl-2-oxypyridine chelate rhodium intermediate as the catalyst resting state. The release of the alkenyl ether is calculated as the rate-determining step.

The 2-pyridone scaffold can be found in many biologically relevant compounds, including some drugs approved by the FDA for the treatment of cancer, HIV or pulmonary fibrosis (Scheme 1).[1] Classical multistep synthetic procedures[2] have been gradually substituted by more efficient metal-catalyzed approaches.[3] Thus, while reactivity on the *C*-sites mainly rely on C–H activation,[4] a diverse set of methods for heteroatomic functionalization have been described, including alkylation with organohalides,[5] the use of diazo compounds,[6] addition to unsaturated substrates,[7] or allylic substitution reactions.[8] However, the *N*- vs. *O*-selectivity is far to be controlled and critically depends on the reaction conditions or the ligands, partly as a result of 2-hydroxypyridine vs. 2-pyridone tautomerization.[9]

In particular, preparation of *O*- or *N*-alkenylated 2-pyridones presents unique challenges, especially for the *gem*-olefin derivatives (Scheme 2). Firstly, the access via the *O*-nucleophilic attack of enolates to 2-halogenated-pyridines is hampered. In addition, thermodynamically preferred *N*-substituted *trans*-isomers are prevalent when using alkenyl halides or boronic acids.[10] Other synthetic approaches, such as isomerization within an *O*-unsaturated chain,[11] *O*- to *N*-rearrangement,[12] or aldol condensation,[13] have limited generality lacking the formation of *gem*-isomers. The few existing preparative methods for *gem*-alkenyl pyridones involve multistep procedures[14] or the use of specific precursors such as tosylhydrazones[15] or benzynes,[16] therefore more reliable synthetic methods are desirable. In this context, the Markovnikov-addition of 2-pyridones to triple bonds seems a straightforward atom-economical access.

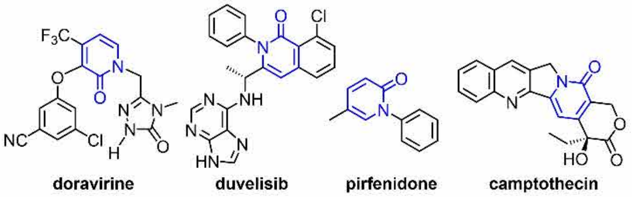

Scheme 1. Some 2-pyridone-based drugs approved by the FDA.

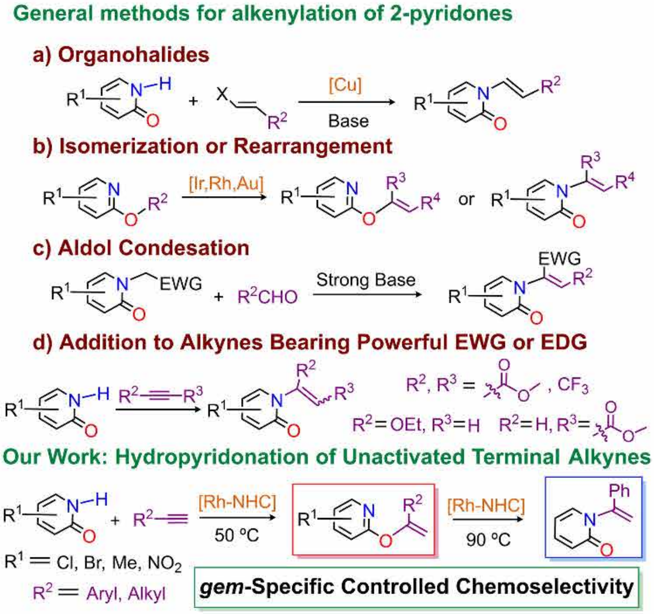

Scheme 2. Previous reports for preparation of *N*- or *O*-alkenylated 2-pyridones and our strategy.

---

[*] M. Galiana-Cameo, R. Romeo, Dr. V. Passarelli,
Prof. Dr. J. J. Pérez-Torrente, Dr. R. Castarlenas
Departamento de Química Inorgánica-Instituto de Síntesis Química y Catálisis Homogénea (ISQCH),
Universidad de Zaragoza-CSIC,
C/Pedro Cerbuna 12, CP, 50009 Zaragoza (Spain)
E-mail: rcastar@unizar.es

A. Urriolabeitia, Prof. Dr. V. Polo
Departamento de Química Física, Universidad de Zaragoza,
C/Pedro Cerbuna 12, CP, 50009 Zaragoza (Spain)
E-mail: vipolo@unizar.es

However, direct addition proceeds only for alkynes bearing powerful EWG or EDG groups,[17] thus, we envisage a transition-metal catalyzed approach for unactivated terminal alkynes. Moreover, we anticipate the different affinity of rhodium for *O*- or *N*-donor functions as a potential tool to control chemoselectivity. Nevertheless, an important handicap for successful catalytic alkyne *hydropyridonation* is the intrinsic high self-reactivity of terminal alkynes to give a myriad of dimeric, polymeric or cyclic structures.[18]

Our research group has recently disclosed efficient rhodium-*N*-heterocyclic carbene (NHC) catalysts for diverse carbon-heteroatom couplings via hydrofunctionalization of alkynes.[19] Particularly, the introduction of 2-pyridone in the Rh-NHC framework results in impressive TOFs for alkyne dimerization.[20] The 2-pyridonato ligand behaves as a fast proton shuttle between the two alkynes. Moreover, the specific *gem*-selectivity of 1,3-enynes arises from the preferred protonation at the terminal position of a π-coordinated alkyne. In the course of mechanistic studies involving $[Rh(\mu\text{-}Cl)(\eta^2\text{-coe})(IPr)]_2$ (**1**) {IPr = 1,3-bis-(2,6-diisopropylphenyl)imidazolin-2-carbene; coe = cyclooctene}, 2-pyridone, and phenylacetylene, we serendipitously observed the formation of a new Rh-IPr complex in small quantities. This compound has now been identified by X-ray diffraction analysis and multinuclear NMR spectroscopy as RhCl(IPr)-$[\kappa N,\eta^2\text{-}\{py\text{-}O\text{–}C(Ph){=}CH_2\}]$ (**2**), featuring an unexpected *O*-alkenyl-2-oxypyridine chelate (Figure 1). Complex **2** was isolated in 79 % yield by treatment of **1** with stoichiometric amounts of phenylacetylene and 2-pyridone. In the solid state, coordination of the alkenyl ether is shown by Rh–N41 {2.0891(15) Å} and Rh–ct1 distances {1.96913(15) Å} (ct1, olefin centroid). Moreover, the appearance of two doublets of doublets, $\delta = 2.61$ ($J_{H\text{-}H} = 4.3$, $J_{H\text{-}Rh} = 2.8$ Hz) and 2.54 ppm ($J_{H\text{-}Rh} = 2.1$ Hz), in the ^{1}H NMR spectrum and two doublets, 103.8 ($J_{C\text{-}Rh} = 18.6$ Hz) and 31.5 ppm ($J_{C\text{-}Rh} = 15.5$ Hz), in the $^{13}C\{^1H\}$-APT NMR experiment, confirms the coordination of the geminal olefin in solution.

In view of the ability of **1** to promote the stoichiometric alkyne-pyridone C–O coupling, we next studied its application to catalytic alkyne hydropyridonation. Gratifyingly, the addition of **1**, 5 mol % of Rh, to the benchmark substrates 2-pyridone (**3a**) and phenylacetylene (**4a**) in $CDCl_3$ resulted in the formation of the *gem*-alkenyl ether 2-(1-phenylvinyl)oxypyridine (**5aa**), after 20 h at 40 °C, as the exclusive heterocoupling product. Only 8 % of the 1,3-enyne arisen from competitive alkyne dimerization was observed. Other polar solvents were tested but alkyne dimerization prevailed (see Supporting Information). Temperature screening revealed a gradual reduction of alkyne conversion over 50 °C, likely due to catalyst decomposition, thus further experiments were performed at this compromise temperature. Interestingly, complex **2** was detected in the first monitoring spectrum. Indeed, similar catalytic outcome was obtained by using **2** as catalyst. Both facts suggest that **2** might be the resting state of the catalytic cycle. Moreover, the presence of an NHC was disclosed to be essential. The precursor of **1**, $[Rh(\mu\text{-}Cl)(\eta^2\text{-coe})_2]_2$, was inactive, while the Wilkinson's catalyst $RhCl(PPh_3)_3$ or the in situ formed $[Rh(\mu\text{-}Cl)(BINAP)]_2$ favored alkyne dimerization vs. hydropyridonation. It is worth a mention of the work of Breit's group showing the Rh-BINAP compound as efficient catalyst for the 2-pyridone addition to allenes.[7a] Other Rh-IPr complexes with κ²acetato or CO ancillary ligands were inefficient.

As for the scope of alkyne hydropyridonation promoted by **1**, catalytic reactions were monitored in NMR tubes using a 5 mol % of Rh and 1:1 pyridone:alkyne ratio in $CDCl_3$ at 50 °C (Figure 2). Organic products were isolated after 20 h (Scheme 3). In general, *gem*-specific *O*-alkenylated derivatives **5** were obtained, with the exception of 6-halogenated-2-pyridone substrates (**3e**,**f**), which also gave *N*-alkenylated products **6** in variable amounts. Competitive alkyne dimerization was limited to 1–12 % in cases of effective hydropyridonation, except for 4-(trifluoromethyl)phenylacetylene (**4d**) (20 %), which agrees with the faster alkyne dimerization previously observed for this alkyne.[20] Otherwise, inefficient substrates such as 6-methyl-2-pyridone or 2-quinolone produced higher amounts of 1,3-enyne. Regarding the functional groups, aromatic alkynes reacted faster than aliphatic ones, while no definite trend was observed for substituted 2-pyridones. The more divergent results were found for 6-substituted ones. Thus, 6-chloro-2-pyridone (**3f**) is the most

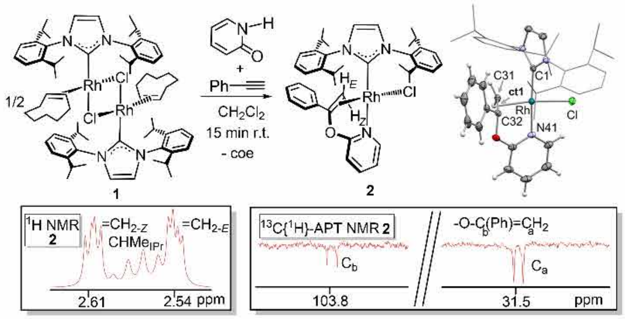

Figure 1. Formation of the chelate *O*-alkenyl-2-oxypyridine rhodium complex **2** and ORTEP view. For clarity a wireframe style is adopted for the NHC wingtips and most hydrogen atoms are omitted. Selected bond lengths [Å] are: Rh–C1 2.0193(18), Rh–Cl 2.3353(5), Rh–ct1 1.96913(15), C31–C32 1.408(3), Rh–N41 2.0891(15); ct1: centroid of C31 and C32.

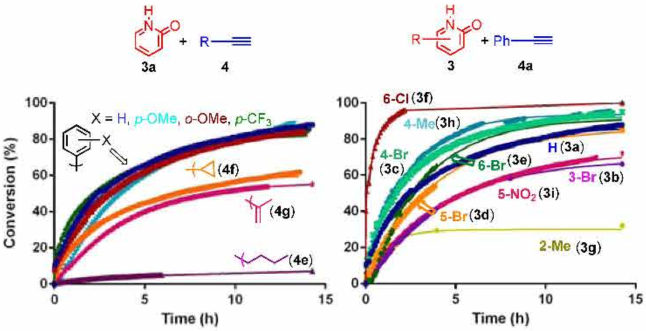

Figure 2. Reaction profile for the hydropyridonation of alkynes with 2-pyridone (left) and phenylacetylene with functionalized 2-pyridone derivatives (right).

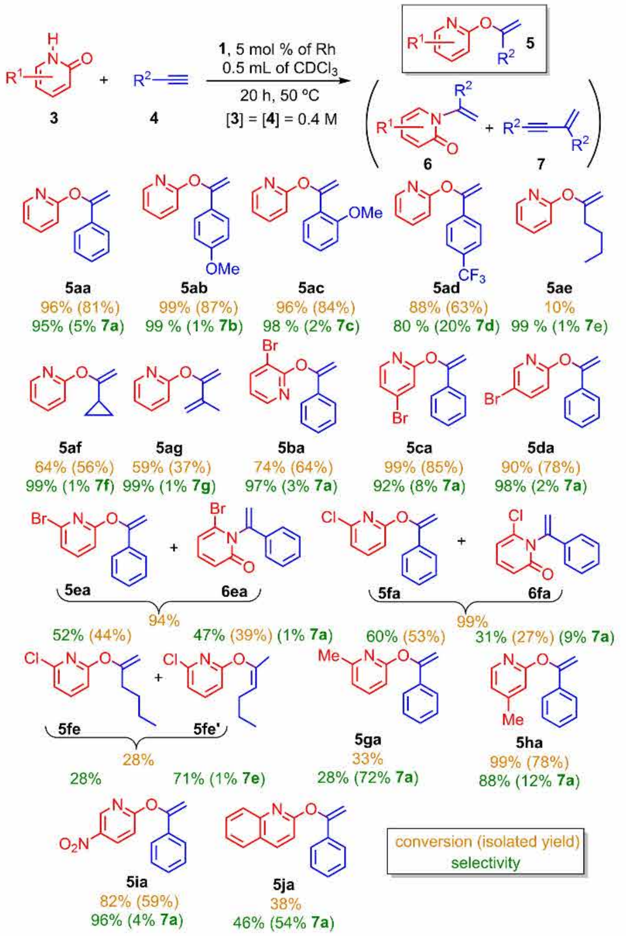

Scheme 3. Scope for the hydropyridonation of alkynes catalysed by **1**.

active substrate in this study, whereas poor conversion was obtained for 6-methyl-2-pyridone (**3g**), with the bromo counterpart **3e** lying in the middle. Substitution in other positions had only moderate influence. The alkenyl ether arising from 6-chloro-2-pyridone and 1-hexyne was obtained as a mixture of two isomers as a result of terminal to internal olefin isomerization. Finally, 4-methyl-2-pyridone (**3h**) slightly overcame the catalytic activity of parent 2-pyridone, while 5-nitro-2-pyridone (**3i**) fell behind. Other bulky, heteroatomic-substituted propargyl derivatives or internal alkynes were catalytically inefficient.

Some control experiments were performed to identify the reaction mechanism. Addition of 2-pyridone and phenylacetylene to **1** at −60 °C resulted in the immediate formation of complex **2** and no other intermediates, including Rh–H species, could be detected. Besides, H/D exchange between the *N*-deuterated 2-pyridone and the terminal proton of phenylacetylene preclude us from obtaining accurate information from deuterium labelling experiments (See Supporting Information). Catalytic tests in which 2-pyridone was replaced by phenol, *N*-methyl-2-aminopyridine, 2-thiopyridine, or 2-(hydroxymethyl)pyridine were unproductive, indicating that the presence of both N and O atoms located at 1,3-positions is essential.

The mechanism of the alkyne hydropyridonation catalyzed by **1** was studied by DFT computational analysis using 2-pyridone and phenylacetylene as model substrates (Figure 3, ΔG in $\mathrm{kcal\,mol^{-1}}$). A plausible first step is the π-alkyne and κ^1*N*-hydroxypyridine coordination to the labile precursor **1** to yield **A**, which has been selected as the energetic reference. The O–H oxidative addition seems unfeasible since the corresponding Rh–H species **K**, located $13.7\,\mathrm{kcal\,mol^{-1}}$ above **A**, requires to surmount a barrier of $31.2\,\mathrm{kcal\,mol^{-1}}$ (see Figure S124 in Supporting Information). Alternatively, we propose a hydride-free pathway entailing oxidative protonation and reductive coupling steps (Scheme 4).[20,21] Thus, the κ^1*N*-hydroxypyridine ligand of **A** can behave as an intramolecular Brønsted acid able to protonate the terminal position of the π-alkyne to form the Rh^{III}-alkenyl species **B**, via **TSAB**. Protonation of internal position of the triple bond is disfavored

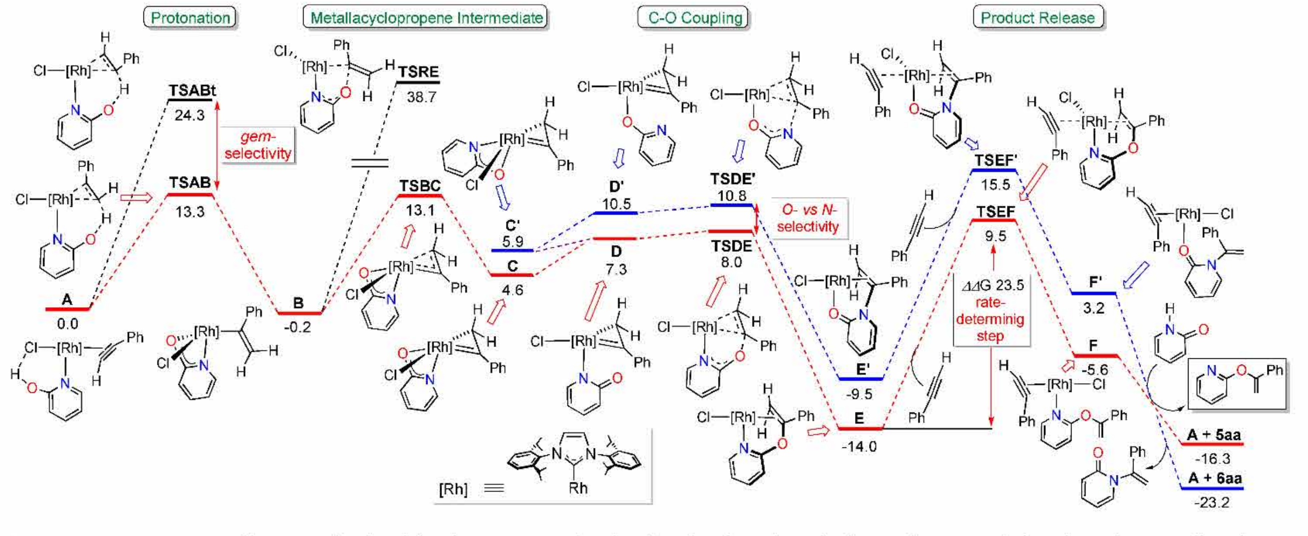

Figure 3. DFT energetic profile (ΔG in $\mathrm{kcal\,mol^{-1}}$, relative to **A** and isolated molecules) along hydropyridonation of phenylacetylene. *O*-alkenylation, red pathway, and *N*-alkenylation, blue pathway.

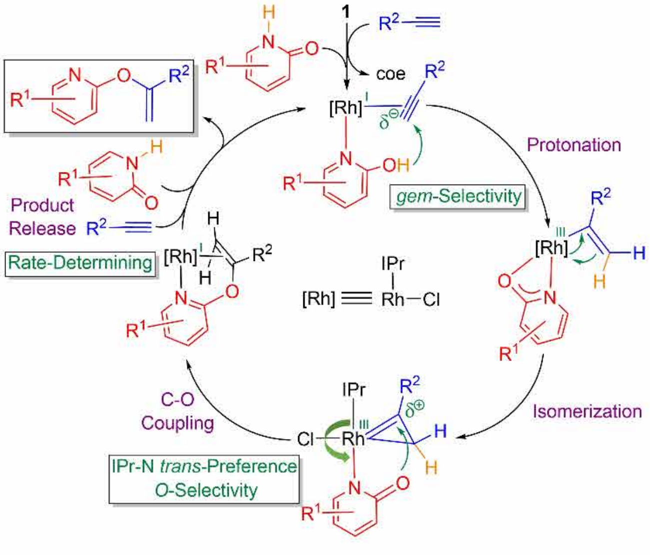

Scheme 4. Mechanistic proposal for alkyne hydropyridonation.

(**TSABt**, $\Delta\Delta G$ of 11.0 kcal mol^{-1}), which ultimately determines the high *gem*-selectivity.

The direct C–O reductive coupling within **B** was found to be unaffordable under catalytic conditions,[22] which is in sharp contrast to that observed for alkenyl-alkynyl C–C coupling in alkyne dimerization.[20] However, the isomerization of the alkenyl derivative **B** to the metallacyclopropene species **C**, though destabilized by 4.8 kcal mol^{-1}, opens an accessible pathway to the *O*-alkenyl-oxypyridine species **E** (-14.0 kcal mol^{-1}), in agreement with the isolation of **2**. This stage entails the decoordination of the oxygen atom of the pyridonato (**C**→**D**) and subsequent *O*-nucleophilic attack, in turn facilitated by increased positive charge at the carbenic carbon atom of the metallacyclopropene in **D** (see Figure S131 in Supporting Information).[21c,23] In contrast, the attack of the nitrogen atom has a higher barrier (**TSDE′**, $\Delta\Delta G$ 2.8 kcal mol^{-1}), in accordance with the preferential *O*-alkenylation. Most likely, the ultimate reason for the chemoselectivity could be the preferred coordination of a pyridine scaffold *trans* to IPr, thus causing a seesaw effect responsible of the *O*-nucleophilic attack.[24] Moreover, the particular stereoelectronic properties of the bulky powerful electron releasing IPr might play a role in the stabilization of metallacyclopropene species (See Figure S125 in Supporting Information for comparison with a PPh$_3$ analogue). In fact, these uncommon structures can be considered as essential intermediates in the *gem*-selective alkyne hydroalkoxylation in analogy to the role played by vinylidenes in the formation of *E*/*Z* isomers.[25]

The catalytic cycle ends with the associative release of the alkenyl ether (**TSEF**, 23.5 kcal mol^{-1}), which is the rate-determining step (see Figure S126 in Supporting Information). At this point, the interplay between steric hindrance and the high *trans* effect imparted by the NHC might trigger the release of the catalytic product from **2**.[19a] It is interesting to note that the final *N*-alkenyl product is more stable than the *O*-alkenyl one indicating a kinetic control under catalytic conditions. Calculations involving the 1-hexyne show a higher barrier of 25.9 kcal mol^{-1}, consistent with the slower reaction rate. Besides, the higher rate observed for 6-chloro-2-pyridone **3f** is likely due to steric effects, which might be responsible for the decrease of the product release barrier, whereas the similar energies of **5fa** and **6fa** account for the formation of both isomers (See Supporting Information).

Analysis of the energetic profiles of Figure 3 reveals that isomerization of *O*-alkenyl-oxypyridines to thermodynamically preferred *N*-alkenyl derivatives is feasible by breaking back the C–O bond (overall barrier for **A**+**5aa**→**C** via **TSEF**: 25.8 kcal mol^{-1}).[23a] Thus, heating isolated **5aa** or **5ia** in the presence of catalytic amounts of **1** for 72 h at 90 °C resulted in the formation of the *N*-alkenyl-pyridone derivatives **6** (Figure 4). Formation of **6** was not observed when simply heating the NMR tube containing crude **5** from catalytic hydropyridonation, likely due to decomposition of active species. In fact, the isomerization did not proceed either in the absence of **1** or using $[\mathrm{Rh}(\mu\text{-Cl})(\eta^2\text{-coe})_2]_2$ as catalyst. Given the small difference in the chemical shift of intuitively representative C$_2$-imidic (**5aa**, $\delta = 163.3$ ppm) or C$_2$-amidic (**6aa**, $\delta = 162.2$ ppm) atoms in the ^{13}C{^{1}H}-APT NMR spectra, the 2D ^{1}H-^{15}N long-range HMQC NMR experiment was key to the characterization of **6**. Thus, correlation between one olefinic proton and the nitrogen atom was observed for **6**, but it is absent in **5** where both atoms are located five bonds away. Similarly to the formation of **2**, the *N*-alkenyl-pyridone derivative **6aa** reacts with **1** to yield $\mathrm{RhCl[\kappa \mathit{O},\eta^2\text{-}\{C_4H_4(C{=}O)N\}\text{-}C(Ph){=}CH_2](IPr)}$ (**8**). Multinuclear NMR data agree with the proposed pyridone-alkenyl structure exhibiting a $\kappa^1 O,\eta^2$-coordination mode.

In conclusion, we have disclosed herein a Rh-NHC efficient catalytic system for *gem*-specific and *O*-selective alkyne hydropyridonation. Mechanistic studies in combination with DFT calculations support a hydride-free pathway. After initial coordination of both substrates, intramolecular oxidative protonation at the terminal position of a π-alkyne by a $\kappa^1 N$-hydroxypyridine ligand is responsible for *gem*-specificity. Since direct C–O reductive elimination within the resulting alkenyl-pyridonato intermediate was found to be unaffordable, isomerization to a metallacyclopropene species opens the way to nucleophilic attack. Chemoselectivity control towards the less

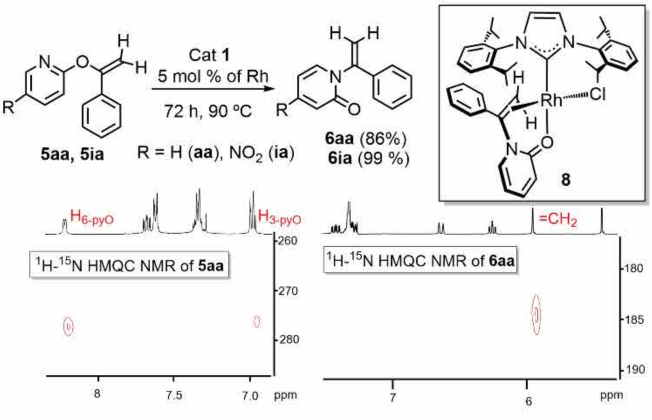

Figure 4. *O*- to *N*-alkenyl isomerization and ^{1}H-^{15}N HMQC NMR correlations.

thermodynamically favoured *O*-alkenylated products arises from the preferred *N*- vs. *O*-coordination of the κ^1pyridonato ligand in Rh-IPr systems. In addition, the key role of the bulky electron-releasing IPr ligand in the stabilization of the metallacyclopropene species has been identified. Research efforts are underway for the design of more efficient catalysts that will open future opportunities for functionalization of other biologically active heterocycles.

Acknowledgements

Financial support from the Spanish Ministerio de Ciencia e Innovación MCIN/AEI/10.13039/501100011033, under the Projects PID2019-103965GB-I00 and PGC2018-099383-B-I00, and the Departamento de Ciencia, Universidad y Sociedad del Conocimiento del Gobierno de Aragón (group E42_20R) is gratefully acknowledged.

Conflict of Interest

The authors declare no conflict of interest.

Data Availability Statement

The data that support the findings of this study are available from the corresponding author upon reasonable request.

Keywords: Alkenylation · Alkyne Hydrofunctionalization · C–O Coupling · N-Heterocyclic Carbene · Pyridone

---

[1] a) H. J. Jessen, K. Gademann, *Nat. Rev. Cancer* **2010**, *27*, 1168–1185; b) Y. Zhang, A. Pike, *Bioorg. Med. Chem. Lett.* **2021**, *38*, 127849.

[2] a) M. Torres, S. Gil, M. Parra, *Curr. Org. Chem.* **2005**, *9*, 1757–1779; b) J. G. Sośnicki, T. J. Idzik, *Synthesis* **2019**, *51*, 3369–3396.

[3] See for example: a) H. Imase, K. Noguchi, M. Hirano, K. Tanaka, *Org. Lett.* **2008**, *10*, 3563–3566; b) T. K. Hyster, T. Rovis, *Chem. Sci.* **2011**, *2*, 1606–1610; c) J.-F. Tan, C. T. Bormann, K. Severin, N. Cramer, *ACS Catal.* **2020**, *10*, 3790–3796.

[4] a) K. Hirano, M. Miura, *Chem. Sci.* **2018**, *9*, 22–32; b) A. Biswas, S. Mayti, S. Pan, R. Samanta, *Chem. Asian J.* **2020**, *15*, 2092–2109.

[5] a) R. A. Altman, S. L. Buchwald, *Org. Lett.* **2007**, *9*, 643–646; b) M. Kuriyama, N. Hanazawa, Y. Abe, K. Katagiri, S. Ono, K. Yamamoto, O. Onomura, *Chem. Sci.* **2020**, *11*, 8295–8300.

[6] a) G. Xu, P. Chen, P. Liu, S. Tang, X. Zhang, J. Sun, *Angew. Chem. Int. Ed.* **2019**, *58*, 1980–1984; *Angew. Chem.* **2019**, *131*, 2002–2006; b) J. Yang, G. Wang, H. Zhou, Z. Li, B. Ma, M. Song, R. Sun, C. Huo, *Org. Biomol. Chem.* **2021**, *19*, 394–398.

[7] a) C. Li, M. Kähny, B. Breit, *Angew. Chem. Int. Ed.* **2014**, *53*, 13780–13784; *Angew. Chem.* **2014**, *126*, 14000–14004; b) Y.-C. Wu, Y. Jhong, H.-J. Lin, S. P. Swain, H.-H. G. Tsai, D.-R. Hou, *Adv. Synth. Catal.* **2019**, *361*, 4966–4982.

[8] a) X. Zhang, Z.-P. Yang, L. Huang, S.-L. You, *Angew. Chem. Int. Ed.* **2015**, *54*, 1873–1876; *Angew. Chem.* **2015**, *127*, 1893–1896; b) S. Khan, B. H. Shah, I. Khan, M. Li, Y. J. Zhang, *Chem. Commun.* **2019**, *55*, 13168–13171.

[9] M. Breugst, H. Mayr, *J. Am. Chem. Soc.* **2010**, *132*, 15380–15389.

[10] a) P. S. Mariano, E. Krochmal, R. Beamer, P. L. Huesmann, D. Dunaway-Mariano, *Tetrahedron* **1978**, *34*, 2609–2616; b) Y. Bolshan, R. A. Batey, *Angew. Chem. Int. Ed.* **2008**, *47*, 2109–2112; *Angew. Chem.* **2008**, *120*, 2139–2142.

[11] a) X. Chew, Y. Lin, Y. H. Lim, *RSC Adv.* **2014**, *4*, 16765–16768; b) C. Sun, X. Qi, X.-L. Min, X.-D. Bai, P. Liu, Y. He, *Chem. Sci.* **2020**, *11*, 10119–10126.

[12] a) S. Z. Tasker, B. M. Brandsen, K. A. Ryu, G. S. Snapper, R. J. Staples, R. L. DeKock, C. E. Anderson, *Org. Lett.* **2011**, *13*, 6224–6227; b) G. Xu, Y. Shao, S. Tang, Q. Chen, J. Sun, *Org. Lett.* **2020**, *22*, 9303–9307.

[13] G. N. Shivers, F. C. Pigge, *J. Org. Chem.* **2021**, *86*, 13134–13142.

[14] J. Yang, G. B. Dudley, *Adv. Synth. Catal.* **2010**, *352*, 3438–3442.

[15] R. Lingayya, M. Vellakkaran, K. Nagaiah, P. R. Tadikamalla, J. B. Nanubolu, *Chem. Commun.* **2017**, *53*, 1672–1675.

[16] P. Singh, A. G. Cairns, D. E. Adolfsson, J. Ådén, U. H. Sauer, F. Almqvist, *Org. Lett.* **2019**, *21*, 6946–6950.

[17] a) L. A. Paquette, *J. Org. Chem.* **1965**, *30*, 2107–2108; b) R. M. Acheson, P. A. Parker, *J. Chem. Soc. C* **1967**, 1542–1543; c) B. Weinstein, D. N. Brattesani, *J. Org. Chem.* **1967**, *32*, 4107–4108; d) L. Mola, J. Font, L. Bosch, J. Caner, A. M. Costa, G. Etxebarría-Jardí, O. Pineda, D. de Vicente, J. Vilarrasa, *J. Org. Chem.* **2013**, *78*, 5832–5842.

[18] See references therein: L. Rubio-Pérez, R. Azpíroz, A. Di Giuseppe, V. Polo, R. Castarlenas, J. J. Pérez-Torrente, L. A. Oro, *Chem. Eur. J.* **2013**, *19*, 15304–15314.

[19] For C–P see: a) A. Di Giuseppe, R. De Luca, R. Castarlenas, J. J. Pérez-Torrente, M. Crucianelli, L. A. Oro, *Chem. Commun.* **2016**, *52*, 5554–5557; for C–S see: b) L. Palacios, Y. Meheut, M. Galiana-Cameo, M. J. Artigas, A. Di Giuseppe, F. J. Lahoz, V. Polo, R. Castarlenas, J. J. Pérez-Torrente, L. A. Oro, *Organometallics* **2017**, *36*, 2198–2207; for C–N see: c) R. Azpíroz, A. Di Giuseppe, V. Passarelli, J. J. Pérez-Torrente, L. A. Oro, R. Castarlenas, *Organometallics* **2019**, *38*, 1695–1707; for C–O see: d) M. Galiana-Cameo, V. Passarelli, J. J. Pérez-Torrente, A. Di Giuseppe, R. Castarlenas, *Eur. J. Inorg. Chem.* **2021**, 2947–2957.

[20] M. Galiana-Cameo, A. Urriolabeitia, E. Barrenas, V. Passarelli, J. J. Pérez-Torrente, A. Di Giuseppe, V. Polo, R. Castarlenas, *ACS Catal.* **2021**, *11*, 7553–7557.

[21] a) R. Shen, T. Chen, Y. Zhao, R. Qiu, Y. Zhou, S. Yin, X. Wang, M. Goto, L.-B. Han, *J. Am. Chem. Soc.* **2011**, *133*, 17037–17044; b) U. Gellrich, A. Meißner, A. Steffani, M. Kähny, H.-J. Drexler, D. Heller, D. A. Plattner, B. Breit, *J. Am. Chem. Soc.* **2014**, *136*, 1097–1104; c) L.-J. Song, T. Wang, X. Zhang, L. W. Chung, Y.-D. Wu, *ACS Catal.* **2017**, *7*, 1361–1368.

[22] For an example of hampered C–O reductive elimination within Rh-alkenyl species see: T. D. Marder, D. M.-T. Chan, W. C. Fultz, D. Milstein, *J. Chem. Soc. Chem. Commun.* **1988**, 996–998.

[23] a) H. Chen, D. Harman, *J. Am. Chem. Soc.* **1996**, *118*, 5672–5683; b) M. Zhang, G. Huang, *Chem. Eur. J.* **2016**, *22*, 9356–9365.

[24] L. Palacios, A. Di Giuseppe, R. Castarlenas, F. J. Lahoz, J. J. Pérez-Torrente, L. A. Oro, *Dalton Trans.* **2015**, *44*, 5777–5789.

[25] F. Kakiuchi, S. Takano, T. Kochi, *ACS Catal.* **2018**, *8*, 6127–6137.

[26] Deposition number 2114691 for **2** contains the supplementary crystallographic data for this paper. These data are provided free of charge by the joint Cambridge Crystallographic Data Centre and Fachinformationszentrum Karlsruhe Access Structures service.

Manuscript received: December 13, 2021
Accepted manuscript online: March 8, 2022
Version of record online: March 19, 2022